The Response of Concave Singly Curved Fibre Reinforced Moulded Sandwich and Laminated Composite Panels to Blast Loading

Dissertation presented in partial fulfilment of the
requirements of the degree MSc in Mechanical Engineering

Ismail B Ghoor

Supervisors:
A/Prof. Chris von Klemperer
Prof. Genevieve Langdon

October 2017

Blast Impact and Survivability Research Unit
Department of Mechanical Engineering
University of Cape Town

Abstract

Composite materials are increasingly being used in a wide range of structural applications. These applications range from bicycle frames and building facades to hulls of marine ships. Their popularity is due to the high specific strength and stiffness properties, corrosion resistance, and the ability to tailor their properties to a required application. With the increasing use of composites, there is a need to better understand the material and damage behaviour of these structures.

In recent years, the increased frequency of wars and terror attacks have prompted investigations into composite failure processes resulting from air-blast. Most of the research has been focused on flat panels, whereas there is relatively little on curved structures. This dissertation reports on the effect of air-blast loading on concave, singly curved fibre reinforced sandwich and composite panels.

Sandwich panels and equivalent mass glass fibre laminates were manufactured and tested. Three types of curvature namely a flat panel (with infinite curvature), a curvature of 1000 mm radius and a curvature of 500 mm radius were produced, to determine the influence of curvature on panel response. The laminates were made from 16 layers of 400 g/m^2 plain weave glass fibre infused with Prime 20 LV epoxy resin. The sandwich panels consisted of a 15 mm thick Airex C70:75 core sandwiched between the 12 layers of 400 g/m^2 plain weave glass fibre and infused with Prime 20 LV epoxy resin. This arrangement produced a balanced sandwich panel with 6 layers of glass fibre on the front and back respectively. For all panels, vacuum infusion was used to manufacture in a single shot process. Mechanical properties of samples were tested for consistency in manufacturing. It was found that mechanical properties of the samples tested were consistent with low standard deviations on tensile and flexural strength.

The panels were tested in the blast chamber at the University of Cape Town. Blast specimens were clamped onto a pendulum to facilitate impulse measurement. Discs of plastic explosive, with charge masses ranging from 10 g to 25 g, were detonated. After blast testing, a post-mortem analysis of the damaged panels was conducted.

Post-mortem analysis revealed that the failure progression was the same irrespective of curvature for both the sandwich panels and the laminates. Sandwich panels exhibited the following failure progression: delamination, matrix failure, core crushing, core shear, core fragmentation, core penetration and fibre fracture. The laminates displayed the following progression: delamination, matrix failure and fibre fracture. Curved panels exhibited failure initiation at lower charge masses than the flat panels. As the curvature increased, the failure modes initiated at lower charge masses. For example, as the charge mass was increased to 12.5 g the front face sheets of the flat and the 1000 mm radius sandwich panels exhibited fibre fracture, but the 500 mm radius sandwich panel exhibited fibre fracture and rupture through the thickness of the front face sheet. The 500 mm radius laminate exhibited front face failure earlier (15 g) than the 1000 mm radius (22.5 g) and flat panel (20 g). Curved laminates exhibited a favoured delamination pattern along the curved edges of the panel for both 1000 mm and 500 mm radii laminates. As the curvature increased, more delamination was evident on the curved edges. The curved panels displayed more severe damage than flat panels at identical charge masses. Curved sandwich panels experienced through thickness rupture at 20 g charge mass whereas the curved laminates did not exhibit rupture at 25 g charge mass. The flat laminates were the most blast resistant, showing no through-thickness penetration at 25 g (the highest charge mass tested) and initiated failure modes at higher charge masses when compared to the other configurations.

Declaration

I, Ismail Bashyr Ghoor fully understand the meaning of plagiarism and declare that each significant contribution to, and quotation in, this MSc dissertation from the work, or works, of other people have been acknowledged through the use of the IEEE convention for citation and referencing. This dissertation has been submitted to the Turnitin module (or equivalent similarity and originality checking software) and I confirm that my supervisor has seen my report and any concerns revealed by such have been resolved with my supervisor.

Signed by candidate

I.B. GHOOR

October 2017

Acknowledgements

The author would like to thank the following people for their significant contribution to the present work:

- The National Research Foundation who provided financial support for this project.
- BISRU (Blast Impact and Survivability Research Unit) for the financial support and the all the students in the unit, who made the workspace a fun, productive environment.
- James Stock, who was my “buddy” in the composites lab and a great research fellow.
- Vinay Shehkar, who helped debugging my model and provided helpful advice.
- Sherlyn Gabriel, who helped tirelessly in manufacturing, was a great sounding board for ideas and a friend who was always there ready to help and encourage me to finish.
- Aamirah Sonday, the last minute proofreader and editor.
- Deloitte Digital and Director Valter Adao for granting me a six month sabbatical to finish this MSc.
- Oom Peter, Dillon, Grant, Brendon, Horst, Gavin, Oom Willie, Oom Hubert, Tyrone and Oom Pierre, who helped to manufacture my rig and provided critical insight on certain aspects of manufacturing.
- University of Cape Town’s ICTS High Performance Computing team on whose facilities computations were performed.
- All those with whom I have had small impromptu discussions in corridors whose names are too many to mention.
- My supervisors, A/Prof. Chris von Klemperer and Prof. Genevieve Langdon who read and re-read my dissertation, provided guidance and support, and arranged for the financial aid to finish this MSc.
- My parents, family and close friends - for this has not only been a journey for me but for them as well. I cannot thank them enough for their support and fierce encouragement to finish this MSc.
- Lastly to the One who holds my soul in His Hand and who has never left my side throughout all my difficulties and has given me the strength and commitment to finish this MSc.

Contents

List of Figures

List of Tables

Chapter 1

Introduction

1.1 Background

The number of people impacted by explosive violence is on the increase [1]. The total number of incidents has increased from 30,301 (2011) to 45,624 (2016). Civilian casualties make up an average of 76%, with this number rising to 92 % in populated areas [1]. Figure 1.1 shows a map of explosive incidents. It shows that 111 countries reported explosive violence over the last 6 years and that incidents occur throughout the world. There is a need to protect people from accidental and malicious explosive incidents, and this requires a sound knowledge of structural response to blast loading. This endeavour makes the understanding of blast response not only useful, but crucial.

Figure 1.1: World map detailing the number of explosive incidents per country from 2011 to 2016 [1]

Composite materials are increasingly being used in a wide range of structural applications [2]. This is due to their many advantages such as high specific strength and stiffness properties, corrosion resistance and the ability to tailor their properties to a required application to name but a few [2, 3]. Fibre-reinforced polymers are used in a number of applications which range from bicycle frames to hulls of marine ships [2, 4]. They are also used in the manufacture of hybrid structures such as sandwich panels [2, 4]. With increasing use of composites, there is a need to understand the material and damage behaviour of these structures [2,4]. Some examples of composites in everyday use are displayed in Figure 1.2.

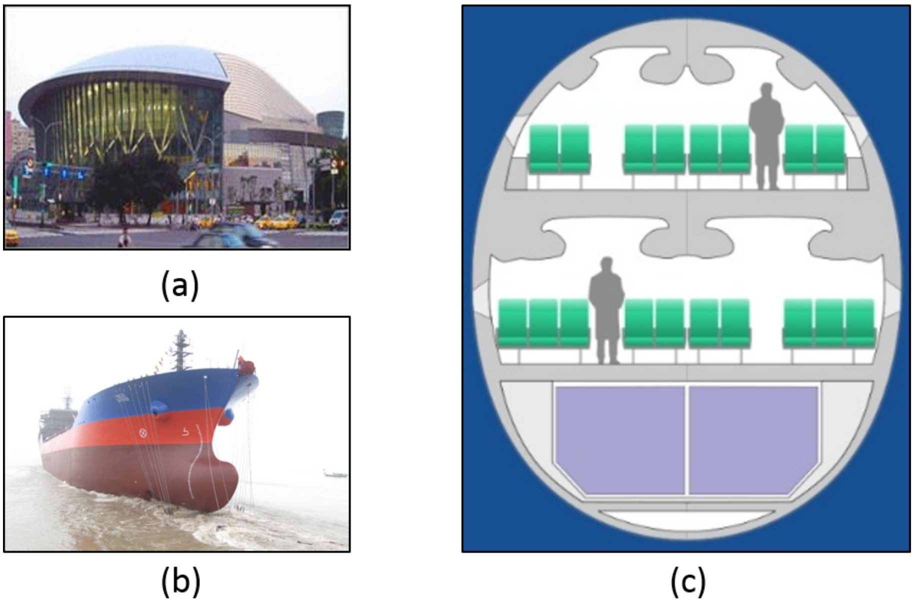

Figure 1.2: Examples of curved geometries (a) A building with curved a roof [5]. (b) Ship hull [6]. (c) A cross section of an A380 fuselage [7].

While there is much research related to steel structures and their response is well understood, there is relatively little research on composites and their response with respect to blast loading that is publicly available. In recent years, a number of investigations into the failure processes of composites in air blast have been performed with a focus on E glass and carbon fibre composites [2]. These investigations tend to focus on flat panels and there is relatively little on curved structures [8–10]. At the time of writing there has been no investigation into the blast response of concave sandwich and laminate composites in the available literature. This project aims to investigate the response of singly curved concave composites to blast loading.

1.2 Objectives and Method

The aim of the research is to investigate the response of singly concave curved composite panels to blast loading. The objectives of the dissertation are:

- To investigate the failure initiation of concave singly curved FRP composite structures
- To assess the manufacturing of the composite panels with respect to:
    - Ease of manufacture
    - Consistency of material properties
- To investigate the influence of geometry on failure modes
- To investigate the failure initiation of concave singly curved FRP composite structures
- To investigate the influence of geometry on the severity of failure modes
- To ascertain which geometry and material has better blast resistance

In order to complete the objectives, equivalent mass glass fibre sandwich panels with three types of curvature namely a flat panel (with infinite curvature), a curvature of 1000 mm radius and a curvature of 500 mm radius were manufactured. The panels were blast tested and post-mortem failure analysis was conducted. Failure analysis was conducted through visual inspection of the observed failure modes. Failure modes were noted and the panels were photographed. Failure initiation maps were created to ascertain the onset of failure mode initiation for all panel types. A failure masking technique was used to investigate the spatial distribution of failure of all panel types. Image processing software was used to calculate the areas of delamination. Impulse readings for different panel types were also collected, analysed and compared.

1.3 Report Outline

Chapter 2 contains a review of relevant literature on blast loading and the response of composite structures. Chapter 3 details the manufacturing of the blast specimens and the material strength testing samples. Results from the material strength testing are presented in Chapter 4 and discussed with respect to mechanical property variability. Chapter 5 describes the experimental design and stand-off distance determination, blast testing apparatus and experimental method. Chapter 6 reports the results of the blast testing in the form of recorded impulses, failure modes encountered, failure progression, delamination area and debonded lengths. Chapter 7 discusses the results obtained in Chapter 6 with respect to literature. Chapter 8 summarises the conclusions and provides recommendations for future work.

Chapter 2

Literature Review

This chapter starts with a brief introduction to explosions and the different types of blast loading categories. It then describes various Fibre-Reinforced Polymer (FRP) composites, materials and manufacturing options. Lastly, it describes research on the response of blast loaded composite structures with special attention to FRP laminates and FRP sandwiches.

2.1 An Explosion

An explosion is defined as a sudden and rapid release of energy into the surrounding environment [11–13]. The energy could come from many possible sources [11]. According to Gregory [14], an explosive is a "solid or liquid substance or mixture of substances which, on the application of a suitable stimulus to a small portion of the mass, is converted *in a short interval of time* into other more stable substances, largely or entirely gaseous, with the development of high pressure and heat". The stimulus may be provided accidentally by friction, impact or heat, or under controlled conditions by the shock wave produced by a detonator incorporated into an explosive charge [14].

Once the explosive source is detonated, there is a localised accumulation of energy at the point of detonation. This energy is abruptly dissipated into the environment in the form of light, heat, sound and products of the detonation mostly in the form of gases [13, 15]. The gases that are produced are released rapidly at very high temperatures. This leads to a wave-type propagation that is transmitted spherically through an unbounded surrounding medium. If the unbounded surrounding medium is air, then the produced gases will pile up against the surrounding air causing a region of highly compressed air. The region of compressed air is known as the blast wave, which is characterised by an almost instantaneous increase in pressure from the ambient pressure (P_o) to the peak overpressure (P_s) [11, 13, 16, 17]. As the blast wave moves away from the source at supersonic speeds, the velocity and pressure subsequently decrease [11]. It should be noted that the pressure history of a blast wave is extremely complex and for practical purposes is simplified for structural analyses.

2.1.1 Blast Wave

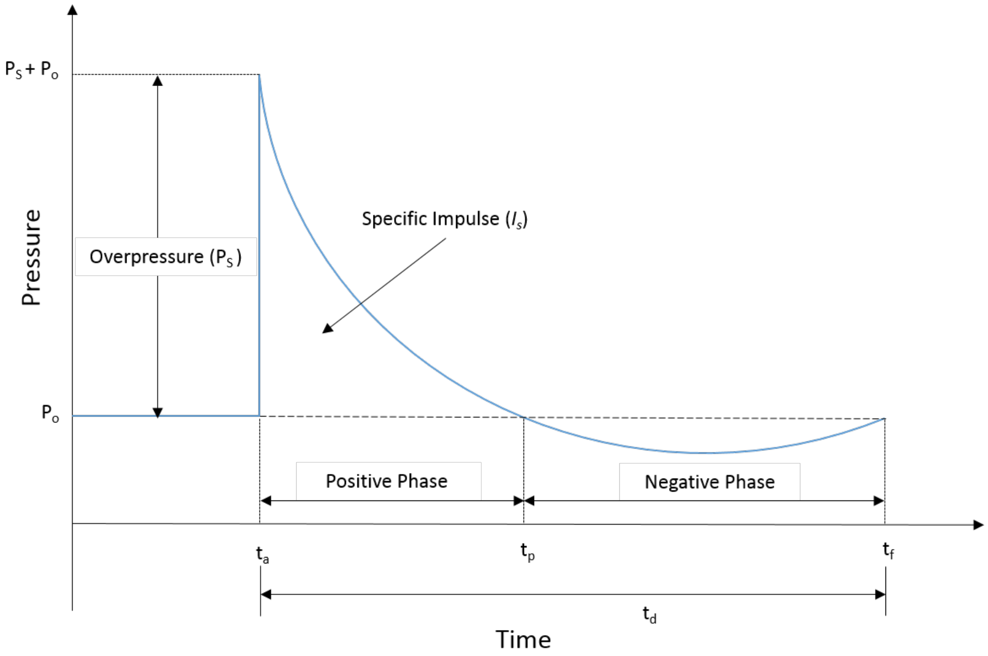

Figure 2.1: Typical free air pressure profile of a far-field explosion adapted from [15]

Figure 2.1 shows a simplified pressure profile for a free air blast wave passing through a point in space in the far-field. Prior to the arrival of the blast wave, the pressure at a point is at ambient pressure P_o. Upon arrival of the blast wave at time t_a there is an instantaneous pressure increase, known as the overpressure P_s, from atmospheric pressure (P_o) to a peak incident pressure ($P_s + P_o$). As the blast wave moves past the point, the pressure decays in a quasi-exponential manner back to atmospheric pressure [11,12,17]. At time t_p, the shock wave pressure drops below atmospheric pressure, due to the contraction of the over expanded gas in the positive phase and the reversal of particle flow [11,13]. At time t_f, the pressure returns to atmospheric pressure as equilibrium is reached. The period from t_a to t_p is know as the positive phase of the blast wave. The period from t_p to t_f is known as the negative phase of the blast wave. It should be noted that the pressure in the positive phase is much larger than in the negative phase. It would be safe to assume that the pressure in the negative phase does not have a large effect on the structural integrity of most structures [17]. The blast duration t_d is measured from the arrival time t_a to the time the pressure finally returns to ambient pressure t_f [13]. The magnitude of peak overpressure is dependent on the type and mass of the explosive material, the location of the detonation point relative to the point/surface of interest and whether any magnification or refraction occurs prior to interaction with a structure [18].

2.1.2 Modified Friedlander's Equation

The area under the pressure-time graph in Figure 2.1 is referred to as the specific impulse. The positive phase of the pressure history is more important for design of rigid structures and components [15]. However if the design consideration is the relative flexibility of the structure, then the negative phase of the pressure history also needs to be considered [15].

The modified Friedlander equation (Equation 2.1) can be used to approximate the positive phase of the incident pressure pulse over time for $t_a \leq t \leq t_p$ [15].

$$P_s(t) = (P_s + P_o)(1 - \frac{t - t_a}{t_p - t_a})\mathrm{e}^{(\frac{-(t-t_a)}{\theta})} \tag{2.1}$$

Where t is the time relative to the detonation of the charge and θ is the time constant of the pressure pulse [15].

The positive incident impulse can be calculated by integrating the positive phase of the pressure history. This is shown in Equation 2.2:

$$i_s = \int_{t_a}^{t_p} P_s(t)dt \tag{2.2}$$

2.1.3 Scaling Laws

One of the most critical parameters for blast load computations is the distance of the detonation point from the structure of interest [17, 18]. The peak pressure and velocity of a blast wave decrease rapidly with increasing stand-off. The effect of distance on blast wave characteristics is often accounted for by using scaling laws [17]. The most common scaling laws are Hopkinson-Cranz and Sachs [17]. Both formulations state that similar blast waves can be produced at a point by different weight charges (assuming the same explosive and charge geometry) which are situated at the same scaled distance from the target under the same atmospheric conditions [17]. It is important to note that Sachs scaling can also be used in cases of different atmospheric conditions [17]. According to the Hopkinson-Cranz law, a dimensionless scaled distance Z can be introduced and is described in Equation 2.3:

$$Z = \frac{R}{\sqrt[3]{W}} \tag{2.3}$$

where R is the distance from the detonation source to the point of interest in meters (m) and W is the mass of the explosives in kilograms (kg) [17].

Now suppose one has an explosive charge of mass W_1 and characteristic dimension d_1 at a distance R_1 from the point of interest. After detonation a blast wave with peak overpressure P_1, impluse i_1, duration t_{o1},with arrival time t_{a1}. Using Equation 2.3 the Z value would be

$$Z = \frac{R_1}{\sqrt[3]{W_1}} \tag{2.4}$$

Thus if one wanted a blast wave with the same peak overpressure P_1 and similar form with a mass of explosive of W_2 then the characteristic dimension $d_2 = Zd_1$, situated at a distance $R_2 = ZR_1$. Also at any given point in the domain one would have impulse $i_2 = Zi_2$, a duration of $t_{o2} = Zt_{o1}$ and an arrival time of $t_{a2} = Zt_{a1}$ [17].

2.2 Blast Loading Categories

Blast loading of a structure can be classified into two main categories defined by their confinement. For the purposes of this study the focus will be on unconfined explosions.

2.2.1 Unconfined Blast Loading

Unconfined explosions are those that produce shock waves that propagate through the air without confinement [15]. Unconfined explosions can be one of three types [15] [12]:

- Free-air explosion: these occur in free air and produce a shock wave which propagates radially outward. The blast wave strikes the target and the wave does not encounter any obstructions [12,15].
- Air explosion: these explosions are located at a distance from and above the protective structure so that the ground reflections of the initial wave occur prior to the arrival of the blast wave [12,15]. Air explosions are limited to heights up to two to three times that of a one or two storey building.
- Surface explosion: A surface explosion is located on or very near the ground. The blast waves are amplified at the point of detonation due to the ground reflections.

2.2.2 Uniform and Localised Loading

Much of the experimental blast literature is divided into uniform and localised blast loading. According to the Technical Manual TM 5-1300 [12],a localised loading condition is defined by a load concentration to a localised region of the test area, whereas the uniform loading condition is where the load distribution is spread evenly across the test area.

Localised loading conditions are developed by detonating the charge in close proximity to the target. Langdon et al [19, 20] achieved this by using polystyrene pads between the charge and the target (see Figure 2.2 a). In Figure 2.2 b) Shekhar [21] used a polystyrene bridge, similar to Langdon et al [22] and Sinclair [23]. Ackland et al suspended the explosive from a wooden frame (see Figure 2.2 c)) [24] to create localised loading. Shen et al [9] suspended the explosive from a piece of a wire (see Figure 2.2 d)). Uniform loading conditions can be approximated by allowing a blast wave to develop and expand in a steel tube, as achieved by Langdon et al [19].

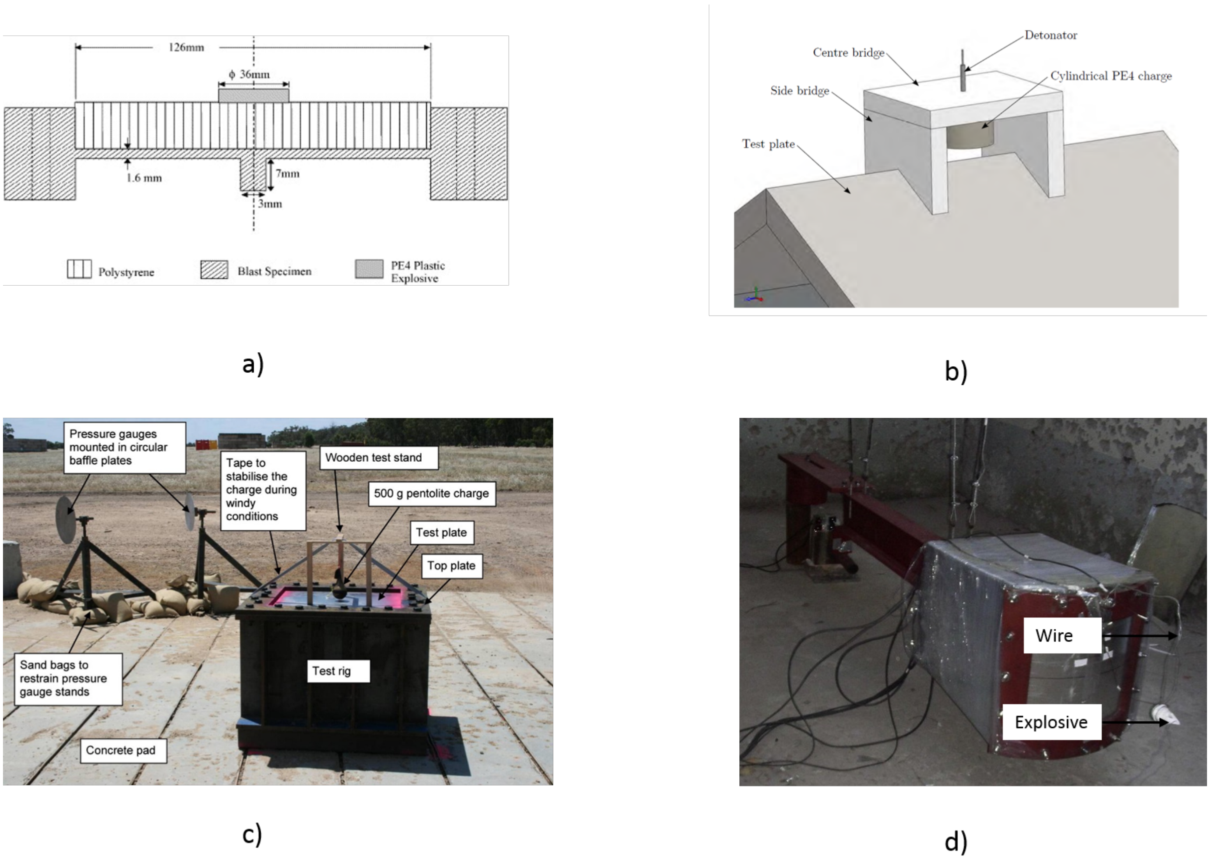

Figure 2.2: a) Schematic of the localised loading conditions using a polystyrene pad [19]. b) Schematic of a localised loading using a polystyrene bridge [21]. c) A setup using a wood frame [24]. d) A setup suspending the explosive with a piece of wire [9].

2.3 Composites

2.3.1 Basic Concept

A composite structure is formed by the combination of two or more distinct materials (or constituents) to form a new material with enhanced properties [25–29]. Jones [28] makes the point that the constituents need to be combined on a macroscopic level and be able to be identified with the naked eye. This definition is used to make a case that composites are different to alloys which "mix" on a molecular level. Gibson [25] points out that in the past, composites were usually made from macroscopic constituents, hence the reason for the previous definitions being worded as they are. Composite technology has advanced over the last few decades and has seen a marked decrease in reinforcement size leading to "nanocomposites" which have nanometer reinforcements [25].

Composites usually comprise a reinforcement held together in a binder [29]. The reinforcement could be particles, flakes or fibres. It should be noted however that relatively long fibres are more effective reinforcement than particles or flakes [29]. For the purpose of this work, fibre-reinforced polymeric composites will be focused on. Some examples of composites include straw reinforced clay bricks and fibreglass boats (which are usually made of polymer resin reinforced with glass fibre) [29].

The main advantage that composites have is that, if designed well, they will display the best qualities of their constituent parts [28, 29]. Sometimes those qualities are not possessed by the individual constituents themselves, but only by the newly formed composite [28, 29]. The attractiveness of composites is due to the fact that one is able to create a material for a specific design task that needs to be accomplished.

2.3.2 Constituents of a FR Composite

The main components of a fibre-reinforced composite are the fibres and the matrix. The stiffness and strength of the composite is provided by the fibres. The matrix provides a load transfer mechanism between the composite and external loads by binding the fibres together. The matrix also protects the fibres from environmental attack [29].

2.3.2.1 Fibres

Fibres can be of many types and are classified accordingly to their aspect ratio. The aspect ratio is the length-to-diameter ratio of a fibre. Continuous fibres have large aspect ratios whereas discontinuous fibres have small aspect ratios [30]. Continuous fibre composites tend to have a preferred orientation while discontinuous fibres generally have random orientation. Examples of different fibre types are shown in Figure 2.3.

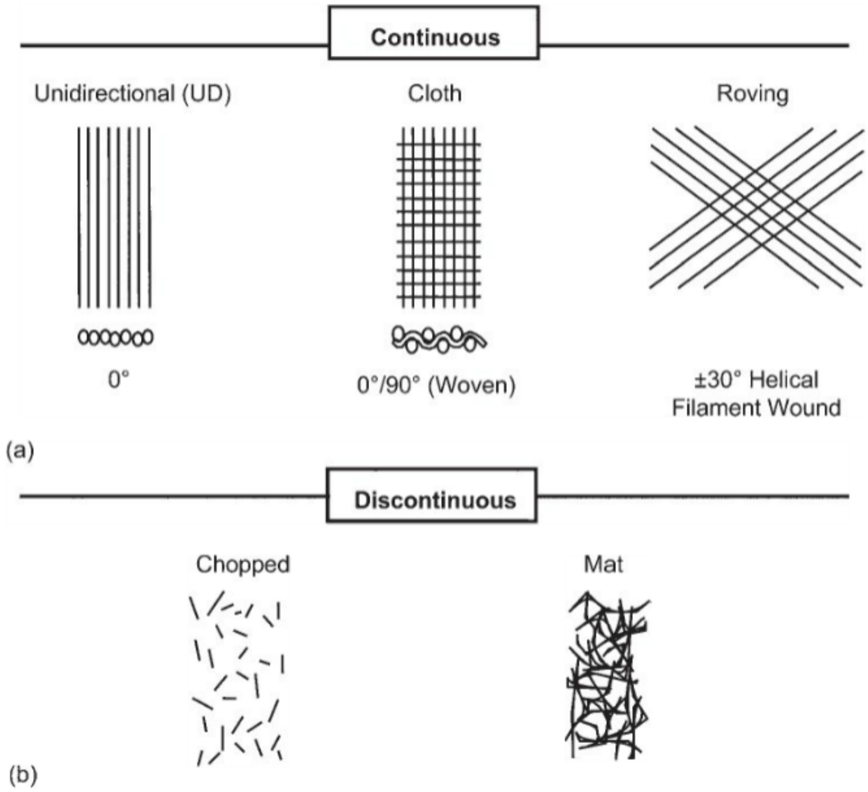

Figure 2.3: Typical types of fibre arrangements in fibre-reinforced composites [30]

Textile reinforcements provide an alternative to using continuous or discontinuous fibres as reinforcements, and may lead to increased performance while reducing manufacturing costs. Textile designs and manufacturing processes have led to the following classifications of textile structures [29]:

- 1D Textile, or individual threads. These can be further categorised into [29]:
  - A strand which is an untwisted bundle of continuous filaments (fibres)
  - A yarn or thread is a twisted strand
  - A roving is a collection of strands and they may be twisted or untwisted.
- 2D Textile, or fabric which is produced by laying threads in various patterns as to make a 2D structure (Figure 2.4). These come in mainly two forms [29]:
  - Non-woven fabrics which are usually randomly orientated 1D textiles pressed with a binder or stitched together.
  - Woven fabrics which are made by interlacing yarns in a weaving machine to form a two-dimensional reinforcement. The yarns are normally interlaced along two orthogonal directions. The yarn along the weaving direction is called the warp yarn. The interlacing yarn orthogonal to the warp is called the fill or weft yarn. This type of

weaving architecture is called the biaxial woven fabric. This is due to the balanced reinforcing properties in both the warp and weft directions.

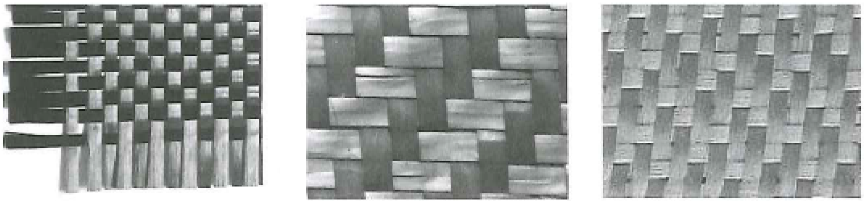

plain twill satin

triaxial stitched basket

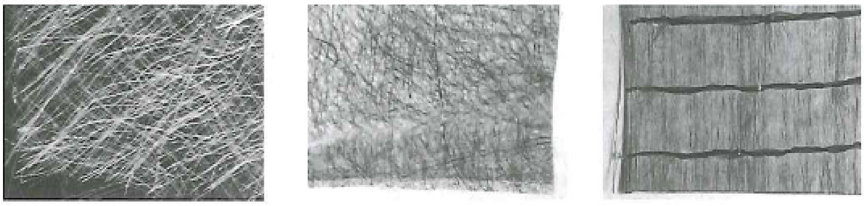

continuous strand mat veil stitched

Figure 2.4: Examples of 2D textiles [29]

2.3.2.2 Matrix

Many materials can be used for the matrix such as polymers, metals and ceramics [25, 29]. Polymer matrices are the most common, due to the ease of fabrication and the potential to manufacture complex parts with low tooling and capital investment [29]. Polymers come in two basic types which can be either thermoset or thermoplastic in nature.

Generally, a polymer is called a resin system during processing, and a matrix after it has cured [29]. Thermoset resins are the most common resin systems used in composite manufacturing [29], due to their ease of processing and wide range of use [29]. In order to initiate the resin to cure, one needs to add a catalyst or a hardener. This is an irreversible reaction and might be endo- or exothermic in nature [29]. Cure times vary depending on the type of hardener cure used.

Polyesters, vinyl esters, phenolics and epoxies are the most common thermoset resins used in composite manufacturing [29]. Barbero [29] states that although vinyl esters are more ductile and corrosion resistant than polyesters, polyesters have moderate physical properties and are cost effective. Epoxy resins exhibit higher elongation to failure and higher service temperature than most other thermoset resins and are usually considered high performance resins [29]. Phenolic resins are chosen in applications where limiting smoke generation and longer-term flame spread are important characteristics [29]. A summary of some typical thermoset resin properties are given in Table 2.1.

Table 2.1: Tensile modulus and strength of selected resins [29, 31]

Thermoset Resins	Tensile Modulus (GPa)	Tensile Strength (MPa)
Polyester		
Orthophthalic	3.4	55.2
Isophthalic	3.4	75.9
Vinyl Ester		
Derakane	3.4	82.7
Epoxy		
8551-7	4.089	99.2
Prime 20LV	3.2	75

2.3.3 Manufacturing of Composites

There are many different types of composites manufacturing processes that exist but the choice of manufacturing technique is matrix and fibre dependant. These include, but are not limited to [29]:

- Hand lay-up (Also known as wet lay-up).
- Prepreg lay-up.
- Vacuum bag moulding.
- Autoclave processing.
- Compression moulding.
- Resin transfer moulding (RTM).
- Vacuum assisted resin transfer moulding (VARTM).
- Pultrusion.
- Filament winding.

The processing of polymer matrix composites involves the following unit operations:

1. Fibre placement in the required orientation.
2. Impregnation of the fibres with resin.

3. Consolidation of the impregnated fibres to remove excess resin, air and volatile substances.
4. Cure or solidification of the polymer.
5. Extraction from mould.
6. Finishing operations, such as trimmings, etc.

All of these operations need to be executed, although some of the manufacturing processes, are performed differently and often combined to save time. Barbero [29] states that VARTM over the last decade has become very popular. This will be examined in more detail.

2.3.3.1 Vacuum Assisted Resin Transfer Moulding (VARTM)

During a Vacuum Assisted Resin Transfer Moulding (VARTM) operation a vacuum is applied to the bag outlet and resin is drawn into the mould and through the part that needs to be impregnated with the resin [29]. A schematic of the process is shown in Figure 2.5. Epoxy, polyester, vinyl ester and phenolic resins can all be used for VARTM. A typical sequence of events in a VARTM operation can be divided into four main steps featured in Figure 2.6.

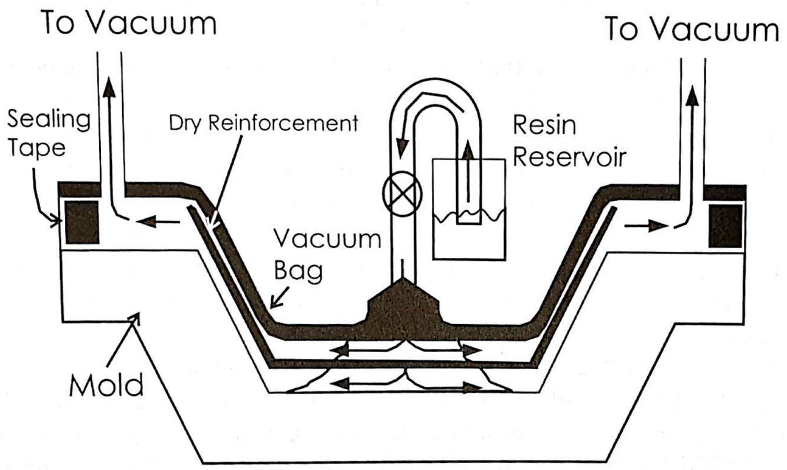

Figure 2.5: Vacuum Assisted Resin Transfer Moulding (VARTM) [29]

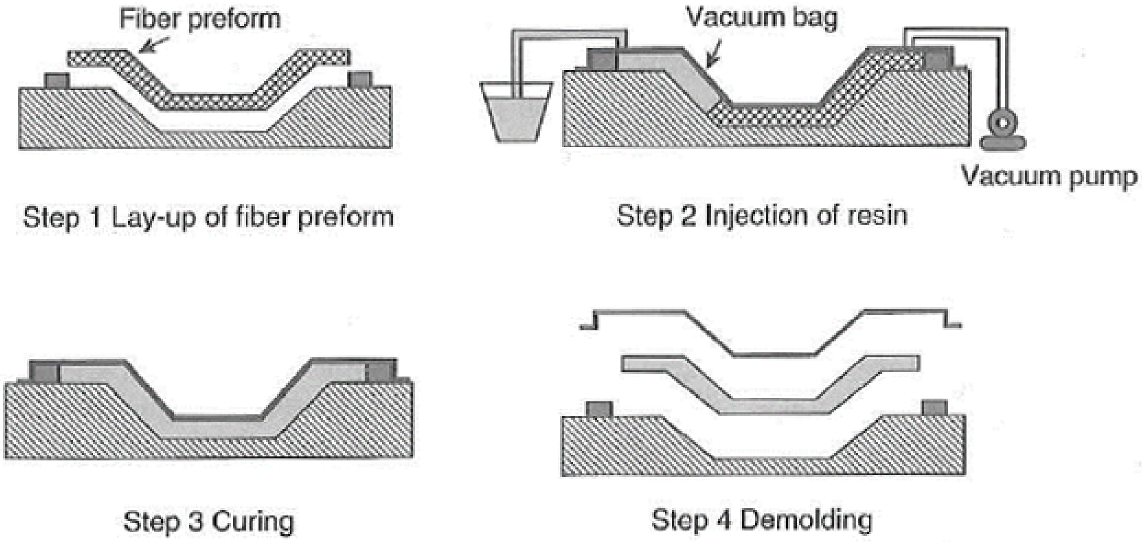

Figure 2.6: Main manufacturing steps in Vacuum Assisted Resin Transfer Moulding (VARTM) [15]

The lay-up of the fibre preform has many sub-steps, unlike the other steps described in Figure 2.6, which are listed as follows [29]:

1. First lay-up all dry material on the mould.
2. Cover with a highly permeable resin distribution medium on top of the dry fabric to help spread the resin quickly.
3. Cover with a vacuum bag.
4. Place one or more resin inlet ports so as to strategically impregnate the part, trying to ensure no dry spots.
5. Evacuate the trapped air with the vacuum pump and check for air leaks.

For the purposes of this project two types of composite structures were made using VARTM:

- Laminates - which are made from multiple layers of fibre fabric infused with resin.
- Sandwich panels - made from a PVC foam sandwiched between layers of reinforcement.

These composites and current research around their response due to blast loading will be dealt with in the following sections.

2.4 Blasting of Composites and Sandwich Structures

The creation of a blast load on composites for research purposes has been mainly accomplished experimentally through three types of method; shock tube testing, small laboratory-scale explosive detonations in close proximity to the test specimen and in the field by medium scale testing of explosive detonations at large distances from the test specimen [2]. The two prominent testing methods are the small scale laboratory testing with explosives and shock tube testing methods. Each method has its advantages and disadvantages. The shock tube, for example, can replicate the essential features of the pressure loading that may arise from an unconfined far-field air-blast explosion [2]. In addition the shock tube is a cost-effective and easily controllable alternative to explosive testing [2, 9]. Shock tube testing is useful for validating numerical simulations that require certainty regarding the loading definitions and can also be used to compare materials loaded under similar conditions [2]. The near field effects of the explosive cannot be determined by shock tubes. Small scale laboratory experiments are another cost effective way (as compared to medium scale in field explosive testing), provided the structural dimensions can be scaled to below 0.5 m [2]. It has been noted that when employing explosives testing, the pressure signatures are spatially complex and at times difficult to measure [9]. Even so, many successful tests have been performed with similar outcomes as the shock tube tests [2]. It should be noted that clearing effects can not be determined by shock tube testing [15].

2.4.1 Fibre Reinforced Polymer (FRP) Composites

There have been a number of investigations into the response of different types of composites to air blast loading. The most common FRP laminates that have been tested are carbon and glass-fibre reinforcement with a range range of matrix types including epoxies, polyetherimides (PEI) and vinyl esters [2].

Many investigations have performed detailed analyses of the failure processes of air blasted FRP composites [2]. Yahya et al [32] investigated the damage characteristics of carbon fiber-reinforced polyetherimides (PEI) and a glass fiber-reinforced PEI to air blast loading. The testing was performed on a blast pendulum using plastic explosives. A number of different panel thicknesses were tested for the carbon fibre laminates whereas only one thickness was tested for the glass fibre laminate. For the carbon fibre laminates it was observed that as laminate thickness increased (increase of ply stacking) the laminate could withstand higher impulses before failure. In all panels, failure progression began with front face fibre buckling and small rear face fibre fractures. It was suggested that the panel exhibited a flexural response during the test. Increasing the charge mass (and consequently the impulse) resulted in further front face fibre buckling and rear face fibre fracture deeper into the specimen without generating measurable delamination. Yahya et al [32] suggested that the reduced delamination was due to very high values of interlaminar fracture toughness of the carbon laminate, which lower the overall blast resistance of the laminate [32]. It was observed that fibre fracture thresholds were close to complete failure on the carbon fibre panels [32, 33]. It was noted that similar failure mechanisms were observed for the glass fibre panels.

Photographs of the rear faces of 12-ply carbon and the 18-ply glass fibre laminates at varying impulse values are shown in Figures 2.7 and 2.8 respectively. It is observed from Figures 2.7 and 2.8 that similar failure mechanisms are present in both laminates, and that minimal delamination was observed.

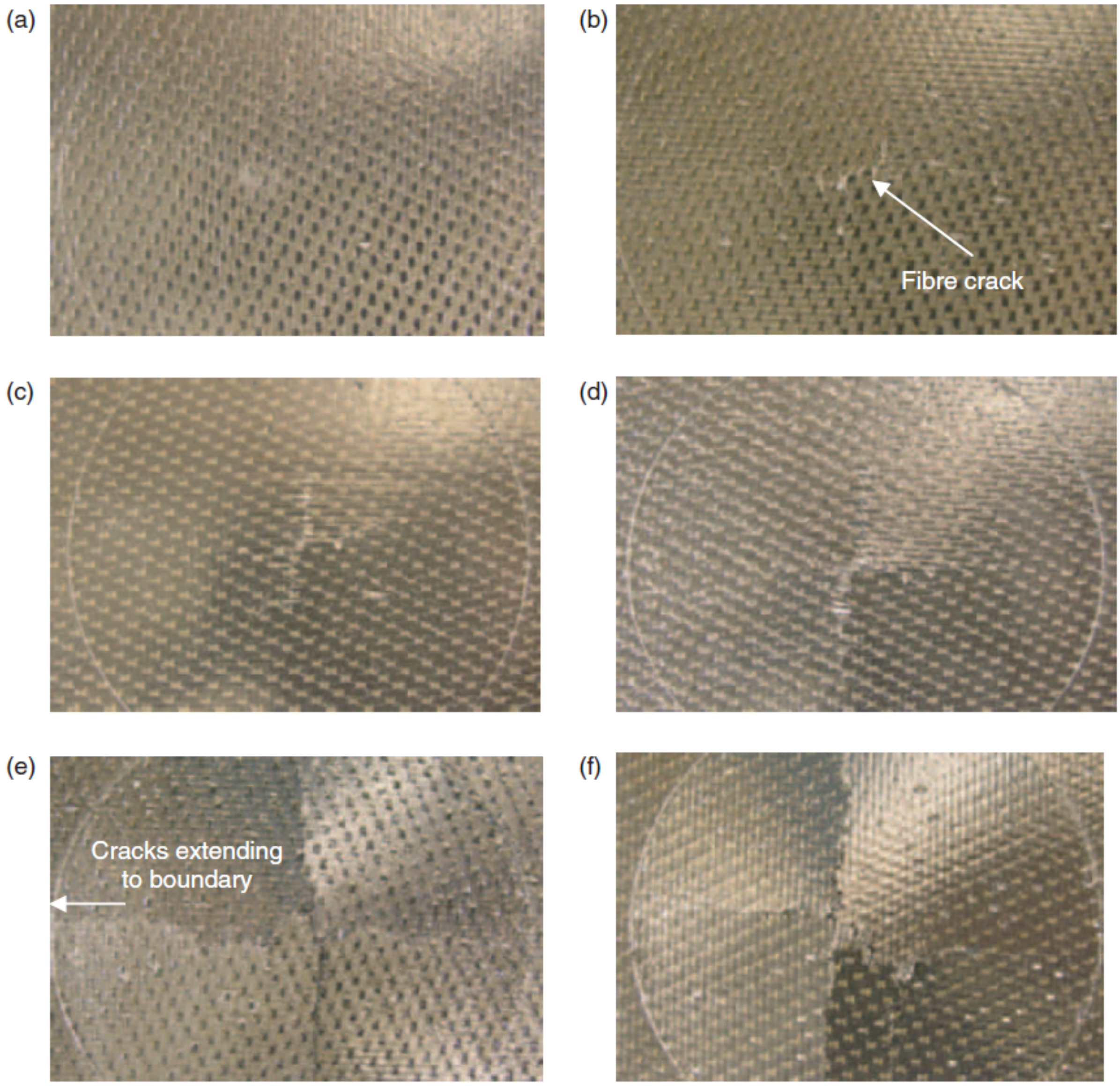

Figure 2.7: Rear surfaces of the 12-ply CF/PEI panels (a) impulse=2.46 Ns, (b) impulse=3.33 Ns, (c) impulse=3.74 Ns, (d) impulse=4.98 Ns, (e) impulse=5.47 Ns, and (f) impulse=6.06 Ns. [32]

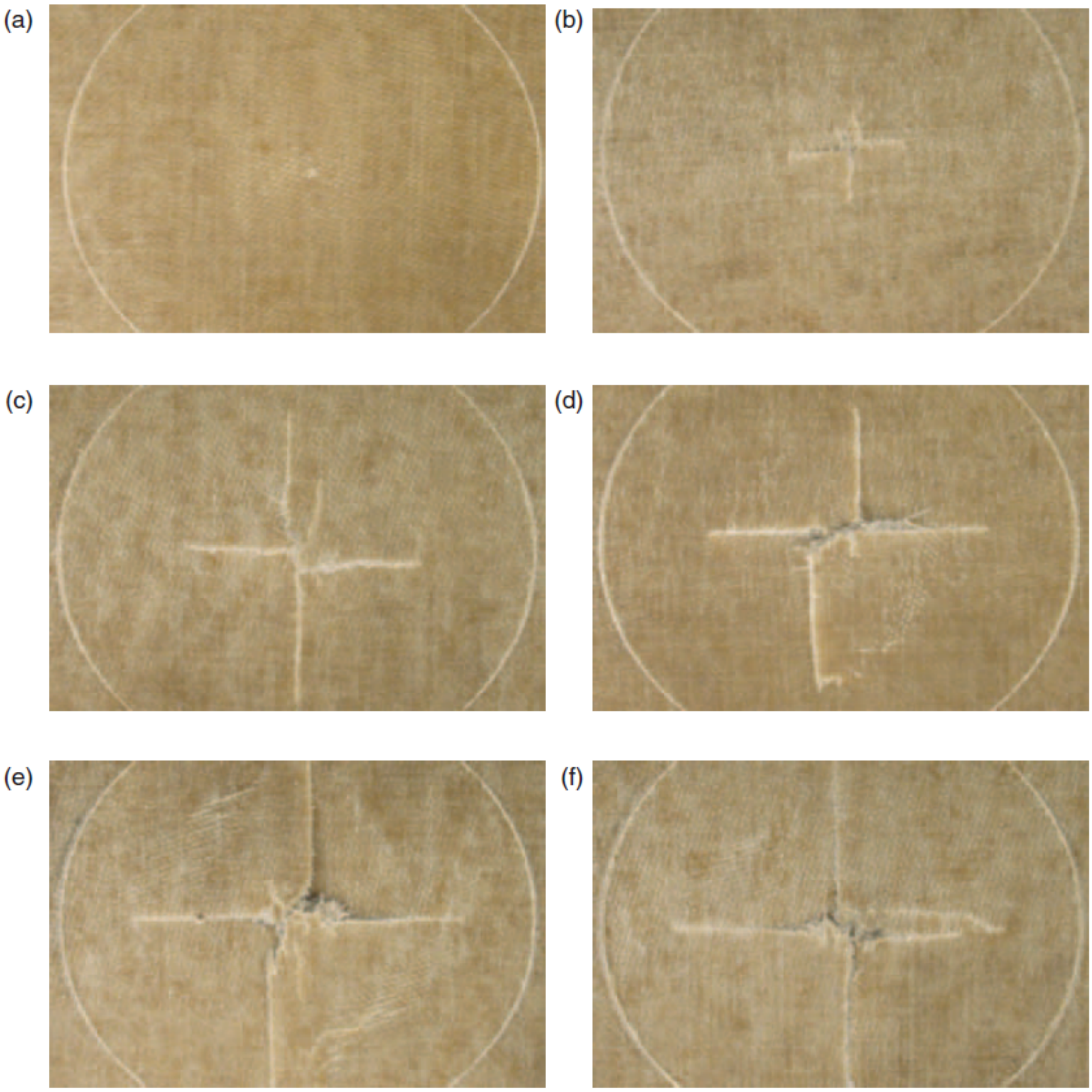

Figure 2.8: Rear surfaces of the 18-ply GF/PEI panels (a) impulse=6.36 Ns, (b) impulse=7.93 Ns, (c) impulse=7.98 Ns, (d) impulse=8.21 Ns, (e) impulse=9.02 Ns, and (f) impulse=9.4 Ns. [32]

Tekalur et al [4] investigated the damage progression in E-glass/vinyl ester and carbon fibre/vinyl ester composites under both quasi-static and dynamic loading rates. Quasi-static testing was performed as per ASTM standards. The dynamic loading rates were achieved by shock tube testing and laboratory-scale explosive testing. Shock tube testing revealed that the spread and area of damage increased with increasing shock pressure as can be seen in Figure 2.9. The panels had also undergone permanent deformation. The magnitude of the permanent deformation increased with increasing shock pressure [4].

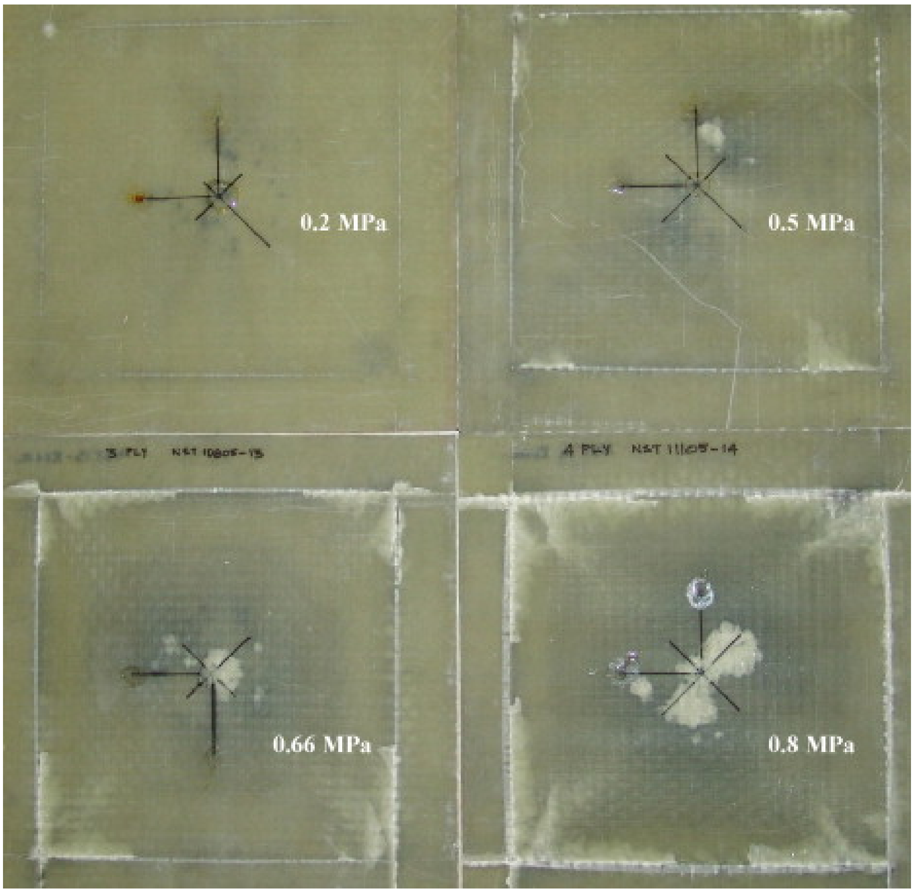

Figure 2.9: Damage progression in E-glass/vinyl ester composites, subjected to shock blast loading. Shown here is the rear face of the panels with shock levels overlaid on the images [4]

The carbon fibre/vinyl ester composites displayed a significantly different mode of damage to the E-glass/vinyl ester composites [4]. In Figure 2.10 the damage progression of the carbon fibre panel front face (blast side face) is shown for differing pressures. The panels resisted damage until a certain level of shock pressure (0.6 MPa) and this was referred to as the "threshold" pressure [4]; thereafter the panels exhibited extensive delamination and fibre breakage on the front face. This phenomenon was also observed by Yahya et al [32, 33]. Although the E-glass/vinyl ester composites had a relatively low threshold pressure (0.2 MPa), the panels exhibited slow and progressive damage behaviour. This can be seen in Figure 2.9 where delamination increases with increasing impulse. Failure modes observed in the carbon fibre/vinyl ester composites were more drastic and sudden in nature. This suggested that carbon fibre/vinyl ester composites would suit applications where absolute integrity of the structure is needed, as long as the shock levels are well below the threshold pressure. In applications where permanent deformation, rather than drastic failure is preferred, E-glass/vinyl ester composites would be more suited.

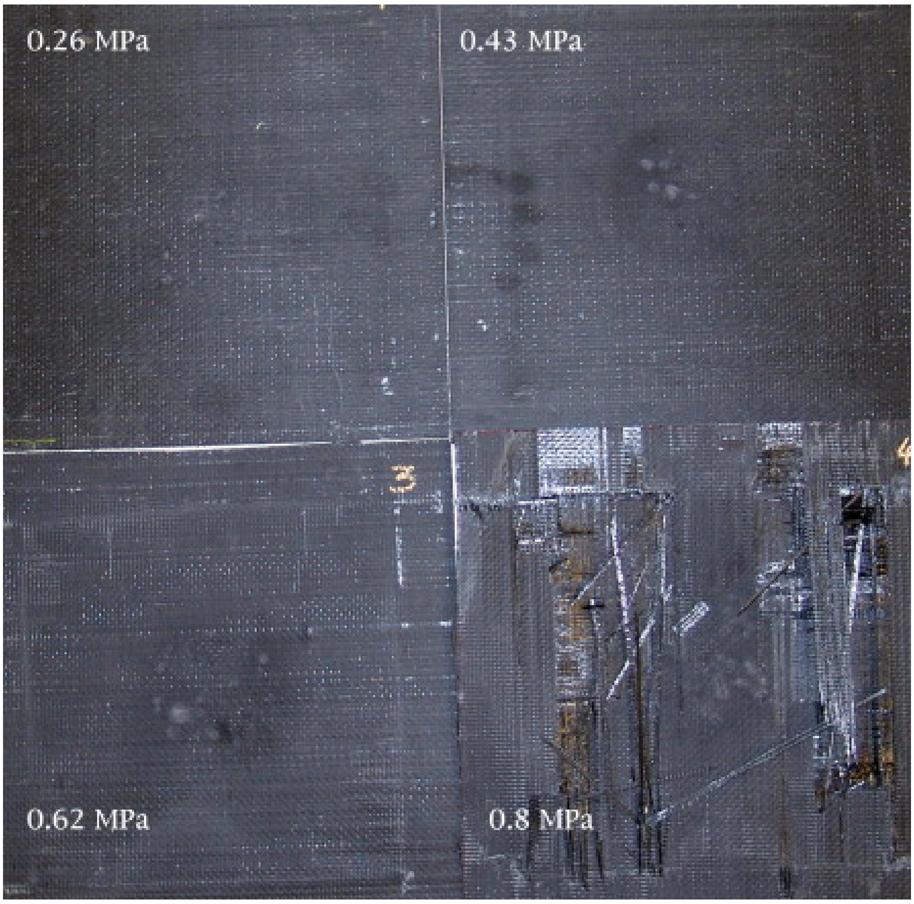

Figure 2.10: Strike face damage progression in carbon fibre/vinyl ester composites, subjected to shock blast loading with shock pressures overlaid on the images [4]

Both composites were also blast tested with a blast tube [4]. In this case E-glass/vinyl ester composites showed delamination and fibre breakage on the front face. A central burn region was also observed post testing. When viewed under a microscope, this region was devoid of matrix material and fibre breakage was observed. This suggested inadequate load transfer between fibre and matrix under these high loading rates as the cause of the drastic increase in delamination. The carbon fibre/vinyl ester composite damage observed was in the form of fibre breakage on the front face due to spalling [4]. The rear face of these panels revealed no visible external damage. Again the E-glass/vinyl ester composites showed a more progressive form of failure than the carbon fiber/vinyl ester composites.

Comtois et al [34] investigated the behaviour of composite laminates (carbon and glass fibre) when subjected to blast loading with a focus on the effects of the clamping methods used. Two types of clamping were tested. The composites were either adhesively bonded or clamped with a bolted connection to the test rig. The explosive used was the military explosive PE4. Testing revealed that the extent of damage of specimens was greater for closed chamber tests than for open chamber tests. An increase in charge mass increased the amount of delamination whereas an increase in stand-off distance decreased the delamination. When the clamp areas were investigated, the adhesively bonded area showed a positive increase in inter-ply delamination as the severity of the explosive event worsened. It is important to note that delamination was confined to the adhesive area with minimal penetration into the diaphragm as seen in Figure 2.11 a). In the case of the bolted arrangement the delaminations associated with the clamp areas ran into the diaphragm region much more than in the adhesively bonded specimens. In certain instances, delamination in the clamped area would join up to the diaphragm area to produce a delamination area that ran across the cross section as shown in Figure 2.11 b).

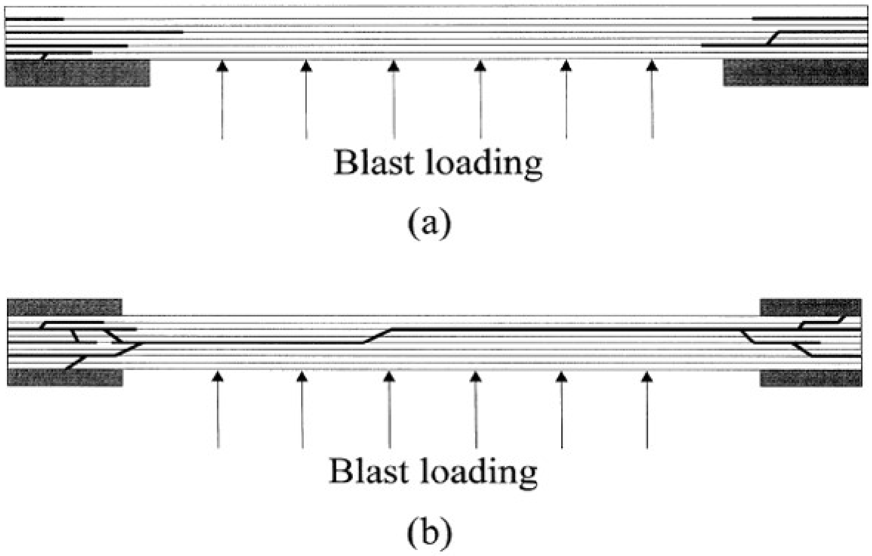

Figure 2.11: Schematic of delamination for (a) bonded and (b) clamped specimens [34]

Fibre breakage was observed around the clamping points for both types of composite. With carbon laminates showing less breakage than glass fibre laminates. The extent of fibre breakage was less for the adhesively bonded specimen when compared to the bolted arrangement. This highlights the importance of the clamping arrangement of composites to the parent structure as this affects the mode of failure [34].

Gargano et al [3] conducted an experimental investigation into the blast response of fibre-reinforced polymer laminates. The laminates were woven carbon polyester, glass fibre polyester, carbon vinyl ester and glass vinyl ester. To ensure that the carbon and glass composites had the same thickness, the carbon and glass composites contained 7 and 10 plies respectively. Blast tests were performed in air with plastic explosives. The specimen frame was lined with a soft rubber. This allowed the laminate to flex freely under the impulsive load exerted by the shock wave. A schematic of the experimental setup can be seen in Figure 2.12. The laminates were tested under near-field and far-field conditions.

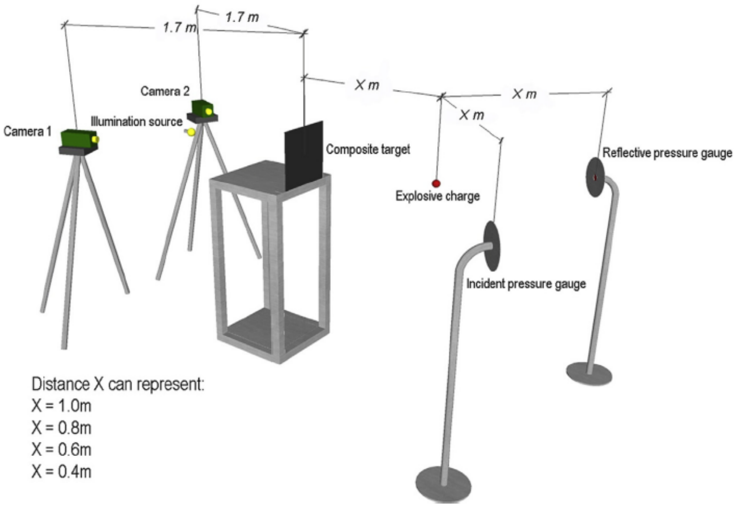

Figure 2.12: Schematic representation of the explosive blast tests [3]

Gargano et al [3] described the near-field condition by the laminate being impulsively loaded by both the shock wave and detonation products within the fire-ball generated by the explosive. This would occur when the stand-off distance between the laminate and the explosive is less than the maximum radius of the fire-ball, as shown schematically Figure 2.13 (a) and using high-speed photography Figure 2.13 (b). The near-field loading condition is complex due to combined effect of the incident shock wave and detonation products.

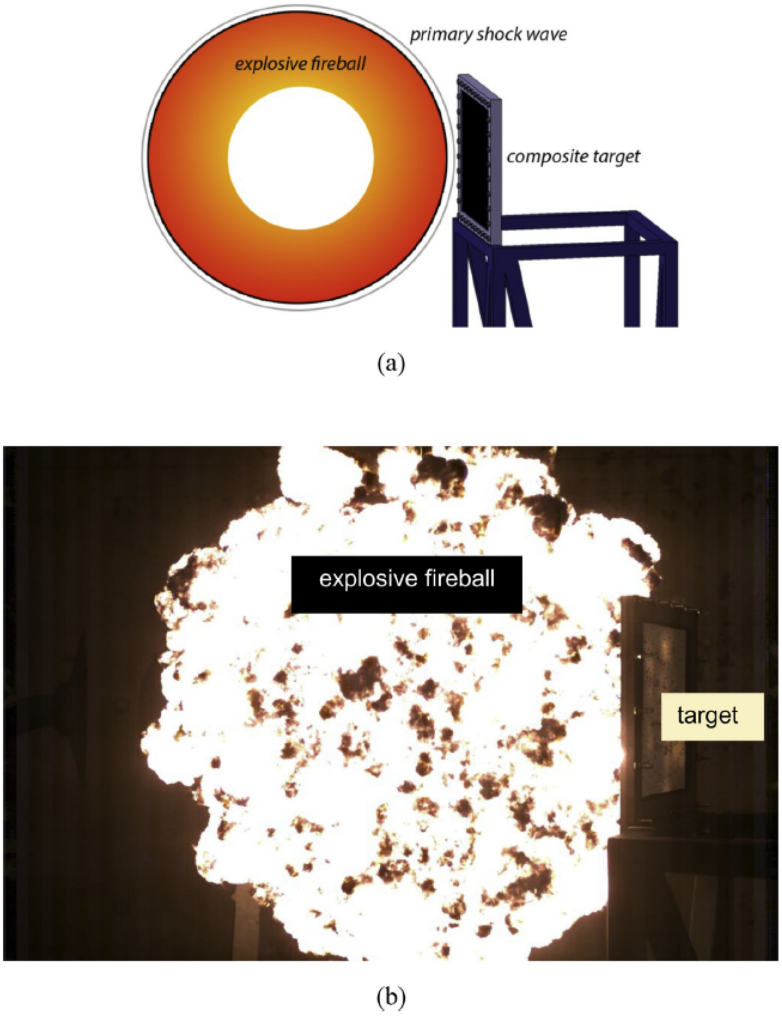

Figure 2.13: (a) Schematic diagram and (b) time-lapse photograph of a near-field explosive test [3]

The far-field loading condition is defined by the laminate only being loaded by the shock wave and not the detonation products i.e. fire-ball. This occurs when the stand-off distance from the explosive charge exceeds the size of the fire-ball, as shown in Figure 2.14 .

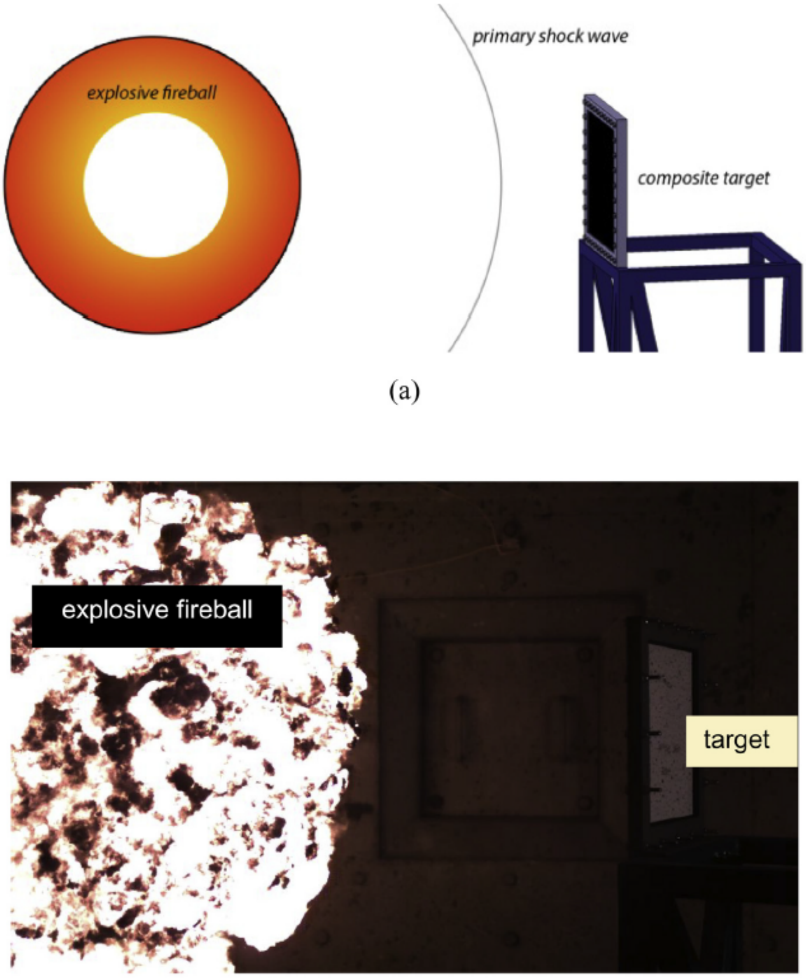

(a)

(b)

Figure 2.14: (a) Schematic diagram and (b) time-lapse photograph of a far-field explosive test [3]

Following blast testing, the laminates were inspected using electron microscopy and ultrasound to determine the types and amount of damage [3]. Shown in Figure 2.15 are the different types of damage within the laminates caused by blast loading. In Figure 2.16 the blast impulse needed to initiate the different types of damage in the laminates have been mapped. Damage initiated as inter-facial cracks between the fibres and polymer matrix, together with transverse cracks within the polymer-rich regions and fibre tows (see Figure 2.15 (a)). These types of damage occurred in all the laminates. Gargano et al [3] notes that these failures developed at lower impulse loads in the carbon fibre laminates and the composites with the polyester matrix. At higher shock impulses (above 150 Pa.s), the two carbon fibre laminates and the glass polyester composite experienced delamination cracking at one or multiple ply interfaces (see Figure 2.15 (b)), whereas no delaminations were detected in the glass vinyl ester laminates. The carbon fibres broke under shock loading, leading to fibre rupture and ultimately to complete rupture of the carbon composite (see Figure 2.15 (b)). No damage to the glass fibres was detected in the polyester or vinyl ester laminates, even at the highest blast impulse level (500 Pa.s).

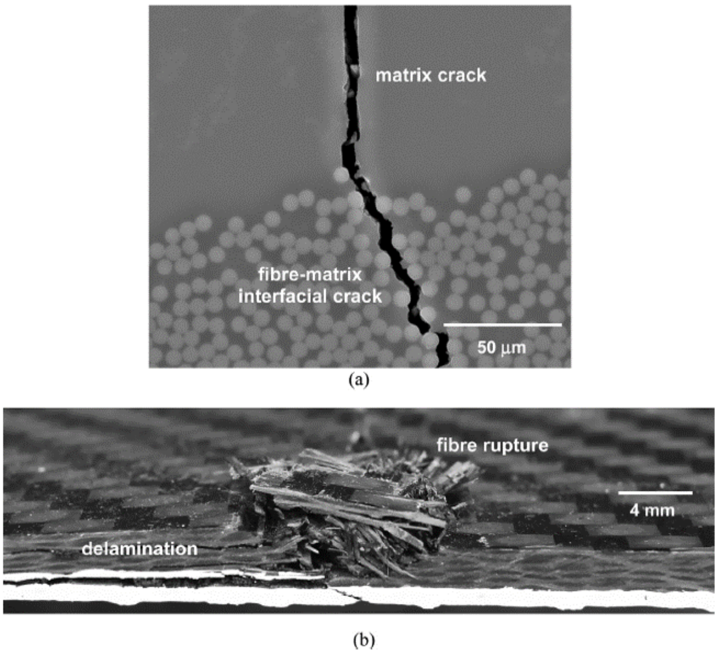

Figure 2.15: Blast-induced damage. (a) Fibre-matrix interfacial debonding and matrix cracking. (b) Delamination cracking and rupture of carbon fibres [3]

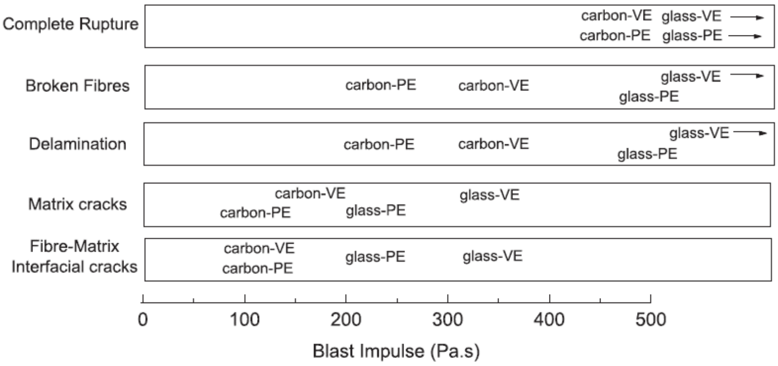

Figure 2.16: Failure initiation plots for the laminates. PE and VE indicate polyester and vinyl ester, respectively. The arrows indicate that the damage does not initiate within the range of blast impulses, but at a higher value [3]

Gargano et al [3] compared results to those of Comtois et al [34]. Comtois et al [34] found that the glass fibre laminate experienced more damage than the carbon fibre laminate, attributed to glass fibres having a lower tensile failure stress. Gargano et al [3] notes that mechanical property data were lacking for their composites, but highlighted that the carbon fibre used in their experiments had an higher tensile strength (similar to Comtois et al [34]), and lower tensile strain energy density compared to the glass fibre. This would imply that glass fibre laminates can absorb more tensile strain energy than the carbon fibre laminates before breaking [3]. This led Gargano et al [3] to conclude this may be part of the reason why glass composites in this study seem to be more damage resistant than the carbon composites. Another consideration is that Comtois et al [34] employed experimental boundary conditions that were rigidly clamped unlike the Gargano et al [3] where it was simply supported. This would alter the deformation and damage to the composite [34].

Delamination in the carbon fibre laminates initiated at a lower shock wave impulse and was always greater in size than for the glass fibre composites. This result is similar to Tekalur et al [4]. Gargano et al [3] found that carbon fibre laminates experience sudden failure, whereas glass fibre composites display progressive failure under increasing shock wave loading conditions. It is also shown in Figure 2.16 that delamination initiated in the polyester laminates at lower blast impulse levels when compared to the vinyl ester composites.

2.4.2 Sandwich Structures

Sandwich structures typically comprise of a relatively soft core which is “sandwiched” between two stiff outer face sheets. The inclusion of the core increases the bending stiffness of the sandwich structure by increasing the second moment of area without a significant weight penalty [2]. This has allowed a multitude of possible combinations of face sheet and cores including variations in geometries (thickness of face sheet and cores), material (resin, reinforcement, core material) bonding and manufacturing methods [2]. This has resulted in a range of blast research being performed on various panel types with many different test methods [2].

Langdon et al [22] investigated the response of sandwich structures to blast loading. Two configurations of sandwich panels were manufactured and tested. Both sandwich configurations were balanced, having equal number of plies on both front and back face sides of the core. The first type was constructed from 15 layers of plain weave glass fibre (400 g/m^2) and PVC foam core with a density of 80 kg/m^3 (Divinycell H80) infused with a vinyl ester resin. The second configuration was similar, only differing in the core density which was 200 kg/m^3 (Divinycell H200). Testing was performed on a ballistic pendulum. A schematic can be seen in Figure 2.17. The panels were clamped between two steel clamps, leaving an exposed circular region with a diameter of 200 mm. PE4 explosive was moulded into a disk of 38 mm diameter and mounted to a polystyrene bridge. The space between the explosive and the test panel also known as stand-off distance (SOD) was 50 mm [22]. Photographs of typical panels are shown in Figures 2.18 and 2.19 post-testing.

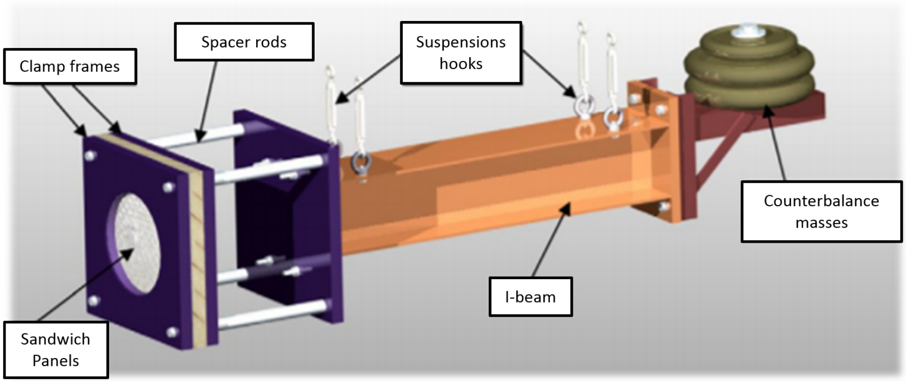

Figure 2.17: Localised blast loading experimental arrangement of Langdon et al [22]

Post-test inspection and sectioning of the panels revealed the that the major failure processes were [22]:

- Delamination of front and back face sheets (Figures 2.18 (a), (b), (d) and 2.19 (a), (d))
- Core damage (Figure 2.18 (d) and 2.19 (d), including; permanent core compression, fragmentation, and complete core penetration, from the front face sheet to the back face sheet
- Matrix failure prior to fibre fracture
- Fibre fracture (Figures 2.18 (c), (d) and 2.19 (c), (d))
- Front face sheet rupture (Figures 2.18 (d) and 2.19 (d))
- Debonding of back face (Figures 2.18 (d) and 2.19 (d))
- Plastic deformation of back face (Figures 2.18 (d) and 2.19 (d))

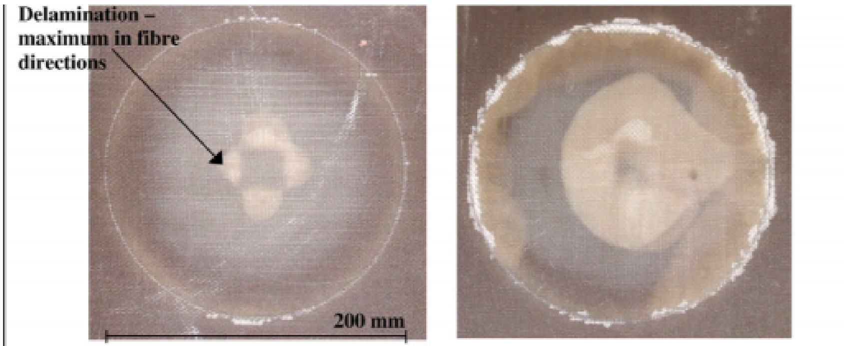

(a) Back face of panel H80_3 (18.1 Ns) (b) Back face of panel H80_4 (23.1 Ns)

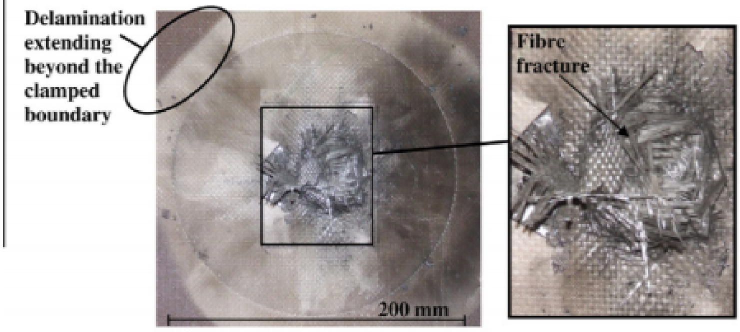

(c) Front face of panel H80_4 (23.1 Ns)

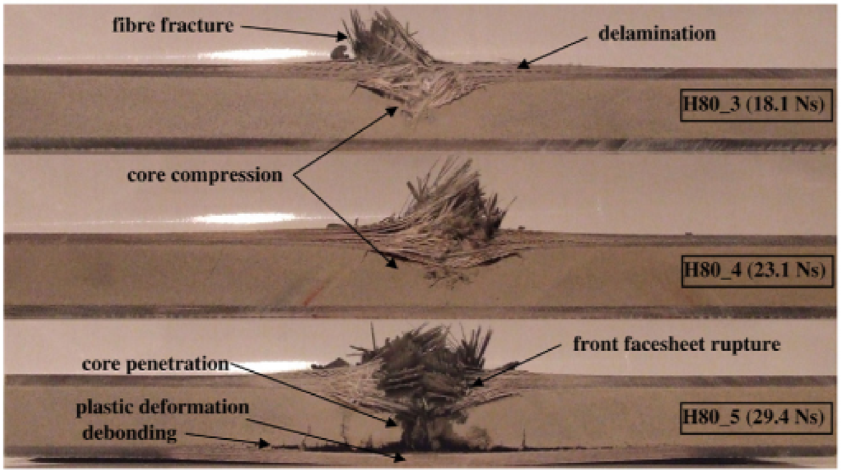

(d) Various panel cross-sections

Figure 2.18: Photographs of selected H80 sandwich panels tested by Langdon et al [22]

Increasing levels of damage were observed in the panels as the impulse was increased [22]. Core compression, as seen in Figures 2.18 (d) and 2.19 (d), initiated from the front side of the core (the side nearest to the blast), showing that the compression resulted from the deflection of the front face sheet into the core.

G.S. Langdon et al. / Engineering Structures 36 (2012) 104–112

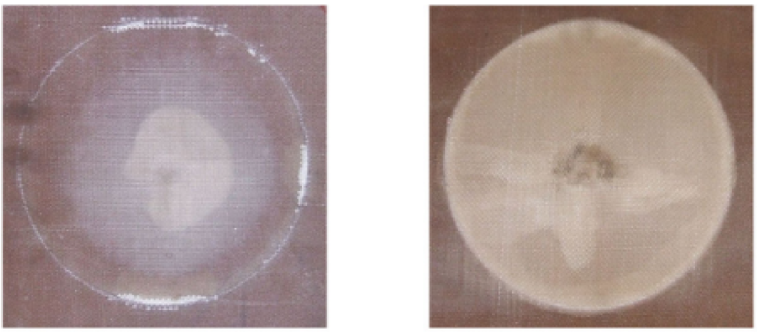

(a) Back face of panel H200_3 (24.51 Ns) (b) Back face of panel H200_5 (44.6 Ns)

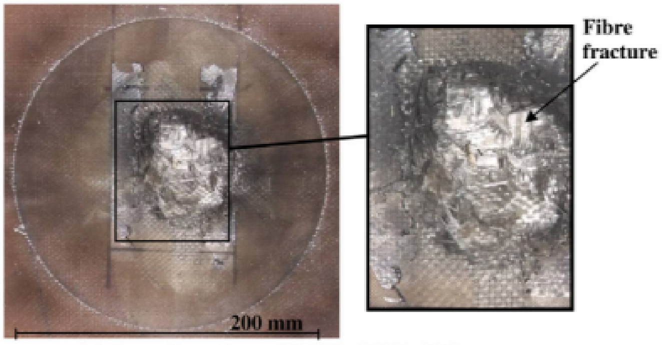

(c) Front face of panel H200_5 (44.6 Ns)

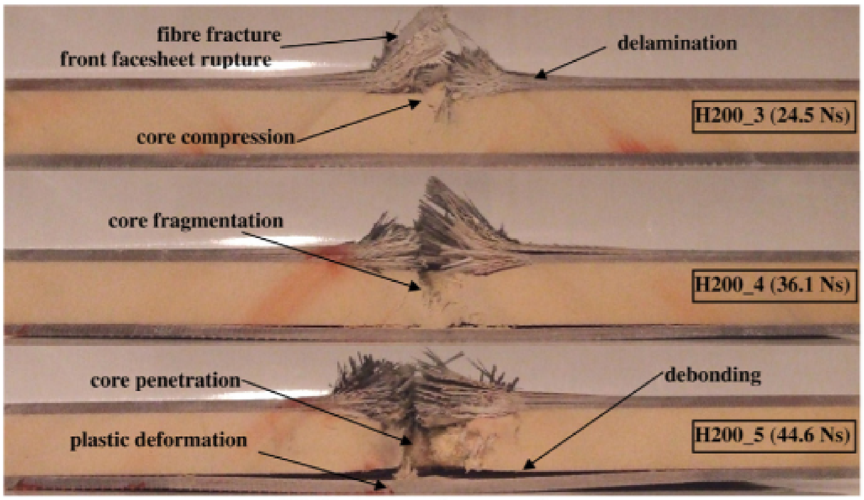

(d) Various panel cross-sections

Figure 2.19: Photographs of selected H200 sandwich panels tested by Langdon et al [22]

Failure progression initially occurred on the front face sheet and then travelled through the thickness of the panel. Once the front face sheet was compromised, the core received the brunt of the blast wave. It was also discovered that delamination lengths in the front face sheet increased with increasing impulse, up to a plateau of between 35% and 45% of the exposed length of the panel. This was due to the localisation of the loading. Energy is then absorbed due to other failure modes as damage progresses. Considerable damage, including core fragmentation and front face sheet rupture precedes damage to the back sheet, with the exception of delamination damage which occurs early in the failure progression as seen in Figure 2.20 [22].

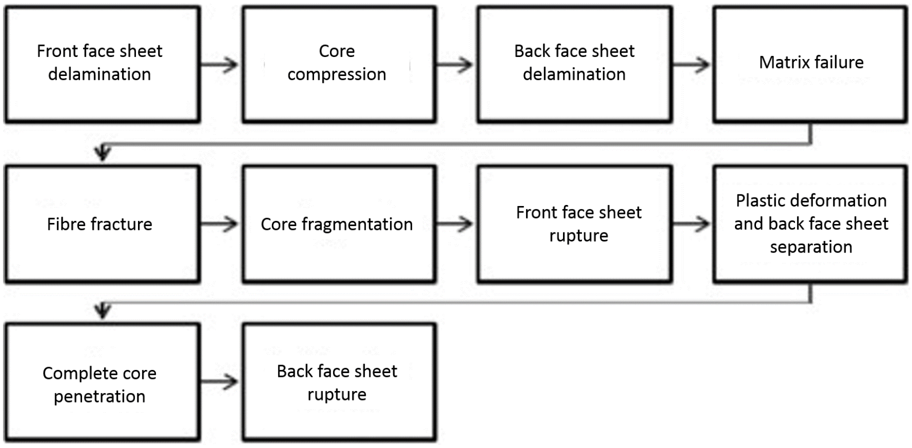

Figure 2.20: Block diagram showing failure progression in the sandwich panels with increasing impulse [22]

The sandwich with the denser core (H200 Divinycell) outperformed the sandwich panel with the less denser core (H80 Divinycell) in terms of blast resistance [22]. The was attributed to the higher compression strength and stiffness of the H200 core. This resulted in the H200 sandwich having more structural support for the front face sheet during transient deformation which resulted in less fibre fracture and less core compression and fragmentation.

Langdon et al [35] further investigated the effects of blast on sandwich panels and compared these to composite laminates. Sandwich panels were manufactured using the same method and configurations as in [22] except that the face sheets comprised 8 layers of 400 g/m^2 plain weave E-glass fibre instead of 15 layers [22]. The panels were infused with the same resin (Hydrex 100HF vinyl ester) which resulted in a nominal face sheet thickness of 2.5 mm, in contrast to previous work on thicker face sheets [22]. The composite laminate panels were manufactured using the same composite material as the sandwich panel face sheet. The laminate panels had 21 layers of glass fibre, corresponding to a laminate only panel with mass equivalent to the sandwich panel with the H80 foam core (80 kg/m^3).

All panels were blast tested using the same type of explosive (PE4) with the same SOD (50 mm) as reference [22]. The sandwich panels exhibited the same failure progression as noted in previous work on thicker face sheet panels [22]. Post-test inspection revealed the same failure process occurring: face sheet delamination (Figures 2.21 and 2.21), core compression, from the front side (Figures 2.21a and 2.22a), core cracking, fragmentation and penetration of the core (Figures 2.21b, 2.21c, 2.22b) back face debonding (Figures 2.21b and 2.22b), permanent deformation of back face (Figures 2.21b and 2.22b), fibre fracture (Figures 2.21 and 2.22), face sheet rupture (Figures 2.21 and 2.22) and complete panel perforation (Figure 2.21c).

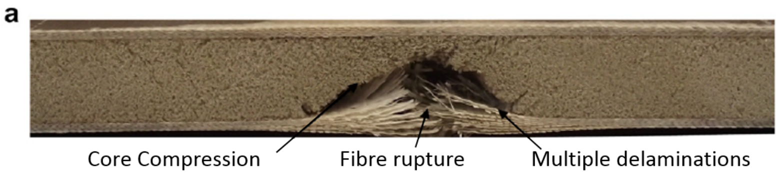

Cross-section of H80 panel, Impulse = 10.5 Ns, 6 g (PE4)

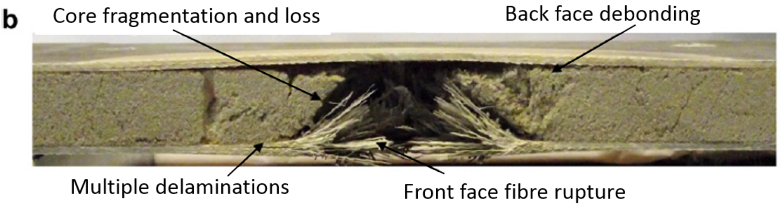

Cross-section H80 panel, Impulse = 19.1 Ns, 10 g (PE4)

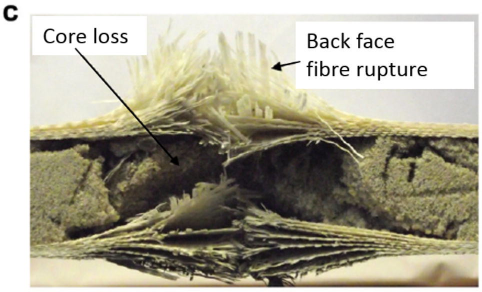

Central part of H80 panel cross-section showing complete panel rupture, Impulse = 20.4 Ns, 11 g (PE4)

Figure 2.21: Cross-section photographs of various blast-loaded H80 sandwich panels [35]

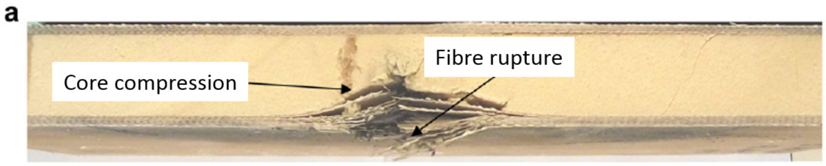

Cross-section H200 panel, Impulse = 17.7 Ns, 9 g (PE4)

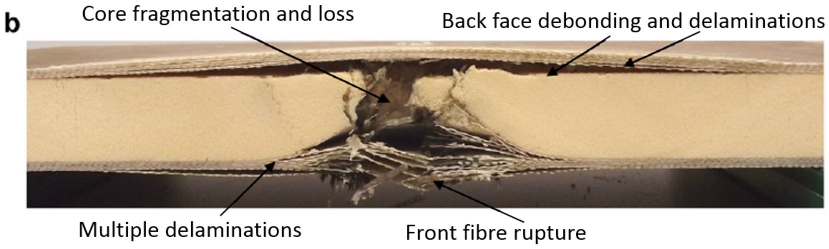

Cross-section H200 panel, Impulse = 25.9 Ns, 13 g (PE4)

Figure 2.22: Cross-section photographs of various blast-loaded H200 sandwich panels [35]

The composite laminate panels exhibited delamination failure and fibre breakage but did not exhibit penetration failure at impulses that caused penetration failures in both sets of sandwich panels [35]. Failure was in the form of multiple delaminations throughout the cross-section, as shown in the photograph in Figure 2.23. The average delamination length increased linearly with impulse and fibre rupture occurred on the front face of the composite laminate. Langdon et al [35] concluded that this is due to the high intensity of the loading which caused a large local through-thickness compression of the plies. Rupture occurred on the back face of the panel in tension which was due to the displacement of the panel. The number of ruptured layers on the back faces of the laminate panels increased at higher impulses, although complete penetration of the panels was not observed for the range of tests performed (up to 16 g PE4, impulse = 30 Ns).

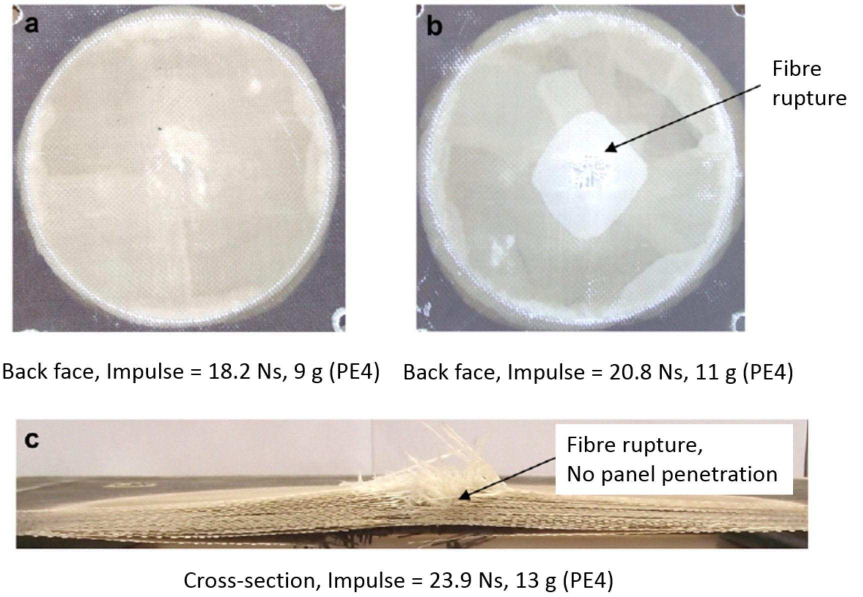

Back face, Impulse = 18.2 Ns, 9 g (PE4) Back face, Impulse = 20.8 Ns, 11 g (PE4)

Cross-section, Impulse = 23.9 Ns, 13 g (PE4)

Figure 2.23: Photographs of blast-loaded laminate panels showing typical responses. [35]

Wang et al [36] performed shock tube experiments to study the dynamic response of sandwich panels with E-Glass Vinyl Ester (EVE) composite face sheets and stepwise graded styrene foam cores. Two types of core configuration, with identical areal density, were tested. The core layers were arranged according to the density of the respective foam. Configuration 1 consisted of low/middle/high (A300/A500/A800) density foams and configuration 2 consisted of middle/low/high (A500/A300/A800) density foams [36]. A schematic of the configuration can be seen in Figure 2.24.

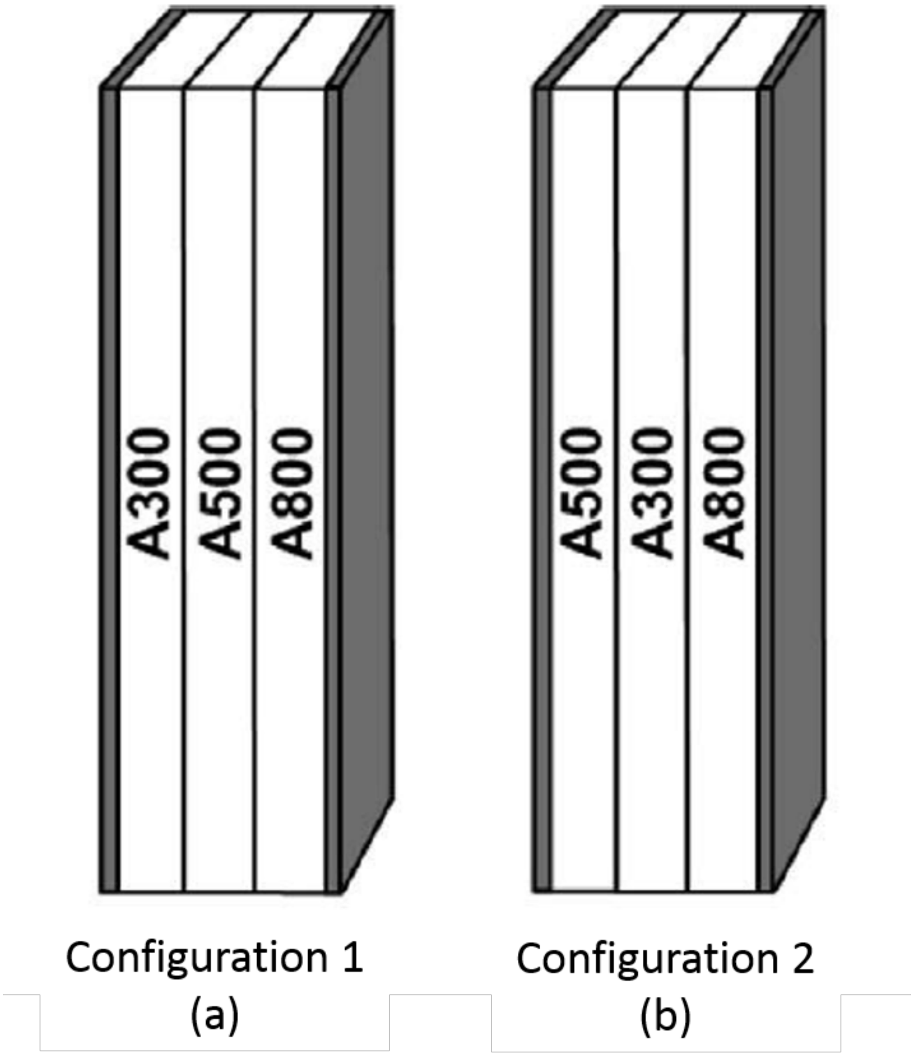

Figure 2.24: Schematic of specimen configuration [36]

It was discovered that the overall performance of configuration 1 (A300/A500/A800) was better than that of configuration 2 (A500/A300/A800). This was due to the large compression which was visible in the core when the least dense foam (A300) is first in contact with the blast load. This configuration reduced the dynamic pressures on the back face sheet, and thus limited the amount of damage imparted to the specimen. When the A500 foam was in contact with the blast first, the overall deformation process of the sample was completely different. Compression of the core was limited which resulted in the specimen showing a heavy amount of damage. The authors also noted that energy loss and deformation energies were the same for both configurations [36].

Post-mortem analysis revealed that the panels had exhibited multiple failure modes. Failure modes exhibited were: core compression (Figure 2.25 (b)), core cracking (Figure 2.25 (b)), delamination (Figure 2.25 (a)) and inelastic deformation (Figure 2.25 (b)) similar to those observed by Langdon et al [22,35].

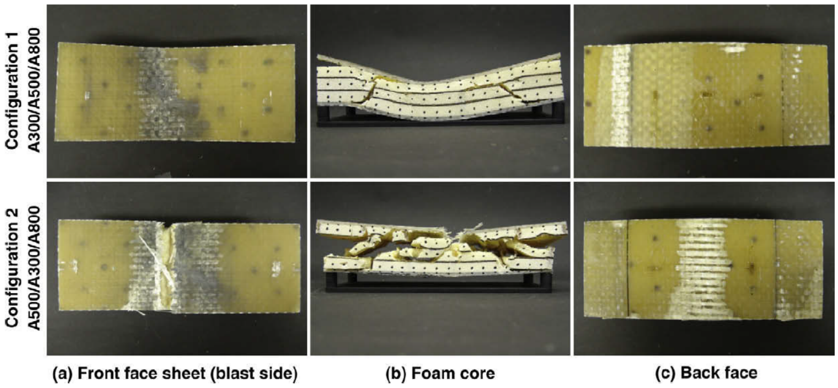

(a) Front face sheet (blast side) (b) Foam core (c) Back face

Figure 2.25: Visual examination of sandwich composites after being subjected to high intensity blast load [36]

2.5 Curved Composite and Sandwich Structures

Accidental explosions or bomb blast can cause extreme loading on any structure irrespective of their geometry [8]. The majority of work performed over the past few years has been on flat structures, and relatively little on curved structures [8–10].

Kumar et al [8] performed a comparative study of the effect of plate curvature on blast response of aluminium panels. Panels were tested on the convex side. Three types of curvature were tested in this study which can be seen in Figure 2.26.

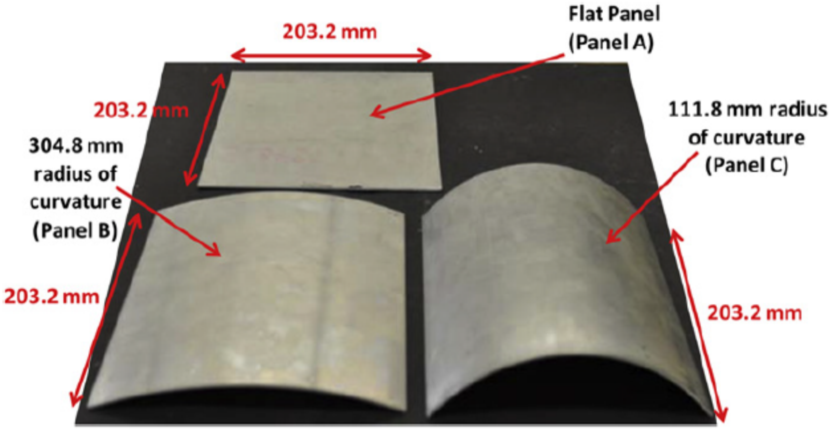

Figure 2.26: Different types of curved specimen tested by Kumar et al [8]

The experimental study made use of a shock tube to deliver the shock to the target plates. The 3D DIC technique coupled with high speed photography was used to analyse the blast response.

Post-mortem analysis was also performed on the plates. Through DIC it was revealed that the panels undergo two distinct types of transient deflections. An indentation response mode would develop first followed by a flexural response mode. During the indentation mode, localised deflection superposes on the overall deflection. The flexural mode occurred when the overall deflection surpassed the localised deflection. In the flat panel's case (Panel A in Figure 2.27), the indentation is represented as a circular deflection contour [8]. The indentation mode for Panel A lasted until 400 μs, after which the deformation mode changed to flexural. On the curved panels (Panel B and Panel C) the indentation mode appears as an elliptical deflection contour in Figure 2.27. Panel B's indentation mode lasted until 600 μs and then changed to flexural. The deformation for panel C is primarily indentation. The flat panel has a circular indention whereas the curved panels have a more elliptical indentation mode. Kumar et al [8] noted that during indentation, boundary conditions do not affect the deflection contours. This occurs during flexural mode [8].

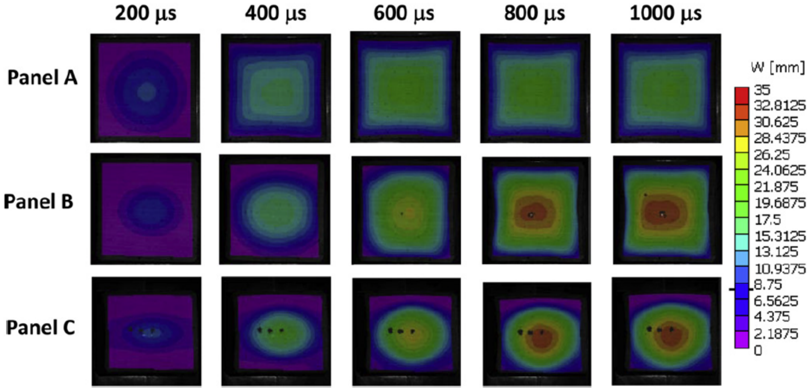

Figure 2.27: Full field deformation of panels from 3D-DIC analysis [8]

Macroscopic post-mortem analysis revealed panels A and B exhibited large inelastic deformation (Figure 2.28 a and b), whereas panel C showed localised indentation (Figure 2.28 c). Panels A and B displayed plastic deformation over the whole exposed surface. Panel C displayed plastic deformation over an arc length of 105 mm around the central region [8].

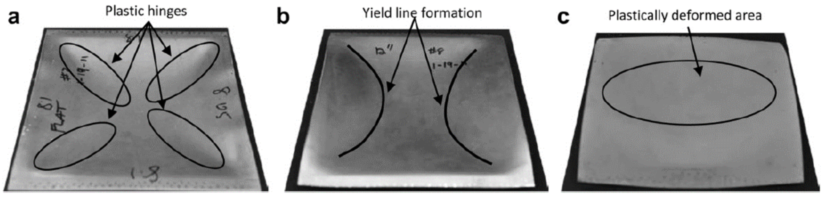

Figure 2.28: Post-mortem evaluation of (a) Flat Panel (b) 304.8 mm radius of curvature and (c) 111.8 mm radius of curvature [8]

Similar observations were made from shock tube experiments on singly curved carbon FRP laminated panels [10]. Kumar et al [10] reported flexural deformation decreases and indentation deformation increases as the radius of curvature decreases. Post-mortem evaluation revealed many common laminate failure modes including delamination and fibre breakage (see Figure 2.29). The indentation mode was more significant for characterising the response of curved panels than for flat ones.

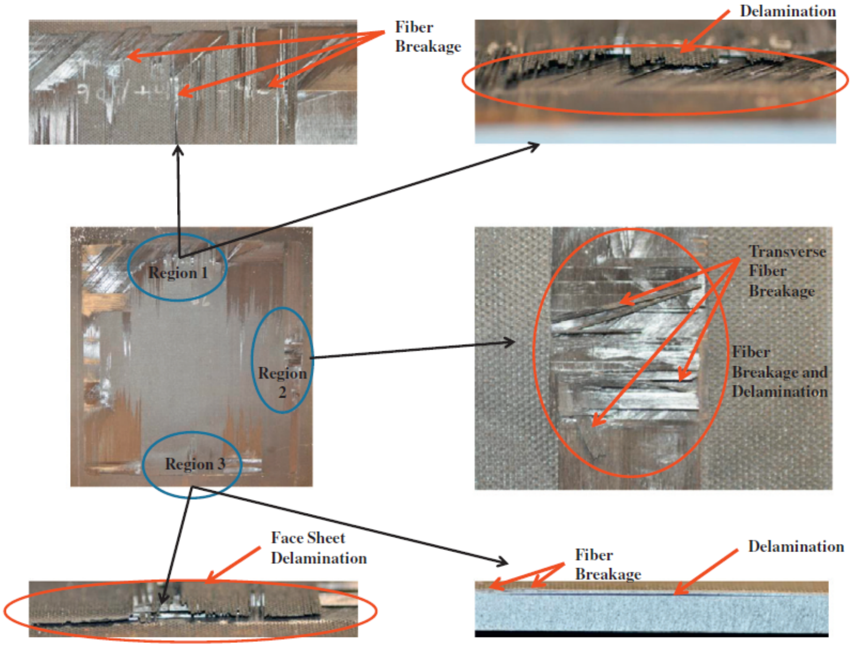

Figure 2.29: Post-mortem evaluation of flat Panel [10]

Shen et al [9] conducted a study where curved sandwich panels with two aluminium face sheets and an aluminium foam core under air blast loadings were investigated experimentally. Specimens had two different curvatures (300 mm and 600 mm) and different core and face sheet configurations were tested. The curvature changed the reflective angle of the reflected blast wave, which resulted in a reduction of the impulse acting on the front face of sandwich panels. Secondly, the curvature caused wrinkling of the back face sheet of the sandwich panels which was not observed in the flat sandwich panels. Lastly, the curvature changed the deformation regimes in terms of bending and stretching. For the flat panels, there were two regimes during the overall deflection process under blast loads, i.e. the bending regime and stretching regime. The introduction of curvature extended the bending dominant deformation range in the circumference direction; the overall deflection process of curved sandwich panels may be divided into three regimes, i.e. the bending only regime, bending (along circumferential direction) coupled with stretching (along longitudinal direction) regime and finally stretching only regime [9]. The experimental data showed that the initial curvature of a curved sandwich panel may extend the range for bending dominated deformation failures. This led Shen et al [9] to suggest that the performance of the sandwich shell structures may exceed that of both their equivalent solid counterpart and a flat sandwich plate.

Langdon et al [37] performed blast tests on on singly curved polymeric foam core FRP sandwich panels. Three external radii of curvature were investigated - infinite (flat), 1000 mm and 500 mm. Panels were clamped between steel frames using 20 equally spaced bolts around the perimeter, as shown in Figure 2.30. Three clamping frames were designed to accommodate the three different radii of curvature. This provided an exposed area of 400 mm x 400 mm (projected). PE4 plastic explosive was used to create the blast wave. The PE4 was mounted to a polystyrene bridge and located centrally at a stand-off distance of 100 mm.

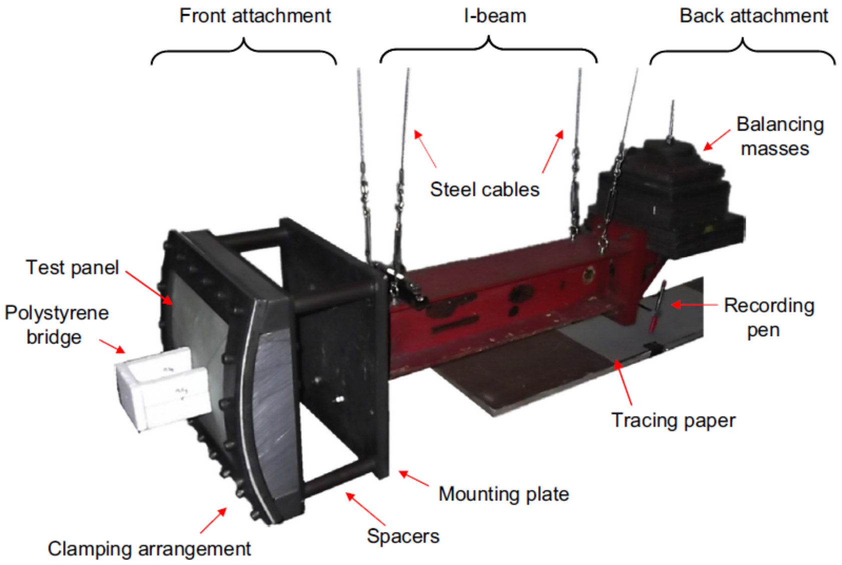

Figure 2.30: Photograph of the ballistic pendulum arranged with an FRP laminate panel (1000 mm radius of curvature) [37]

The charge mass required to initiate failure in the air-blasted sandwich panels increased with decreasing radius of curvature [37]. The panel geometry did not influence the failure initiation path which occurred, although the introduction of curvature to the FRP sandwich caused failures that were initially more prominent parallel to the axis of curvature than perpendicular.

Delamination, debonding of core and face sheets, matrix failure and fibre fracture were exhibited in the panels. Similar types of failure for flat sandwich panels were encountered in [22, 35] that employed different core materials, resins and face sheet thickness. In Figure 2.31 some failure modes are shown for the flat sandwich composites tested by Langdon et al [37].

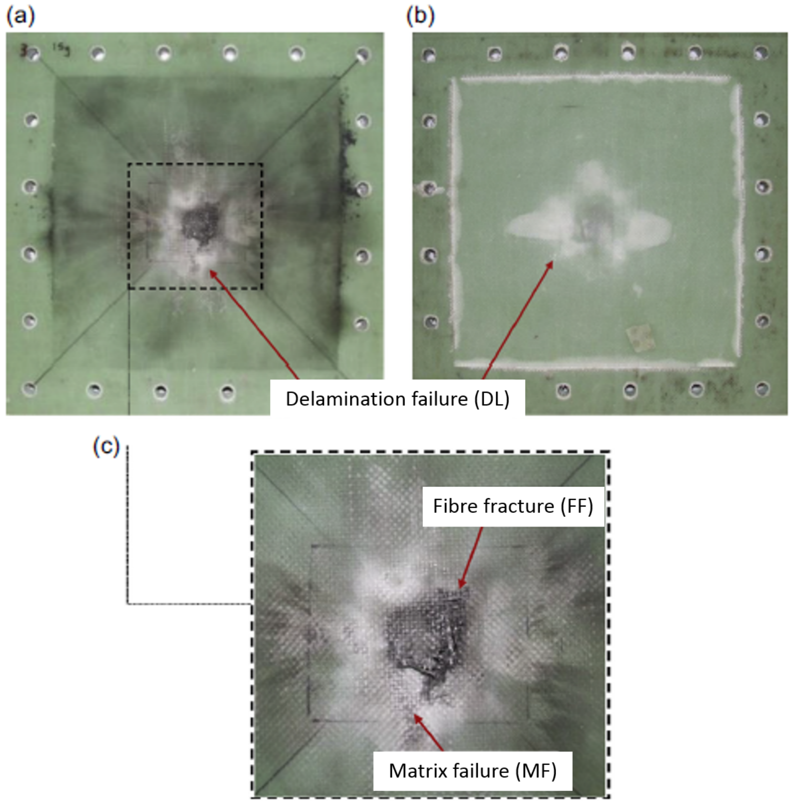

Figure 2.31: Photographs of a flat sandwich panel (1b) subjected to a 15-g detonation. (a) Front face sheet. (b) Back face sheet. (c) Magnified image from the front face sheet. [37]

It is important to note that the curved panels decreased the impulse transfer when compared to the impulse transferred to a flat panel for the same charge mass detonation, but researchers noted no significant difference in impulse transferred between the 500 mm and 1000 mm panels [37]. Debonded lengths also were observed in the central and exterior regions. These increased on the back face once complete rupture of the front face sheet and penetration of the core occurred. After this point debonding increased on the back interface more than the front interface. This relationship was delayed with decreasing radius of curvature. Lastly the complete rupture threshold of the FRP sandwich panels was similar for the flat and 1000 mm curved panels, but was significantly increased for 500 mm curved panels.

Chapter 3

Manufacturing of Composite Specimens

This chapter details the manufacture of the FRP laminates and sandwich panels with three radii of curvature namely, infinite (flat), 1000 mm and 500 mm. The FRP laminates and the sandwich panels had approximately equal areal densities, so that panel response could be compared on an equivalent mass basis.

3.1 Manufacturing Parameters

The following parameters were used in the development and manufacturing of the composite specimens.

3.1.1 Panel Requirements

Three radii of curvature were defined, namely flat, 1000 mm and 500 mm. All panels were singly curved and the radii were measured from the convex side of the panel. Figure 3.1 shows a rendered image of a panel with a 500 mm radius of curvature.

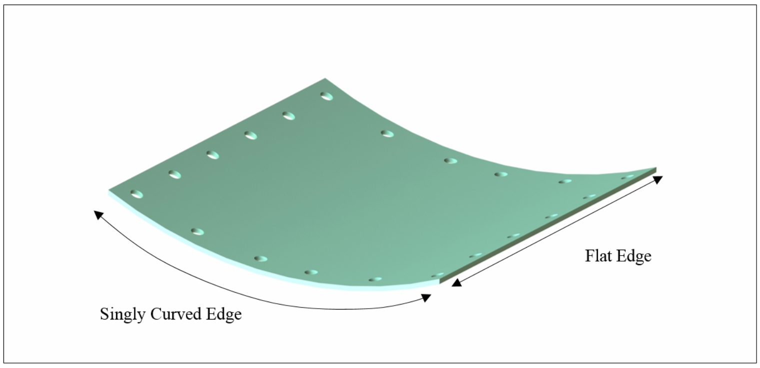

Figure 3.1: Schematic showing singly curved blast test specimen

All panels were designed to have a projected area of 400 mm × 400 mm for comparisons to work by Sinclair [23]. Sinclair [23] performed similar tests with the explosive on the convex side of the panel. In this work the explosive is located on the concave side.

The FRP laminate panels were constructed with 16 layers of fibre glass and the sandwich panel had face sheets of six layers of fibre glass and a core 15 mm thick. The final dry composition of the two types of composites are listed in Table 3.1. It is important to note that the two types of panels absorbed similar amounts of resin. This would imply that the panels would have equivalent mass after manufacture.

Composite Type	Composition
FRP Laminate	16 Layers of fibre glass
Sandwich	12 layers of fibre glass and 15 mm Airex core

Table 3.1: Final dry composition of FRP laminate and Sandwich

3.1.2 Constituent Materials

FRP Laminates

FRP Laminates consisted of 16 layers of plain weave fibre glass. The fibre glass had an approximate areal density of 400 g/m^2. A marine grade epoxy, Prime 20 LV was used. A 50:50 mixture of fast and slow hardener was used to decrease the amount of time the part needed to cure thereby decreasing moulding time from 7 hours to 5 hours. In Table 3.2 the cured system mechanical properties are displayed.

Material Property	Fast Hardener	Slow Hardener
Tensile Strength (MPa)	75	73
Tensile Modulus (GPa)	3.2	3.5
Strain to failure (%)	4.1	3.5
Cured Density (g/cm^3)	1.153	1.144

Table 3.2: Prime 20 LV cure system mechanical properties [31]

Sandwich Panels

The composite sandwich panels comprised of three parts - a PVC foam core and two fibre glass epoxy skins on either side. The Prime 20 LV resin was used with VARTM manufacture to bind the skins and core together in a single shot process.

The skins consisted of 6 layers of the same 400 g/m^2 plain weave fibre glass as the FRP laminates. The chosen core material was Airex C70:75. Airex C70:75 is a closed cell cross-linked polymer foam, which has good impact resistance and low resin absorption. The basic material properties of Airex C70.75 is shown in Table 3.3. An example of a curved sandwich panel is shown in Figure 3.2.

Property	Airex C70.75
Compressive Strength (MPa)	1.45
Compressive Modulus (MPa)	104
Density (kg/m^3)	80
Colour	Green

Table 3.3: Basic mechanical properties of Airex C70.75 [38]

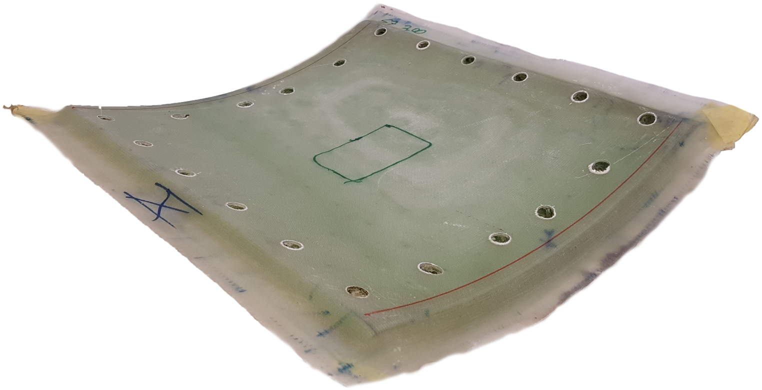

Figure 3.2: A photograph of a R1000 sandwich panel

3.1.3 Consumables

During the manufacturing process many consumables were used and are briefly described below:

- **Infusion Mesh** is a flow promoter and is used to assist the flow of resin though the part during the VARTM process. It is a diamond pattern mesh made from high density polyethylene [39].
- **Peel Ply** is typically a nylon or polyester fabric used in the manufacturing of composite parts. [40] [41] It is used to protect the part from foreign materials becoming integrated into it and to ensure a flat textured surface [42].
- **Infusion Pipe** is a polyethylene pipe (10 mm in diameter) used to transport the resin from the resin bucket into the spiral tubing.

- **Spiral Tubing** is a polyethylene helically wound ribbon used to distribute the resin onto the composite part during an infusion.
- **Vacuum Bag** is a plastic bag used to cover the composite part and create a vacuum with the aid of sealant tape and a vacuum pump.
- **Sealant Tape** is a double-sided tape used to stick the vacuum bag to the mould surface in order to create a seal so that the vacuum is preserved.
- **Mixing Buckets** are simply buckets used to mix the resin and hardener.

3.2 Manufacturing Processes

3.2.1 Sandwich Panel Manufacturing Process

Two processes were trialled for the manufacture of the sandwich panels, namely moulding and developing of flat panels.

3.2.1.1 Developing of Sandwich Panels

In order to develop a flat sandwich panel, a premanufactured flat sandwich panel is elastically deformed in a rig and held in place. After some time the residual stresses in the sandwich relax and the sandwich remains in the new developed state. This manufacturing method was trialled but the test specimen failed before it could reach the required deflection. The observed failure mode was front face sheet fibre fracture and core compression.

3.2.1.2 Moulding of Sandwich Panels

Moulded sandwich panels were made using the VARTM process. The moulding table in the UCT Composites lab was used to manufacture the flat sandwich specimens. The curved sandwich specimens were made using the curved moulds previously used by Sinclair [23], one of which is shown in the photograph in Figure 3.3.

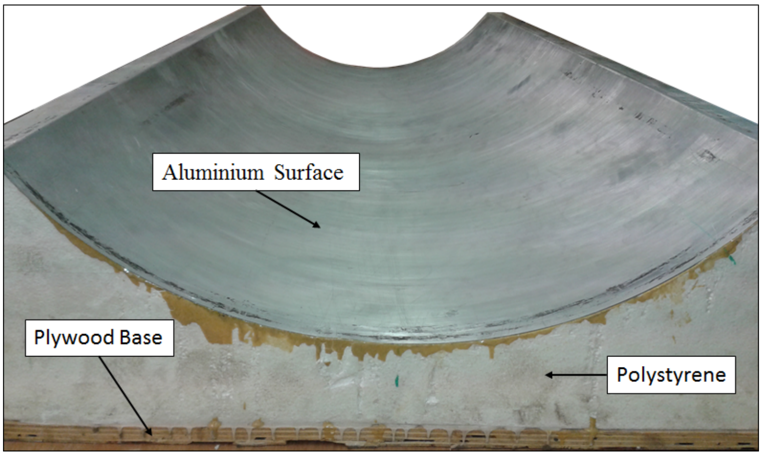

Figure 3.3: Photograph showing curved mould with 500 mm radius of curvature

Thermoforming

The PVC foam cores for the curved sandwich panels were thermoformed prior to the lay up for the VARTM process. Thermoforming involved heating the core to its glass transition temperature and then applying a vacuum pressure to mould it to the required curvature. Some spring back was observed, but this was negligible since further forming would occur during the infusion step. A photograph of a thermoformed core (radius of curvature of 500 mm) is shown in Figure 3.4.

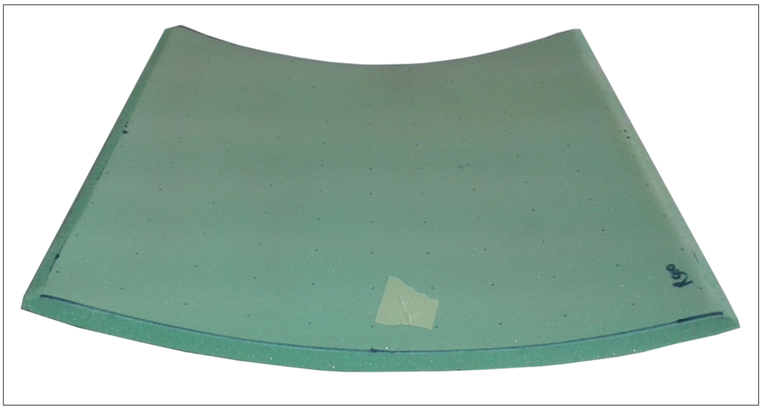

Figure 3.4: Photograph of a typical 500 mm radius of curvature core after thermoforming

In order to prepare the mould for thermoforming, the mould was first waxed with three layers of wax to prevent the core from sticking to the aluminium surface. The cores were cut to size and then chamfered at 45° on all edges. This allowed the fibre glass fabric layers to better drape over the core. A maximum of two cores could be thermoformed at a time. A thermocouple was connected to a core on both the top side and bottom side. The border was marked out with tacky tape. Bleeder cloth was used to cover the cores and a flexible heating blanket was placed between the bleeder cloth and the cores. The vacuum bag with pleats and a vacuum port were constructed. The complete thermoforming setup is shown in Figure 3.5. The process of thermoforming involved heating the core to 90°C and maintaining the temperature at this point. The temperature was monitored with the use of a thermocouple and care was taken not to burn the cores. Once the cores reached their glass transition temperature, a vacuum was drawn by means of a vacuum pump. The vacuum would only be applied when through thickness-heating of core was achieved, which took approximately 15 to 20 minutes. The vacuum and the maintained heat was applied for 30 minutes then the heat was removed while the vacuum was held until the core returned to ambient temperature, after which the vacuum was released.

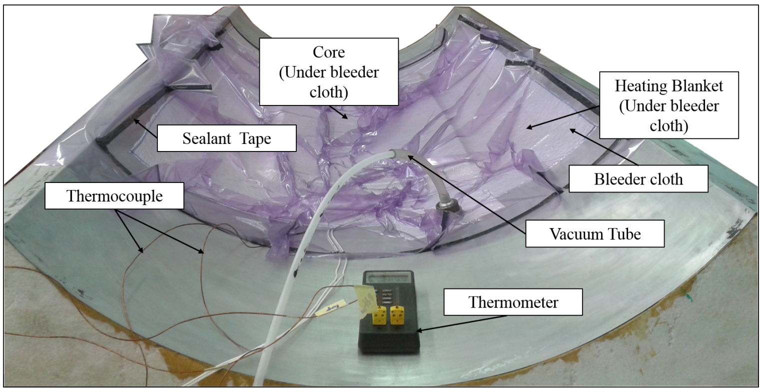

Figure 3.5: Photograph of the thermoforming process

Vacuum Assisted Resin Transfer Moulding (VARTM)

The Vacuum Assisted Resin Transfer Moulding process was used to manufacture the sandwich panels was as follows: the mould was first cleaned with acetone, and then polished with five layers of wax to help release the part from the mould after the infusion. The dry materials were laid up.The layers of glass fibre were placed in the same orientation, such that for the curved panels the 0° fibres lined up with the axis of curvature and the 90° fibres lines up with the flat side. In the case of the flat panels the 0° fibres line up with the one side of the panel and the 90° fibres line up to the perpendicular side of the panel. This is illustrated in Figure 3.6. Next sealant (tacky) tape and piping were set up and a vacuum bag was put over the whole part. The high level activities are illustrated in the flow chart shown in Figure 3.7.

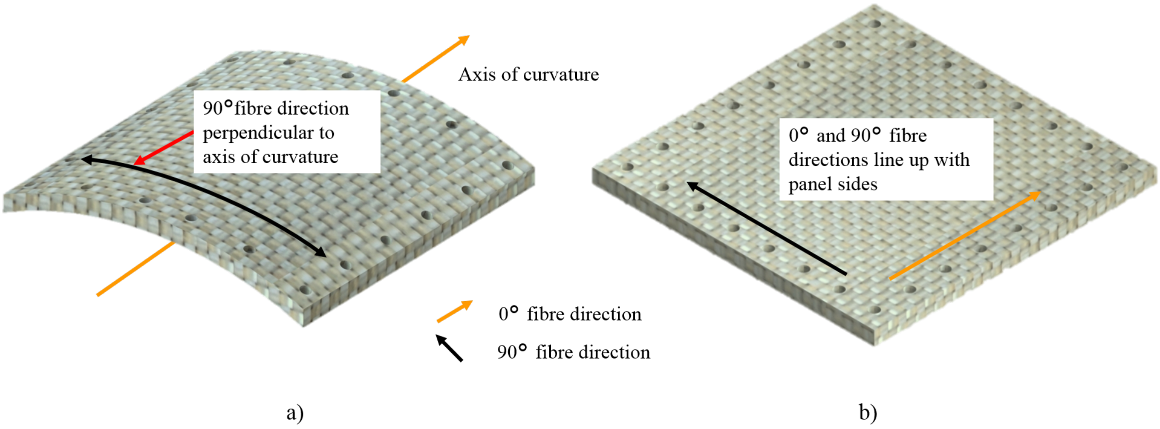

Figure 3.6: : Schematic of fibre orientation and layup for laminates:
a) Curved laminate b) Flat laminate

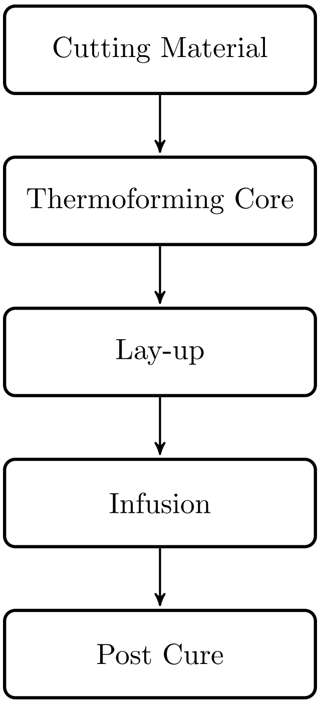

Figure 3.7: Flow chart of sandwich manufacturing method

Quantities of resin and hardener were prepared and the vacuum pump was switched on. The resin was mixed with hardener and then fed into the infusion through the inlet pipe. Once the infusion was complete, the inlet was closed off and the part was left overnight to cure under vacuum. Once cured at room temperature, the parts were post-cured in an oven at elevated temperature to reach its full strength. Figure 3.8 is a photograph of the dry material laid up for an infusion.

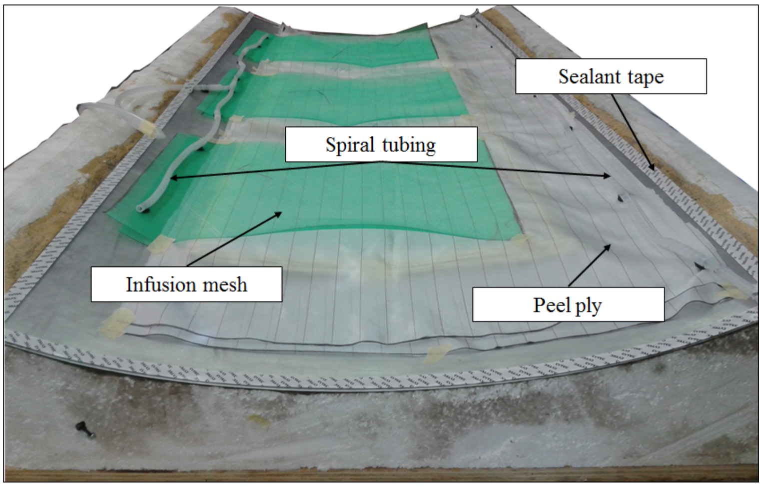

Figure 3.8: Photograph showing the dry lay up before the vacuum bag is applied prior to the infusion process

3.2.2 FRP Laminates

Vacuum Assisted Resin Transfer Moulding (VARTM)

The same process was used as with the moulded sandwich panels, excluding the thermoforming step, since the FRP laminates did not contain a core. The method is described by means of a flow chart in Figure 3.9.

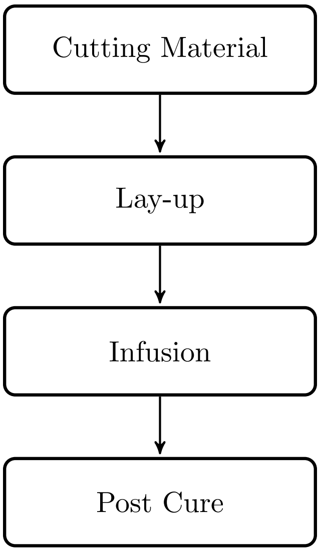

Figure 3.9: Flow chart of laminate manufacturing method

3.2.3 Finishing Operations

This section describes the finishing operations used to prepare the composites for manufacturing consistency testing and blast testing. Once the panels were de-moulded, the panels were post-cured in an oven to reach full strength. Both sandwich panels and laminates underwent this process for 16 hours at 50°C.

Flat sandwich panels and flat laminates were each made in one large infusion. These were cut into the correct size for the testing. Material consistency testing specimens were cut according to ASTM D7250/D7250M-07 [43] for three point bend testing for sandwich panels while laminates were cut according ASTM D7264/D7264M-07 [44] and ASTM D3039/D3039M [45] for three point bend and tensile testing respectively. Next, 400 mm × 400 mm panels were cut for blast testing. A drill press was used to drill bolt holes in the panels and the clamp frame guide was used to guide the drill bit during the drilling process. In total, six flat sandwich panels and six three point bend test specimens were manufactured. The average mass and thickness and corresponding standard deviations of the sandwich panels are displayed in Table 3.4 with their manufacturing variability. The areal density of the sandwich panels are displayed in Table 3.6.

Individual 400 mm × 400 mm panels were manufactured for the curved panels. This ensured that only the bolt holes needed to be drilled to complete the finishing of the panels. A hand drill was used to drill the holes in the panels using the curved clamps as a guide. A total of 12 curved laminates and 15 curved sandwich panels were manufactured. In Table 3.5 average mass and thickness per panel are displayed with their manufacturing variability. The areal density of the laminates is shown in Table 3.6. The fibre and resin volume fractions of the laminates are displayed in Table 3.7.

It should be noted that during manufacturing it was observed that, in the curved mould, some racetracking would occur along the edges of the manufactured panel. This could have caused a small amount of excess resin to accumulate thereby making the curved parts heavier, and explaining the small discrepancy. In addition, the fibre volume and resin volume fractions for the laminates are based on the measured mass of the dry fibre pre-manufacture and the mass of the panels post infusion. Densities from datasheets [31] were used. This calculation is approximate and does not include the effect of any void formation, but is considered sufficiently representative. The fibre and resin volume fraction could not be calculated for the sandwich panel. This is due to resin being absorbed to into both the core and the interface between the core and the face sheet. The skins of the sandwich panel would need to be removed. A burnout test would need to be performed on the skins to determine the fibre volume fraction. This would have added cost and time delays to the project as burnout tests cannot be performed at UCT.

Table 3.4: Average mass and thickness for different sandwich panels manufactured with corresponding standard deviations, minimum and maximum values

Sandwich Panels								
	Mass (kg)				Thickness (mm)			
	Avg	Std. Dev.	Min	Max	Avg	Std. Dev.	Min	Max
Flat	1.36	0.01	1.34	1.38	19.03	0.11	18.86	19.24
R1000	1.95	0.08	1.78	2.06	18.64	0.82	16.34	18.99
R500	1.97	0.09	1.8	2.1	18.86	0.21	18.61	19.29

Table 3.5: Average mass and thickness for different laminates manufactured with corresponding standard deviations, minimum and maximum values

Laminates								
	Mass (kg)				Thickness (mm)			
	Avg	Std. Dev.	Min	Max	Avg	Std. Dev.	Min	Max
Flat	1.50	0.01	1.48	1.52	5.10	0.09	5.02	5.28
R1000	1.80	0.02	1.76	1.82	5.26	0.09	5.11	5.36
R500	1.82	0.02	1.8	1.86	5.26	0.11	5.13	5.43

Table 3.6: Areal density for different curvature of sandwich panels and laminates

Areal Density (kg/m^2)		
	Sandwich Panels	Laminates
Flat	8.48	9.38
R1000	8.19	9.97
R500	9.12	9.84

Table 3.7: Areal density, fibre volume faction and resin volume fraction for the different laminates manufactured

Laminates		
	Fibre Volume Fraction	Resin Volume Fraction
Flat	68%	32%
R1000	64%	36%
R500	65%	35%

3.3 Manufacturing Time

The manufacturing process was completed in six weeks. It should be noted that each of the following took up a full day (8 hours) - cutting the material for three curved laminates, the dry lay-up and infusion preparation. The infusion took another day. Mould preparation took 2 hours and post curing took 16 hours. This totals three and half working days for three curved laminate panels (note that post curing was usually scheduled during non working hours). The sandwich panels required an extra 6 hours to manufacture which included chamfering and thermoforming the core.

The two (sandwich and laminate) large infusion panels were made. The two large infusion panels took three days each to manufacture, and a day each to cut into the required panel sizes (for blast testing) and to post cure. This would give 8 days to manufacture 2 sheets. In total this yielded 10 laminates and 10 sandwich panels which approximated to 10 hours per panel.

The manufacturing process is complex and time consuming when compared to traditional steels used for blast testing. The long processing time and the special safety precautions (the use of full body suit and inhalation mask to prevent glass fibre contamination) needed when drilling and cutting and the inability to automate the process are the main contributing factors that make the manufacturing process lengthy.

Chapter 4

Material Strength Testing

This chapter reports on the results of quasi-static material strength tests, performed on specimens cut from the FRP laminate and sandwich composites. Quasi-static three point bend tests were used to verify the consistency of the manufacturing process. In addition this data was used to ascertain the bending strength the FRP laminate and sandwich. Quasi-static compression tests were used to determine the compressive strength of the foam used in the sandwich. Tensile tests were performed to determine the maximum stress, strain and approximate stiffness of composite laminates. This chapter details the results obtained from the aforementioned tests.

4.1 FRP Laminate Panel Characterisation

The following tests were performed to determine the strength and stiffness of the FRP laminate panel.

4.1.1 Quasi-Static Three-point Flexural Test

The three-point bend tests were conducted in accordance with ASTM D7264/D7264M-07 [44]. The specimen characteristic dimensions were as follows: The nominal span to thickness ratio of 32:1 was used. The specimens had a mean thickness of $5.14\,\text{mm} \pm 0.02\,\text{mm}$. The span length was 160 mm. A total specimen length of 200 mm was used to ensure suitable overhang.

The six test specimens were cut from a flat moulded laminate panel and tested using a Zwick Universal Testing machine. The crosshead speed was 1 mm/min. The three point bend configuration is displayed in Figure 4.1. The supports had a diameter of 10 mm.

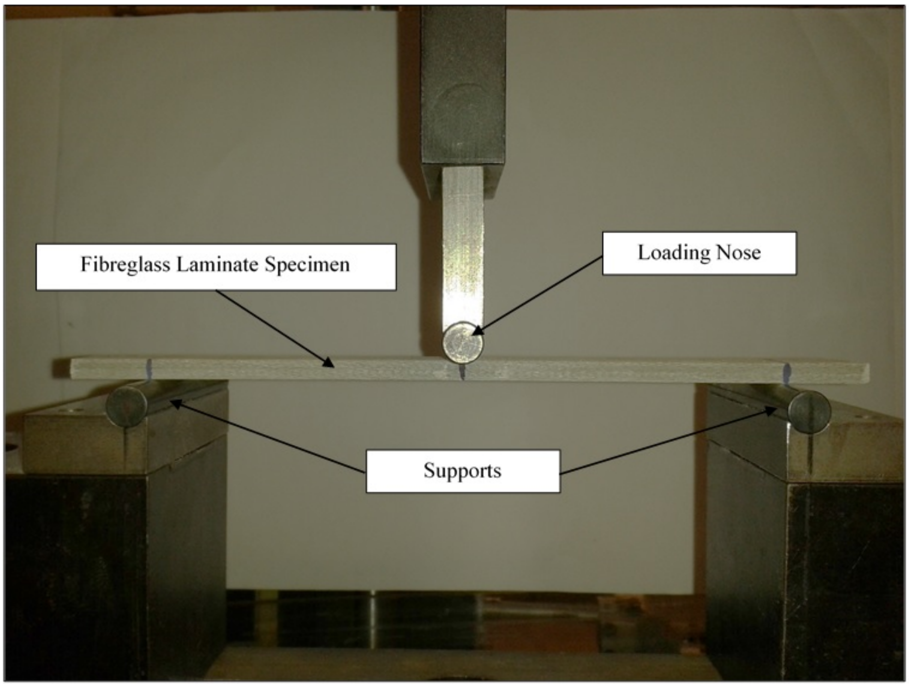

Figure 4.1: Photograph of the three-point bend setup on the Zwick universal testing machine

The Zwick Universal testing machine outputs the force and displacement data of the three-point bend test. The graph of flexural stress versus strain are shown in Figure 4.2. According to ASTM D7264/D7264M [44] the following equations can be used to determine basic material properties.

$$\sigma = \frac{3PL}{4bh^2} \tag{4.1}$$

$$\epsilon = \frac{6\delta h}{L^2} \tag{4.2}$$

$$E_f^{chord} = \frac{\delta\sigma}{\delta\epsilon} \tag{4.3}$$

where σ = stress in MPa, ϵ = strain, E_f^{chord} = Young's Chord Modulus in GPa, P = force in Newtons, L = span length in millimetres, b = specimen width in millimetres, h = specimen thickness in millimetres and δ = deflection in millimetres.

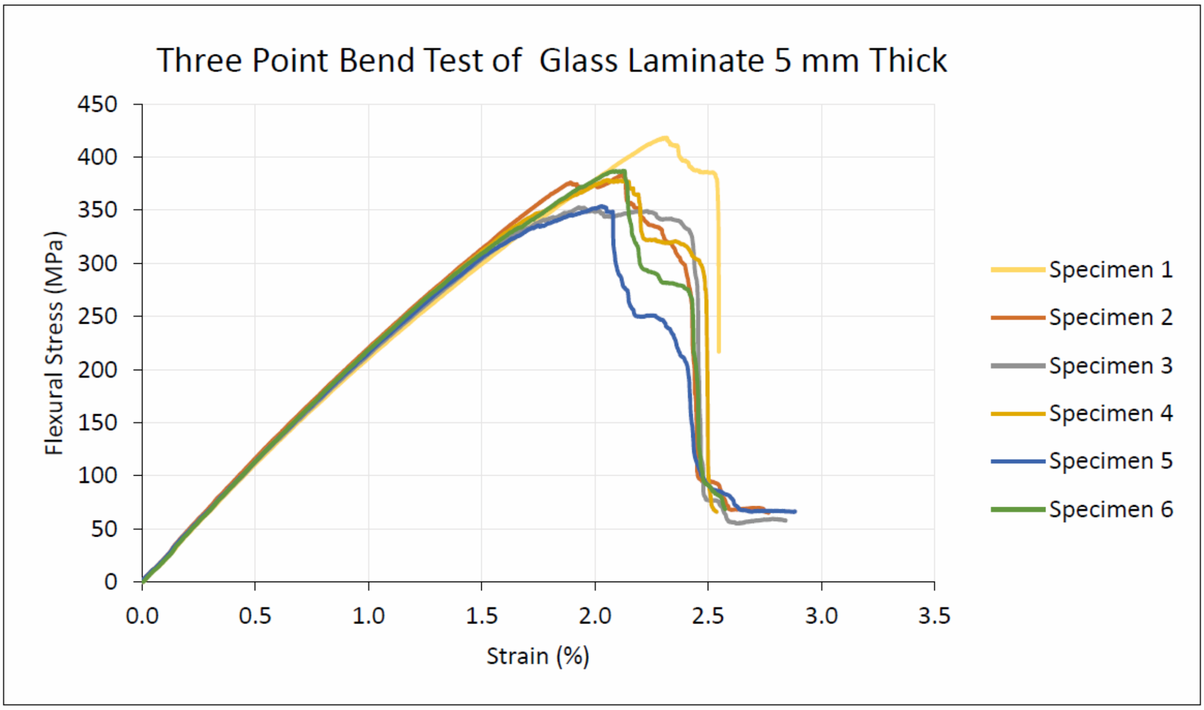

Figure 4.2: Graph of flexural stress vs strain obtained from three point tests on FRP laminates

A summary of results are provided in Table 4.1. Only two types failure modes were observed, namely Fibre Fracture (FF) and Matrix Failure (MF). In addition, all specimens exhibited a linear elastic response up to failure and the location of the failure was observed to be directly underneath the loading nose. The maximum mean stress at failure was 381.0 MPa ± 22.2 MPa. The maximum mean strain at failure was 1.76 % ± 0.86 %. The mean flexural stiffness was 24.04 GPa ± 0.42 GPa.

Table 4.1: Summary of FRP three-point bend test results

Specimen Number	1	2	3	4	5	6
Max Force (N)	967.48	870.76	809.23	867.06	789.39	898.85
Max Stress (MPa)	418.42	383.18	352.99	378.71	365.85	387.20
Strain at Max Stress (%)	2.32	2.12	1.93	2.05	0.02	2.13
Max Deflection at max load (mm)	19.82	18.47	16.88	17.70	17.53	18.09
E (GPa)	23.79	24.76	23.71	24.18	23.65	24.16
Measured Density (g/mm^3)	0.00178	0.00180	0.00178	0.00181	0.00181	0.00178

4.1.2 Quasi-static Tensile Test

Quasi-static tensile tests were conducted in accordance with ASTM D3039/D3039M [45]. Specimens were cut from the flat laminate panels manufactured for the blast test specimens. The specimens were nominally 250 mm long, 25 mm wide and 5 mm thick. End tabs, approximately 50 mm long and 30 mm wide, were bonded to the specimen in order to improve grip during the test. Six test specimens were cut from a flat laminate panel at a 0 - 90°orientation, with the length and width cut were along the weave directions (as shown in Figure 4.3 a)). Another five specimens were cut at a 45° orientation to the 0° weave (fill yarn) as shown in Figure 4.3 b).

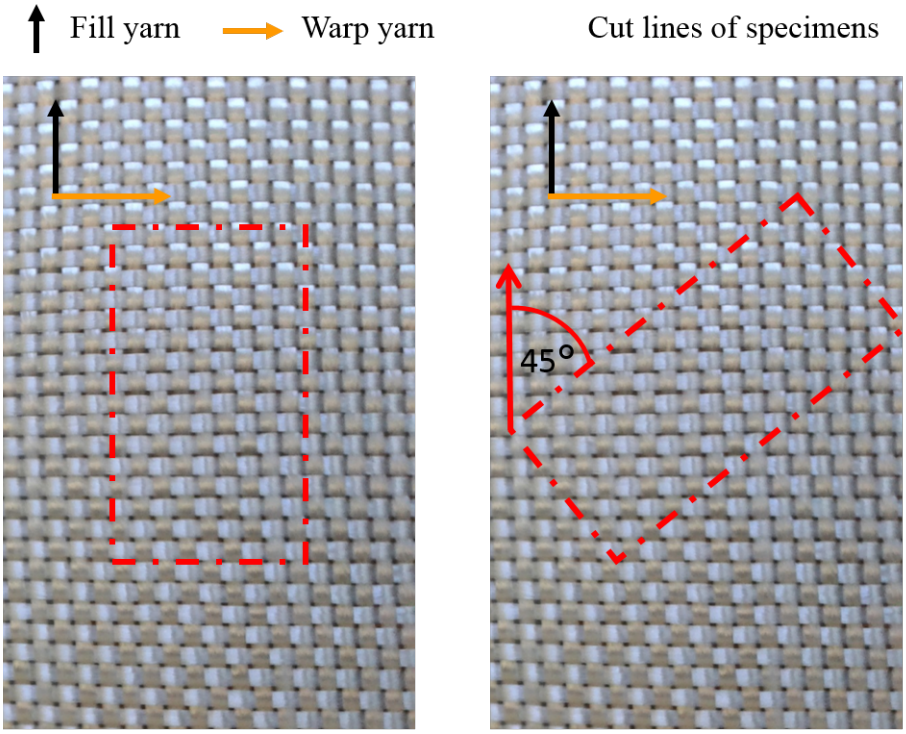

a) b)

Figure 4.3: Photograph of the fabric weave with associated specimen cut patterns: a) Cut pattern of the 0/90° b) Cut pattern of the 45°

The Zwick Universal testing machine was used at a crosshead speed of 2 mm/min. According to D3039/D3039M-14, the Equations 4.3, 4.4 and 4.5 are used to determine basic material properties. Tables 4.2 and 4.3 feature the basic specimen dimensions of the 90° and 45° specimens.

$$\sigma = \frac{P}{A} \tag{4.4}$$

$$\epsilon = \frac{\delta L}{L} \tag{4.5}$$

Table 4.2: Basic FRP tensile laminate specimen dimensions at 0/90° fibre orientation with corresponding means and standard deviations

Specimen Number	Length (mm)	Gauge Length (mm)	Mean Width of Specimen (mm)	Mean Thickness of Specimen (mm)
TL901	200	150	25.67	5.15
TL902	200	151	25.42	5.19
TL903	200	150	25.33	5.12
TL904	200	153	25.35	5.00
TL905	200	150	24.68	5.07
TL906	200	154	24.91	5.11
Mean	200.00	151.14	25.23	5.12
Std dev.	0.00	1.55	0.31	0.06

Table 4.3: Basic FRP tensile laminate specimen dimensions at 45° fibre orientation with corresponding means and standard deviations

Specimen Number	Length (mm)	Gauge Length (mm)	Mean Width of Specimen (mm)	Mean Thickness of Specimen (mm)
TL451	200	150	26.22	5.04
TL452	200	150	26.33	5.05
TL453	200	151	26.27	5.02
TL454	200	151	26.39	5.11
TL455	200	149	26.28	4.98
Mean	200.00	150.20	26.30	5.04
Std dev.	0.00	0.75	0.06	0.04

The results from the tensile tests on the 0/90° specimens are shown in Figure 4.4. The specimens displayed a linear-elastic response up to the point of rupture. Rupture occurred suddenly without plastically deforming the specimen. A summary of the test results are presented in Table 4.4. The ASTM failure designations observed were XGM which is an explosive failure within the gauge length in the middle of the specimen (see Figure 4.5 and 4.6) and LAT which is lateral break at the grip/tab located at the top of the specimen [45]. An extract from ASTM D3039/D3039M-14 [45] is presented in Figure 4.7. The maximum mean stress at failure was 413.0 MPa ± 32.0 MPa, the maximum mean strain at failure was 6.93 % ± 0.35 % and the mean flexural stiffness was 72.24 GPa ± 4.90 GPa.

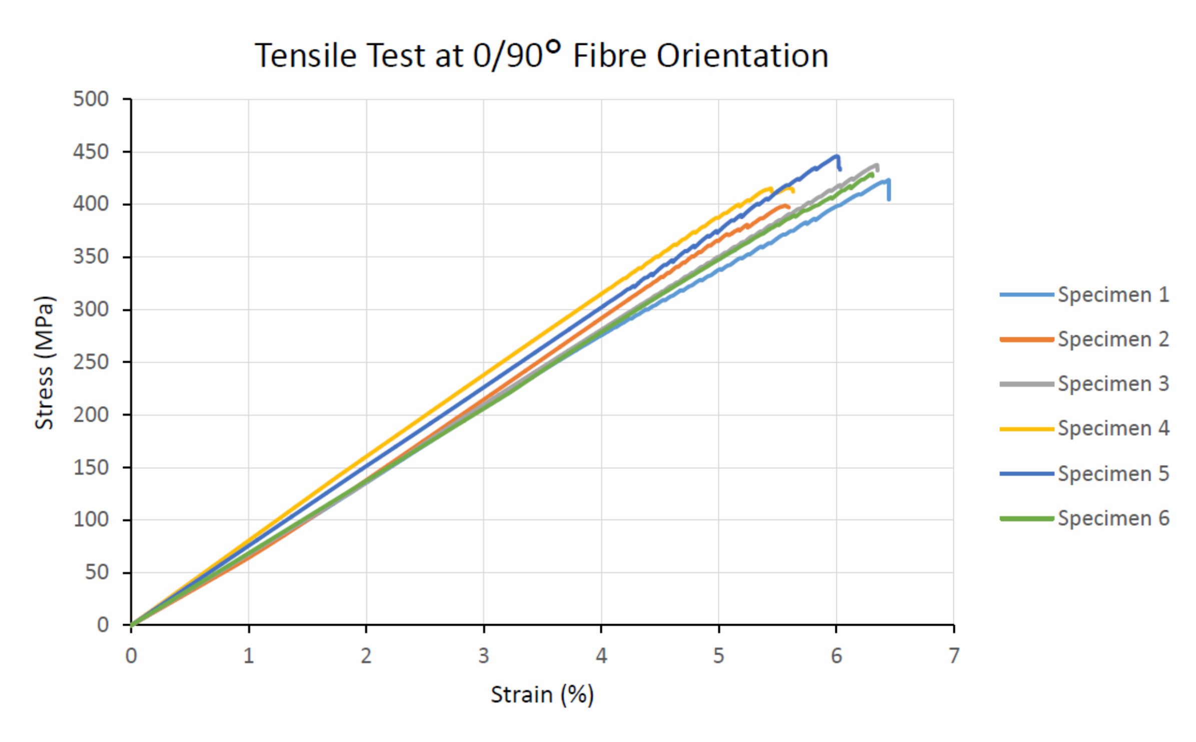

Figure 4.4: Stress-strain plot the of FRP tensile laminate specimen dimensions at 90° fibre orientation

Table 4.4: Basic material data processed from the tensile test data

Specimen Number	1	2	3	4	5	6
Max Force (N)	55900	52603	56744	52730	55808	54572
Max Stress (MPa)	423.17	398.91	437.54	415.76	445.93	428.58
Strain at max Stress (%)	7.27	6.21	7.24	6.69	6.89	7.08
Max elongation at max load (mm)	10.91	9.37	10.86	10.23	10.33	10.91
E (GPa)	71.34	75.85	73.58	76.05	71.97	75.89
Measured Density (g/mm^3)	0.00310	0.00311	0.00312	0.00315	0.00316	0.00314
Failure Designation	XGM	LAT	LAT	LAT	XGM	XGM

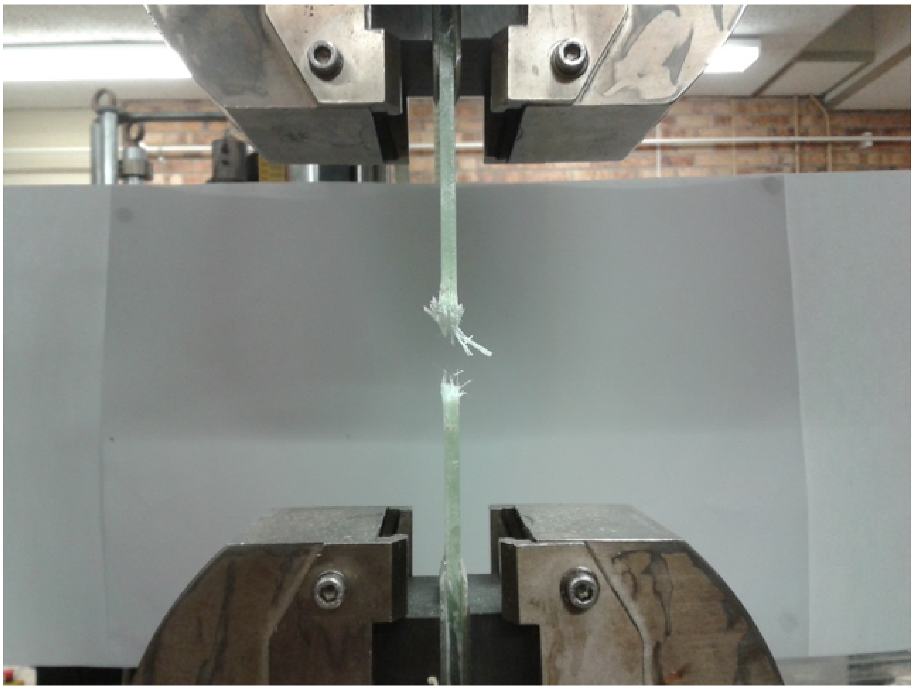

Figure 4.5: Photograph of 90° fibre orientation test with XGM failure

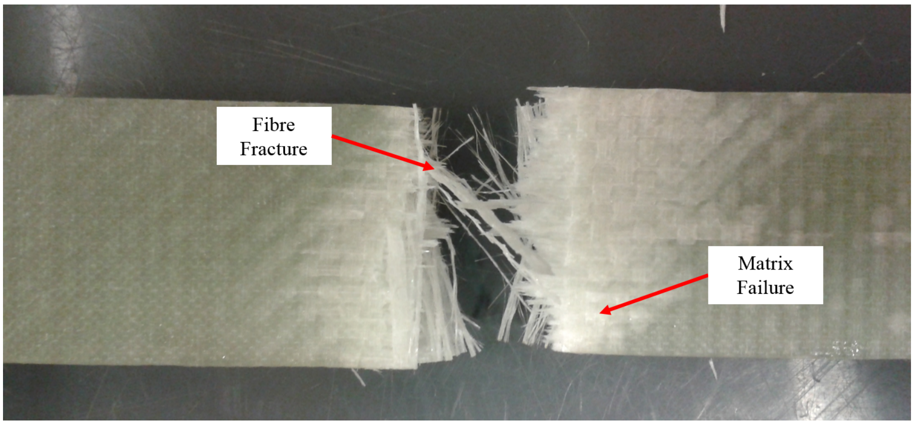

Figure 4.6: Photograph of XGM failure showing fibre breakage and matrix failure

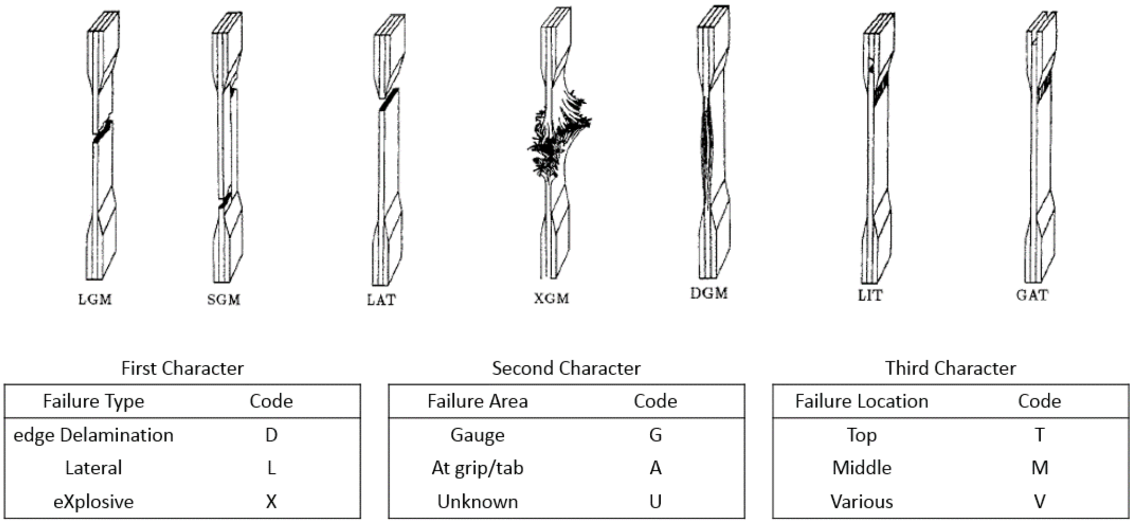

First Character

Failure Type	Code
edge Delamination	D
Lateral	L
eXplosive	X

Second Character

Failure Area	Code
Gauge	G
At grip/tab	A
Unknown	U

Third Character

Failure Location	Code
Top	T
Middle	M
Various	V

Figure 4.7: Tensile test failure codes adapted from [45]

The stress versus strain graph of the tensile FRP laminate at 45° fibre orientation is shown in Figure 4.8. A summary of the test results are presented in Table 4.5. The failure designations observed were DGM (edge delamination occurring within the gauge length at the middle of the specimen) and XGV (explosive break within the gauge length occurring at various locations) [45]. Specimens exhibited linear-elastic behaviour until 5% strain, and then “plastically deform” as the multiple plies delaminated until fibre fracture occurred. In Figure 4.9, the green colour of the matrix is hidden by the delamination that has occurred. Lastly, from Table 4.5 it can be concluded that that the maximum mean stress at failure is 102.74 MPa 103.0 MPa ± 2.6 MPa, maximum mean strain at failure is 7.56 % ± 0.38 % and mean flexural stiffness is 33.89 GPa ± 2.40 GPa.

Table 4.5: Basic material data processed from the tensile test data

Specimen Number	1	2	3	4	5
Max Force (N)	13135	13452	13400	14202	13890
Max Stress (MPa)	99.42	101.24	101.56	105.40	106.10
Strain at max Stress (%)	7.27	7.27	7.22	7.94	8.12
Max Deflection at max load (mm)	10.91	10.91	10.91	11.99	12.09
E (GPa)	29.31	35.03	35.01	36.17	33.92
Density (g/mm^3)	0.00314	0.00312	0.00315	0.00304	0.00317
Failure Designation	DGM	DGM	XGV	XGV	XGV

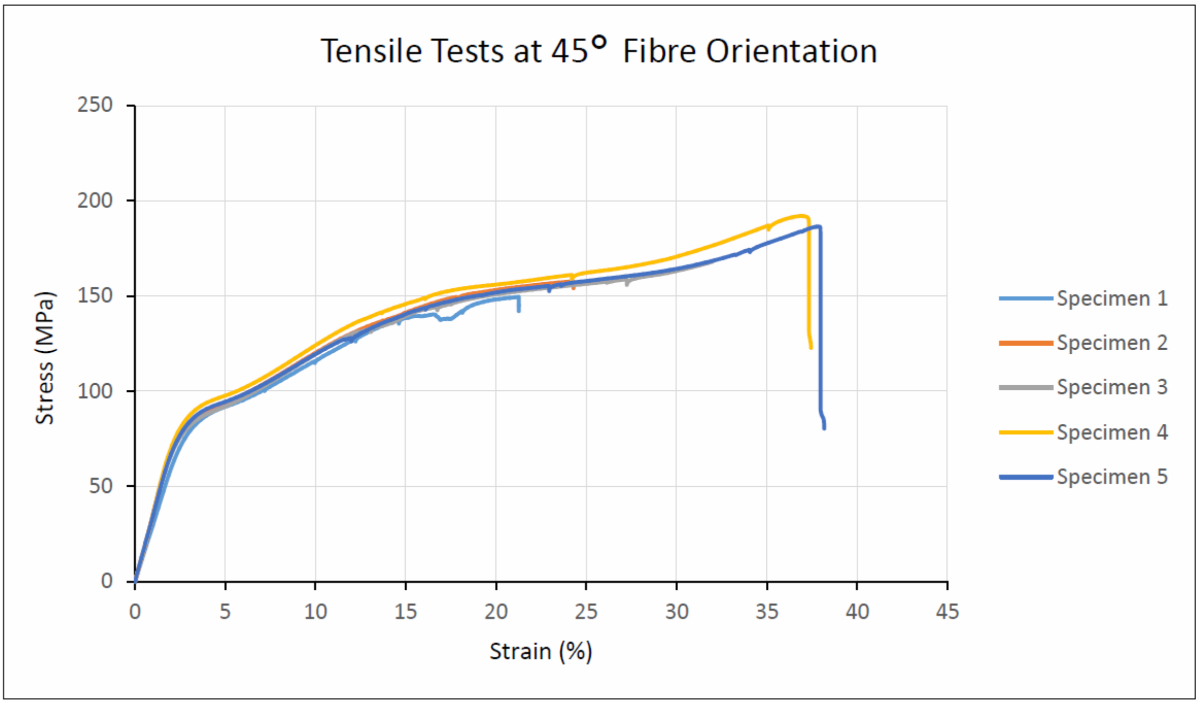

Figure 4.8: Stress-strain plot the of FRP tensile laminate specimen dimensions at 45° fibre orientation

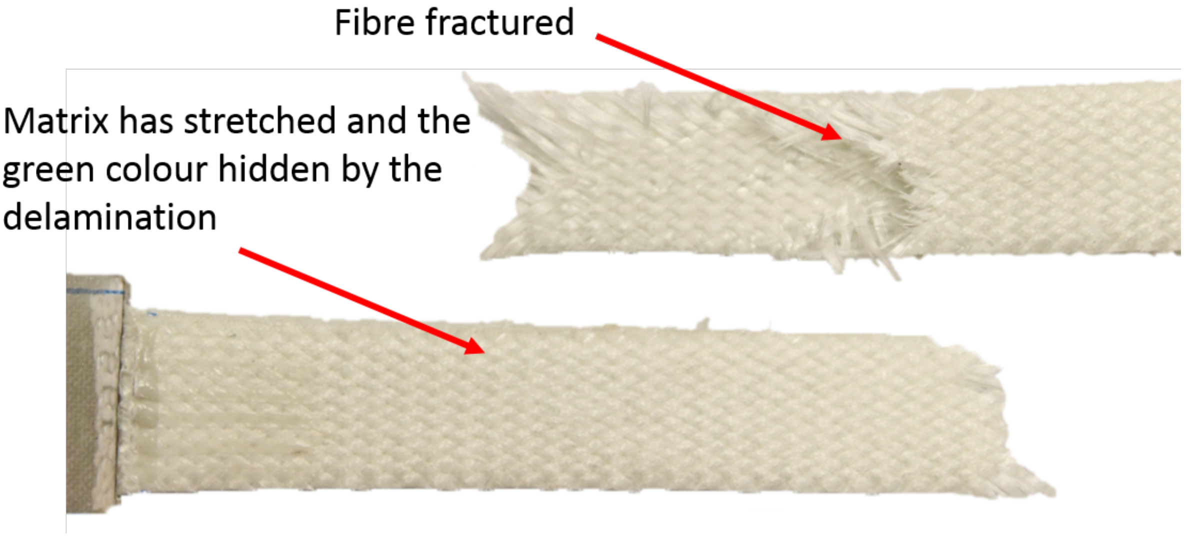

Figure 4.9: Photograph of a 45° specimen post failure

4.2 Sandwich Panel Strength Testing

4.2.1 Quasi-static Three-Point Flexural Test

Quasi-static three-point flexural tests were performed on sandwich beams, in accordance with ASTM D7250/D7250M-07 [43]. The aim of this test is mainly to understand the consistency of manufacturing of the samples produced. The specimens were nominally 350 mm long, 50 mm wide and had a span of 300 mm (and an average span to thickness ratio of 15.8). The mean total length of the specimens was 350.75 mm to ensure suitable overhang. The mean thickness of a specimen was 19.04 mm and the sandwich beams were cut from a flat moulded sandwich panel.

The stress vs strain graph in Figure 4.10 has been produced with the aid of the equations 4.1, 4.2 and 4.3. All specimens exhibited linear elastic behaviour in the beginning as reported by Langdon et al [22, 35] and Sinclair [23], after which core compression would occur and eventual failure when face sheet rupture occurred. A summary of results from the test are shown in Table 4.6. A photograph of a sandwich specimen is shown in Figure 4.11 with associated observed modes. Failure occurred under the centre loading nose. The observed failure modes displayed in Figure 4.11 are Fibre Fracture (FF), Matrix Cracking (MC) and Core Crushing (CC). From the test results it was observed that the maximum mean stress at failure was 45.0 MPa ± 0.7 MPa. The maximum mean strain at failure was 1.26 % ± 0.05 %. The mean flexural stiffness was 4.92 GPa ± 0.06 GPa.

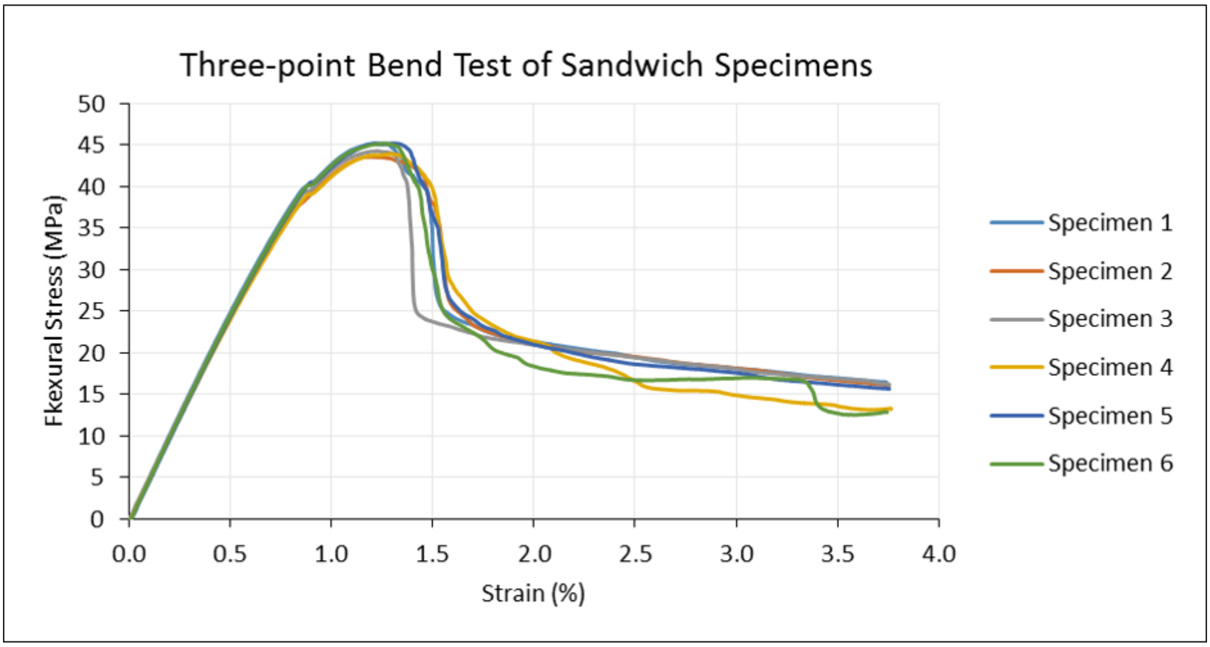

Figure 4.10: Stress-strain plot of the three-point bend sandwich composite

Table 4.6: Basic material data processed from the three-point bend test data

Specimen Number	1	2	3	4	5	6
Max Force (N)	1854	1804	1832	1826	1866	1856
Max Stress (MPa)	45.22	43.60	44.28	43.95	45.23	45.20
Stain at max Stress (%)	1.26	1.19	1.23	1.29	1.32	1.26
Max Deflection at max load (mm)	10.43	9.80	10.13	10.57	10.81	10.38
E (GPa)	4.97	4.92	4.91	4.82	4.95	4.96
Density (g/mm^3)	0.00046	0.00046	0.00046	0.00046	0.00046	0.00046

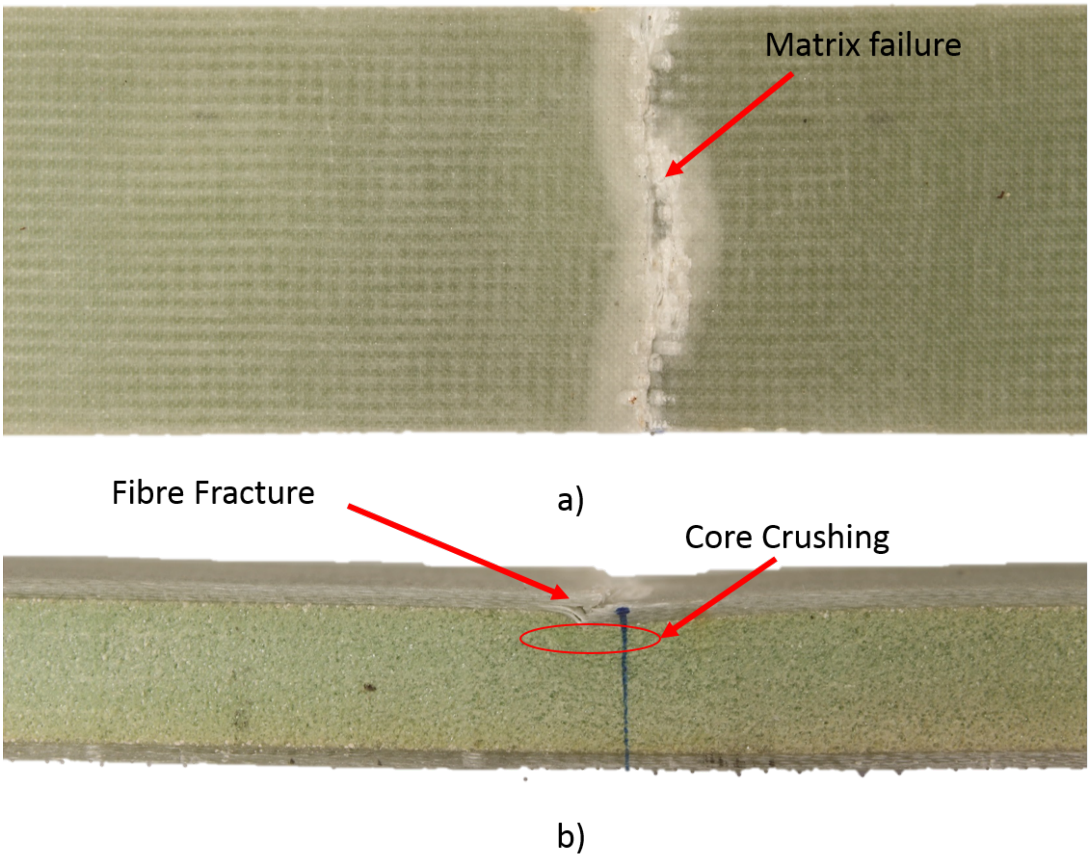

Figure 4.11: Photograph of three-point bend specimen a) Top view b) Side view

4.2.2 Quasi-Static Compression Test

Quasi-static compression tests were conducted in accordance with ASTM D1621-10 [46] on the foam specimens that were nominally 60 mm × 60 mm × 15 mm. Note the ASTM standard for the specimen height could not be used due to the low thickness of the foam supplied. The test apparatus can be seen in Figure 4.12. The seven test specimens were cut from a single sheet of Airex C70:75. Table 4.7 features their basic dimensions only.

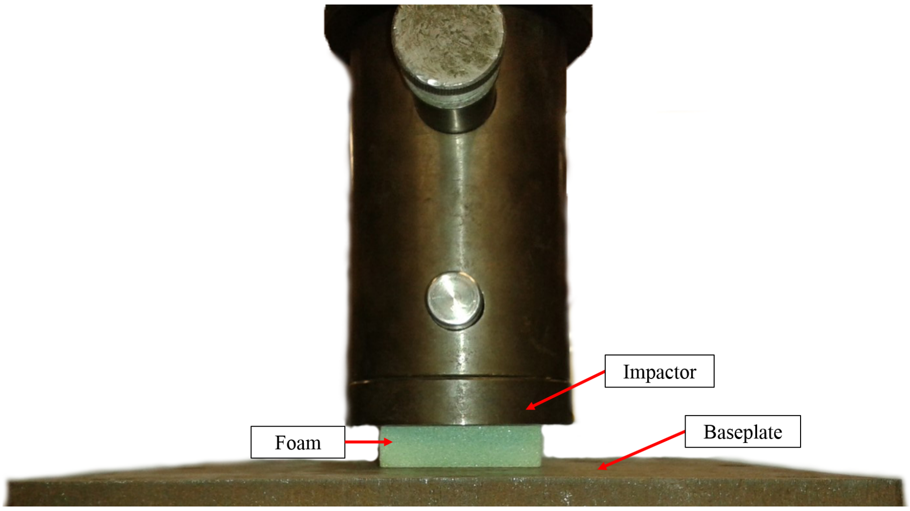

Figure 4.12: Photograph of the compression rig setup

Specimen Number	Avg. Thickness (mm)	Avg. Side Length (mm)	Avg. Compressive Area (mm^2)
CC1	14.99	60.27	3632
CC2	15.02	60.38	3646
CC3	15.01	61.61	3796
CC4	15.00	60.77	3693
CC5	14.96	61.23	3749
CC6	14.98	61.60	3795
CC7	14.98	61.51	3783
Mean	14.99	61.05	3728
Std dev.	0.02	0.53	65

Table 4.7: Mean average dimensions of the compression specimens, ordered by specimen number

The Zwick Universal testing machine outputs the force and displacement data of the compression test. The following equations (from ASTM D1621-10 [46]) were used to determine basic material properties.

$$\sigma = \frac{W}{A} \tag{4.6}$$

$$\epsilon = \frac{\delta L}{L} \tag{4.7}$$

$$E_C = \frac{WH}{AD} \tag{4.8}$$

where W = force in Newtons, A = initial horizontal cross-sectional area in millimetres squared, L = specimen thickness in millimetres, E_C = modulus of elasticity in compression in MPa, H = initial specimen height in millimetres and D = deformation in millimetres.

The stress versus strain graph in Figure 4.13 has been produced with the aid of equations 4.6, 4.7 and 4.8. In addition, the expected initial elasticity, plateau region and strain hardening in the densification region were also displayed in Figure 4.13, which is also observed in Langdon et al [22, 35] and Sinclair [23]. In the elastic region deformation is not permanent and when the load is removed the sample should recover. This is due to the elastic bending of the cell walls [23]. As the load was increased the foam entered the plateau region. The plateau region displays the energy absorption capabilities of the foam [23]. As the material densifies, the foam properties start to approach those of the parent material, characterised by a steep rise in stress. A summary of results from the test are shown in Table 4.8. From the test results it was concluded that the maximum mean stress at failure is 1.38 MPa ± 0.05 MPa. The maximum mean strain at failure is 4.75 % ± 0.07 %. The average plateau stress is 1.34 MPa ± 0.06 MPa. The mean compressive stiffness is 34.14 MPa ± 0.98 MPa.

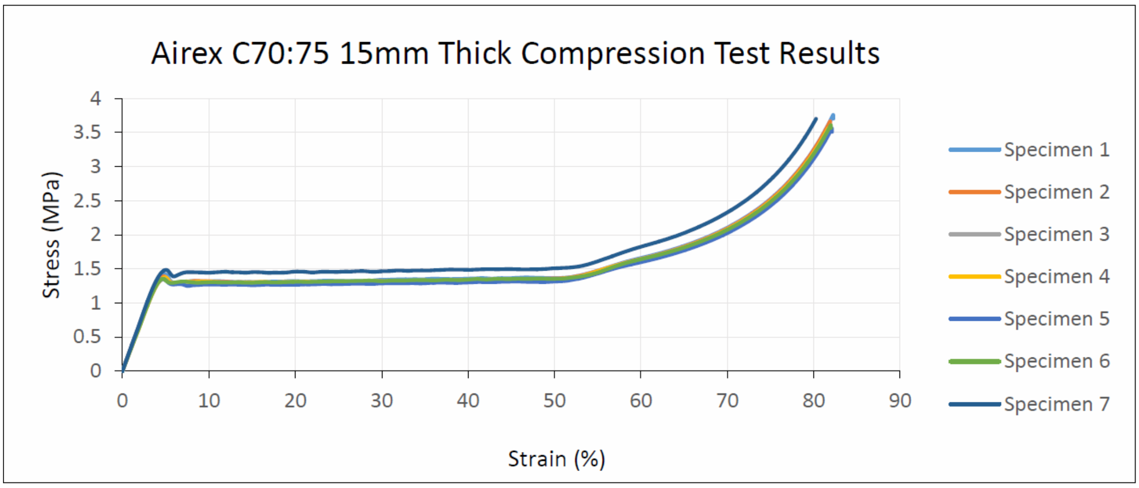

Figure 4.13: Stress-strain plot the of core compression test

Table 4.8: Basic material data processed from the compression test data

Specimen Number	1	2	3	4	5	6	7
Compressive Yield Strength (MPa)	1.42	1.39	1.34	1.37	1.35	1.35	1.47
Strain at max Stress (%)	4.88	4.77	4.73	4.77	4.69	4.68	4.72
Average Plateau Stress (MPa)	1.33	1.31	1.31	1.32	1.28	1.32	1.47
Compressive Stiffness (MPa)	35.33	34.63	33.29	33.07	34.30	33.14	35.25
Measured Density (g/mm^3)	0.00008	0.00008	0.00008	0.00008	0.00008	0.00008	0.00009

4.3 Summary

This chapter explored the material tests that were undertaken to determine the consistency of material properties and manufacturing methods used. Three-point bend tests and tensile tests for laminates were performed. Post-test inspection revealed that the laminate three-point bend specimens failed in compression and exhibited fibre fracture and matrix failure underneath the loading nose. Tensile specimens cut along the 0/90° exhibited linear elastic behaviour until failure, which occurred abruptly, similar to a brittle material. The tensile specimens cut along the 45° line exhibited linear elastic behaviour in the beginning also, after which the specimen "plastically deformed" until fracture. The three-point bend test method was also used to test the sandwich specimens. The specimens failed in compression and exhibited fibre fracture, matrix failure and core crushing. The top face sheet failed in compression whereas the bottom face sheet (which was in tension) showed no damage. The core material used to manufacture the sandwich panel was tested in compression. The foam exhibited linear elastic behaviour initially, but as the load increased, the foam reached the plateau stress where it continued to bear the load until core densification occurred. The tests on all the samples exhibited low standard deviations and highly repeatable results. This is indicative of consistent material properties and the reliability of manufacturing methods used.

Chapter 5

Experimental Apparatus and Procedures

Blast tests were performed on the ballistic pendulum in the Blast Survivability and Impact Research Unit (BISRU) blast chamber. This chapter details the experimental design and setup.

5.1 Experimental Design

5.1.1 Clamp Design

A rendered model of the panel clamps is shown in Figure 5.1. Both sets of the curved panels required new curved clamp frames to be manufactured for testing. A key design requirement was the distance between the back plate and the back of the test specimen. This is marked distance "A" in Figure 5.1. Distance A needed to be large enough so that when transient deformation of the specimen occurred, it would not hit the back plate. If this occurred, the impulse reading would have been adversely affected and potentially other damage modes would occur. In order to determine the required distance, a numerical simulation was made to ascertain the deflection of the specimen under the presumed blast loads.

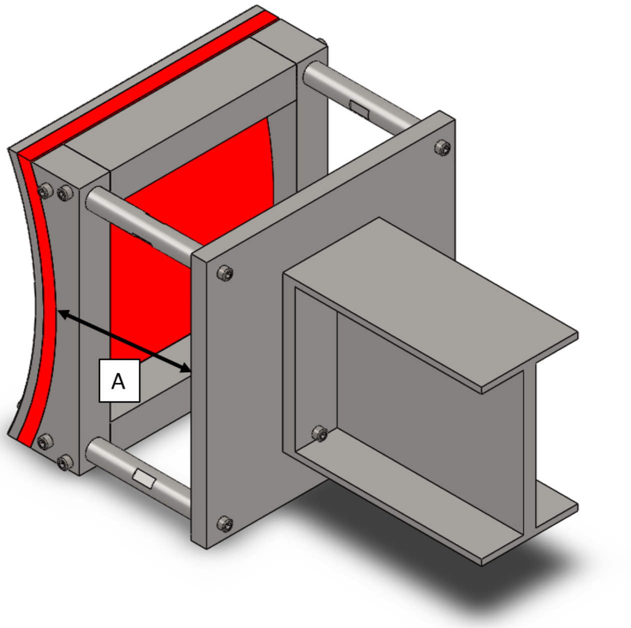

Figure 5.1: 3D rendered model of R500 experimental setup

A finite element package with explicit time integration, LS DYNA V971, was used to numerically model the blast loading. A quarter symmetry model of the explosive (PE4), air, an idealised clamp front clamp and R500 laminate were modelled. The model can be seen in Figure 5.2. The R500 was chosen because it has the tightest curvature and the back face of the specimen would be closest to the back plate. It was also expected to have higher impulse than the flat or R1000 curved panels and therefore experience the most displacement. The laminate was chosen over the sandwich panel due to the laminate having a higher elastic limit. This implied that the laminate would displace more than the sandwich panel before failure.

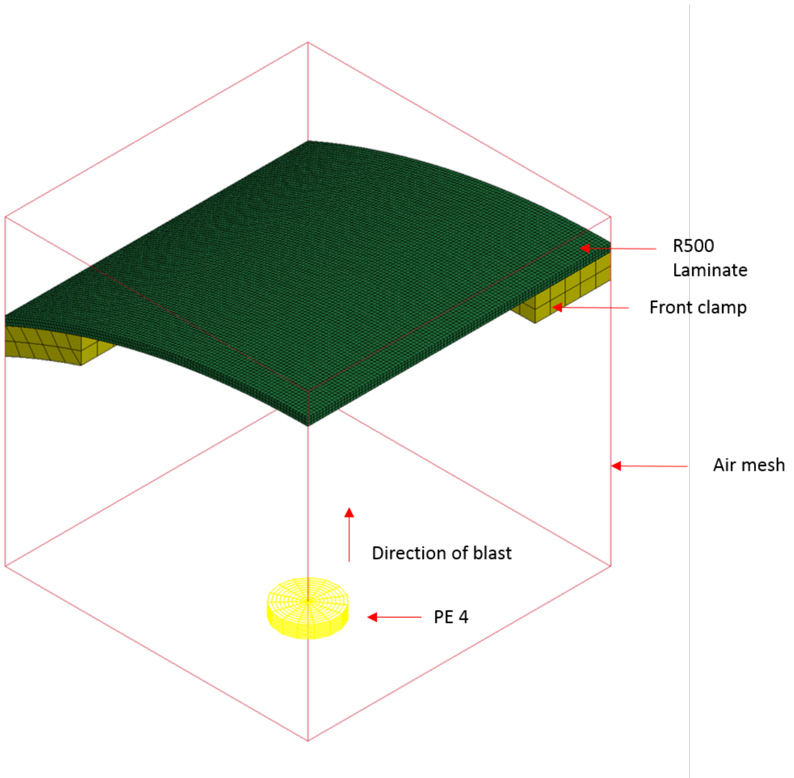

Figure 5.2: 3D rendered quarter symmetry numerical model of the experimental setup

A rigid material model was used to model the clamp as minimal deflection was expected in the experiment. An elastic material model was used to model the FRP laminate to investigate maximum deflection with lowest possible run time. The air was modelled using the ideal gas equation. The PE 4 was modelled using the Jones-Wilkins-Lee equation of state and the LS DYNA High Explosive Material card. The air and PE 4 explosive were formulated using MMALE mesh . The explosive was defined as a volume fraction of the air mesh. In Tables 5.1 and 5.2 the equation of state variables for air and PE 4 respectively are displayed as well as material properties used in the simulation.

Table 5.1: Material and equation of state parameters for air [13]

$\rho_o(\frac{kg}{m^3})$	γ	$\rho_o(E_o\frac{kJ}{m^3})$
1.184	1.4	2.533

Table 5.2: Material and JWL equation of state constants for explosive (PE4) [13]

P_o	D	P_{CJ}	A	B	R_1	R_2	ω	E_o
$\frac{kg}{m^3}$	$\frac{m}{s}$	(GPa)	(GPa)	(GPa)				(GPa)
1601	8193	28	609.77	12.95	4.5	1.4	0.25	9.0

The numerical model revealed that a R500 laminate exposed to 25 g charge at 100 mm SOD would have a maximum displacement of 14.37 mm with a von Mises stress of 608.9 MPa. The laminate fails at 382 MPa. The corresponding displacement at 382 MPa in the numerical model was 12.69 mm. It was concluded that the distance from the back plate to the panel would thus need to be larger than 12.69 mm. The final distance of “A” was 230 mm and 217 mm for the R1000 and R500 configurations respectively.

5.1.2 SOD Determination

The SOD was determined by understanding the cylindrical charge discounting angle. According to Zukas et al [47] the limiting amount of an unconfined cylindrical explosive which can be effective in driving a plate forward is defined by a cone with a 30° half angle (see Figure 5.3)

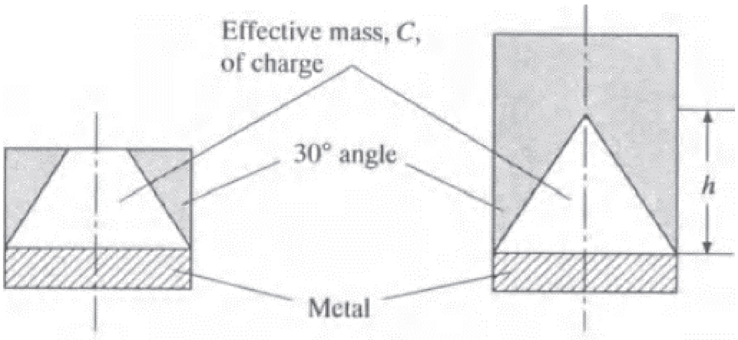

Figure 5.3: Effective charge mass indicated by the cone with the 30° half angle with metal plate below the cylindrical charge [47]

This method of using the 30° half angle was used to ensure that there was adequate impulse transfer between the explosive and the test area considered. A 60° line was drawn from the innermost part of the clamp frame and used to determine the maximum possible stand-off distance. This is shown graphically in Figure 5.4. Once the maximum possible SOD was determined (260 mm, distance A in Figure 5.4), the next task was to ensure localised loading without ripping through the composite. If the SOD is too small, there is risk of initiating too many failures at once. This would make it impossible to determine the failure initiation and progression for a given charge mass. If the SOD is too large, then there is a risk of reflections of the blast wave from the clamps affecting the loading on the composite panel.

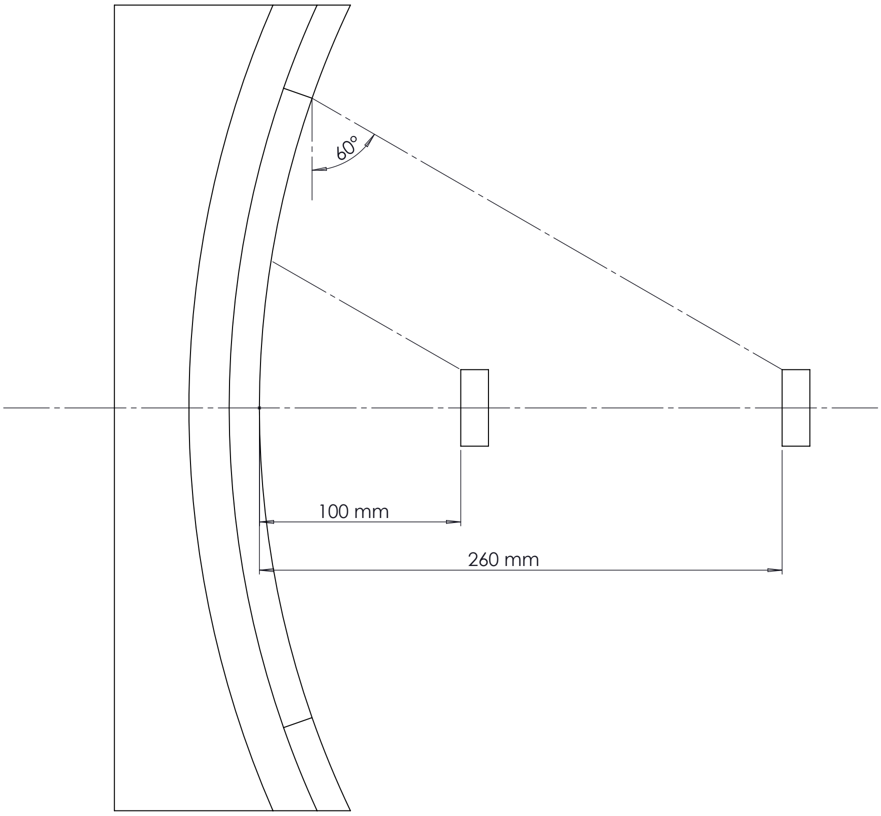

Figure 5.4: Analysis used to determine the effective change mass of the experiment

It was determined that in order to have constant localised regions of failure with respect to all panel curvatures, a SOD of a 100 mm was chosen. This allowed the localised region for the R500 and flat panels to be 20.6% and 18.3% of the total exposed area respectively. Using the numerical model, it was estimated that even at the highest charge mass of 25 g, the impulse applied to the clamp was 0.61 Ns whereas the impulse at the panel was 39,5 Ns. This ensured that 98.5 % of the impulse transfer was directed at the panel rather than the clamp.

5.2 Experimental Setup

All panels were clamped to a ballistic pendulum and an explosive charge was placed near the panel by means of a polystyrene bridge.

5.2.1 Ballistic Pendulum Setup

The ballistic pendulum at the BISRU Laboratory consists of an I-beam suspended by four steel cables. Located at the front of the I-beam is the mounting area for specimens and associated clamping mechanisms. At the rear of the I-beam are the counter weights used to balance the

I-beam. This arrangement can be seen in Figure 5.5. The full description of the theory and impulse derivation can be found in Appendix E.

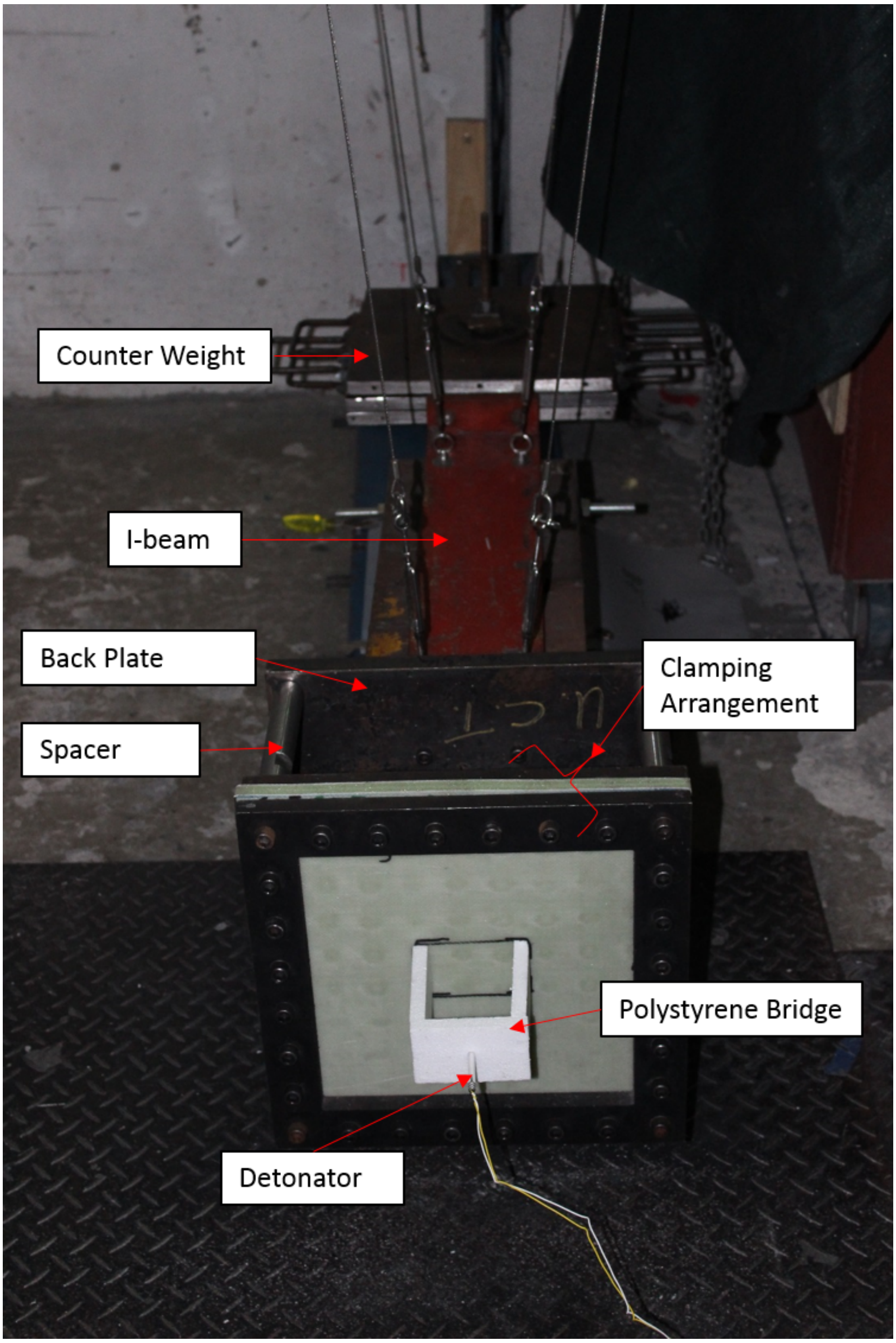

Figure 5.5: Ballistic pendulum with flat composite clamping arrangement

In addition to flat composites, two other curvature types were tested. Two sets of clamping arrangements were designed and manufactured. In Figure 5.6 there are two sets of front clamping members. This is due to the different thicknesses of the laminate and sandwich panels. Detailed design drawings of the clamp frames can be found in Appendix B.

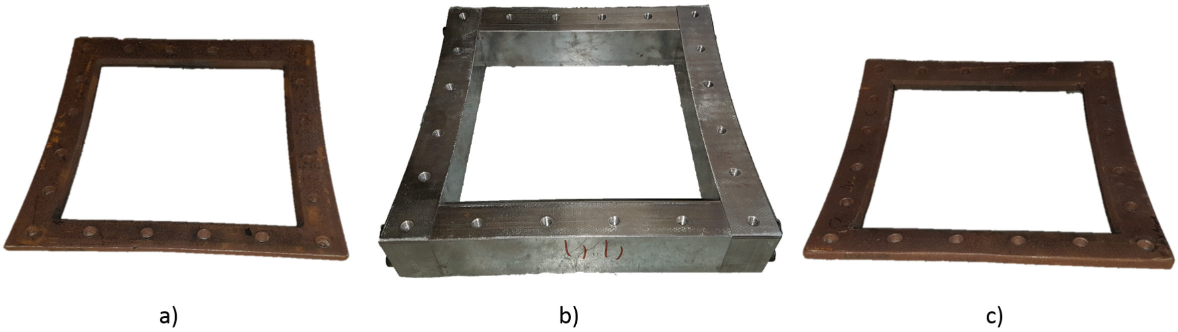

Figure 5.6: R1000 clamping members: a) Front clamp for the sandwich panel b) Base clamp that fits both the sandwich and the laminate c) Front clamp for the laminate panel

5.2.2 Test Parameters

The blast loading of all panels was accomplished by detonating charges of PE 4 plastic explosive. A cylindrical charge was used with a constant diameter of 38 mm. Charge masses started at 10 g and were increased by 2.5 g or 5 g increments depending on the failure modes observed. If too many failure modes were initiated, then the charge mass was reduced in order to determine the onset of that particular failure mode. A constant SOD of 100 mm was used for all panels. In Table 5.3 is a summary of the tests conducted.

Table 5.3: Test matrix with panel types and number of tests performed (note: repeat tests are included)

Panel Type	Number of Tests	PE4 Range (g)
Flat Sandwich	5	10 - 20
R1000 Sandwich	9	10 - 20
R500 Sandwich	7	10 - 20
Flat Laminate	5	10 - 25
R1000 Laminate	6	10 - 25
R500 Laminate	6	10 - 25

Chapter 6

Experimental Results

6.1 Ballistic Pendulum Results

The blast panels were mounted on a ballistic pendulum at BISRU and subjected to a series of localised blast loads. The charge mass was varied in order to investigate the panel responses ranging from minimal damage to catastrophic failure. The corresponding impulses were calculated per panel and possible failure modes and progression were investigated. This section elaborates on the failure modes encountered with brief descriptions of them, the impulse calculated from the tests, delamination of the exposed area and debonded length percentages with respect to the midline distance.

6.1.1 Failure Mode Description

Sandwich panels and laminates that were blast tested exhibited similar failure modes to those encountered by Langdon et al [22] and Tekalur et al [4]. Failure modes are classified according to three distinct regions for the sandwich panel, namely the face sheets, core and the interface between the face sheet and core. The laminates exhibited face sheet type failure modes only. A summary and a brief description of the failure modes encountered during testing can be found in Table 6.1.

Table 6.1: Failure mode region with corresponding abbreviation and description

Region	Failure Mode	Designation	Description
Face Sheet	Delamination	DL	The appearance of white areas that indicate interfacial separation
	Matrix Failure	MF	The appearance of resin missing but the weave remains intact
	Fibre Fracture	FF	Fibres have been rupture or broken
	Fibre Fracture Penetration	FFp	Fibres have been rupture or broken though the thickness of the laminate/skin
Core	Core Crushing	CC	Crushing of the core
	Core Shear	CS	Cracking of the core
	Core Fragmentation	CF	Core is fragmented into pieces
	Core Penetration	CP	Core is penetrated through the thickness
Interface	Debonding	Deb	Separation of core from face sheet

6.1.1.1 Face Sheet Failures

Both sandwich panels and laminates exhibited delamination. Sandwich panels exhibited delamination on both front and back face sheets. The back face of the sandwich is shown in Figure 6.1 by the whitish region. The laminates experienced delamination through the thickness. Delamination occurred close to the front of the panel as seen in Figure 6.2; this would appear as a darker region as compared to the region that delaminated closer to the back of the panel, but usually appeared as white on the back face suggesting the delamination was closer to the back.

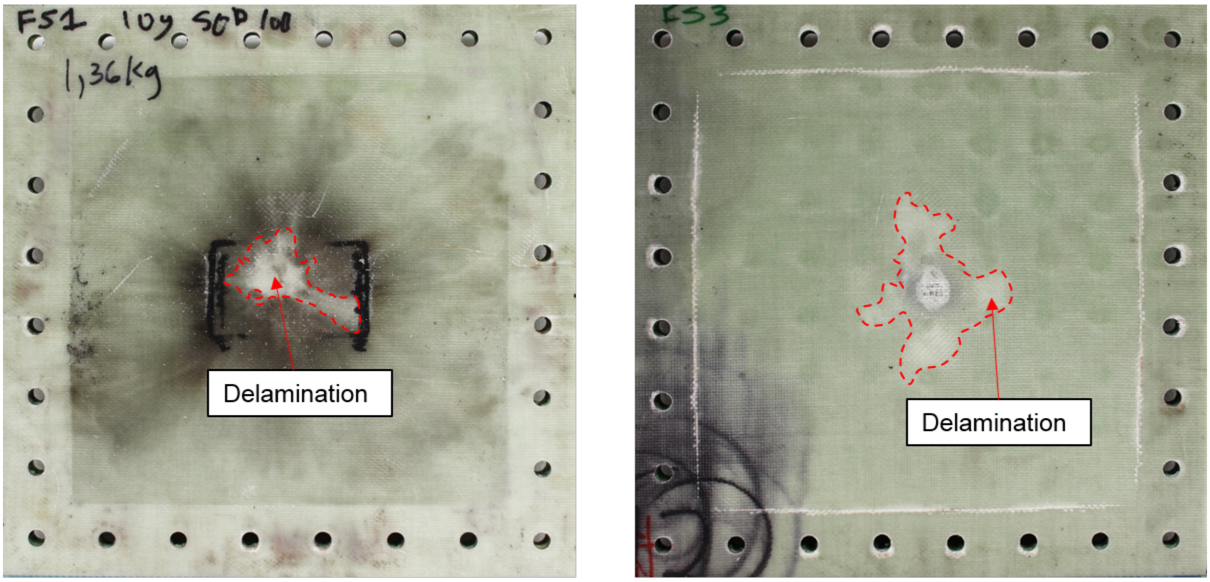

a) b)

Figure 6.1: Delamination (white area) of flat sandwich panels subjected to various charge mass detonation
a) Front face of a panel subjected to a 10 g charge b) Back face of a panel subjected to a 20 g charge mass

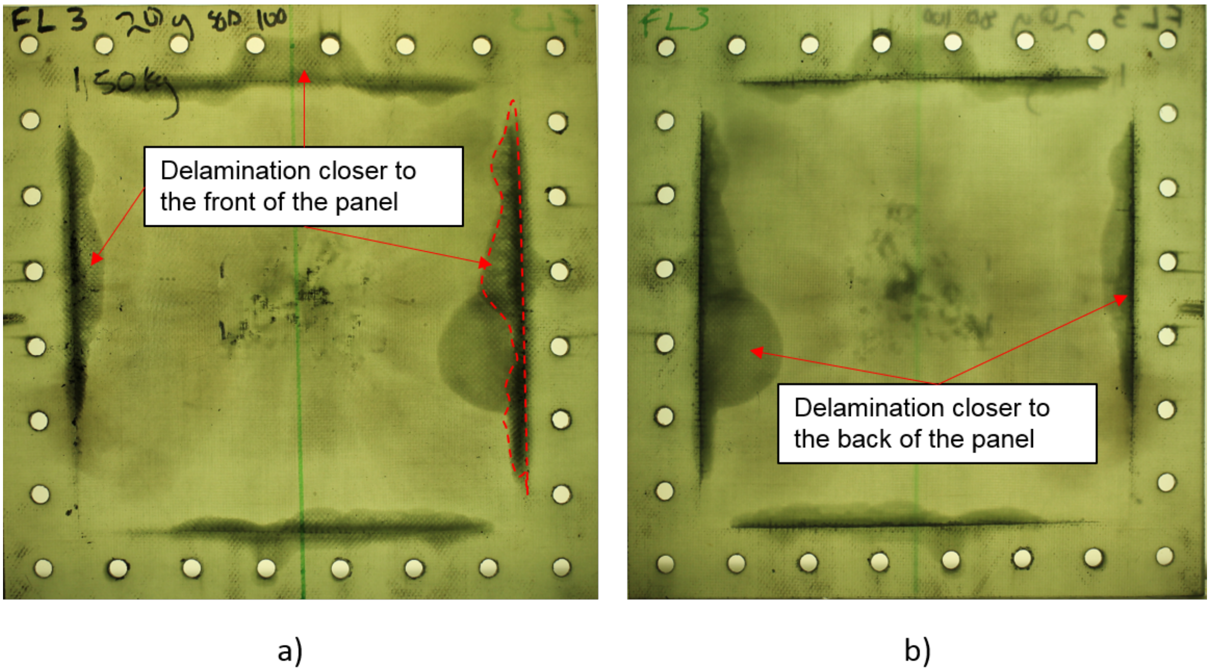

Figure 6.2: Delamination of a flat laminate subjected to a 20 g charge mass denotation a) Front face b) Back face

The next failure mode observed was matrix failure. This is a region found on the front face sheet or laminate characterised by fibres which are intact but are missing resin. An example can be seen in Figure 6.3 b) for the laminate and in Figure 6.4 for the sandwich panel. Figure 6.4 b) shows how the fibres are still intact and the matrix is missing. If the exposed fibres are broken, the failure is termed as fibre fracture. Figure 6.3 shows fibre fracture with only the surfaces fibres torn. In Figure 6.4 a) fibre fracture is manifested in a more intense form as large tears through the back face sheet.

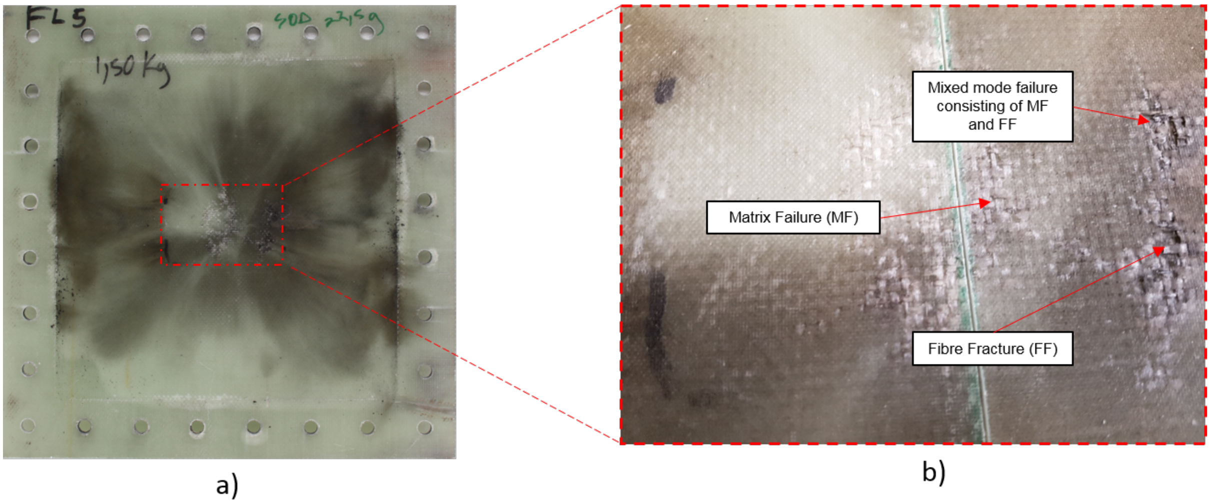

Figure 6.3: Flat laminate tested with 22.5 g charge at 100 mm SOD
a) Full panel view of the front face b) Close up of localised region

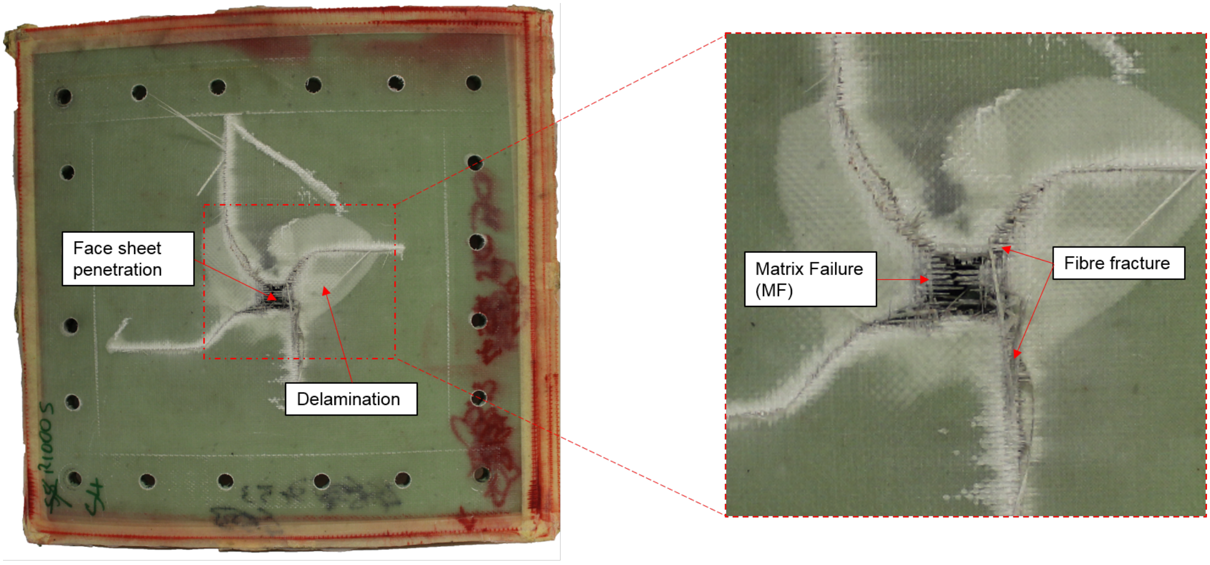

a)

b)

Figure 6.4: R1000 curved sandwich panel tested with a 20 g charge at 100 mm SOD a) Back face sheet on sandwich panel b) Close up of localised region

6.1.1.2 Core Failures

The foam core failed in three ways: core compression/crushing, core shear and core fragmentation. Core compression occurs when the core is permanently crushed and there is evidence of core densification as seen in Chapter 4 (see Figure 6.5). Core shear can be be identified by the fine shear cracks in the core material in Figure 6.5. Core fragmentation is exhibited by the complete destruction of some part of the core material which splits it up into many fragments. This occurred in Figure 6.5 at 17.5 g charge mass. Large scale core fragmentation usually leads to full core penetration as is exhibited at a charge mass of 20 g in Figure 6.5. The progression exhibited is compressive failure, core shear with crack formation, fragmentation then full penetration of the core.

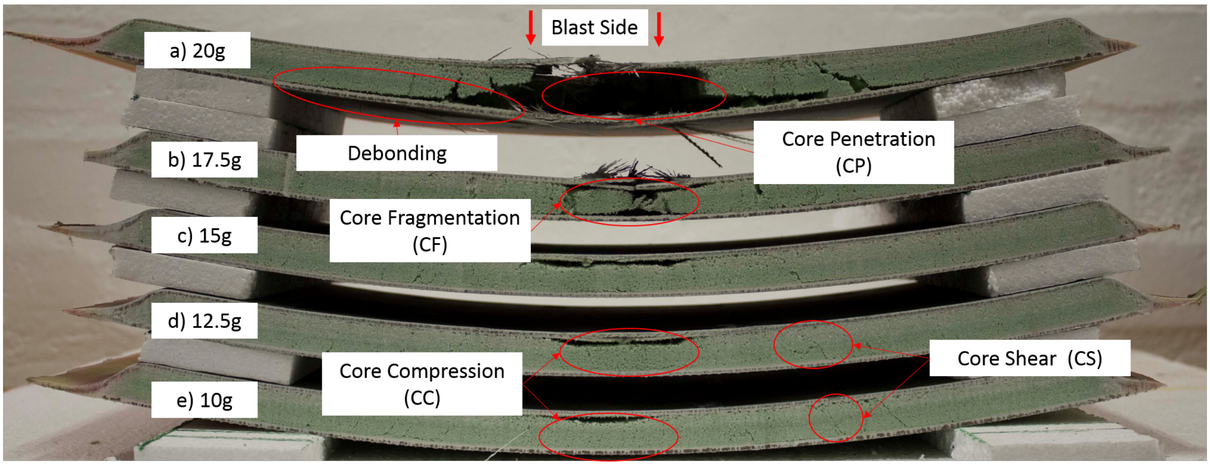

Figure 6.5: R1000 sandwich panel tested at various charge masses show multiple core failures and debonding

6.1.1.3 Interface Failure

Debonding occurs when the face sheets separate from the core material. When localised core compression occurs in the central region, debonding also occurs. In Figure 6.6 a) and b) the core has been crushed and the front face sheet springs back. It was observed that debonding occurred outside the central region of the panel (between the core and the back face sheet) in Figure 6.5 a) to c). Central region debonding was observed in Figure 6.6 c) when subjected to a charge of 10 g. As charge mass was increased, the separation between the back face sheet and the core became more pronounced. This is displayed in Figure 6.6 a) to c) where the charge mass was increased from 10 g to 17.5 g.

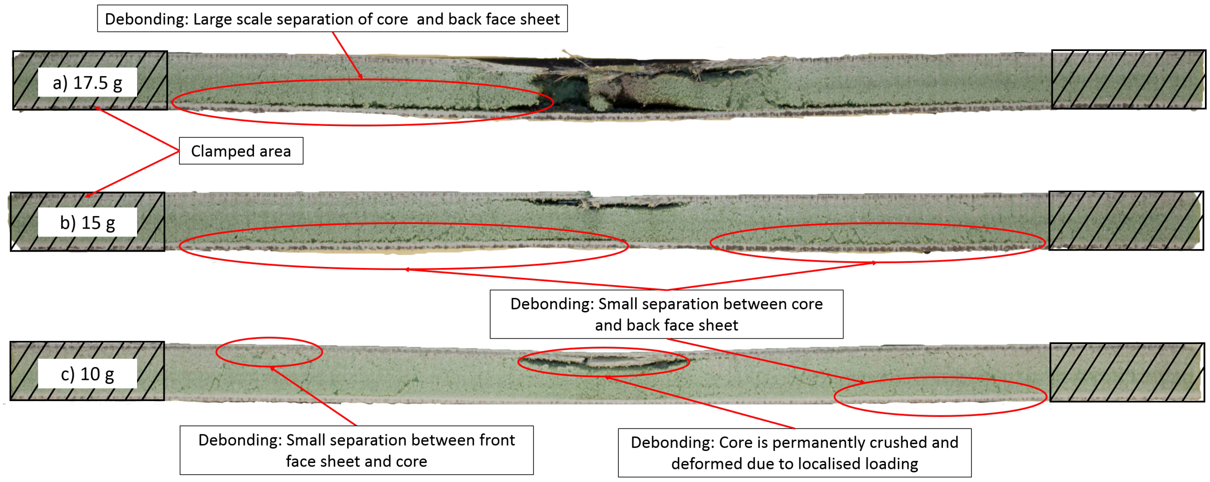

Figure 6.6: Flat sandwich panel tested at various charge masses showing multiple instances of debonding

6.1.1.4 Failure Modes Observed

All panels had some level of delamination at the lowest charge mass of 10 g, with the flat panels exhibiting generally less delamination per charge mass than the curved panels. As the charge mass increased, more failure modes were identified in accordance with Langdon et al [22]. In the laminates as the charge mass increased, delamination would first appear, followed by matrix failure and eventually fibre fracture. In Figure 6.7 the failure progression of the back face of the flat laminates series is shown. When the flat laminate was subjected to a 10 g charge (see Figure 6.7 a)) delamination first appeared in the centre of the panel. As the charge mass was increased, delamination started to appear at the boundary edges also (Figure 6.7 b) and c)). When the charge mass was further increased, the laminate exhibited matrix failure and fibre fracture as shown in Figure 6.7 d) and e). None of the laminates exhibited fibre rupture through the thickness. A summary of the observed failure modes can be seen in Table 6.2.

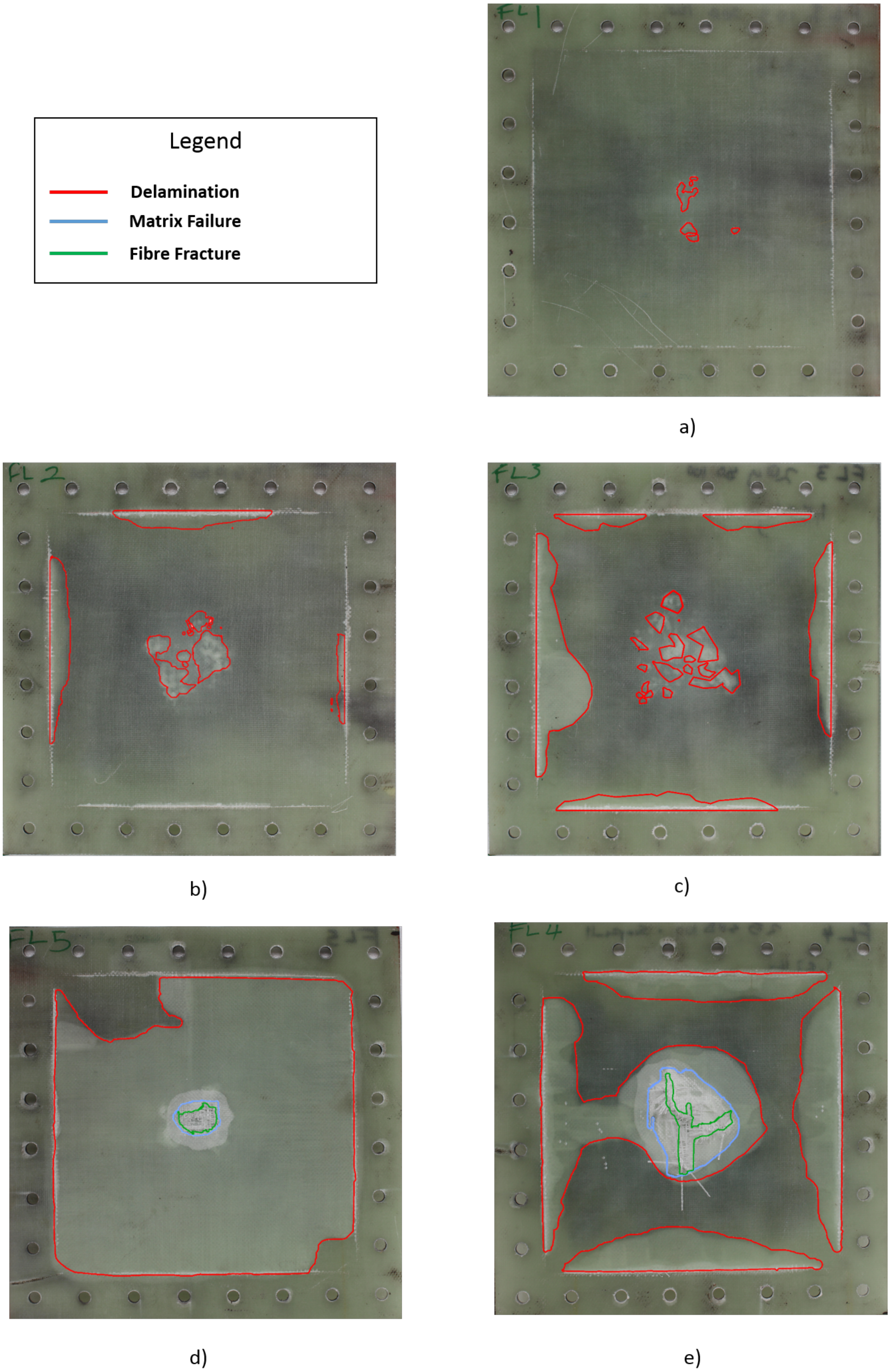

Figure 6.7: The back face of flat laminates subjected to various charge masses a) 10 g charge b) 15 g charge c) 20 g charge d) 22.5 g charge e) 25 g charge

Table 6.2: Laminate failure modes observed after post-test inspection

Panel Designation	Flat Laminates	Failure Designation
FL1	10g	DL
FL2	15g	DL,MF
FL3	20g	DL,MF,FF
FL5	22.5g	DL,MF,FF
FL4	25g	DL,MF,FF
Panel Designation	R1000 Laminates	Failure Designation
R1000L1	10g	DL
R1000L2	15g	DL,MF
R1000L3	20g	DL,MF
R1000L6	22.5g	DL,MF,FF
R1000L5	22.5g	DL,MF,FF
R1000L4	25g	DL,MF,FF
Panel Designation	R500 Laminates	Failure Designation
R500L1	10g	DL
R500L3	15g	DL,MF,FF
R500L2	20g	DL,MF,FF
R500L5	22.5g	DL,MF,FF
R500L6	25g	DL,MF,FF
R500L4	25g	DL,MF,FF (Failure along bolt holes also)

In the case of the sandwich panels, the front and back face sheets exhibited failure progression that was similar to the laminates. First delamination occurred, followed by matrix failure and eventually fibre fracture. In Figure 6.8 the progression of failure is shown of the front face for selected flat sandwich panels. When the flat sandwich panel was subjected to a 10 g charge (see Figure 6.8 a)), it exhibited delamination and matrix failure. As the charge mass was increased matrix failure seemed to spread and fibre fracture initiation also occurred (see Figure 6.8 b) and c)). At higher charge masses the face sheets would experience rupture through the thickness as in Figure 6.5 a) and b). The core sustained core compression and core shear failure even at the lowest charge mass tested which was 10 g. As the charge mass was increased, the cores exhibited fragmentation and eventually core penetration through the thickness as shown in Figure 6.5 a). The interfaces between the core and the face sheets showed debonding from the smallest charge mass tested (10 g). The full testing matrix can be seen in Table 6.3.

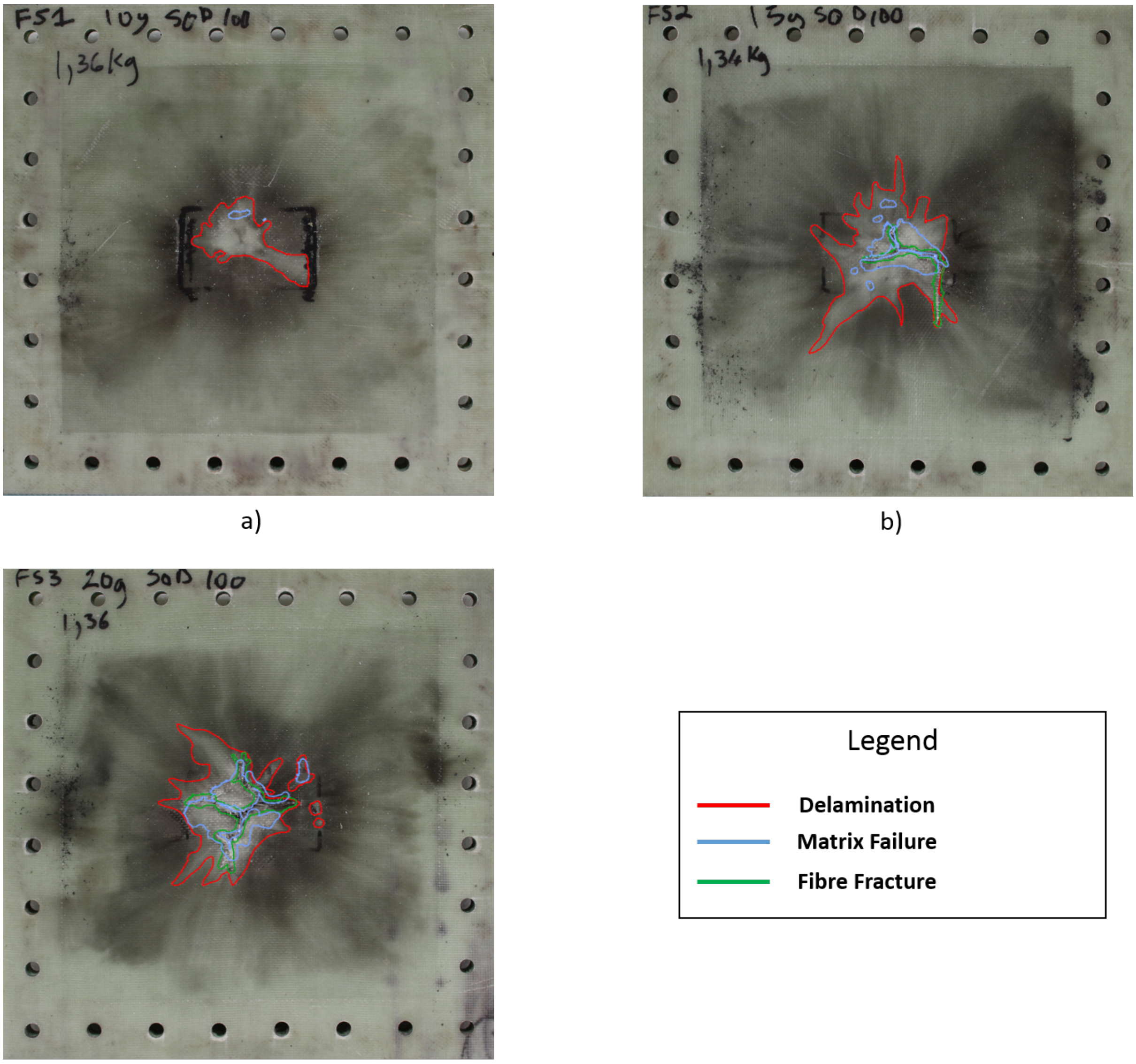

a)

b)

c)

Figure 6.8: The front face of flat sandwich panels subjected to various charge masses a)10 g charge b) 15 g charge c) 20 g charge

Table 6.3: Sandwich failure modes observed after post-test inspection

Panel Designation	Flat Sandwiches	Front Face Sheet Failure Designation	Back Face Sheet Failure Designation	Core	Front Interface	Back Interface
FS1	10g	DL,MF	DL	CC,CS	Deb	Deb
FS5	12.5g	DL,MF,FF	DL	CC,CS	Deb	Deb
FS2	15g	DL,MF,FFp	DL	CC,CS	Deb,FFp	Deb
FS4	17.5g	DL,MF,FFp	DL	CC,CS,CF	Deb,FFp	Deb
FS3	20g	DL,MF,FFp	DL,MF,FF	CC,CS,CF	Deb,FFp	Deb

Panel Designation	R1000 Sandwiches	Front Face Sheet Failure Designation	Back Face Sheet Failure Designation	Core	Front Interface	Back Interface
S1	10g	DL,MF(Very little),FFp (Dry spots)	DL	CC,CS,CF	Deb,FFp	Deb
S3	10g	DL,MF	No Damage	CC,CS	Deb	Deb
S7	10g	DL,MF,FF	No Damage	CC,CS	Deb,FFp	Deb
S6	12.5g	DL,MF,FFp	DL	CC,CS,CF	Deb,FFp	Deb
S9	12.5g	DL,MF,FF	DL	CC,CS	Deb,FFp	Deb
S8	15g	DL,MF,FFp	DL	CC,CS	Deb,FFp	Deb
S2	15g	DL,MF,FF	DL	CC,CS	Deb	Deb
S5	17.5g	DL,MF,FFp	DL	CC,CS,CF	Deb,FFp	Deb
S4	20g	DL,MF,FFp	DL,MF,FFp	CC,CS,CF,CP	Deb,FFp	Deb,FFp

Panel Designation	R500 Sandwiches	Front Face Sheet Failure Designation	Back Face Sheet Failure Designation	Core	Front Interface	Back Interface
S1	10g	DL,MF	No Damage	CC,CS	Deb	Deb
S6	10g	DL,MF,FFp	DL	CC,CS	Deb,FF	Deb
S9	10g	DL,MF,FFp	DL	CC,CS	Deb,FF	Deb
S5	12.5g	DL,MF,FFp	DL	CC,CS,CF	Deb,FFp	Deb
S2	15g	DL,MF,FFp	DL	CC,CS,CF	Deb,FFp	Deb
S4	17.5g	DL,MF,FFp	DL	CC,CS,CF	Deb,FFp	Deb
S3	20g	DL,MF,FFp	DL,MF,FFp	CC,CS,CF,CP	Deb,FFp	Deb,FFp

6.1.2 Impulse Results

In Figure 6.9 impulse values were plotted against charge mass for all the panels tested. The impulse increased linearly as the charge mass was increased. The difference in impulse is negligible between the sandwich panels and laminates. In addition, the impulse differences between the flat and curved geometries were also negligible.

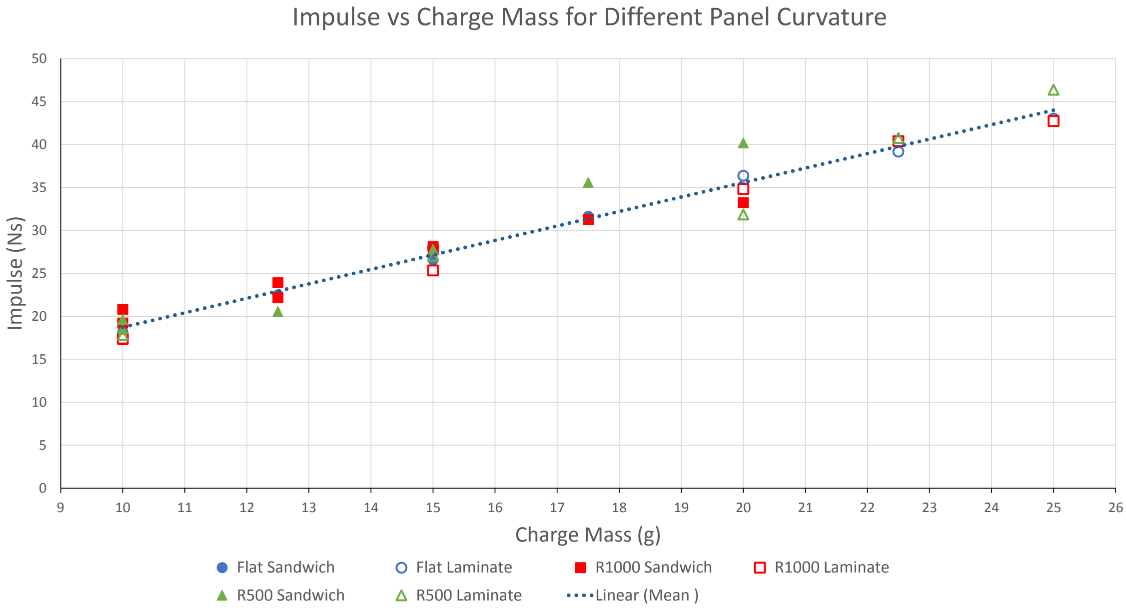

Figure 6.9: Graph of impulse vs charge mass for different panels curvatures

6.1.3 Delamination Areas

The area of delamination was calculated by using the masking method described by Sinclair [23]. A light source placed behind the laminates allowed the delaminated areas to be clearly visible. Figure 6.10 a) shows the back face of a flat laminate subjected to 22.5 g of explosive. The delaminated area was marked out and then masked. The masked version can be seen in Figure 6.10 b). The area of the masked region was calculated from image processing software and a detailed description of this method is presented in Appendix C.

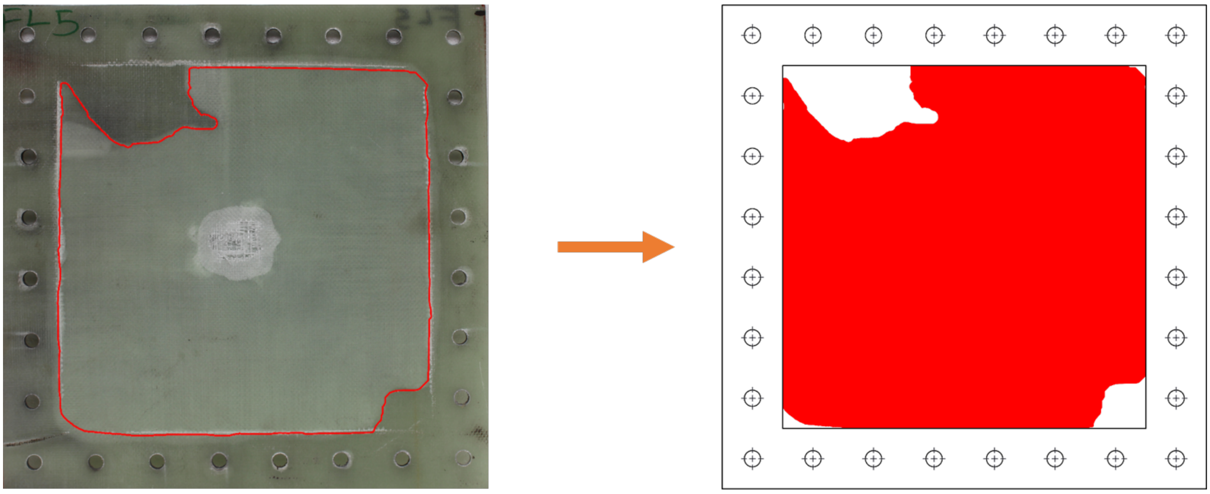

a)

b)

Figure 6.10: Back face of the flat laminate subjected to 22.5 g explosive charge mass: a) Photograph of flat laminated panel b) Masked version of flat laminated panel

The flat laminates showed increasing delamination area with respect to charge mass, up to the point of fibre fracture. The delaminated area decreased after fracture was initiated. This phenomenon was observable as the charge mass was increased from 22.5 g to 25 g while the delaminated area decreased from 92.2 % to 51 % of the exposed panel. Both the R1000 and R500 laminates followed a different trend; the area of delamination kept on increasing, but were much lower than the flat laminates above 20 g. The R1000 laminates showed a steady increase in delamination and then started to plateau between the 22.5 g and the 25 g charge masses with the delaminated area only increasing from 24.6 % to 28.2 %. The R500 laminate showed a sudden increase in delaminated area (1 % to 17.9 %) and then plateaued. The percentage area of delamination of all the types of laminates tested can be seen in Figure 6.11.

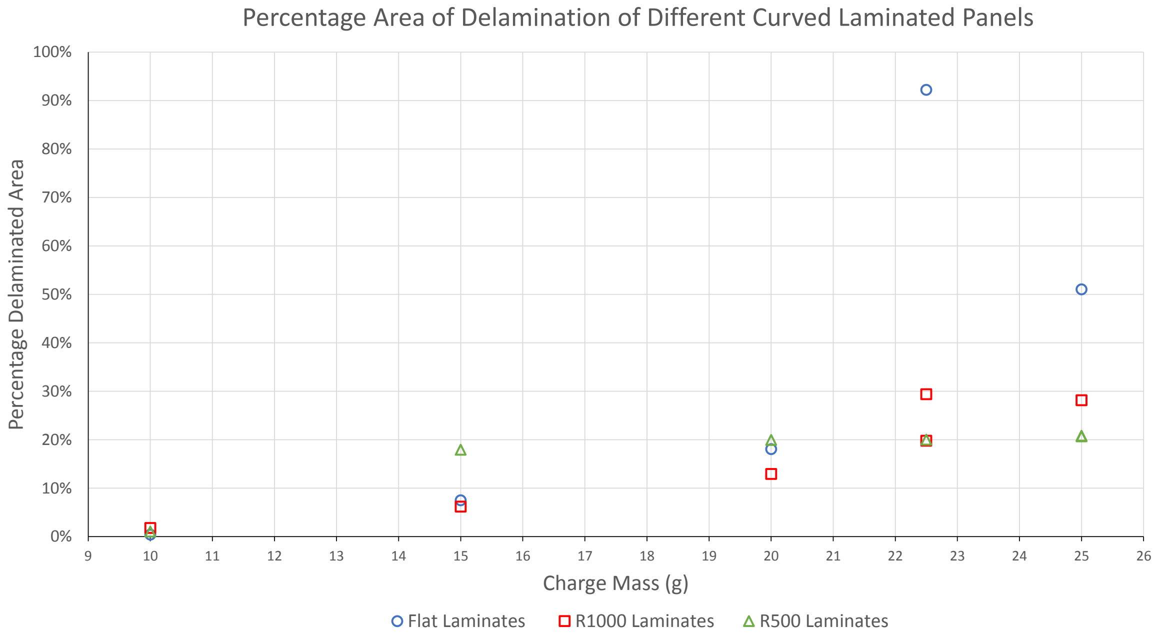

Figure 6.11: Graph of delaminated area as a percentage of the exposed area versus charge mass for different laminate curvatures

For the sandwich panels, the same method used by Sinclair [23] was used, but without back lighting (as the light could not penetrate the core). Although the resulting delamination was measured differently for the sandwich panels(i.e. the front and back face sheets were measured separately), the flat sandwich panels followed the same trend as the flat laminates, while the curved sandwich panels followed a different trend. The delamination increased to a point then would decrease and then increase again. The inflection point charge mass differed for each curvature. The R1000 inflection point charge mass was 12.5 g whereas the R500 was 15 g. In Figure 6.12 the front face sheet percentage area delamination for different sandwich panel curvatures is shown.

The flat panel back face delamination area increased similarly to the front face for each type of curvature. The curved sandwich panels displayed the same charge mass inflection points. An important observation was that at the highest charge mass tested, the curved panels exhibited very large delamination on the back face sheets as compared to the front face sheets. The flat back face sheet had less delamination than the front face sheet. This can be observed in Figure 6.13.

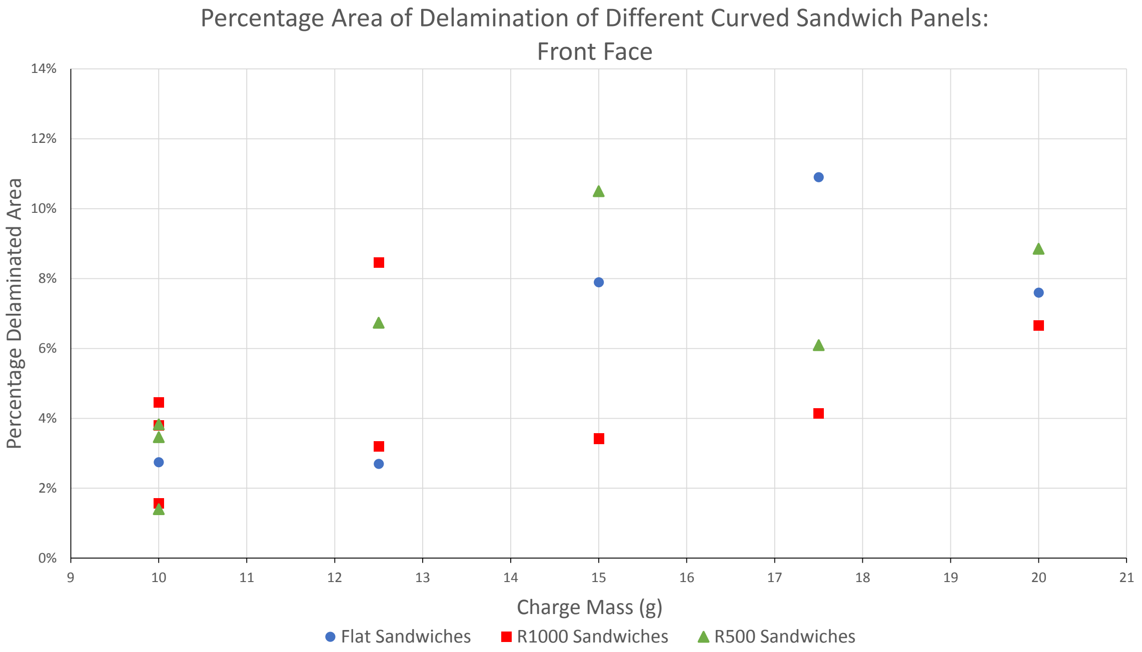

Figure 6.12: Graph of delaminated area of the front face as a percentage of the exposed area versus charge mass for different sandwich panel curvatures

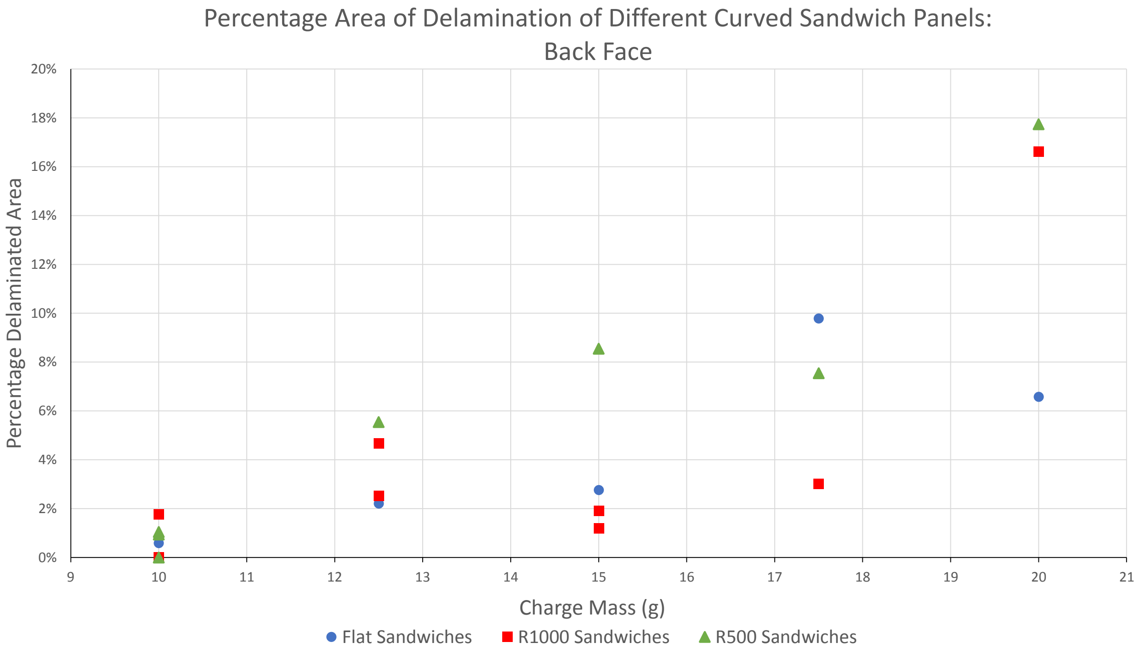

Figure 6.13: Graph of delaminated area of the back face as a percentage of the exposed area versus charge mass for different sandwich panel curvatures

6.1.4 Debonded Lengths

Debonded lengths were measured with a steel rule from the sectioned panels and were calculated as a percentage of the side length of the exposed area (in the case of the flat panels) and arc length (in the case of the curved panels). The flat front debonded length percentages showed a steady decline from 10 g to 15 g then stayed approximately constant between 25% - 28% as shown in Figure 6.14. The curved panels showed fluctuations in percentage debonded length. The R500 sandwich panels showed more fluctuation than the R1000 sandwich panel.

In Figure 6.15 the back interface percentage debonded lengths are shown. The back face debonded lengths increased steadily until 100% for all panel curvatures. At 10 g the percentage debonding of the back interface of the flat sandwich was 42%; it then dropped to 22% after which it kept on increasing until 100%. The curved panels displayed no clear trend. The R1000 sandwiches percentage debonded lengths for the 12.5 g and 15 g charges showed considerable difference after repeat tests were conducted. The 12.5 g differed by 43% and the 15 g differed by 18%. The R500 debonded length percentage also showed considerable scatter.

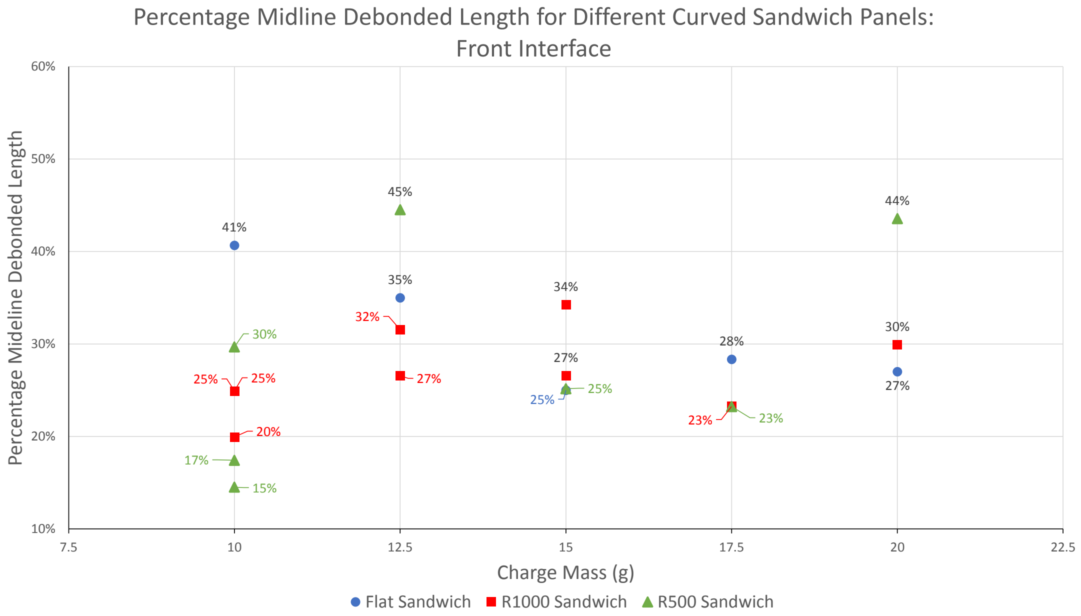

Figure 6.14: Graph of front face sheet-core interface debonded lengths for different sandwich panel curvatures

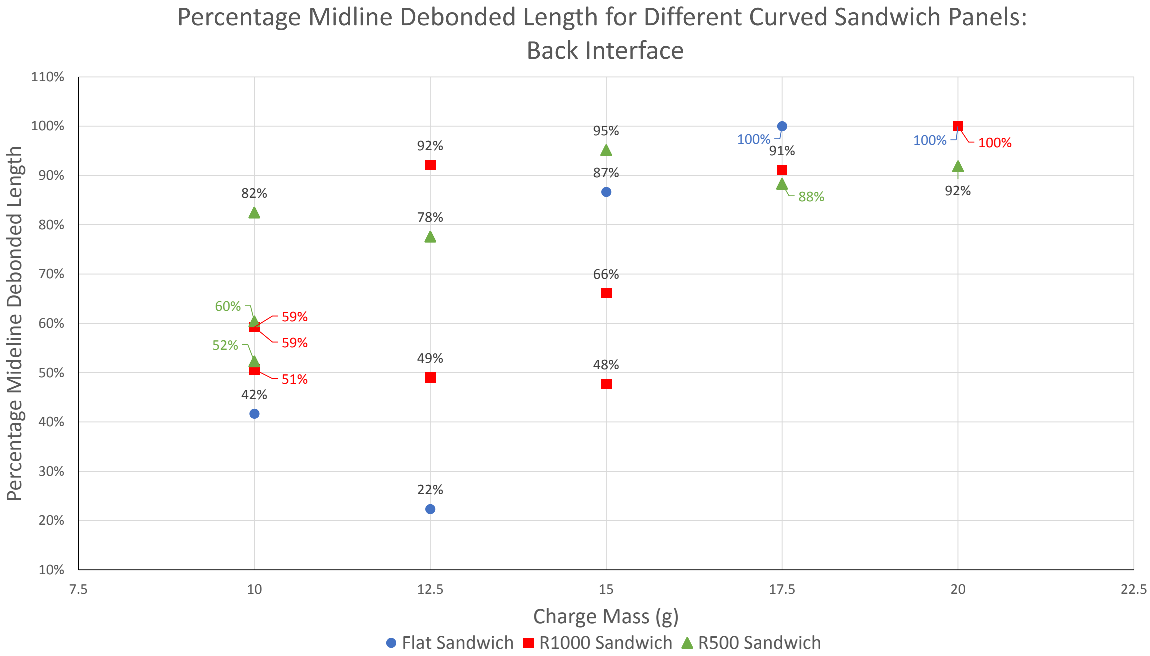

Figure 6.15: Graph of back face sheet-core interface debonded lengths for different sandwich panel curvatures

Chapter 7

Analysis and Discussion

This study set out to assess the impact of concave curvature on composite panels subjected to blast loading. In this chapter the effect on impulse, failure progression, delamination and debonding are discussed.

7.1 Effects of Curvature on Impulse Transfer

A graph of impulse versus charge mass is shown in Figure 7.1 for the different panel types tested. Impulse increases linearly with increasing charge mass, as shown in Figure 7.1, for a given panel type. This trend is consistent with observations made by Langdon et al [22, 37]. There is very little variation in impulse transfer between the flat and concave curved panels for a given charge mass. Hence, the concave curvature does not influence impulse transfer at the SOD tested herein.

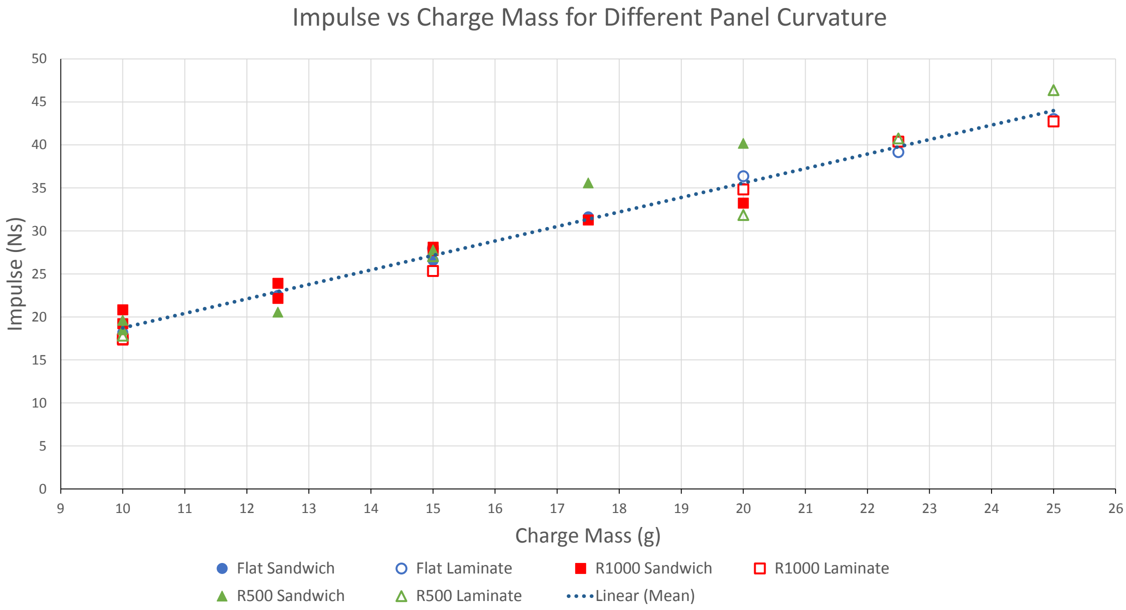

Figure 7.1: Graph of impulse vs charge mass for different panel types

The concave panel results differ from the convex panel results reported by Sinclair [23] and Shen [9]. Sinclair [23] and Shen et al [9] note that at a localised level, the blast wave is dissipated due to the convex curvature, attributed to the convex curvature changing the reflective angle of the blast wave. This would result in a reduction in the impulse acting on the front face of the panel [9]. While one could assume that the concave geometry would increase the impulse at the current SOD of 100 mm, the geometry is unable to change the reflective angle of the blast wave to increase the impulse. Hence at a localised level the curvature has no effect over flat panels on the impulse transfer.

7.2 Failure Mode Initiation

Using the definitions in Section 6.1, failure mode initiation charts for the laminates and sandwich panels were created. The failure modes are charted against the charge mass to determine the onset of a particular failure mode. These are displayed in Figures 7.2 to 7.5.

Coloured markers are used to indicate failure modes in accordance with Table 6.1. The nomenclature is repeated here: DL, delamination; MF, matrix failure; FF, fibre fracture; FFp, fibre fracture through the thickness of laminate or skin of sandwich; CC, core crushing; CS, core shear; CF, core fragmentation; CP, core penetration; and Deb, debonding.

It is important to note that the markers are placed adjacent to each other when multiple failure modes are initiated at a given charge mass. Since the lowest charge mass that was tested was 10 g, the failure modes displayed at 10 g may have initiated at a lower charge mass.

7.2.1 Sandwich Panel Failure Mode Initiation Charts

The failure mode initiation charts for the sandwich panels are displayed in Figures 7.2, 7.3 and 7.4. The sandwich panels exhibited the same failure mode initiation sequence observed by Langdon et al [22] and Shukla et al [4]. At a charge mass of 10 g all front face sheets displayed delamination and matrix failure, while the back face sheets displayed delamination only (see Figures 7.2, 7.3, 7.4).

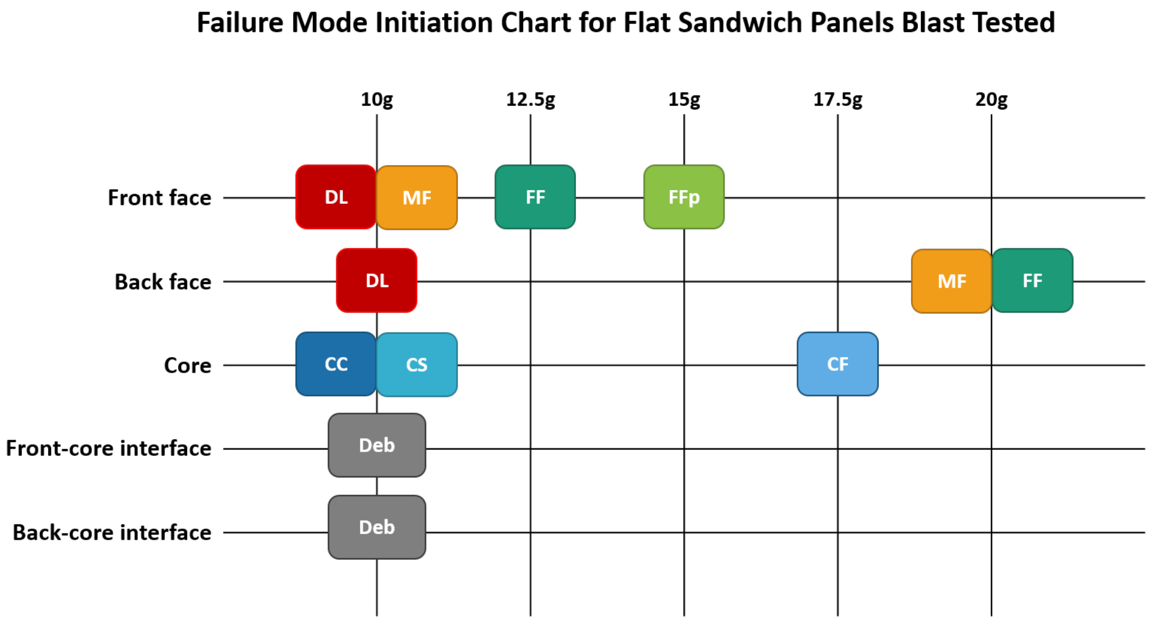

Figure 7.2: Failure mode initiation chart for blast-tested flat sandwich panels

All sandwich cores displayed both core crushing (occurring mostly in the localised blast region) and core shear cracking. Both front and back interfaces displayed debonding. As the charge mass was increased to 12.5 g, the front face sheets for the flat and the R1000 sandwich panels exhibited fibre fracture; but the R500 exhibited fibre fracture and rupture through the thickness of the front face sheet. The flat panels and R1000 sandwich panels exhibited the same failure mode initiation until 17.5 g. At 20 g the flat panel displayed matrix failure and fibre fracture on the back face sheet, with no through thickness penetration. The R1000 and R500 displayed full core penetration, back face matrix failure and face sheet rupture at 20 g as seen in Figures 7.3 and 7.4.

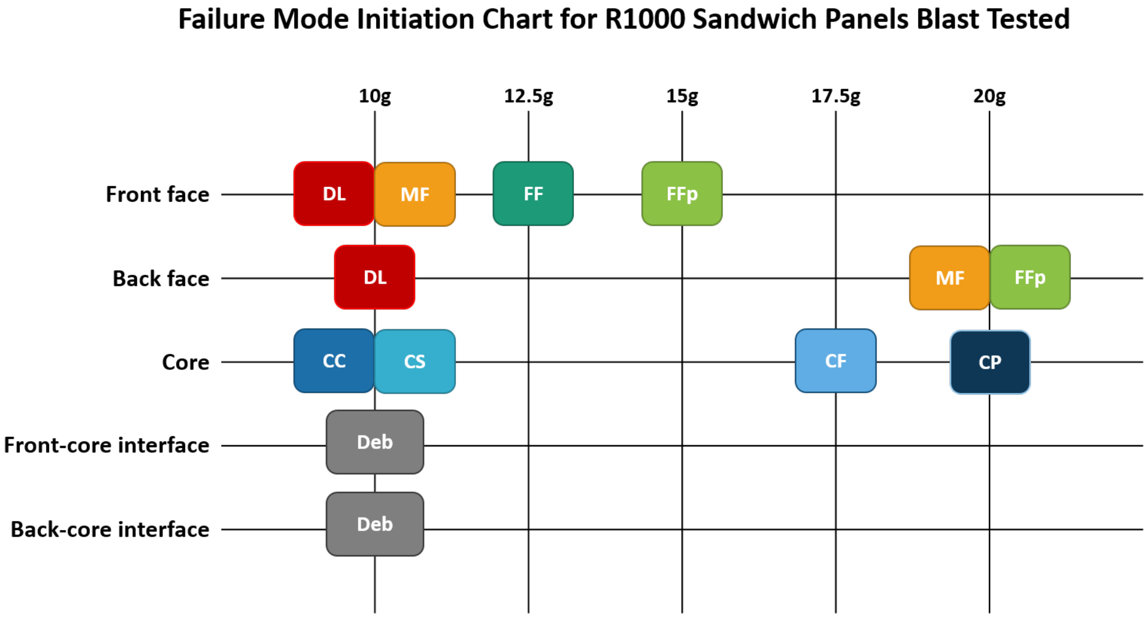

Figure 7.3: Failure mode initiation chart for blast-tested R1000 sandwich panels

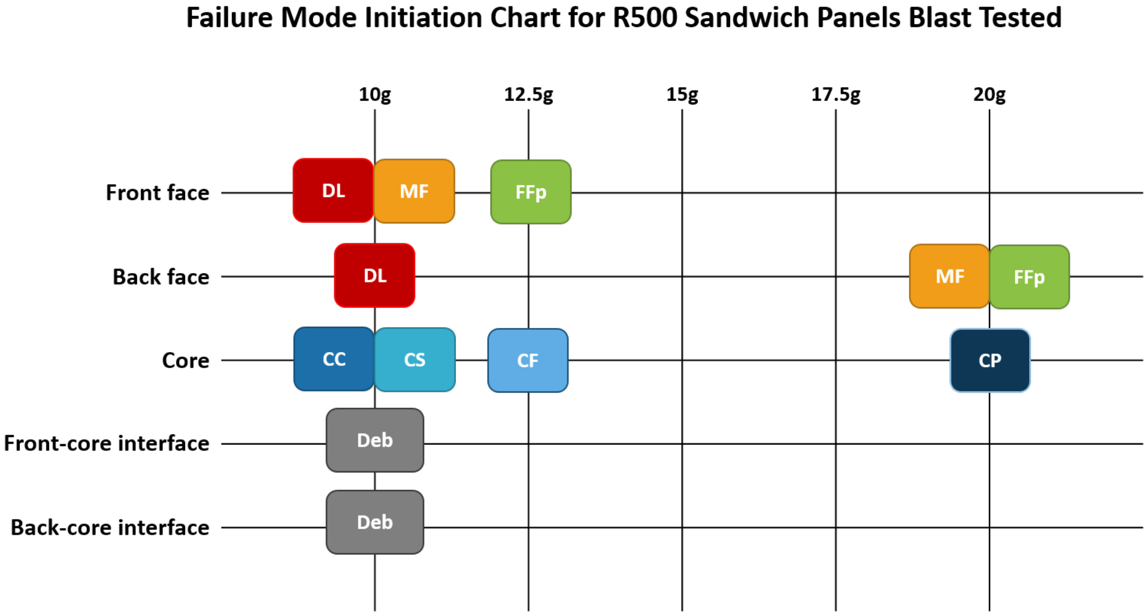

Figure 7.4: Failure mode initiation chart for blast-tested R500 sandwich panels

There are a few points of interest when the failure mode initiation charts of the three curvatures tested are compared. Curvature does not appear to affect the path of failure initiation. All panels, irrespective of curvature, followed the same failure progression sequence observed by Langdon et al [22].

At 10 g most of the failure modes were already initiated in all panel types. The R1000 and flat panels behaved similarly below 20 g, having the same failure mode initiation. At 20 g the R1000 panel experienced core penetration and back face sheet rupture. The R500 panel exhibited front face sheet rupture at a lower charge mass of 12.5 g, shown in Figure 7.4. Despite through-thickness front sheet penetration at 12.5 g, the R500 core was able to resist the blast up to a charge mass of 20 g, when complete through-thickness penetration occurred. At this point it was observed that the R1000 had the same failure. This suggests that curvature affected the initiation point of a particular failure mode, rather than the sequence of failure mode initiation. For example, matrix failure will always occur prior to fibre fracture, but matrix failure can also occur at different charge masses on different radii.

7.2.2 Laminate Failure Mode Initiation Chart

The same method that was used to construct the failure mode initiation charts for sandwich panels was also used for the laminates. As the charge mass was increased, failure mode initiations were observed and noted. The same markers and failure mode nomenclature is used for the laminates. Since the laminate contained no core, there were no core associated failures (i.e. no core crushing, core shear, core fragmentation, core penetration and core face sheet debonding).

All laminates exhibited visible delamination at the lowest charge mass of 10 g. As the charge mass was increased to 15 g, matrix failure was observed on the front (blast side) of all the laminates tested. In addition, it was observed that the R500 laminate experienced fibre fracture on the front side at 15g charge mass. Front face fibre fracture occurred at 20 g for the flat laminate and at 22.5 g for the R1000 laminate, as seen in Figure 7.5. All the back faces exhibited matrix failure and fibre fracture at a charge mass of 22.5 g. None of the panels exhibited through thickness penetration. The R500 curvature exhibited front face failure earlier (15 g) than the R1000 (22.5 g) or flat panel (20 g).

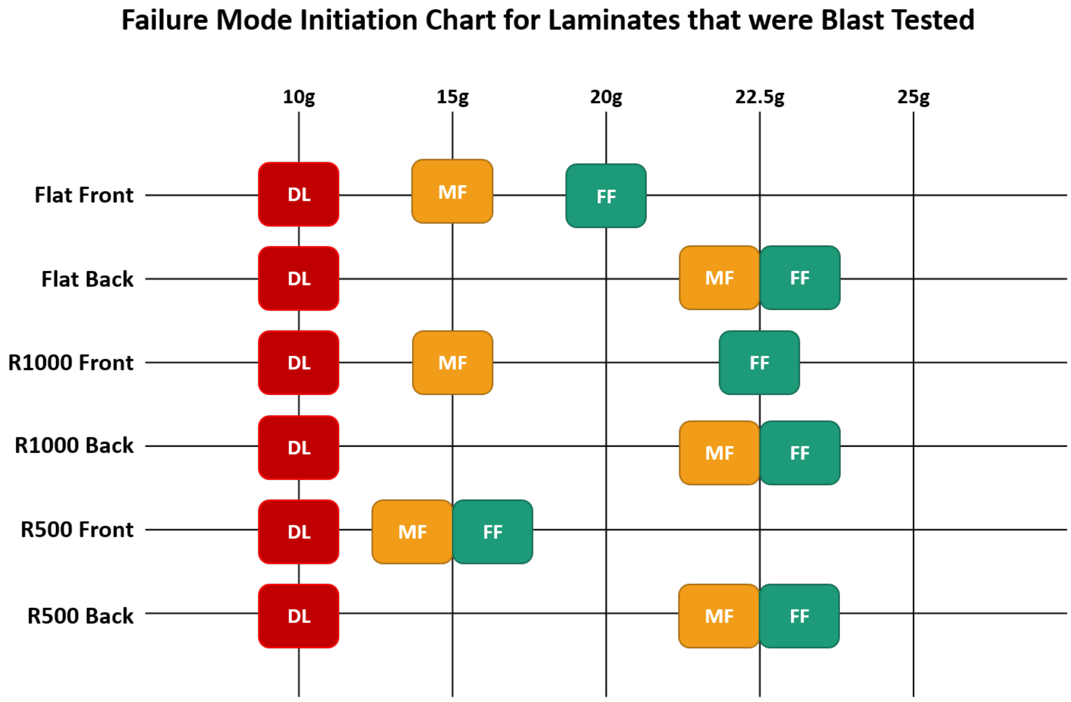

Figure 7.5: Failure mode initiation chart for blast-tested different curvature laminate panels

7.2.3 Laminate and Sandwich Panel Comparison

The curvature mainly influenced failure initiation on the blasted side of the test panels. Laminates exhibited no through thickness penetration up to 25 g, whereas all curved sandwich panel experienced through thickness penetration. This would indicate that laminates offer better localised blast resistance than sandwich panels, when charge mass required to initiate panel rupture is used as a performance measurement. This is in agreement with previous work [23,35].

7.3 Spatial Distribution of Failure

While it is important to understand the initiation of different failure modes, this unfortunately does not give one an indication of the extent or distribution of failure. To quantify the extent and distribution of failure would be highly valuable as delamination can differ from panel to panel.

7.3.1 Laminates

The results of the tests on flat laminates agreed with the trends identified by Sinclair [23] and Langdon et al [35]. It was observed that delamination increased with increasing charge mass until the initiation of fibre fracture; after fracture initiation the delamination area decreased. This is due to the additional energy being used in the fibre fracture mechanism, leaving less energy available for delamination. After fibre fracture, the delamination percentage area decreased from 92.2% (22.5 g charge mass) to 51% (25 g charge mass). In Figure 7.6 delamination started in the centre and then extended inwards from the boundary towards the centre of the laminate. Sinclair [23] identified damage in two regions: a central region which was dominated by localised failure and an exterior region with failure associated with global panel response. Kumar et al [8] also observed the total deflection of their panel comprised of two distinct phases, referred to as the indentation mode and the flexural mode. During indentation localised deflection is superposed onto the overall deflection and during the flexural mode the overall deflection starts to surpass the localized deflection [8]. There is a possibility that the central region failure observed by Sinclair [23] and the indentation mode observed by Kumar et al [8] could be linked, but this cannot be confirmed due to the absence of transient response measurements for both Sinclair and the current work. The exterior region delamination pattern is probably caused by the global panel response and by the specific boundary clamping [34].

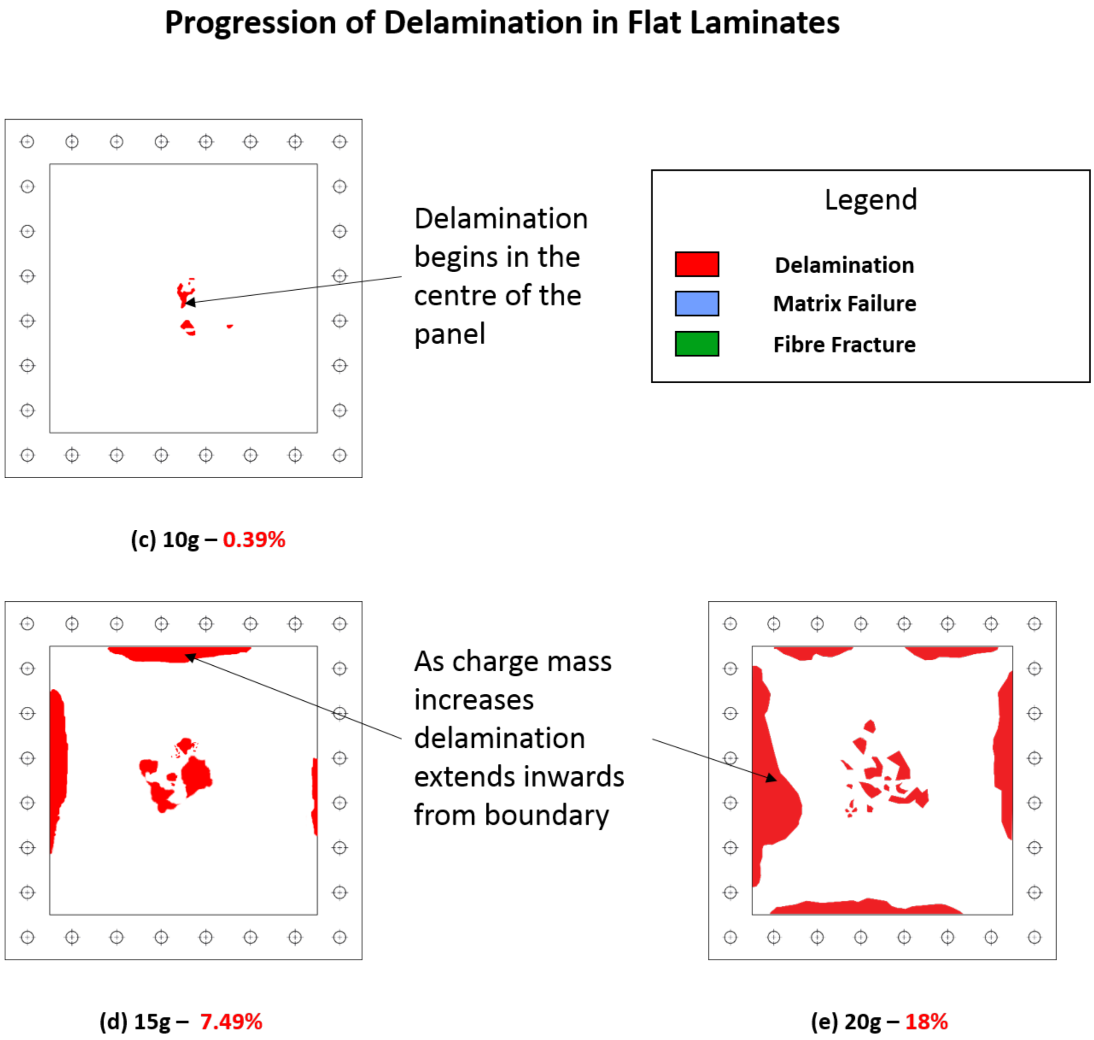

Progression of Delamination in Flat Laminates

Delamination begins in the centre of the panel

As charge mass increases delamination extends inwards from boundary

(c) 10g – 0.39%

(d) 15g – 7.49%

(e) 20g – 18%

Figure 7.6: Delamination progression of selected blast-tested flat laminates

The curved panels exhibited similar trends to the flat one regarding delamination and the interaction between fibre fracture initiation and the delaminated area. In addition, delamination subsequent to the initiation of fibre fracture(on the front face of the flat) was lower in the curved panels than in the flat panels. The broken red line in Figure 7.7 represents the initiation of fibre fracture on the front face of the flat laminate.This is observed at the 22.5 g and 25 g charge masses in Figure 7.7. The area of delamination at 22.5 g of the flat laminates was 92.2 % of exposed area as compared to the curved laminates that had an average of 23.1 % its exposed projected area. At 25 g the area of delamination was 51.0 % for the flat laminate and an average of 23.2 % for the curved laminates.

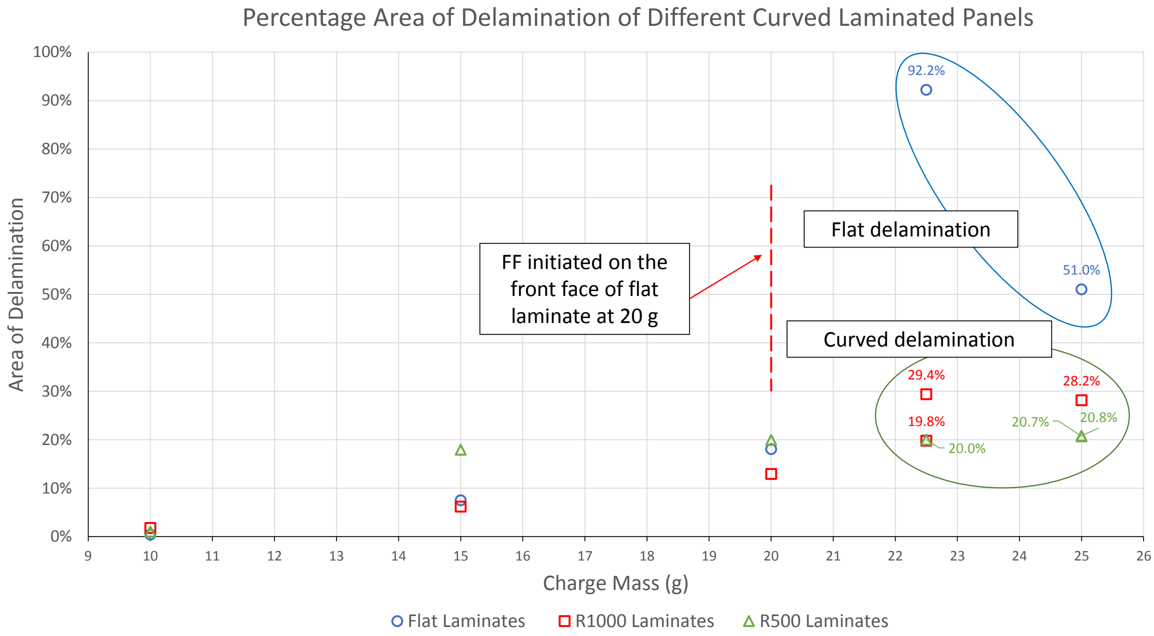

Figure 7.7: Percentage area delamination per charge mass for different laminate curvatures

Post-mortem analysis of the curved laminates revealed that delamination started in the central region of the panel similar to the flat panels, as shown in Figure 7.8 a) and d). As the charge mass was increased, delamination started to extend from the curved edge towards the centre of the panel. In Figure 7.8 the R500 and R1000 the curved edges seemed to delaminate more than the other sides. The pattern becomes more evident as the curvature increases. In the R1000 (Figure 7.8 b) and c)) panels, delamination occurs on both boundaries, but the curved boundary is favoured. In the R500 delamination occurs mainly on the curved boundaries (Figure 7.8 e) and f)) in all panels with the exception of the 22.5 g (with panel designation R500-L5) and 25 g (with panel designation R500-L4). The spatial maps may be found in Appendix F in Figure F.3) g) and i) respectively. Sinclair [23] observed a similar phenomenon with the convex curved laminates. In Figure 7.9 the delamination pattern that is observed at 30 g charge mass shows more delamination on the curved side as opposed to the straight edge.

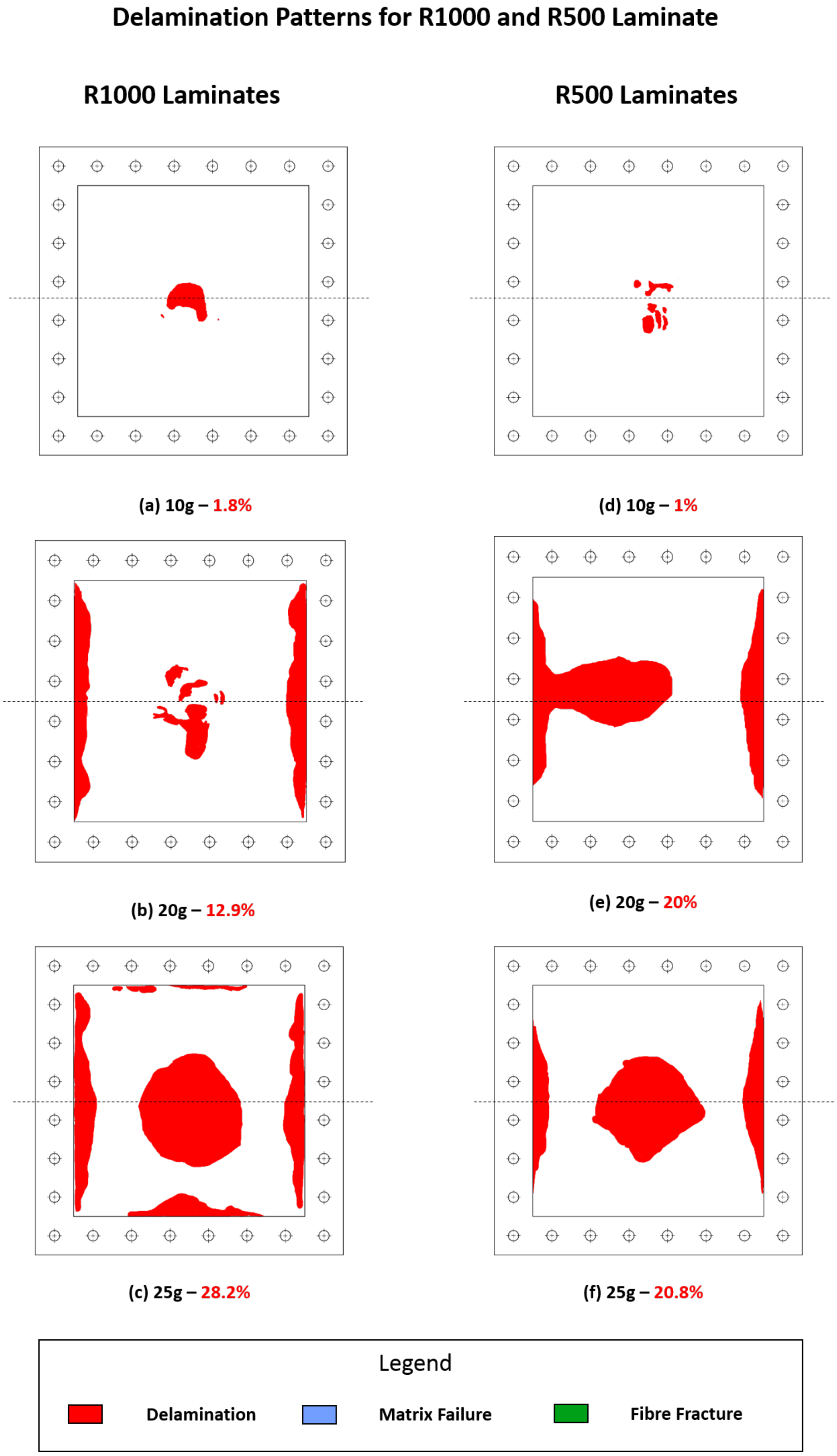

(a) 10g – 1.8%

(d) 10g – 1%

(b) 20g – 12.9%

(e) 20g – 20%

(c) 25g – 28.2%

(f) 25g – 20.8%

Figure 7.8: Delamination patterns of the R1000 and and R500 laminate panels at differing charge masses

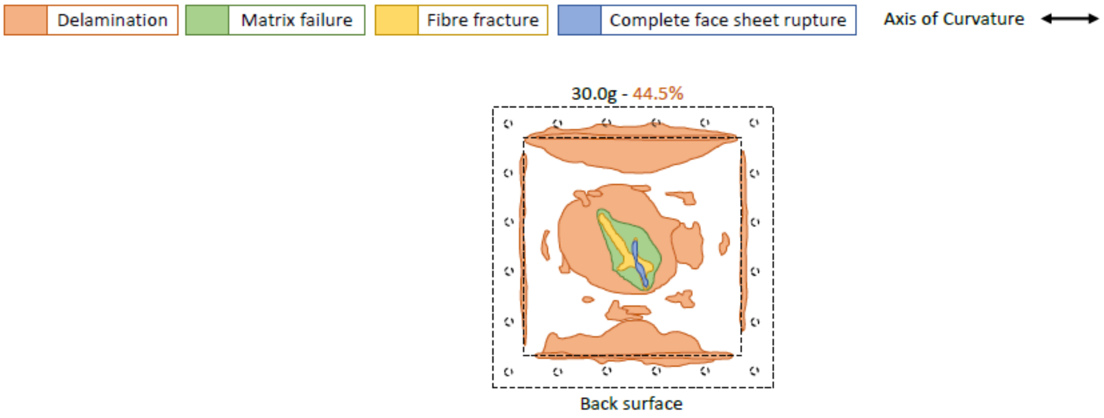

Figure 7.9: Rear view of a masked 1000 mm curved FRP laminate panel subjected to a charge mass of 30 g [23]

It was observed that matrix failure and fibre fracture increase with increasing charge mass for all panel curvatures. Sinclair [23] and Langdon [35] et al have observed the same phenomena for flat laminates. Matrix failure and fibre fracture were concentrated in the central region of the front face of the laminates, due to the localised nature of the loading. On the back face matrix failure occurred in conjunction with fibre fracture, whereas on the front face, matrix failure usually occurred on a lower charge mass than fibre fracture. Although all panels exhibited fibre fracture, none of the panels had through thickness penetration.

The progressive nature of the failure of flat glass fibre laminates observed by Tekalur et al [48] has also been observed in the current study. As charge mass increases the prevalence of different failure modes increased. This increase is not sudden (as in the case of carbon fibre laminates as observed in reference [48]), but rather different failure modes initiate as the charge mass increased.

The numerical simulation described in Section 5.1 revealed high bending stress on the curved edge of the composite laminate. This could be the reason why the R500 and R1000 laminates showed more delamination on the curved edges. In addition, the indentation mode observed by Kumar et al [8] is also seen in the simulation. In Figure 7.10 the numerical displacement contour of the R500 panel is displayed. In Figure 7.11 the displacement contours of Kumar et al [8] are displayed. The indentation region in Figure 7.11 observed by Kumar et al [8] has a more pronounced elliptical shape than the panel in 7.10, which could be due to the tighter radius of curvature. The panel in Figure 7.11 b) has a radius of curvature of 304.8 mm whereas the panel in Figure 7.10 has a radius of curvature of 500 mm. The elliptical shape in Figure 7.11 a) is still evident, although not as pronounced. It is also important to note that the boundary conditions between the two models were different. In the current work the boundary conditions were fully constrained on all sides whereas in Kumar et al [8] the top and bottom edges were fully constrained and the vertical sides were simply supported.

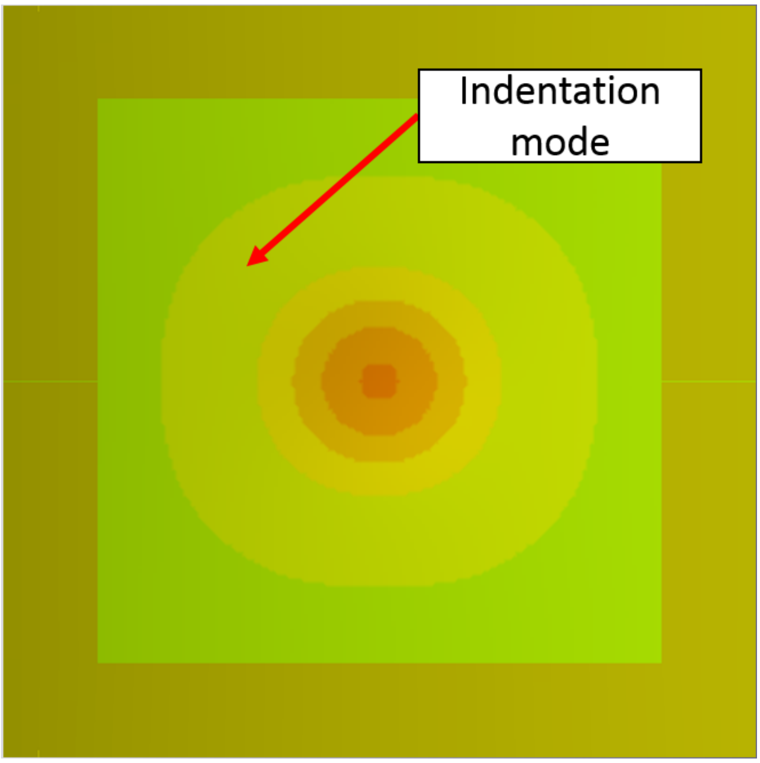

Figure 7.10: Displacement contour plots obtained from computational simulation observed in current work

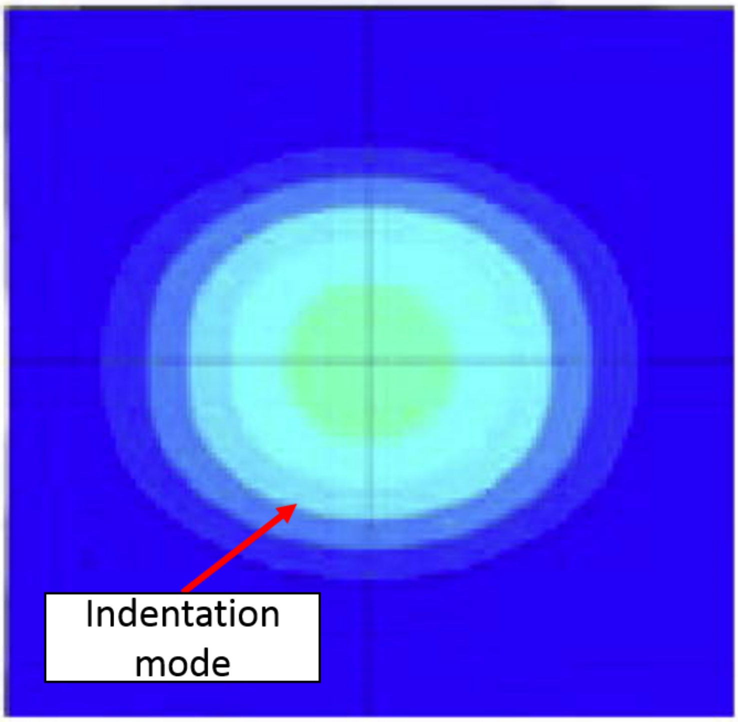

Figure 7.11: Indentation mode in a model by Kumar et al [8]

7.3.2 Sandwich Panels

The area of delamination was calculated by using the masking method described in Section 7.3.1. The overall delamination of the sandwich panels was less than the laminates. Even so, the flat sandwich panels followed a similar trend to the laminates. The front face sheet delamination increased with increasing charge mass up to a point, then decreased. The core failure influenced this; once core fragmentation occurred, delamination decreased. This could be due to less energy being available for delamination. This can be seen in Figure 7.12 when the charge mass was increased from 17.5 g to 20 g. Core fragmentation was initiated at a charge mass of 17.5 g.

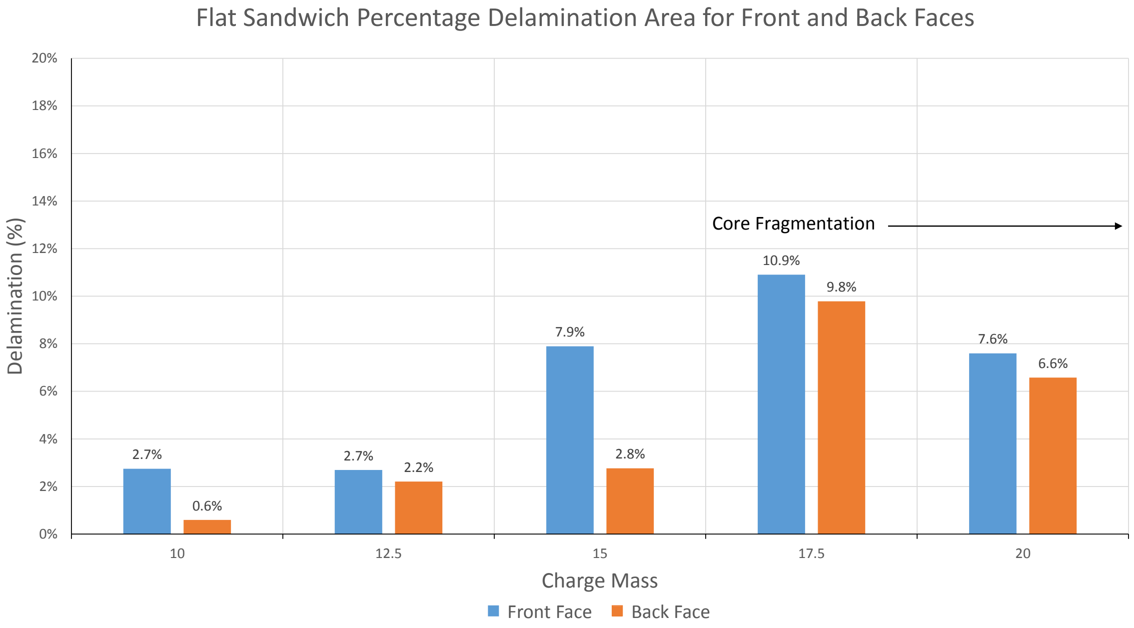

Figure 7.12: Graph of flat sandwich delamination of exposed area

Back face sheet delamination was similar to the front face sheet. The back face sheet delamination continued to increase until the initiation of core fragmentation which occurred at 17.5 g. Thereafter the delamination decreased when the charge mass was increased to 20 g. For the front face sheet similar results were observed by Sinclair [23], but delamination remained consistent on the back face sheet. Matrix failure and fibre fracture severity increased with increasing charge mass. This also evident in the flat sandwich panels tested by Sinclair [23].

When testing the R1000 panels the 10 g charge experiment was repeated (at the same SOD and with the same detonators). This was due to the first test panel exhibiting multiple failure modes. In order to ascertain if this was a true initiation charge mass of these failure modes, the test was repeated. In Figure 7.13 the spatial distribution of all three 10 g tests with observed failure modes have been shown. The first R1000 panel tested, at a 10 g charge mass designation was R1000-S1 which is shown in Figure 7.13 a). The R1000-S1 exhibited delamination, matrix failure and fibre while the other 10 g tests did not. In addition, the front face sheet was also ruptured. After post-test inspection, it seemed that damage exhibited by the R1000-S1 was too severe to have resulted from a 10 g charge. When the impulse values were compared the R1000-S1 (17.32 Ns) was lower than the other two tests (19.23 Ns and 20.84 Ns). It was concluded that the only possible cause could be a localised flaw in the material.

The general observation of the R1000 panel was that the extent/severity of delamination increased with increasing charge mass as in the case of the flat laminates. Underlying this is that less energy is available to cause delamination when new failure mode initiation occurred.

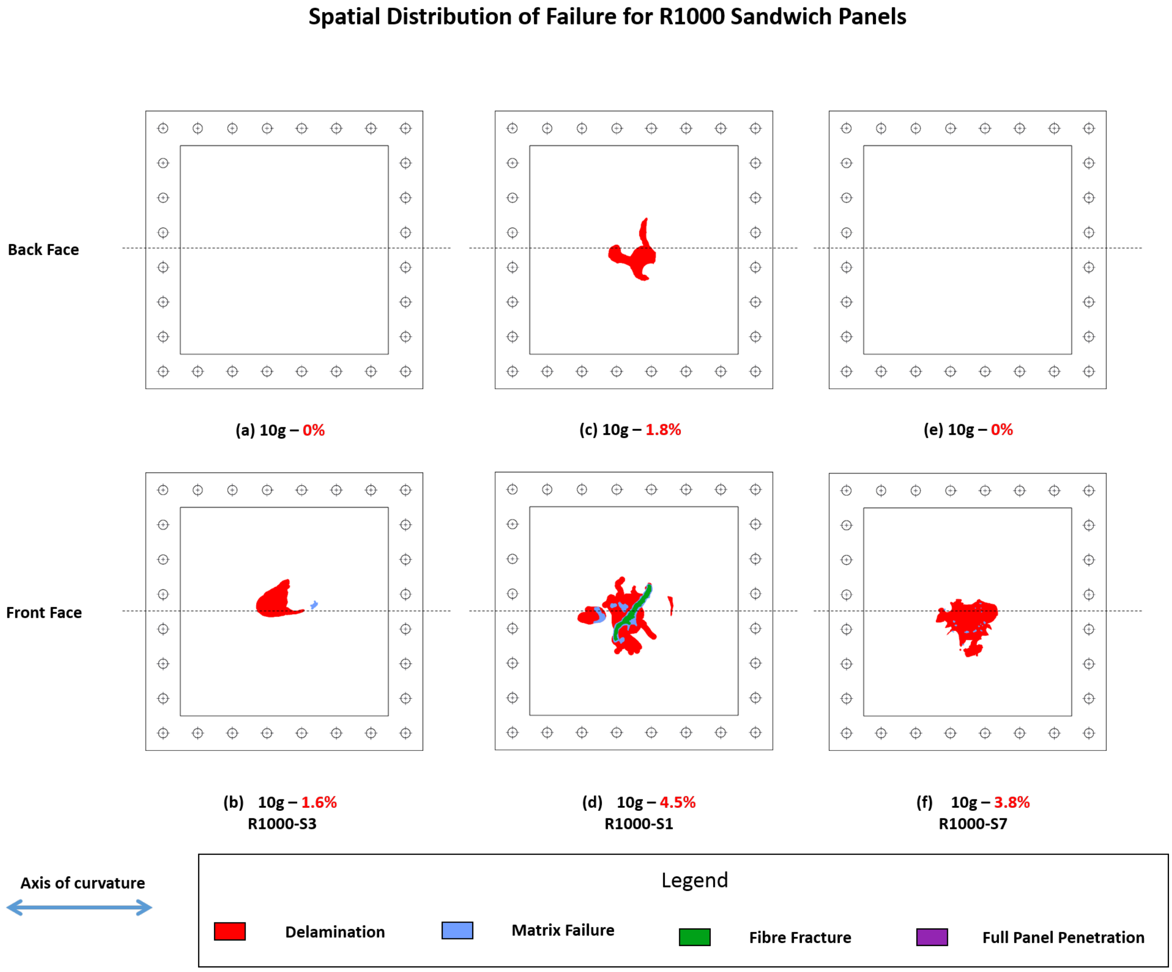

Figure 7.13: Failure maps of the three R1000 Panels tested with a 10 g charge

In the case of the repeat 10 g tests, delamination of the R1000-S1 panel, the front face projected area delamination was more than S1000-S3 and S1000-S7. R1000-S1 exhibited more severe front face failure modes (i.e. FFp, MF, DL) whereas the other panels exhibited fewer failure modes with less severity. Only the back face of the R1000-S1 exhibited delamination. This trend is different to the flat sandwich panels where the back face delamination occurred at 10 g irrespective of fibre fracture and continued to increase as discussed previously. Analysis of Figure 7.14 and 7.16 seemed to indicate that the severity of fibre fracture on the front face (in the case of R1000 panel) increased the percentage of delamination of the back face. This is confirmed by Figure 7.17 where percentage measured delamination area is charted with the occurrence of fibre fracture. In all cases where fibre fracture penetrated the front face sheets, delamination would occur on the back face. This phenomenon was not observed for the 15 g charge mass in Figure 7.17. However, it should be noted that the difference in back face delamination was 0.7% which is negligible. In addition, the severity of matrix failure and fibre fracture increased with increasing charge mass.

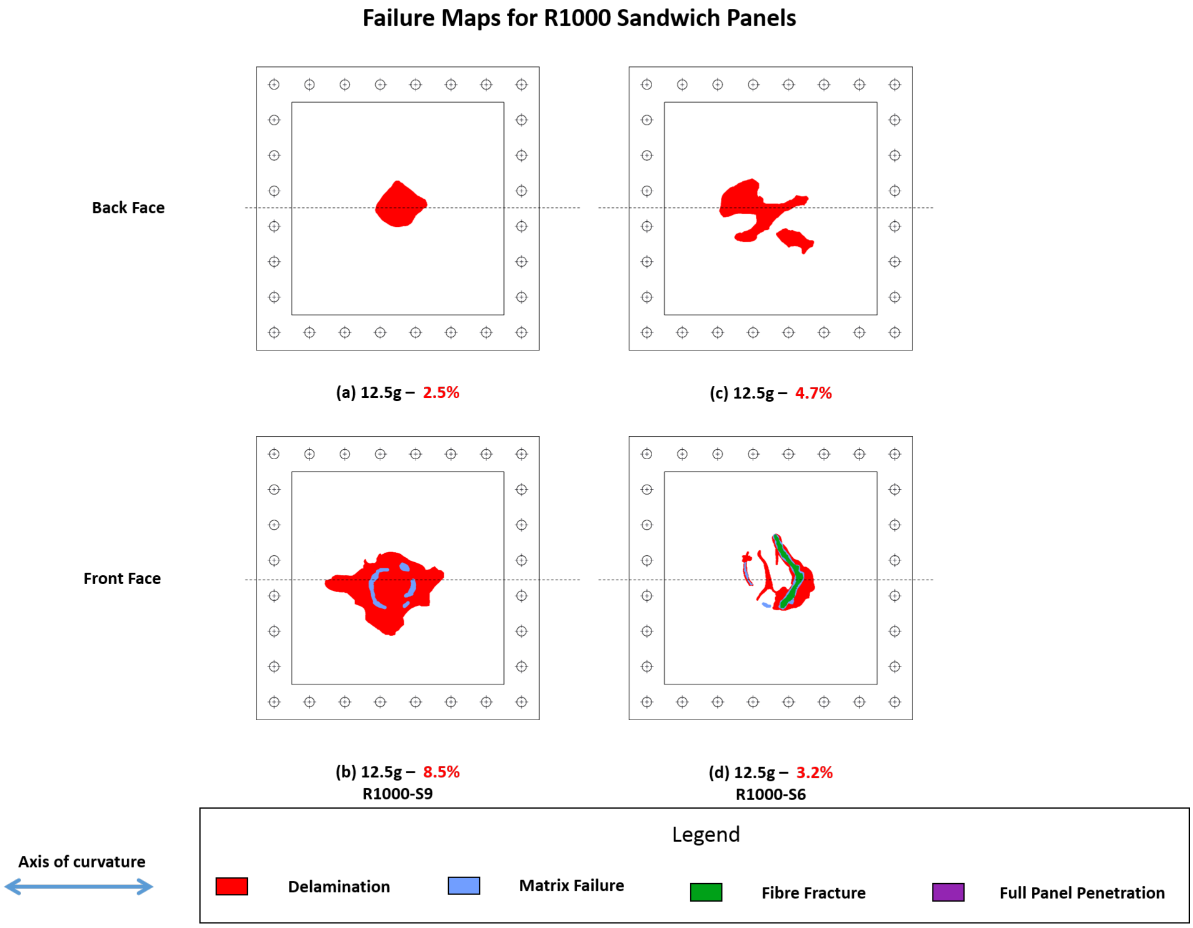

Figure 7.14: Failure maps of the two R1000 Panels tested with a 12.5 g charge

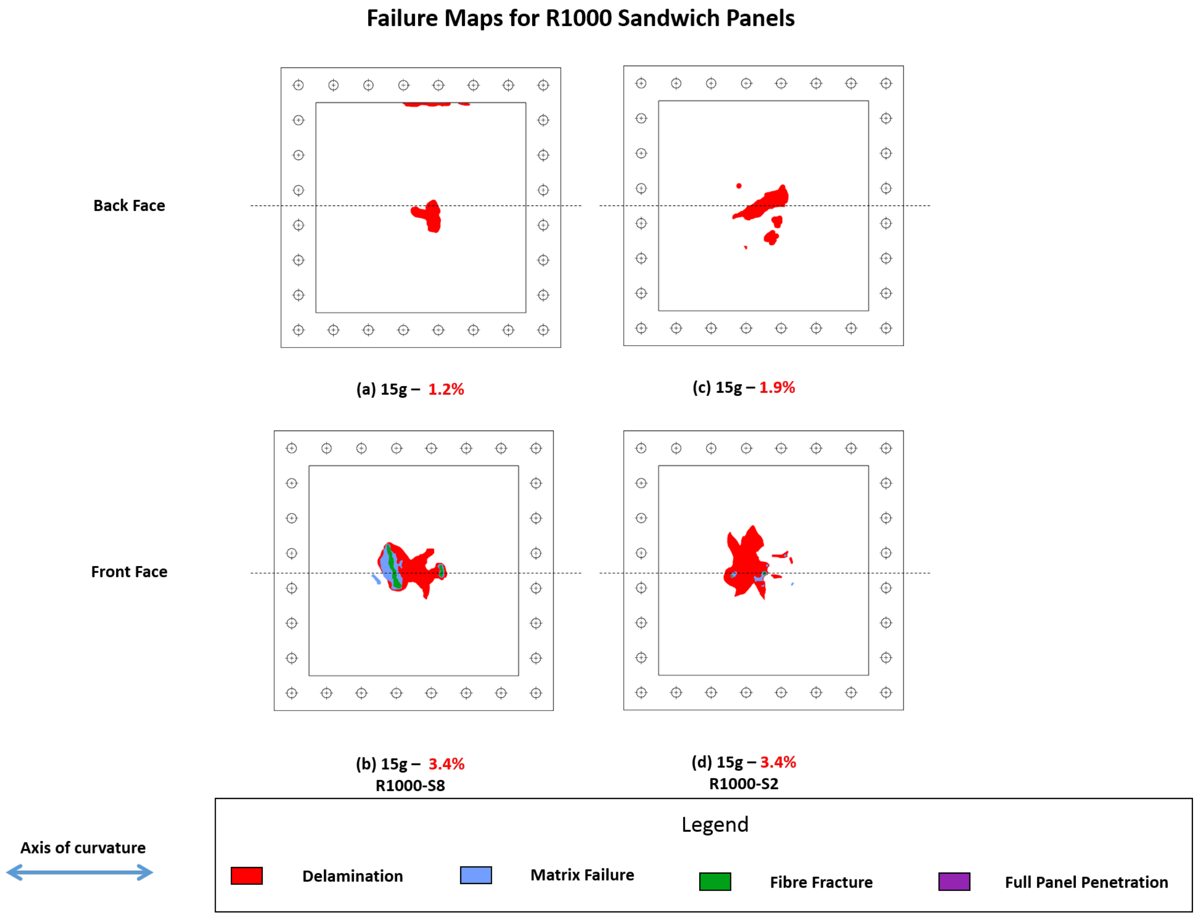

Figure 7.15: Failure maps of the two R1000 Panels tested with a 15 g charge

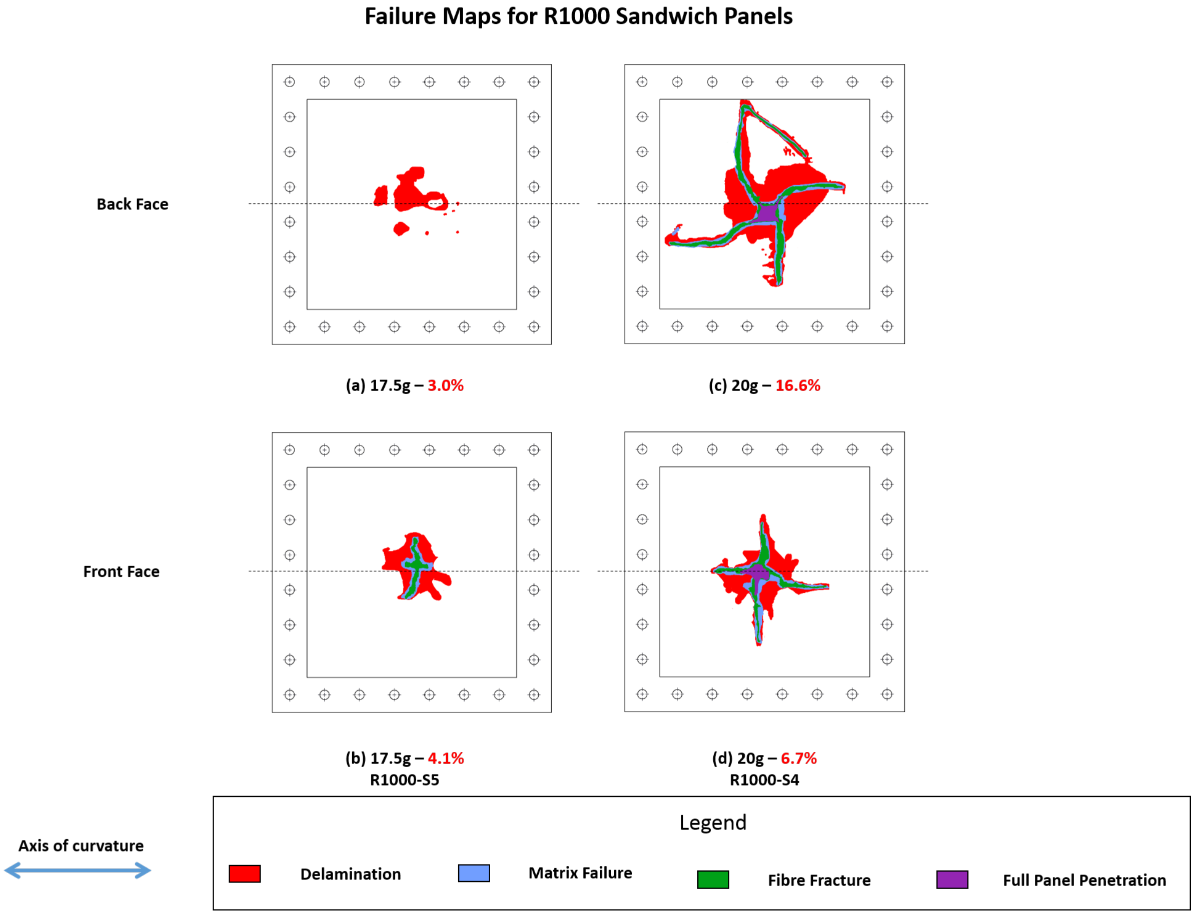

Figure 7.16: Failure maps of the two R1000 Panels tested with a 17.5 g and 20 g charge respectively

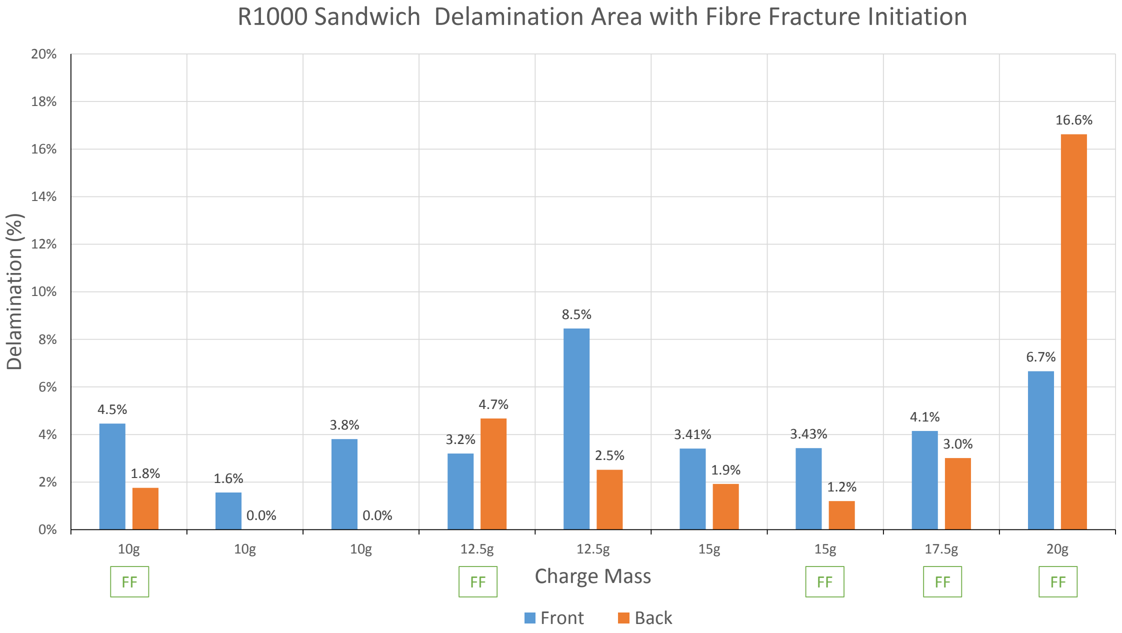

Figure 7.17: R1000 panel delamination area with fibre fracture initiation

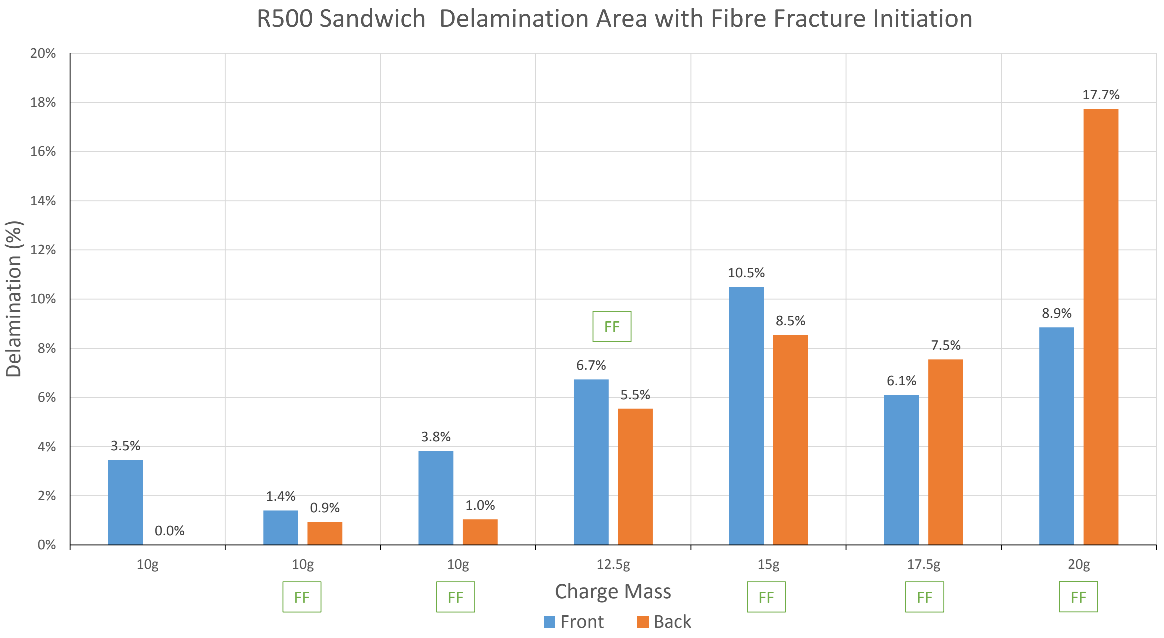

Figure 7.18: R500 panel delamination area with fibre fracture initiation

In the case of the R500 panels the 10 g test was repeated twice. The same trend was observed as in the R1000 panels, where as soon as fibre fracture initiation occurred, delamination on the back face also occurred. In Figure 7.18 there is a 1.0% difference in area delamination between the 15 g and 17.5 g tests despite the large discrepancy in impulse values (27.8 Ns and 35.6 Ns respectively). This could be due to the multiple bolt hole failure in the 17.5 g panel shown in Figure 7.19 a) and b).

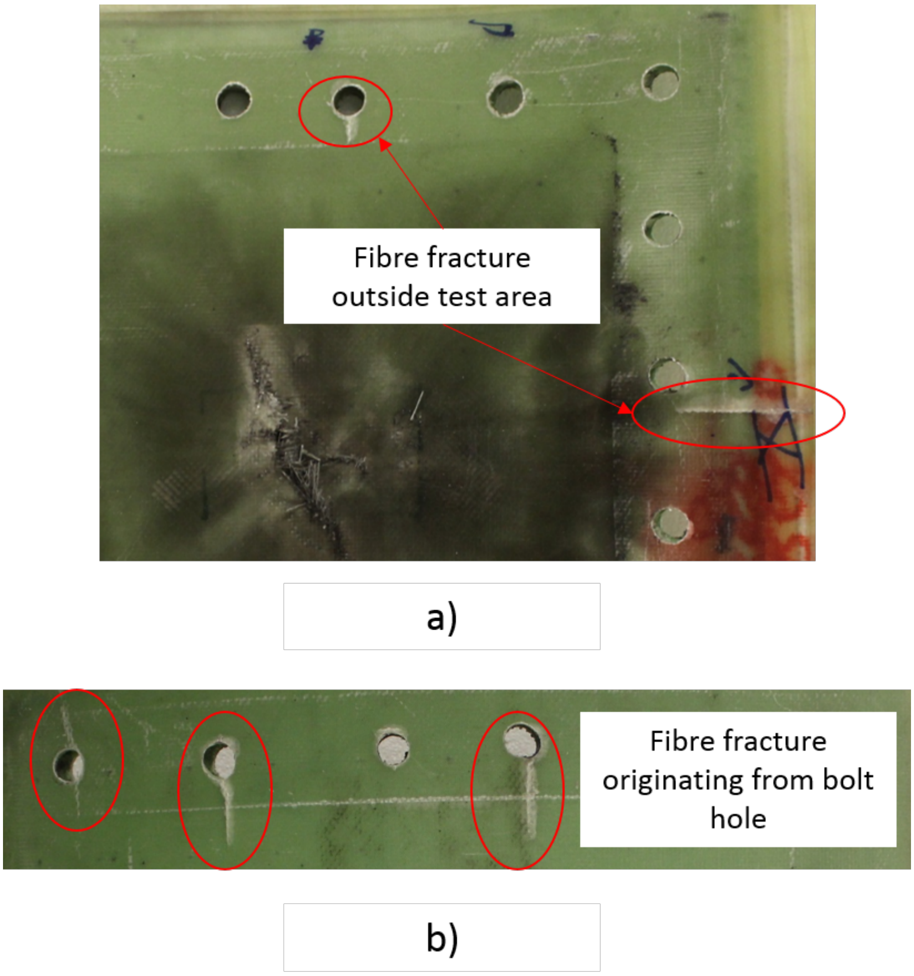

Figure 7.19: R500 sandwich panel subjected to 17.5 g explosive charge: a) Front face with fibre fracture outside test area b) Back face with fibre fracture originating from bolt holes

The R1000 cores exhibited more severe failure with increasing charge mass. At low charge masses localised compression was observed in the centre of the panel, seen in Figure 7.20 and 7.21, with minimal shear cracks. As the charge mass increased, failure escalated to parts of the core being burnt and destroyed (fragmenting into smaller pieces). The same failure progression was observed for the R500 cores, though in certain panels there is a clear distinct shear crack through the thickness of the core. This is shown in Figure 7.21 a), b), c). At 20 g charge mass both the R1000 and R500 displayed through thickness penetration. The R500 panel sustained more damage as a large section of the back face sheet was debonded from the core material.

Figure 7.20: Cross sectional view of selected R1000 panels tested at different charge masses

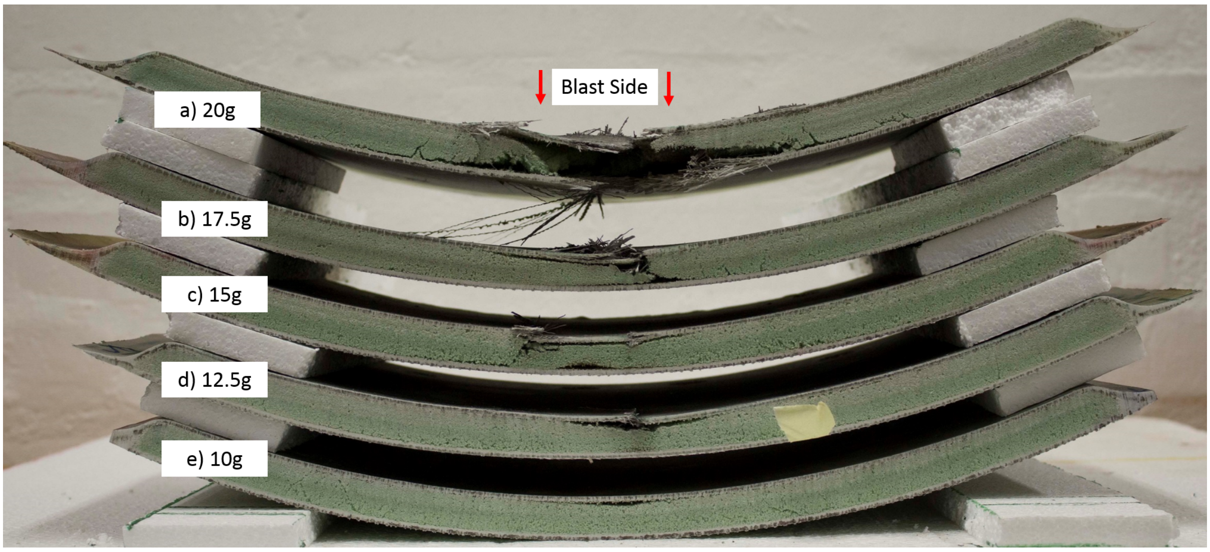

Figure 7.21: Cross sectional view of selected R500 panels tested at different charge masses

7.3.3 Laminate and Sandwich Comparison

Laminates showed more total delamination damage than sandwich panels. The curved laminates showed a defined pattern of delamination where the curved edge seemed to delaminate more than the straight edge. Sandwich panels exhibited full thickness penetration whereas the laminates did not. Front face fibre fracture for the laminates was less than the front face of the sandwich panels. Overall it seemed that the laminates were more resistant to fibre fracture than the sandwich panels, and flat panels more resistant than curved panels.

7.4 Effect of Curvature on Failure Distribution

7.4.1 Debonded Lengths

Debonded lengths of the front interface were much lower than the back debonded lengths similar to observations made by Langdon et al [35]. After fibre fracture initiated, the debonded lengths, in the front interface of curvatures were below 50% of the UML (Undeformed mid-line length) of the sandwich panel as shown in Figure 7.22. The back interface UML debonding percentage after front face sheet penetration remained above 50% as shown in Figure 7.23.

The flat panel debonded percentage of the front interface declined with increasing charge mass and the back interface increased with increasing charge mass. The debonded lengths of the front interface of the curved panels seemed to fluctuate with the highest being 44.5% and the lowest being 20.5%. The back interface had no clear trend.

Similar observations were made by Sinclair [23]. The flat and the R1000 panels showed the same trend as the flat panels test in this work. The R500 panels tested by Sinclair [23] displayed the same trend as the R1000 and R500 panels in this work.

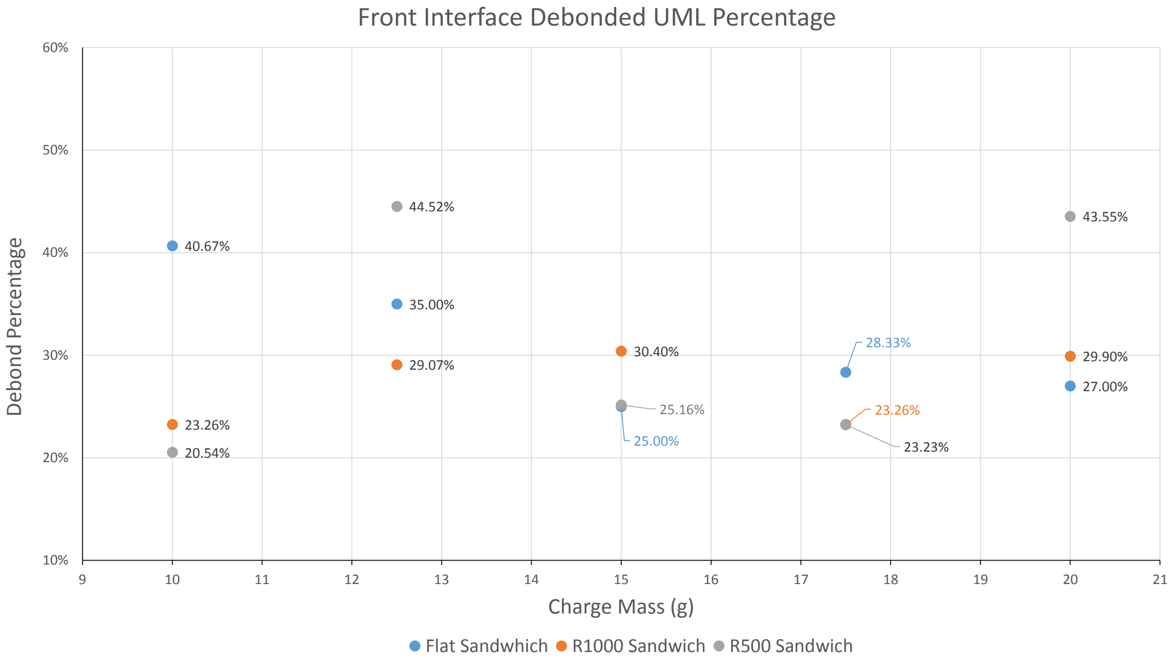

Figure 7.22: Scatter plot of front face sheet-core interface debonding for different sandwich panel curvatures

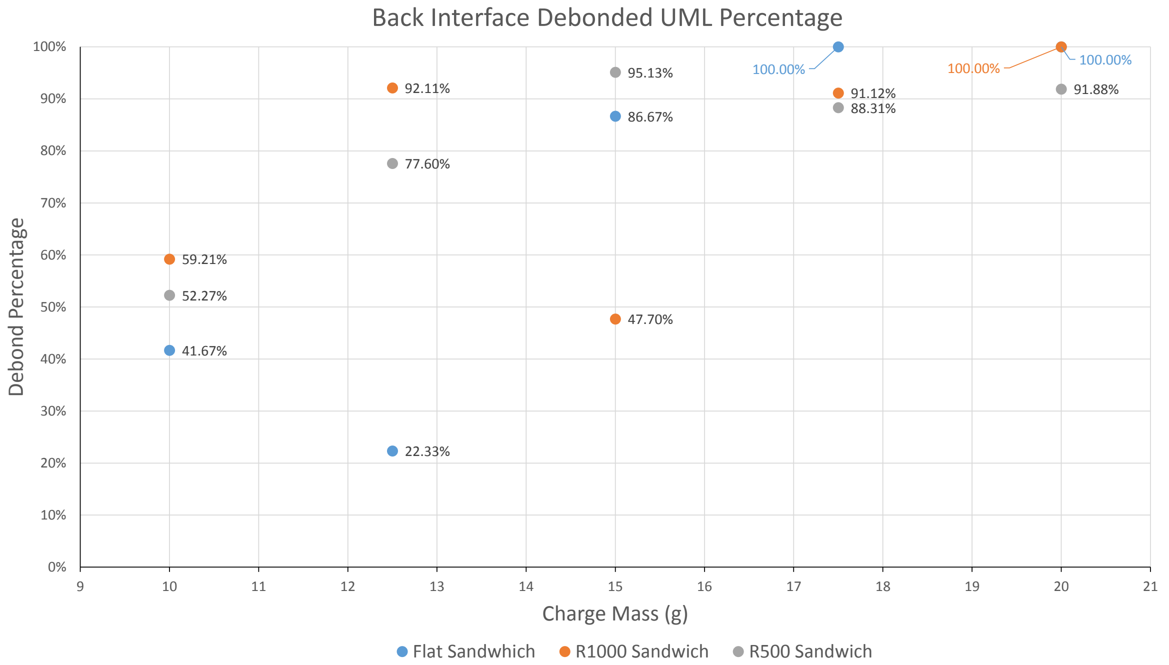

Figure 7.23: Scatter plot of back face sheet-core interface debonding for different sandwich panel curvatures

7.5 Summary

In summary, the curvature radii tested do not appear to affect the impulse transferred significantly. The failure progression was the same irrespective of curvature for both the sandwich panels and the laminates. Similar observations have been made by references [3, 22, 23, 37]. Curved panels exhibited failure initiation at lower charge masses than the flat panels. As the curvature increased, the failure modes initiated at lower charge masses. In the curved laminates it was observed that as the curvature increased, the bias towards more delamination on the curved edge became more evident. Curved panels also displayed more severe damage than flat panels at identical charge masses. Curved laminates outperformed the curved sandwich panels. Curved sandwich panels experienced through thickness rupture at 20 g charge mass whereas the curved laminates did not exhibit rupture at 25 g charge mass. The flat laminates were the most blast resistant, showing no through-thickness penetration at 25 g (the highest charge mass tested) and initiating failure modes at higher charge masses when compared to the other configurations.

Chapter 8

Conclusions and Recommendations

8.1 Conclusions

8.1.1 Curvature Effects

8.1.1.1 Damage Quantity

Curved panels showed more severe damage than the flat panels. The tighter the curvature, the more severe the damage. It was also observed that failure initiation occurred earlier in the R500 panels than the flat or the R1000 panels. This was observed in both laminate and sandwich panels. The spatial distribution of failure was also larger and more severe for the R500 panels, especially for the sandwich panels. Both R500 and R1000 curved sandwich panels exhibited through thickness penetration in the tested range of charge masses (10 g to 25 g).

8.1.1.2 Delamination Pattern

Delamination in the flat laminates extended equally from the boundary to the centre of the laminates. In the curved panels it was observed that there seems to be favoured sides of delamination; the curved edges exhibited more delamination than the straight edges. As the curvature increased these areas continued to have more delamination than the straight edges.

8.1.1.3 Failure Progression

Failure progression was the same irrespective of curvature and lay up. All panels followed the following progression: delamination, matrix failure, core crushing with core shear cracks (sandwich panels only), core fragmentation (sandwich panels only), core penetration (sandwich panels only) and fibre fracture.

8.1.1.4 Impulse Transfer

Impulse measurements were similar with no significant difference for all panels, irrespective of curvature and material type. At 100 mm SOD the localised blast was not noticeably affected by the concave geometry.

8.1.2 Complexity of Manufacture

Composite manufacturing is generally a labour intensive and lengthy process. The curved sandwich panels were the most complex to manufacture, given that the main use of the panels was blast protection, and the choice was between laminates and sandwich composites. This was due to the extra manufacturing step needed to shape the core to the correct curvature. In addition, cores had to be chamfered to create a better drape for the glass fibre layers. All panels that were manufactured had a high degree of mechanical property consistency. This was supported by the low standard deviation for mechanical properties displayed in Chapter 4.

8.1.3 General Overall Performance

At lower charge masses delamination started in the central region. As charge mass increased, delamination also spread inward from the boundary for the laminates. The back faces of the laminates showed more damage at higher charge masses than the front faces. Larger areas of fibre fracture and matrix failure were observed on the back faces of the laminates when compared to the front faces.

For the sandwich panels, delamination was mostly confined to central region. Once the front face sheet was ruptured, total panel rupture quickly ensued. This made the thickness of the front face sheet critical for damage initiation.

None of the laminates displayed through thickness penetration in the 10 g to 25 g charge mass range. Laminates exhibited better blast resistance as no through thickness penetration at 25 g charge mass occurred, while the sandwich panels ruptured at 20 g.

All flat panels showed less damage than the curved panels tested. The flat sandwich panel did not show through thickness penetration unlike the R1000 and R500 curved sandwich panels. Hence, flat panels outperformed the concave curved versions.

8.2 Recommendations

8.2.1 Experimental Tests

In order to confirm the transient response, DIC measurements should be taken. This would allow one to validate the numerical models. In addition, this would allow one also to compare the indentation and flexural response of panels being investigated. This would also provide insight into why there is more delamination on the curved edge as opposed to the straight edge of the curved concave panels.

The number of plies on the front face of the sandwich panel could also be increased, which could delay the front face sheet rupture, which could in turn delay the onset of other failure modes. In order to determine the rupture threshold of the flat panels, higher charge masses could also be tested.

A tighter curvature could be tested to understand the geometric effect on the delamination pattern and panel response. Lastly, investigating the effect of curved composites with a different type of clamping arrangement would allow for greater understanding of different boundary conditions, which could more representative of real life situations.

8.2.2 Numerical Modelling

An advanced numerical model for the concave curved composite panels could be developed. A material model which includes failure modes for laminates and sandwich panels could allow researchers to investigate damage initiation in a more cost effective way and would facilitate researchers developing better counter measures for possible terror scenarios. It could also assist in aiding understanding of the dynamic response of the concave sandwich panels under blast loading and potentially allow researchers to observe indentation and flexural deformation modes under blast loading.

References

[1] J Dathan. Explosive truth: Monitoring explosive violence in 2016. http://www.inew.org/site/wp-content/uploads/2017/05/AOAV-Explosive-Monitor-2017v9.pdf, 2016. Accessed 19 August, 2017.

[2] GS Langdon, WJ Cantwell, ZW Guan, and GN Nurick. The response of polymeric composite structures to air-blast loading: a state-of-the-art. *International Materials Reviews*, 59(3):159–177, 2014.

[3] A Gargano, K Pingkarawat, M Blacklock, V Pickerd, and AP Mouritz. Comparative assessment of the explosive blast performance of carbon and glass fibre-polymer composites used in naval ship structures. *Composite Structures*, 171:306–316, 2017.

[4] SA Tekalur, K Shivakumar, and A Shukla. Mechanical behavior and damage evolution in e-glass vinyl ester and carbon composites subjected to static and blast loads. *Composites Part B: Engineering*, 39(1):57 – 65, 2008.

[5] WeiKu.com. Building facade acp aluminum composite panel board. http://www.weiku.com/products/15145835/, 2015. Accessed 29 September, 2015.

[6] SANFU. Sanfu. http://www.tzsf.com/En/NewsView.asp?ID=173&SortID=11, 2015. Accessed 7 April, 2015.

[7] Ducthops.com. A380. http://www.dutchops.com/AC_Data/Airbus/Airbus_A380/Airbus_A380.htm, 2015. Accessed 7 April, 2015.

[8] P Kumar, J LeBlanc, DS Stargel, and A Shukla. Effect of plate curvature on blast response of aluminum panels. *International Journal of Impact Engineering*, 46:74–85, 2012.

[9] J Shen, G Lu, Z Wang, and L Zhao. Experiments on curved sandwich panels under blast loading. *International Journal of Impact Engineering*, 37(9):960–970, 2010.

[10] P Kumar, DS Stargel, and A Shukla. Effect of plate curvature on blast response of carbon composite panels. *Composite Structures*, 99:19–30, 2013.

[11] GF Kinney and KJ Graham. *Explosive shocks in air*. Springer Science & Business Media, 2013.

[12] US Army, US Navy, and US Air Force. Structures to resist the effects of accidental explosions. *TM5-1300*, page 1400, 1990.

[13] C Geretto. The effects of different degrees of confinement on the deformation of square plates subjected to blast loading. *PhD dissertation*, University of Cape Town, 2012.

[14] CE Gregory. *Explosives for engineers*, volume 10. Trans Tech Publications, 1993.

[15] N Uddin. *Blast protection of civil infrastructures and vehicles using composites.* Elsevier, 2010.

[16] G Mays. *Blast effects on buildings: Design of buildings to optimize resistance to blast loading.* Thomas Telford, 1995.

[17] V Karlos and G Solomos. Calculation of blast loads for application to structural components. *Luxembourg: Publications Office of the European Union*, 2013.

[18] N Dobbs, E Cohen, and S Weissman. Blast pressures and impulse loads for use in the design and analysis of explosive storage and manufacturing facilities. *Annals of the New York Academy of Sciences*, 152(1):317–338, 1968.

[19] GS Langdon, S Chung Kim Yuen, and GN Nurick. Experimental and numerical studies on the response of quadrangular stiffened plates. part ii: localised blast loading. *International Journal of Impact Engineering*, 31(1):85 – 111, 2005.

[20] GS Langdon, GN Nurick, SL Lemanski, MC Simmons, WJ Cantwell, and GK Schleyer. Failure characterisation of blast-loaded fibremetal laminate panels based on aluminium and glassfibre reinforced polypropylene. *Composites Science and Technology*, 67(78):1385 – 1405, 2007.

[21] VR Shekhar. The effect of bend radius on the impulse transfer characteristics of v-hulls. *MSc dissertation*, University of Cape Town, 2015.

[22] GS Langdon, CJ Von Klemperer, BK Rowland, and GN Nurick. The response of sandwich structures with composite face sheets and polymer foam cores to air-blast loading: Preliminary experiments. *Engineering Structures*, 36:104–112, 2012.

[23] GM Sinclair. The response of singly curved fibre reinforced sandwich and laminate composite panels subjected to localised blast loads. *MSc dissertation*, University of Cape Town, 2014.

[24] K Ackland, C Anderson, and TD Ngo. Deformation of polyurea-coated steel plates under localised blast loading. *International Journal of Impact Engineering*, 51:13–22, 2013.

[25] RF Gibson. *Principles of composite material mechanics.* CRC Press, 2016.

[26] AK Kaw. *Mechanics of composite materials.* CRC Press, 2005.

[27] D Hull and TW Clyne. *An introduction to composite materials.* Cambridge University Press, 1996.

[28] RM Jones. *Mechanics of composite materials*, volume 193. Scripta Book Company Washington, DC, 1975.

[29] EJ Barbero. *Introduction to composite materials design.* CRC Press, 2010.

[30] FC Campbell. *Structural composite materials.* ASM international, 2010.

[31] Gurit Composite Technologies. *Prime LV Epoxy Infusion System Datasheet.* 2015.

[32] MY Yahya, WJ Cantwell, GS Langdon, and GN Nurick. The blast behavior of fiber reinforced thermoplastic laminates. *Journal of Composite Materials*, 2008.

[33] M Yazid Yahya, WJ Cantwell, GS Langdon, and GN Nurick. The blast resistance of a woven carbon fiber-reinforced epoxy composite. *Journal of Composite Materials*, 45(7):789–801, 2011.

[34] JLR Comtois, MR Edwards, and MC Oakes. The effect of explosives on polymer matrix composite laminates. *Composites Part A: Applied Science and Manufacturing*, 30(3):181–190, 1999.

[35] GS Langdon, D Karagiozova, CJ Von Klemperer, GN Nurick, A Ozinsky, and EG Pickering. The air-blast response of sandwich panels with composite face sheets and polymer foam cores: Experiments and predictions. *International Journal of Impact Engineering*, 54:64–82, 2013.

[36] E Wang, N Gardner, and A Shukla. The blast resistance of sandwich composites with stepwise graded cores. *International Journal of Solids and Structures*, 46(18):3492–3502, 2009.

[37] GS Langdon, CJ von Klemperer, and GM Sinclair. Blast response of sandwich structures: the influence of curvature. *Dynamic Deformation, Damage and Fracture in Composite Materials and Structures*, page 365, 2016.

[38] Alcan Composite Materials. *Airex C70 Datasheet.* 2015.

[39] Aerontec. Infusion mesh. http://www.aerontec.co.za/products/infusion-mesh/, 2015. Accessed 6 December, 2015.

[40] AMT Composites. Peelply. http://www.amtcomposites.co.za/products/vacuum-bag-infusion-consumables/peelply, 2015. Accessed 6 December, 2015.

[41] Cramer Fabrics Inc. Peel ply. http://www.cramerfabrics.com/products/peel-ply, 2015. Accessed 6 December, 2015.

[42] The Composite Store . Peel-ply & release film tips. http://www.cstsales.com/peel-plies.html, 2015. Accessed 6 December, 2015.

[43] ASTM Standard D7250M-07. *Standard Practice for Determining Sandwich Beam Flexural and Shear Stiffness.* ASTM International, 2016.

[44] ASTM Standard D7264M-07. *Standard Test Method for Flexural Properties of Polymer Matrix Composite Materials.* ASTM International, West Conshohocken, PA, 2015.

[45] ASTM Standard D3039M-14. *Standard Test Method for Tensile Properties of Polymer Matrix Composite Materials.* ASTM International, 2014.

[46] ASTM Standard D1621-10. *Standard Test Method for Compressive Properties of Rigid Cellular Plastics.* ASTM International, 2016.

[47] JA Zukas, W Walters, and WP Walters. *Explosive effects and applications.* Springer Science & Business Media, 2002.

[48] SA Tekalur, A Shukla, and K Shivakumar. Blast resistance of polyurea based layered composite materials. *Composite Structures*, 84(3):271–281, 2008.

Appendix A

FRP Composite Lay Up Arrangement

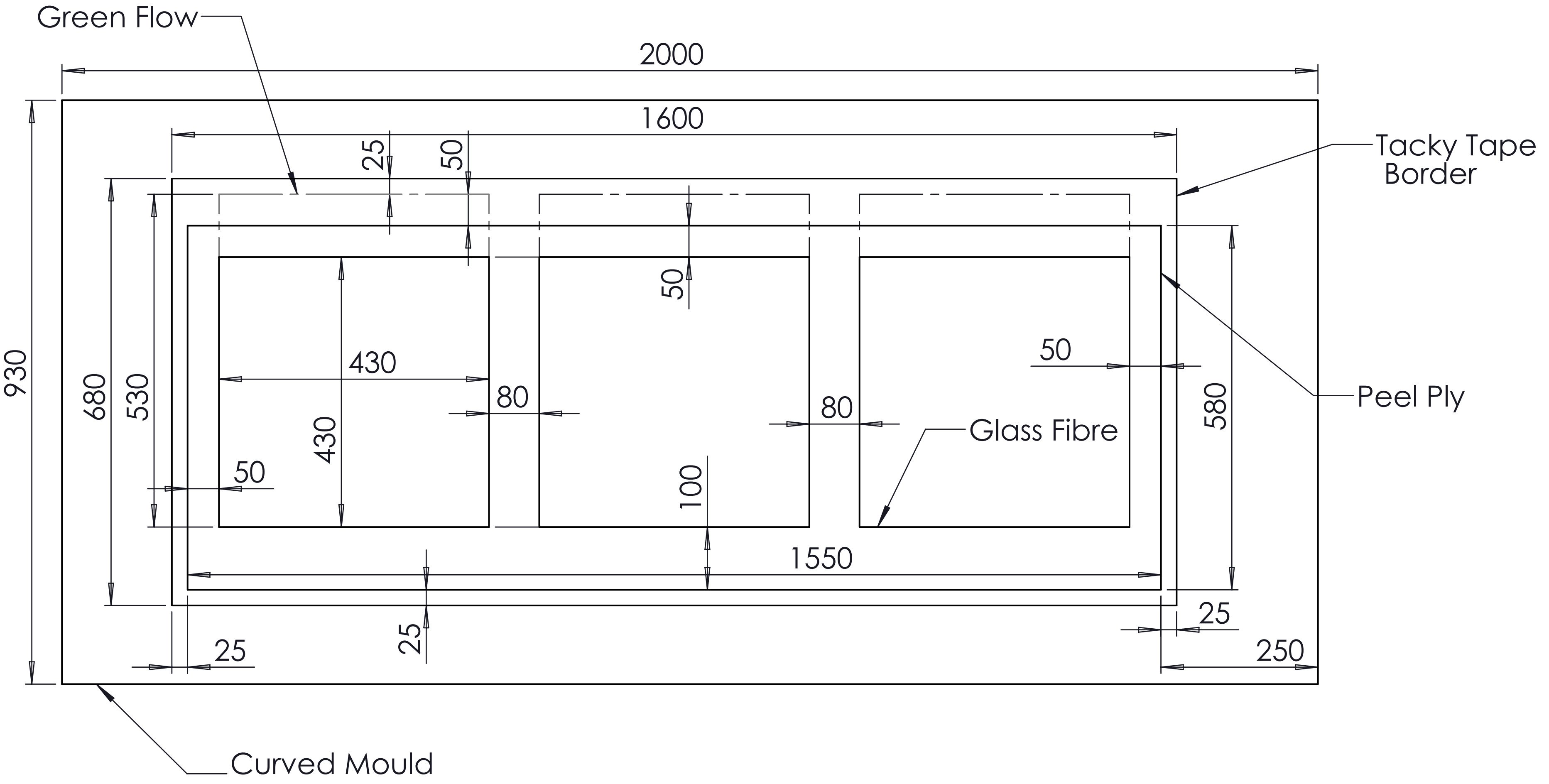

A4 Landscape	University of Cape Town Department of Mechanical Engineering			
	Title: Curved_Specimens_Laminates_Lay_up_File_R500			
Part Finish	Scale: 1:10	Date: 08/09/2017	Sheet1	of 1
Material: Plain Carbon Steel	Drawn By: Ismail Ghoor GHRISM001 082 258 0609 BISRU Ext: 5339		Drawing Number 2015/12/01	

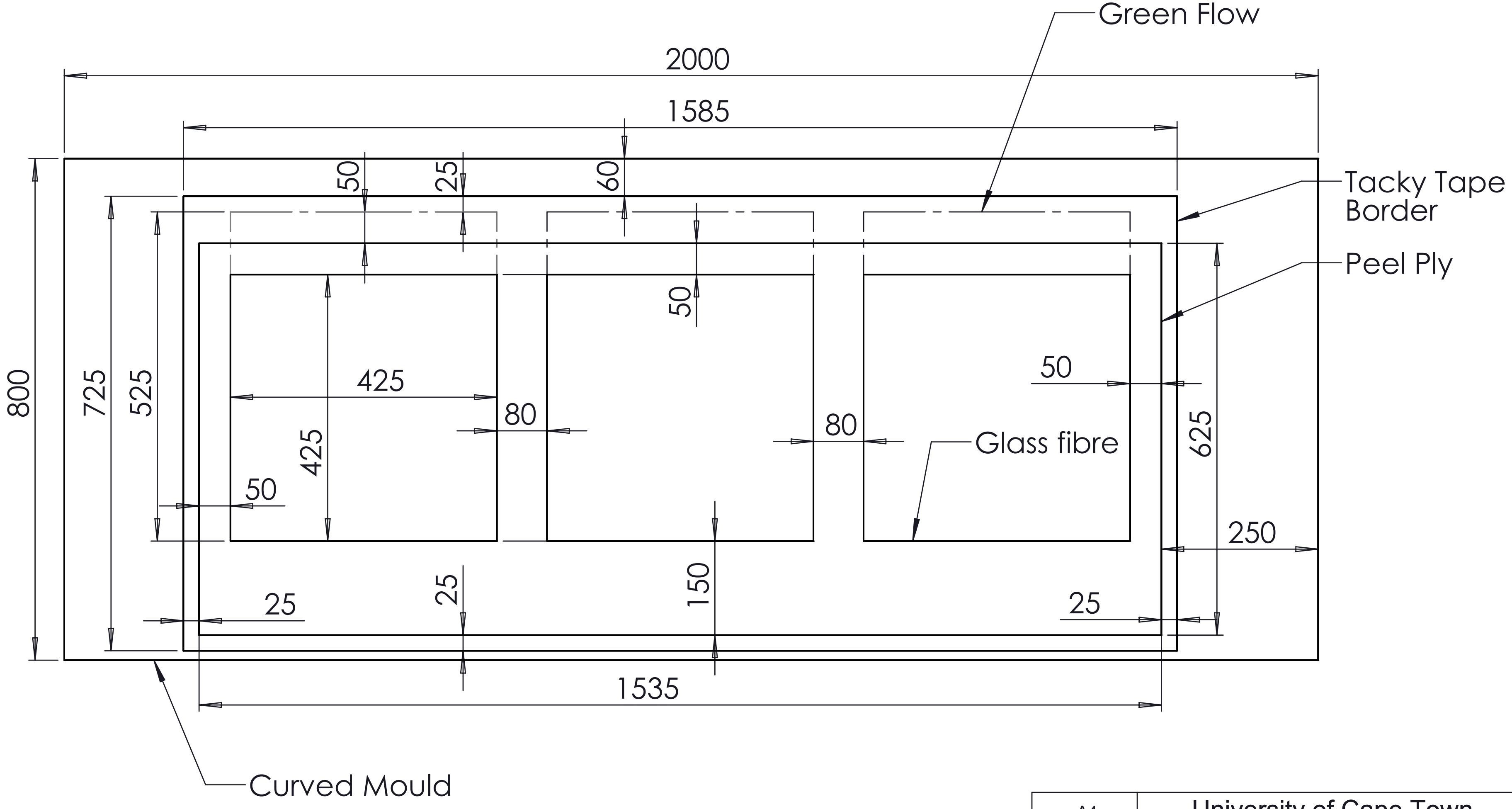

A4 Landscape	University of Cape Town Department of Mechanical Engineering			
	Title: Curved_Specimens_Laminates_Lay_up_File_R1000			
Part Finish	Scale: 1:10	Date: 08/09/2017	Sheet1	of 1
Material: Plain Carbon Steel	Drawn By: Ismail Ghoor GHRISM001 082 258 0609 BISRU Ext: 5339		Drawing Number 2015/12/02	

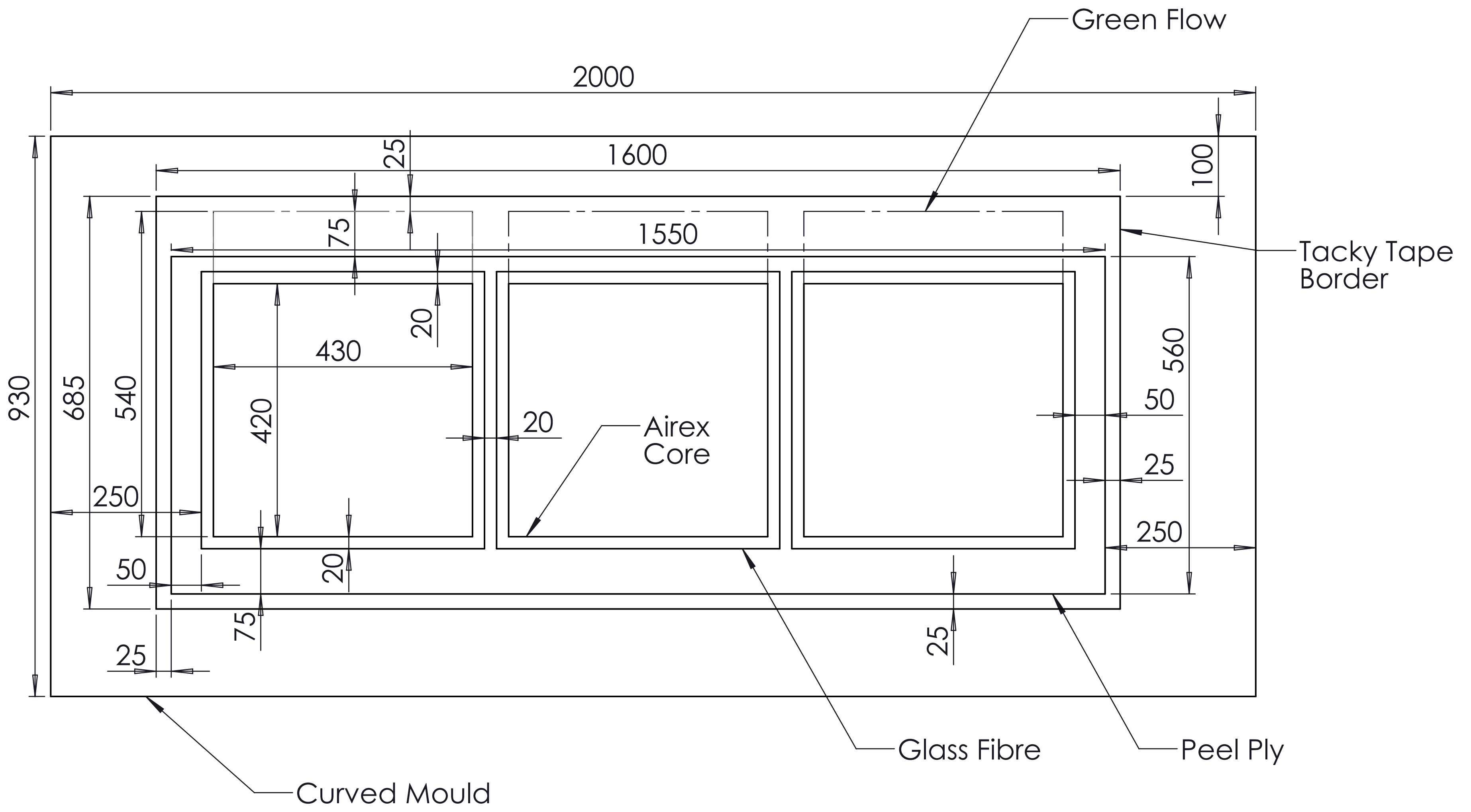

A4 Landscape	University of Cape Town Department of Mechanical Engineering			
	Title: Curved_Specimens_Lay_up_File_R500			
Part Finish	Scale: 1:10	Date: 09/09/2017	Sheet1	of 1
Material: Plain Carbon Steel	Drawn By: Ismail Ghoor GHRISM001 082 258 0609 BISRU Ext: 5339		Drawing Number 2015/012/03	

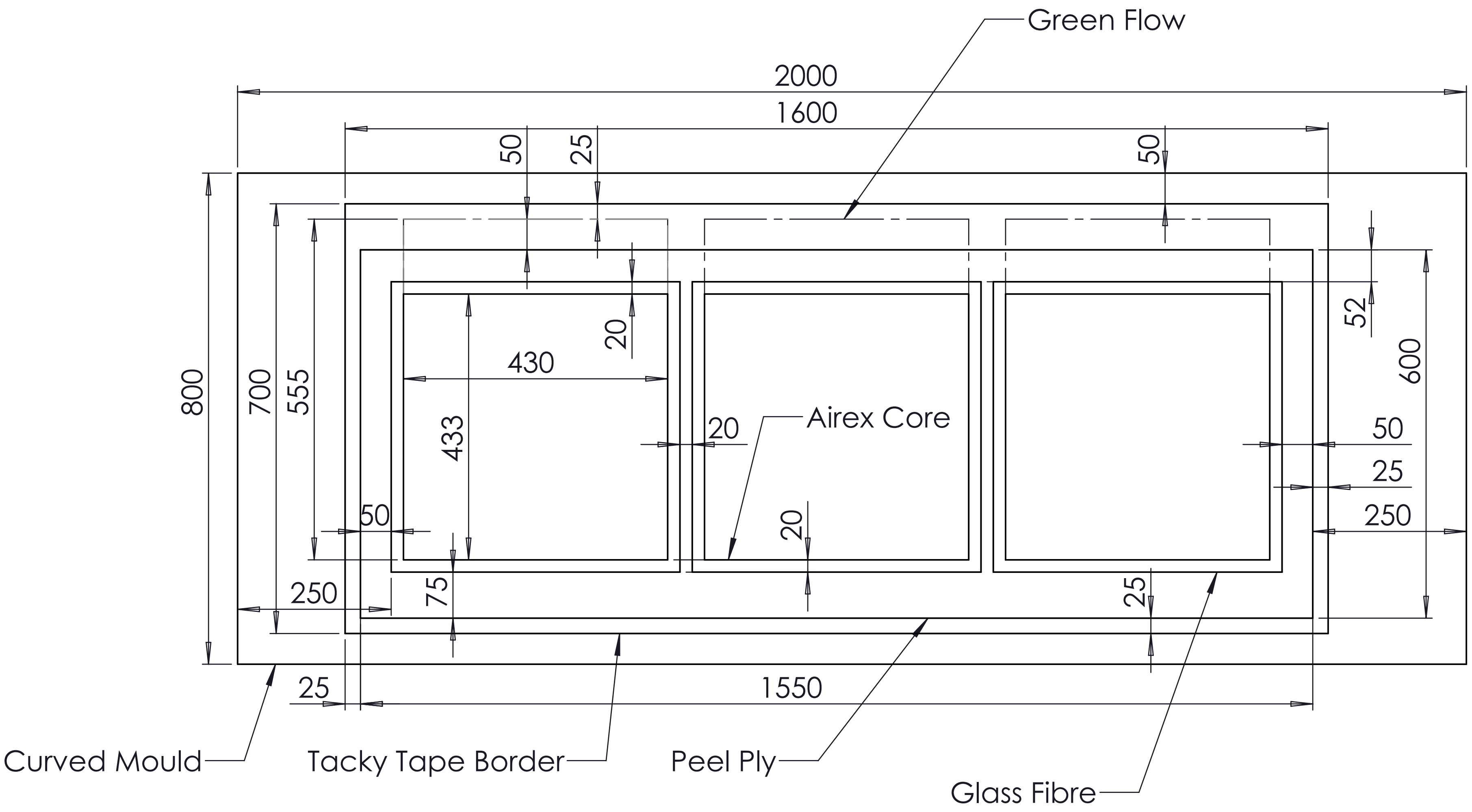

A4 Landscape	University of Cape Town Department of Mechanical Engineering			
	Title: Curved_Specimens_Lay_up_File_R1000			
Part Finish	Scale: 1:10	Date: 08/09/2017	Sheet1	of 1
Material: Plain Carbon Steel	Drawn By: Ismail Ghoor GHRISM001 082 258 0609 BISRU Ext: 5339		Drawing Number 2015/12/04	

SolidWorks Student Edition.
For Academic Use Only.

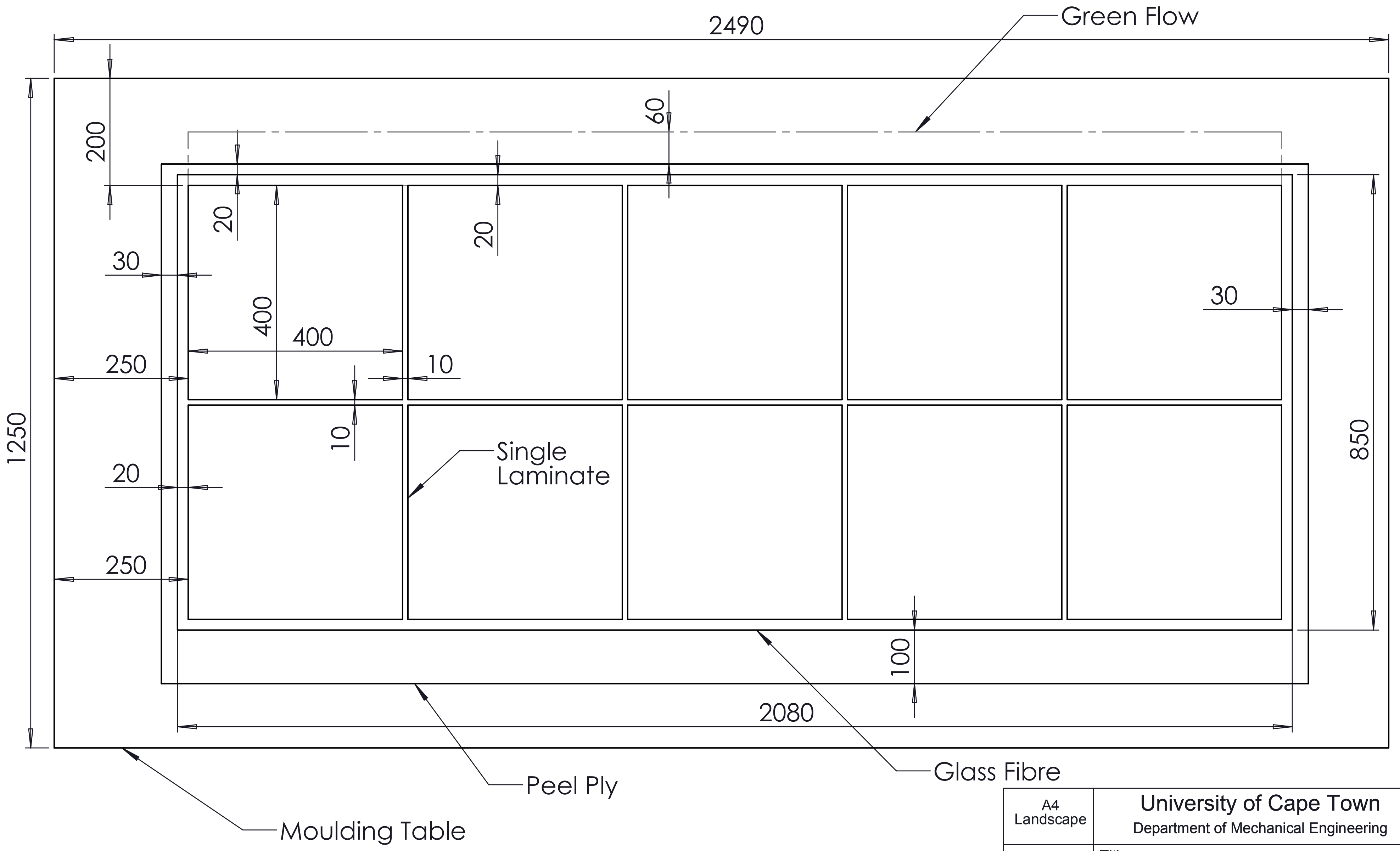

A4 Landscape	University of Cape Town Department of Mechanical Engineering			
	Title: Laminate_Flat_Layup			
Part Finish	Scale: 1:10	Date: 08/09/2017	Sheet1	of 1
Material: Plain Carbon Steel	Drawn By: Ismail Ghoor GHRISM001 082 258 0609 BISRU Ext: 5339		Drawing Number 2015/12/5	

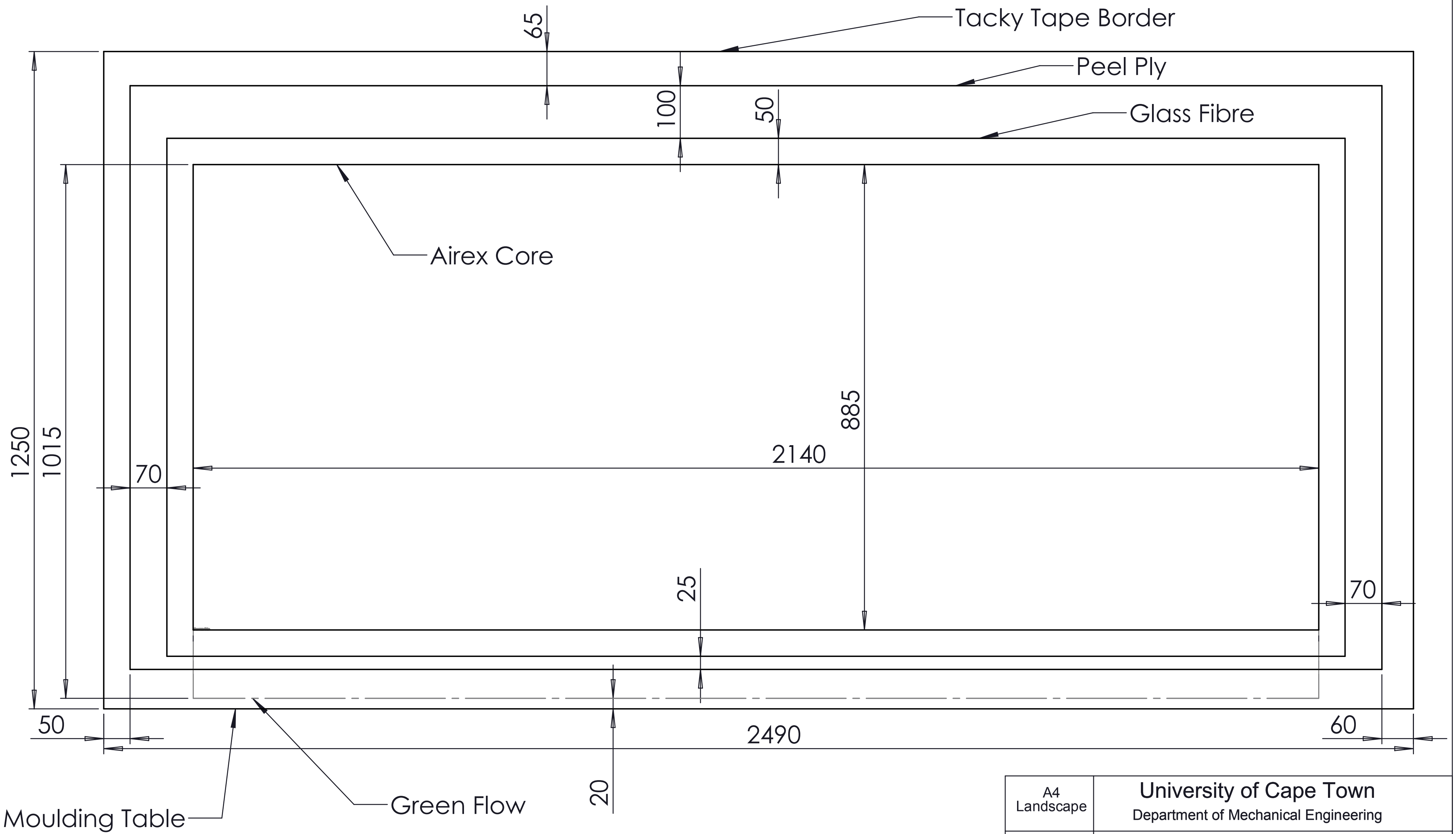

A4 Landscape	University of Cape Town Department of Mechanical Engineering			
	Title: Lay_Up_V3_no_panel_preview			
Part Finish	Scale: 1:10	Date: 08/09/2017	Sheet1	of 1
Material:	Drawn By: Ismail Ghoor GHRISM001 082 258 0609 BISRU Ext: 5339		Drawing Number 2015/12/6	

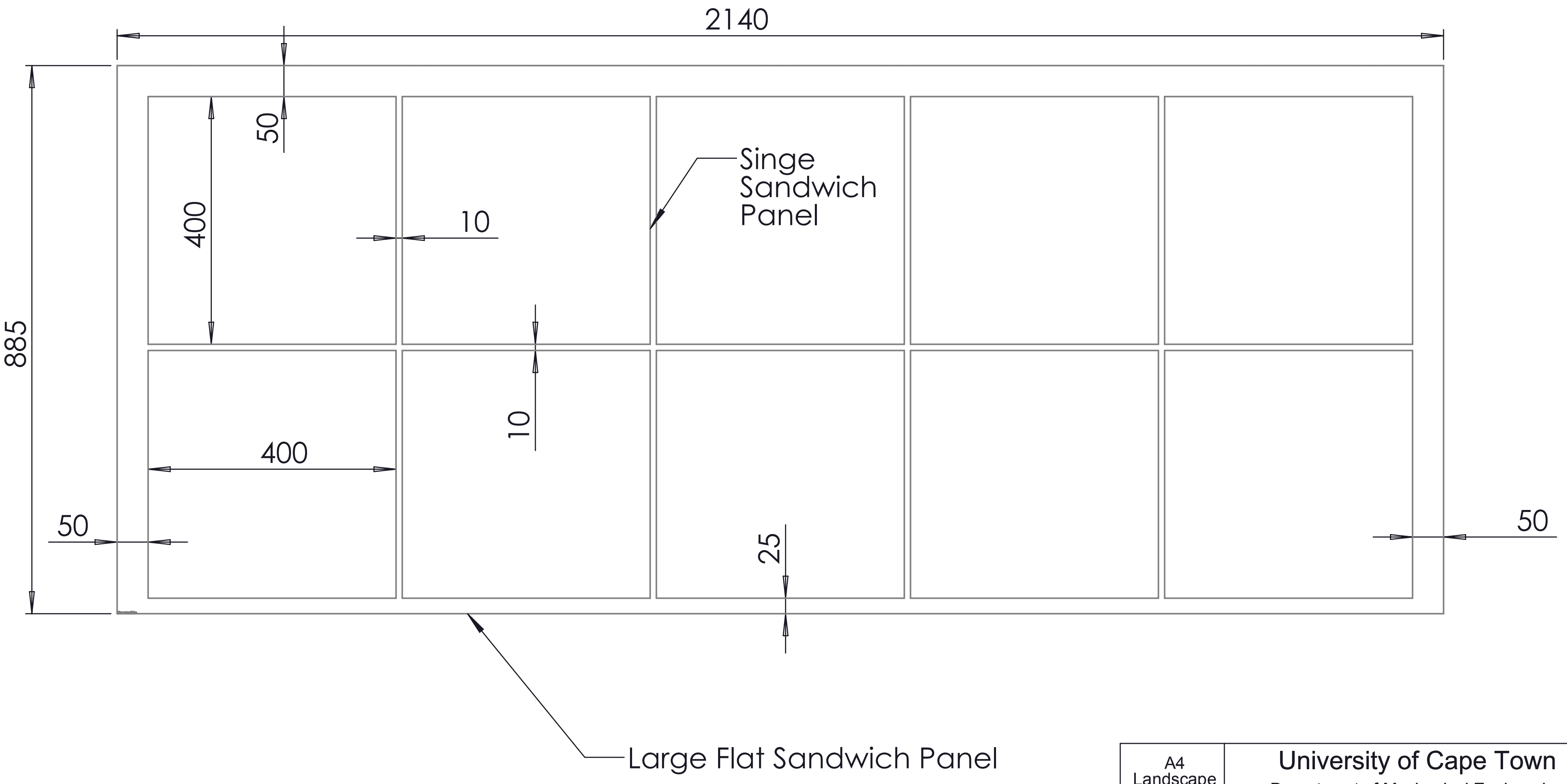

A4 Landscape	University of Cape Town Department of Mechanical Engineering			
	Title: Lay_Up_V3_CORE_CUT			
Part Finish	Scale: 1:10	Date: 08/09/2017	Sheet1	of 1
Material:	Drawn By: Ismail Ghoor GHRISM001 0822580609		Drawing Number 2015/12/7	

Appendix B

Clamp Design Drawings

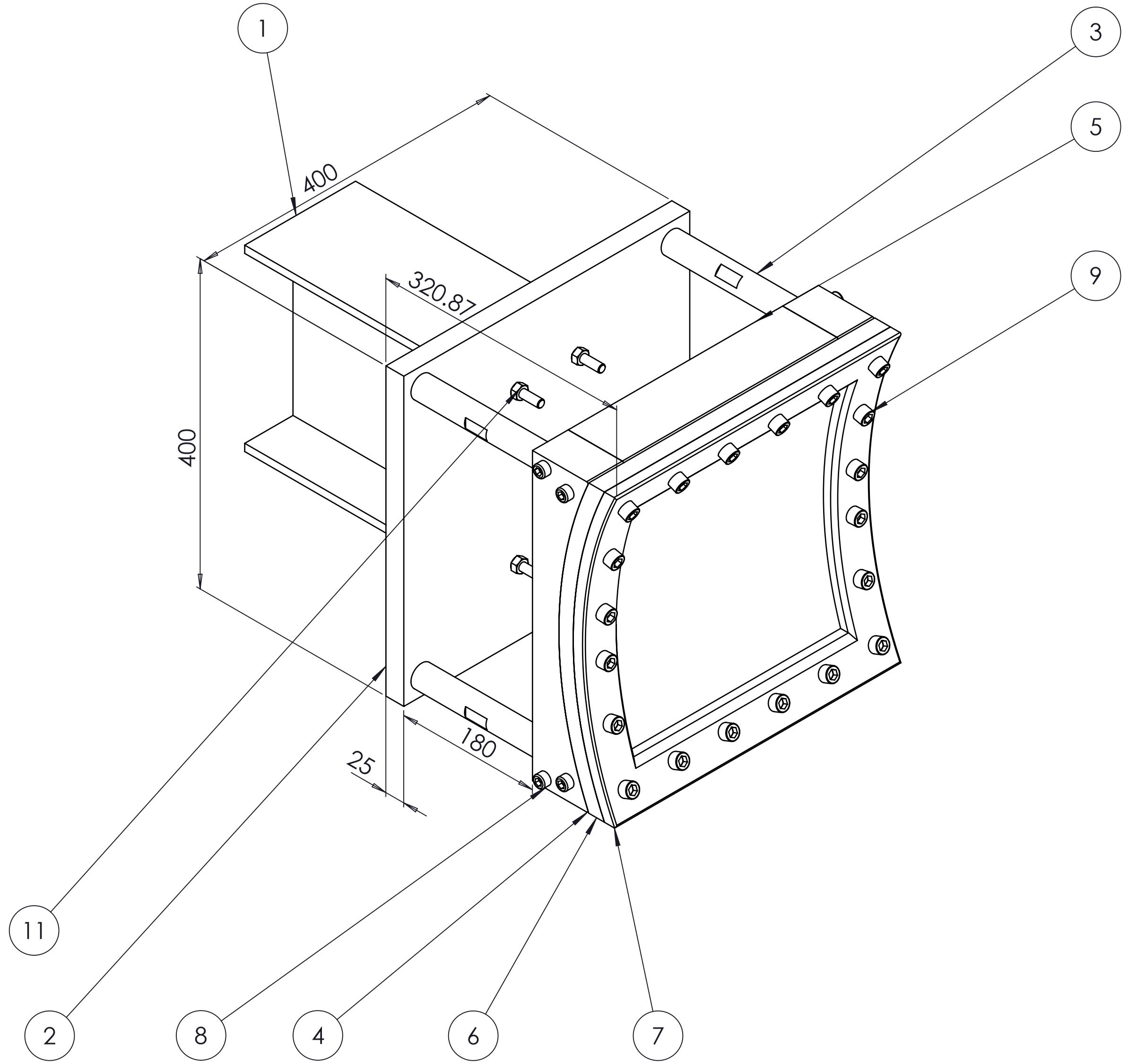

ITEM NO.	PART NUMBER	Material	QTY.
11	Hexagon Nut ISO - 4032 - M10 - W - N	N/A	4
10	ISO 4026 - M12 x 50-C	N/A	4
9	ISO 4762 M12 x 50	N/A	20
8	M10 x 80 --- 32C	N/A	16
7	Outer_Clamp_V3	Plain Carbon Steel	1
6	Sandwhich_R500_V3	Composite	1
5	Base_Clamp_Short_Side_Piece_V4	Plain Carbon Steel	2
4	Base_Clamp_Long_Side_Piece_V4	Plain Carbon Steel	2
3	Spacer	Plain Carbon Steel	4
2	Back_Plate	Plain Carbon Steel	1
1	Pendullum	Plain Carbon Steel	1

A3 Landscape	University of Cape Town Department of Mechanical Engineering			
	Title: Clamp Frame Assembly R500			
Assembly Drawing	Scale: 1:5	Date: 08/09/2017	Sheet1	of 1
	Drawn By:	Ismail Ghoor GHRISM001 082 258 0609 BISRU Ext: 5339	Drawing Number 03/2015/01/0A	

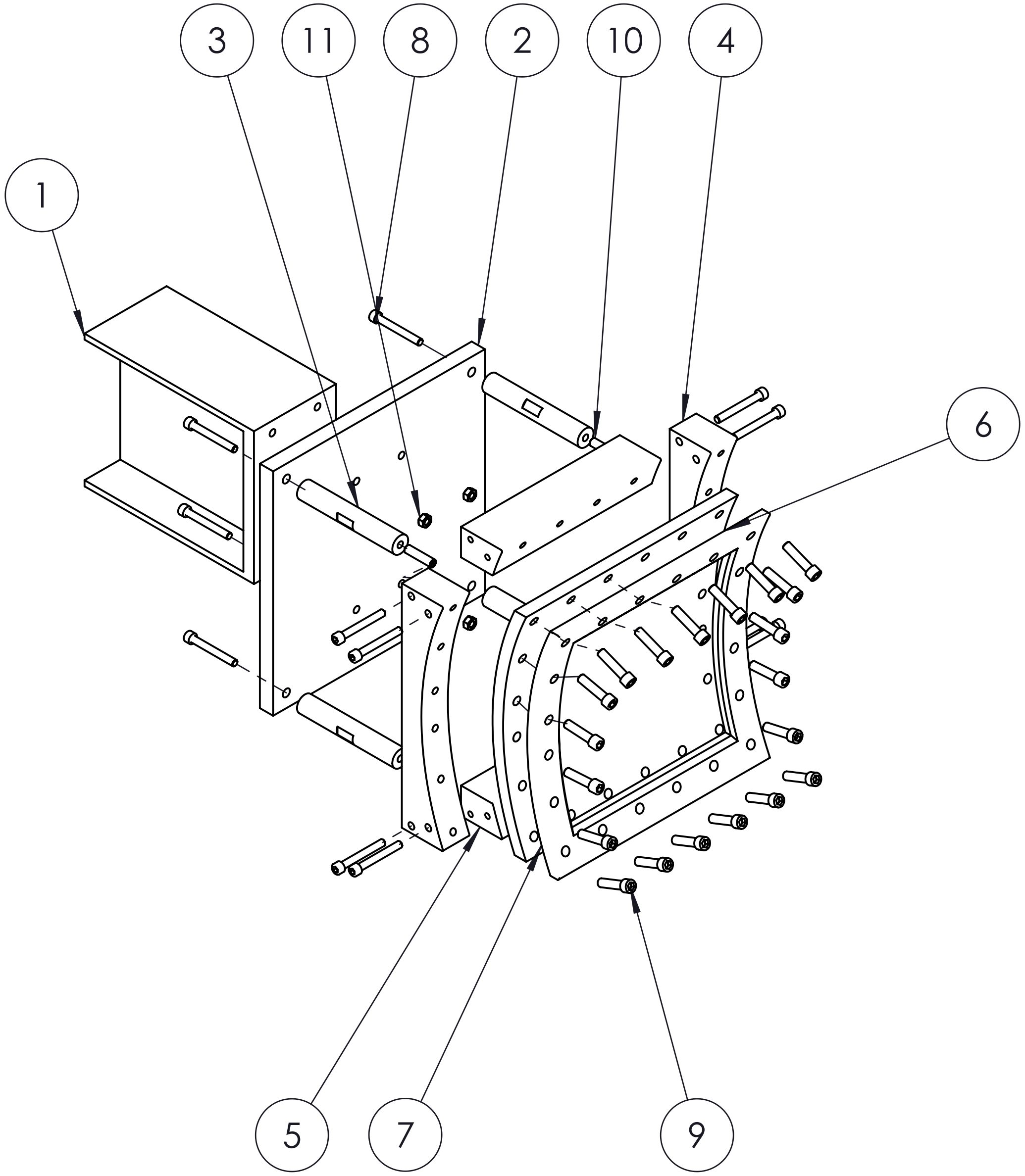

ITEM NO.	PART NUMBER	Material	QTY.
11	Hexagon Nut ISO - 4032 - M10 - W - N	N/A	4
10	ISO 4026 - M12 x 50-C	N/A	4
9	ISO 4762 M12 x 50	N/A	20
8	M10 x 80 --- 32C	N/A	16
7	Outer_Clamp_V3	Plain Carbon Steel	1
6	Sandwhich_R500_V3	Composite	1
5	Base_Clamp_Short_Side_Piece_V4	Plain Carbon Steel	2
4	Base_Clamp_Long_Side_Piece_V4	Plain Carbon Steel	2
3	Spacer	Plain Carbon Steel	4
2	Back_Plate	Plain Carbon Steel	1
1	Pendullum	Plain Carbon Steel	1

A4
Landscape

University of Cape Town
Department of Mechanical Engineering

Title:
Exploded View of R500 Clamp Frame Assembly

Assembly
Drawing

Scale: 1:10
Date: 30/09/2017
Sheet1 of 1
Drawn By: Ismail Ghoor
GHRISM001
082 258 0609
BISRU Ext: 5339
Drawing Number
03/2015/01/0A

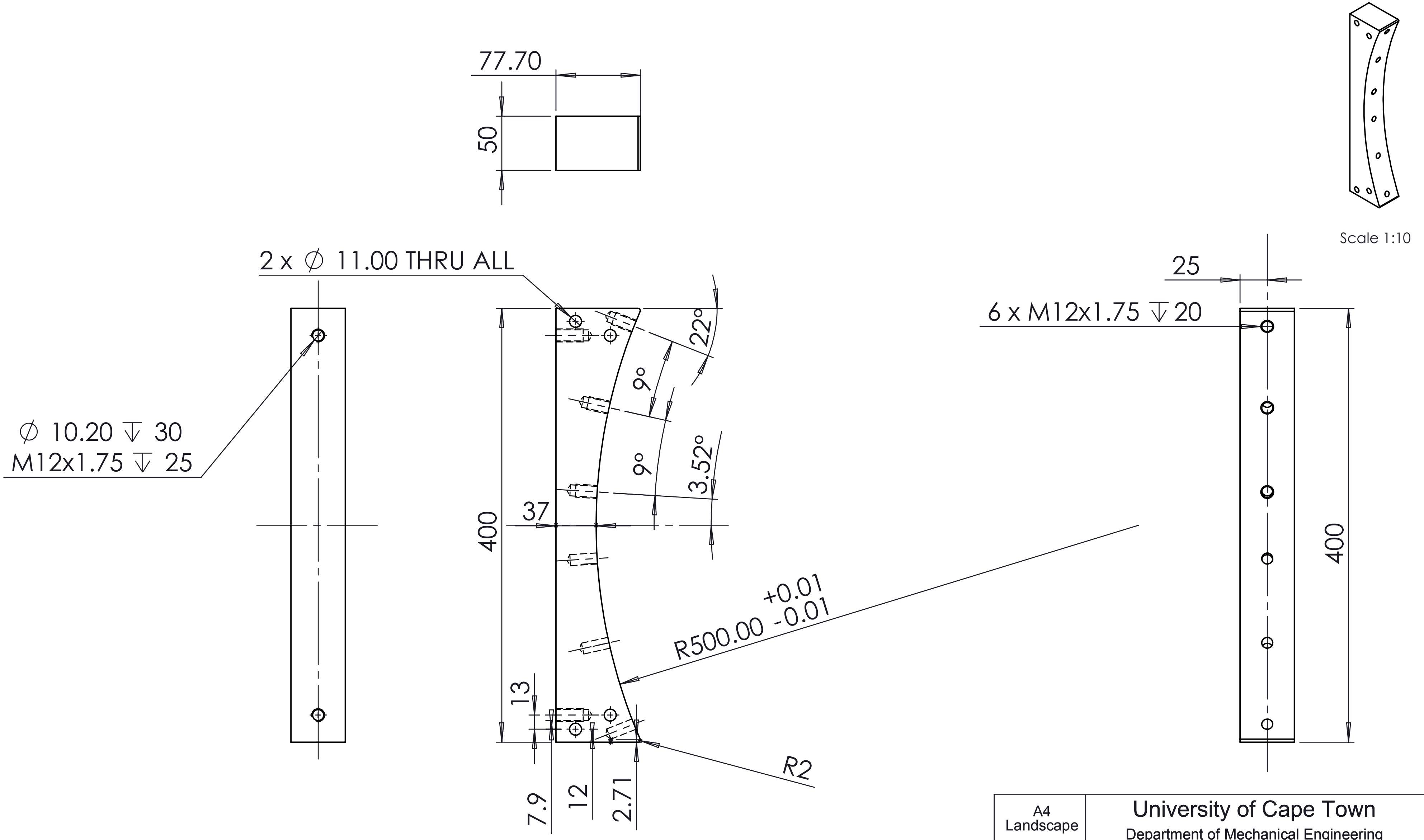

Note:All hole position to be in the tolerence of ±0.05 unless otherwise indicated.

SolidWorks Student Edition.
For Academic Use Only.

A4 Landscape	University of Cape Town Department of Mechanical Engineering				
	Title: Base_Clamp_Long_Side_Piece_V4				
Part Finish	Scale: 1:5		Date: 28/04/2015	Sheet1	of 1
Material: Plain Carbon Steel		Drawn By:	Ismail Ghoor GHRISM001 082 258 0609 BISRU Ext: 5339	Drawing Number 03/2015/01/04	

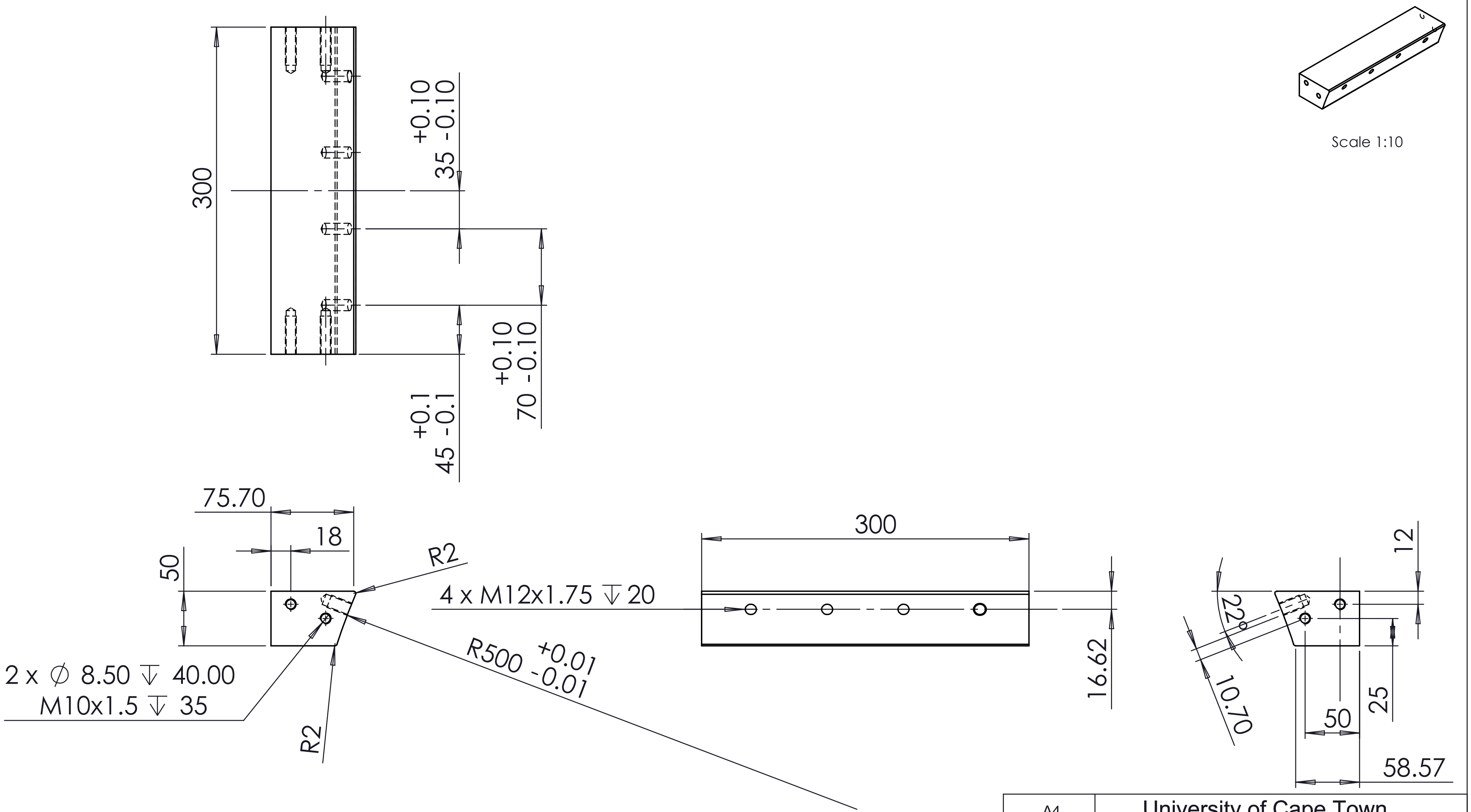

Note:All hole position to be in the tolerence of ±0.05 unless otherwise indicated.

SolidWorks Student Edition.
For Academic Use Only.

A4 Landscape	University of Cape Town Department of Mechanical Engineering			
	Title: Base_Clamp_Short_Side_Piece_V4			
Part Finish	Scale: 1:5	Date: 28/04/2015	Sheet1	of 1
Material: Plain Carbon Steel	Drawn By:	Ismail Ghoor GHRISM001 082 258 0609 BISRU Ext: 5339	Drawing Number 03/2015/01/05	

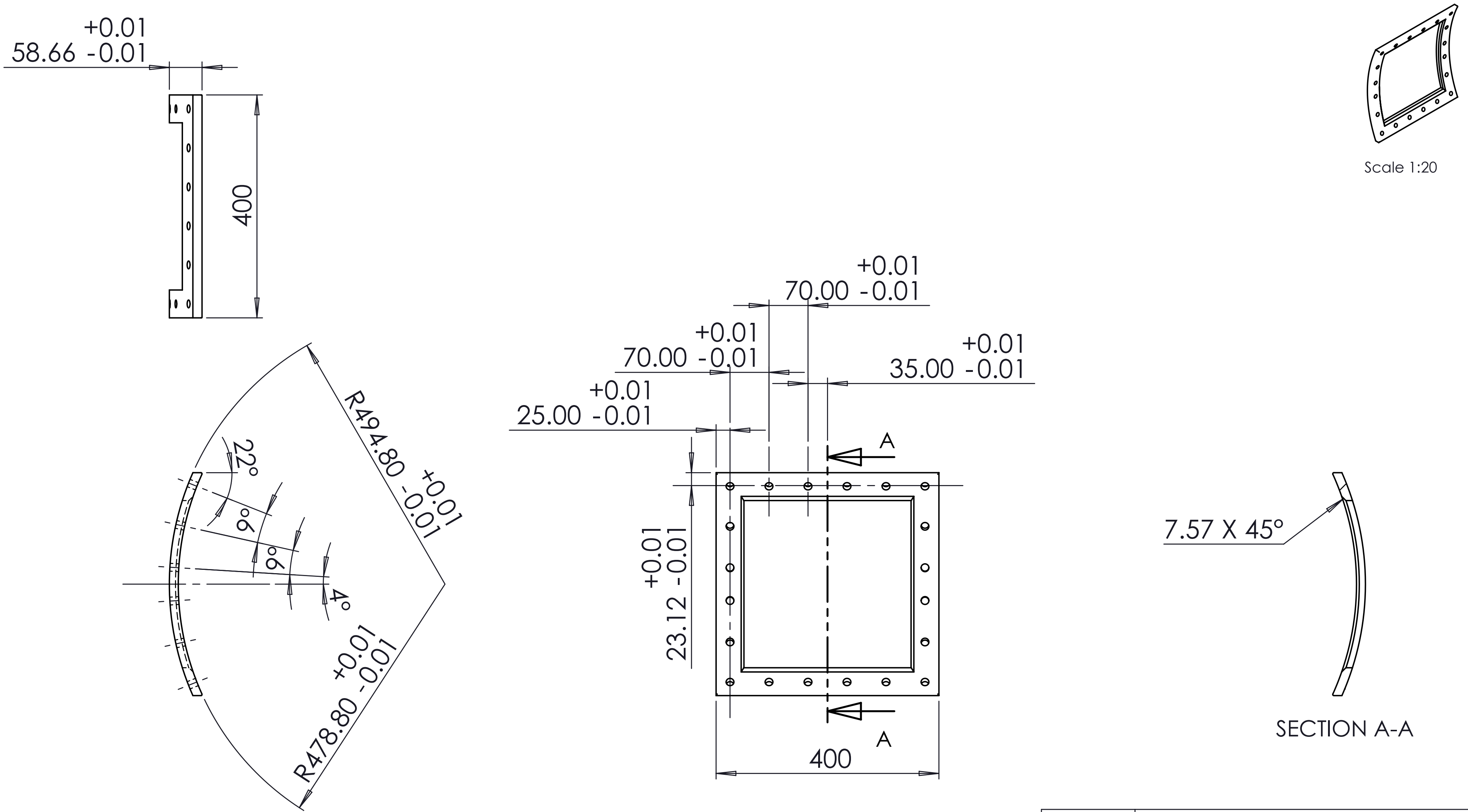

Note: All Fillets are R2
All holes to be Ø14 THRU ALL

A4 Landscape	University of Cape Town Department of Mechanical Engineering				
	Title: Outer_Clamp_Laminate				
Part Finish	Scale: 1:10		Date: 03/08/2017	Sheet1	of 1
Material: Plain Carbon Steel		Drawn By:	Ismail Ghoor GHRISM001 082 258 0609 BISRU Ext: 5339	Drawing Number 04/2015/02/11	

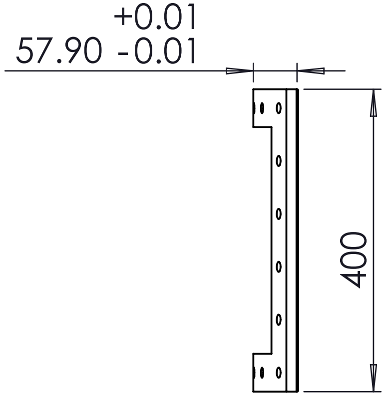

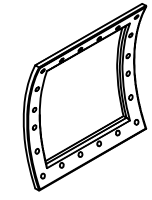
Scale 1:20

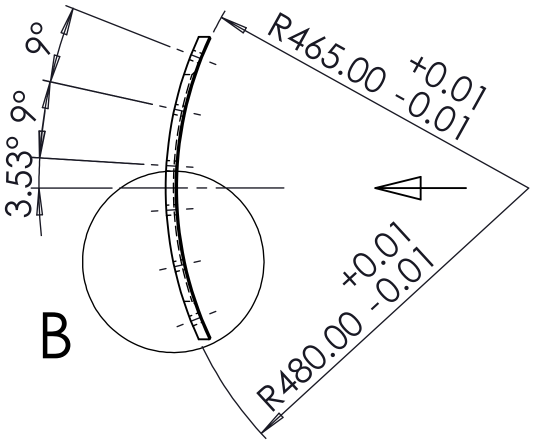

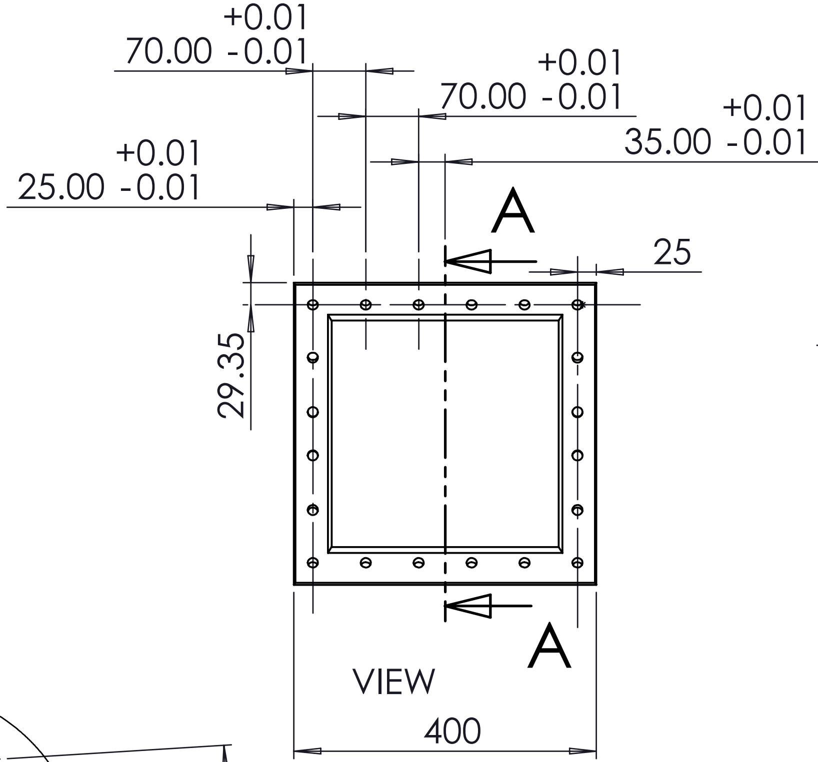

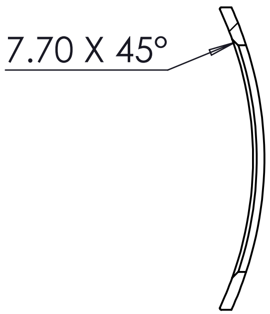

SECTION A-A

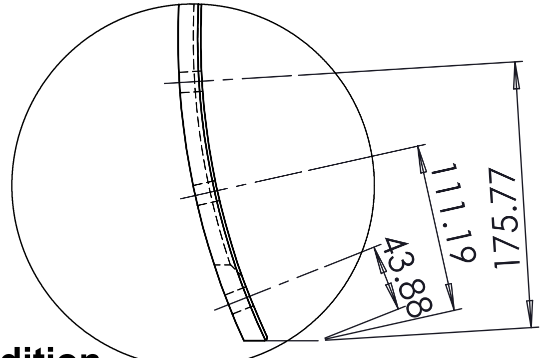

DETAIL B
SCALE 1 : 5

Note: All Fillets are R2
All holes to be Ø14 THRU ALL

A4 Landscape	University of Cape Town Department of Mechanical Engineering			
	Title: Outer_Clamp_V3			
Part Finish	Scale: 1:10	Date: 29/04/2015	Sheet1	of 1
Material: Plain Carbon Steel	Drawn By:	Ismail Ghoor GHRISM001 082 258 0609 BISRU Ext: 5339	Drawing Number 03/2015/01/08	

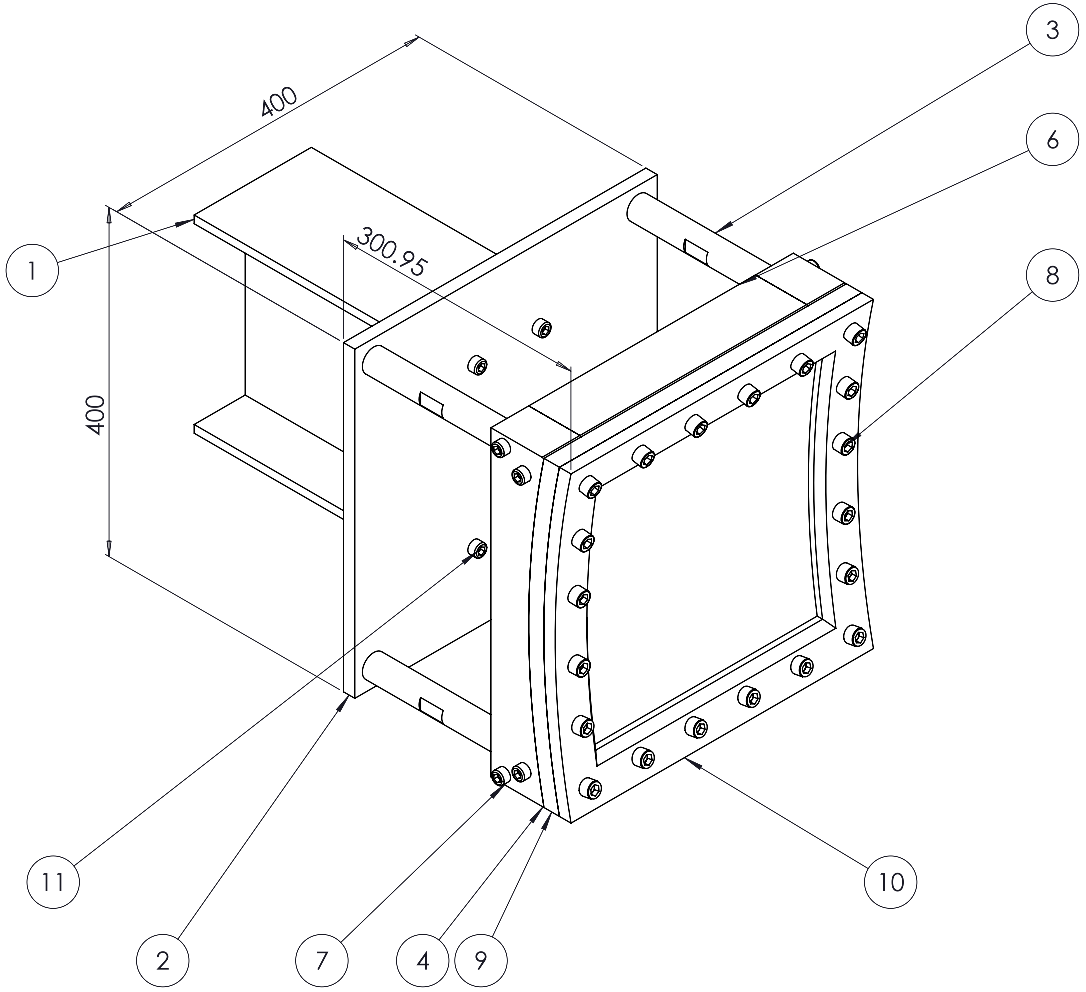

ITEM NO.	PART NUMBER	Material	QTY.
13	ISO 4762 M12 x 40 --- 40C	N/A	4
12	Hexagon Nut ISO - 4032 - M10 - W - N	N/A	4
11	ISO 4762 M10 x 60 --- 60C	N/A	4
10	Outer_Clamp_R1000_V2	Plain Carbon Steel	1
9	Sandwhich_R1000	Composite	1
8	ISO 4762 M12 x 50	N/A	20
7	M10 x 80 --- 32C	N/A	8
6	Base_Clamp_Short_Piece_R1000	Plain Carbon Steel	2
5	ISO 4026 - M12 x 50-C	N/A	4
4	Base_Clamp_Long_Piece_R1000	Plain Carbon Steel	2
3	Spacer	Plain Carbon Steel	4
2	Back_Plate	Plain Carbon Steel	1
1	Pendullum	Plain Carbon Steel	1

A3 Landscape

University of Cape Town
Department of Mechanical Engineering

Title: Clamp Frame Assembly R1000

Assembly Drawing

Scale:	Date:		of
1:5	08/09/2017	Sheet1	1
Drawn By:	Ismail Ghoor GHRISM001 082 258 0609 BISRU Ext: 5339	Drawing Number 04/2015/02/0A	

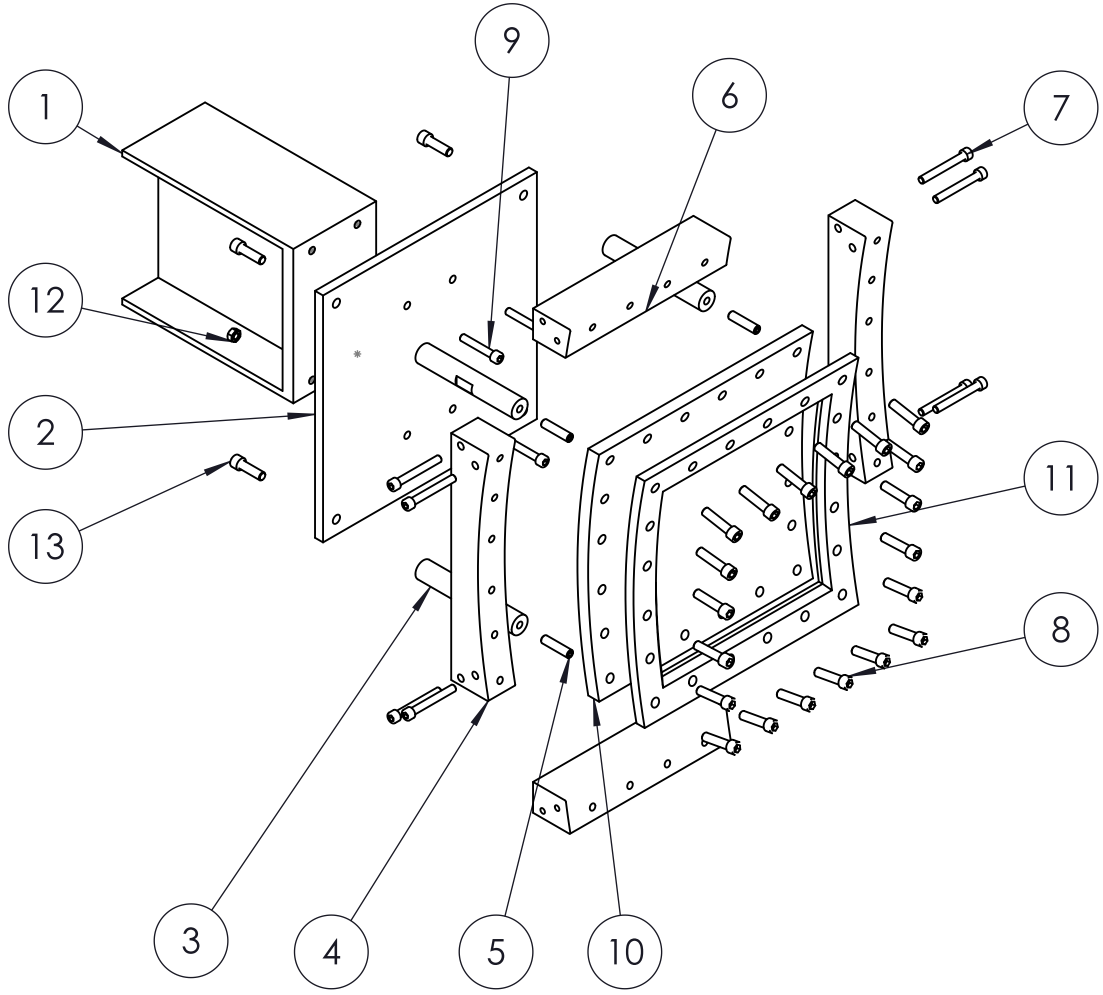

ITEM NO.	PART NUMBER	Material	QTY.
13	ISO 4762 M12 x 40 --- 40C	N/A	4
12	Hexagon Nut ISO - 4032 - M10 - W - N	N/A	4
11	Outer_Clamp_R1000_V2	Plain Carbon Steel	1
10	Sandwhich_R1000	Composite	1
9	ISO 4762 M10 x 60 --- 60C	N/A	4
8	ISO 4762 M12 x 50	N/A	20
7	M10 x 80 --- 32C	N/A	8
6	Base_Clamp_Short_Piece_R1000	Plain Carbon Steel	2
5	ISO 4026 - M12 x 50-C	N/A	4
4	Base_Clamp_Long_Piece_R1000	Plain Carbon Steel	2
3	Spacer	Plain Carbon Steel	4
2	Back_Plate	Plain Carbon Steel	1
1	Pendullum	Plain Carbon Steel	1

A4 Landscape	University of Cape Town Department of Mechanical Engineering			
⊕	Title: Exploded View of R1000 Clamp Frame			
Assembly Drawing	Scale: 1:10	Date: 30/09/2017	Sheet1	of 1
	Drawn By:	Ismail Ghoor GHRISM001 082 258 0609 BISRU Ext: 5339	Drawing Number 04/2015/02/0A	

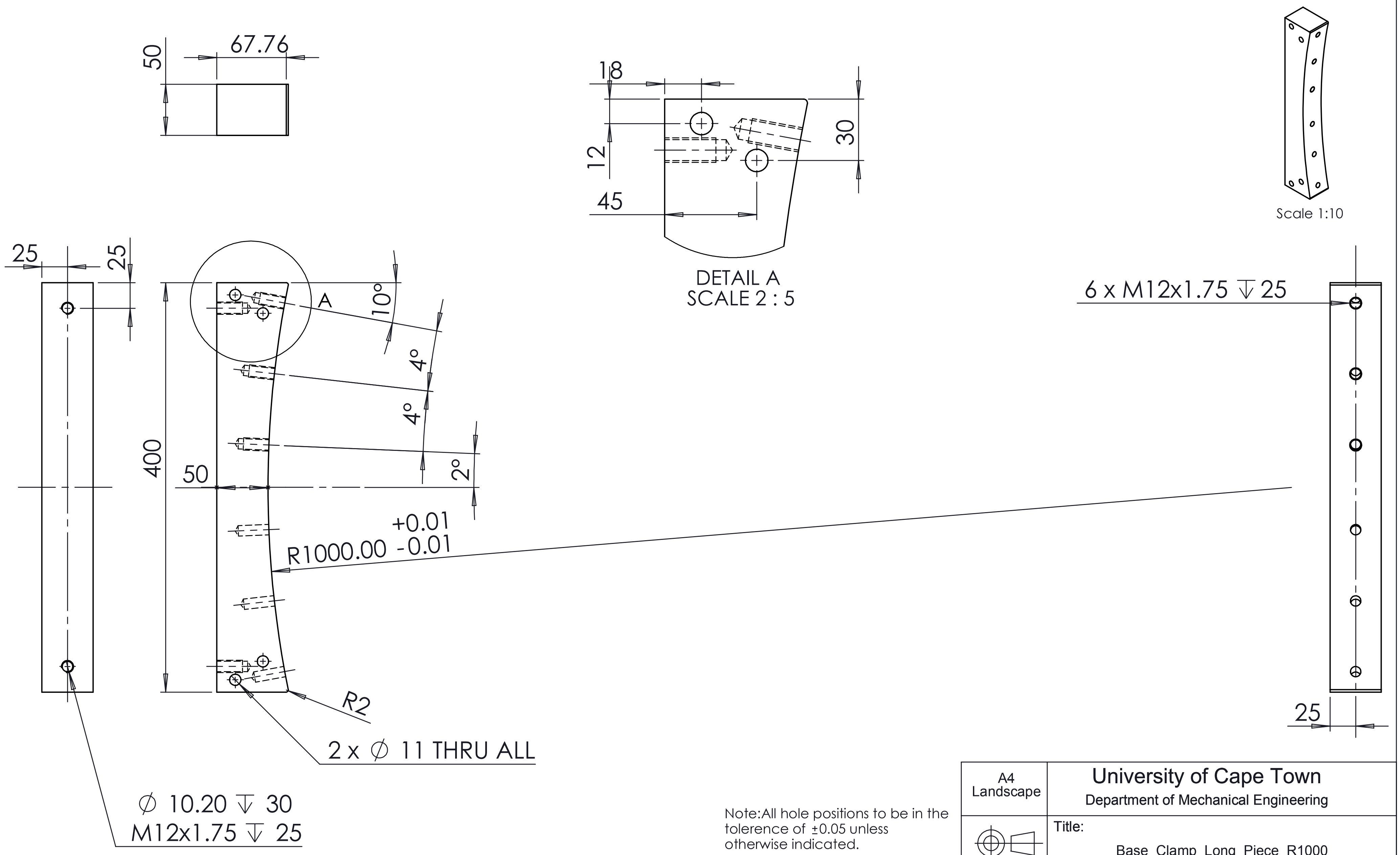

Note:All hole positions to be in the tolerence of ±0.05 unless otherwise indicated.

A4 Landscape	University of Cape Town Department of Mechanical Engineering			
⊕	Title: Base_Clamp_Long_Piece_R1000			
Part Finish	Scale: 1:5	Date: 29/04/2015	Sheet1	of 1
Material: Plain Carbon Steel	Drawn By:	Ismail Ghoor GHRISM001 082 258 0609 BISRU Ext: 5339	Drawing Number 04/2015/02/04	

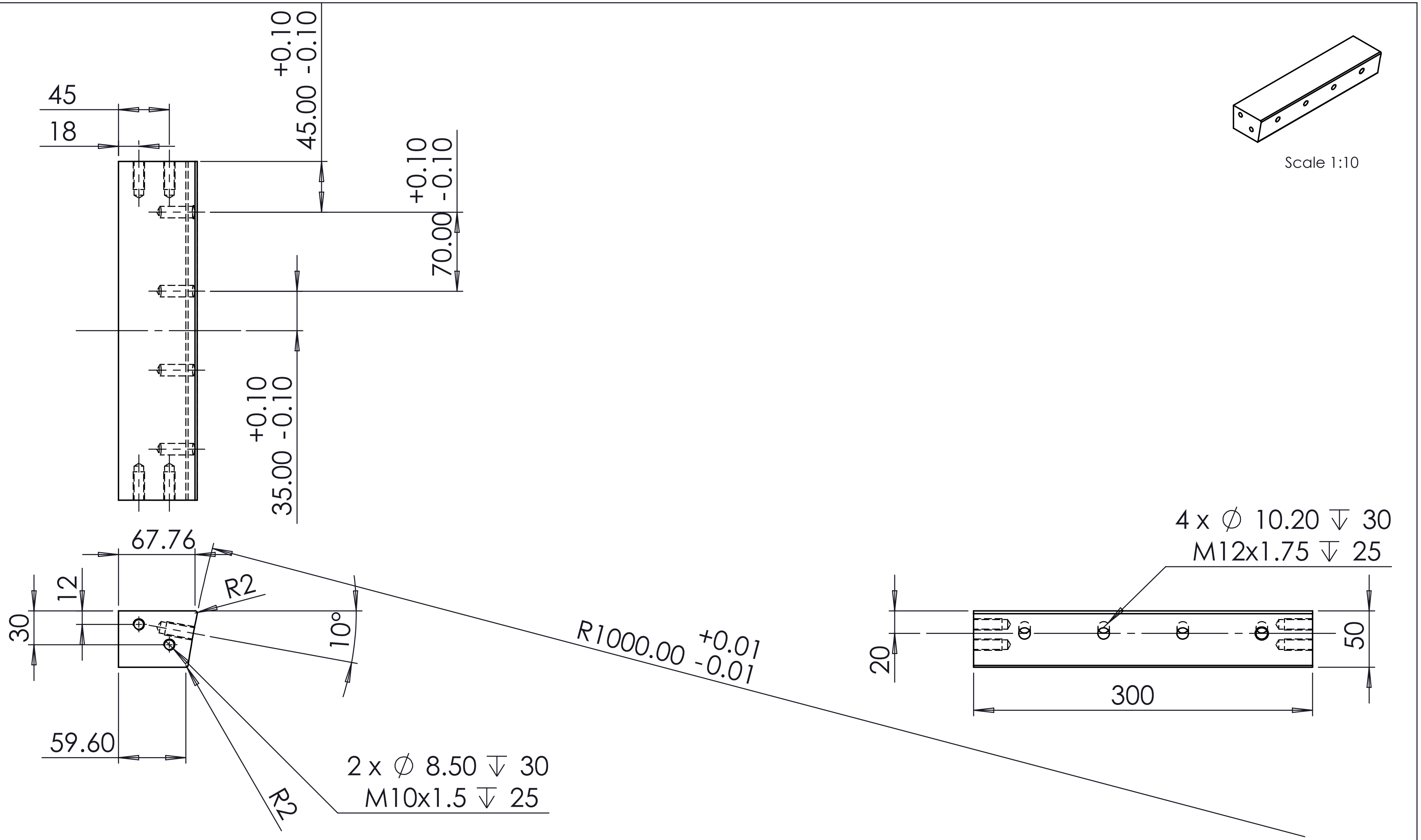

Note:All hole positions to be in the tolerence of ±0.05 unless otherwise indicated.

A4 Landscape	University of Cape Town Department of Mechanical Engineering			
	Title: Base_Clamp_Short_Piece_R1000			
Part Finish	Scale: 1:5	Date: 29/04/2015	Sheet1	of 1
Material: Plain Carbon Steel	Drawn By:	Ismail Ghoor GHRISM001 082 258 0609 BISRU Ext: 5339	Drawing Number 04/2015/02/06	

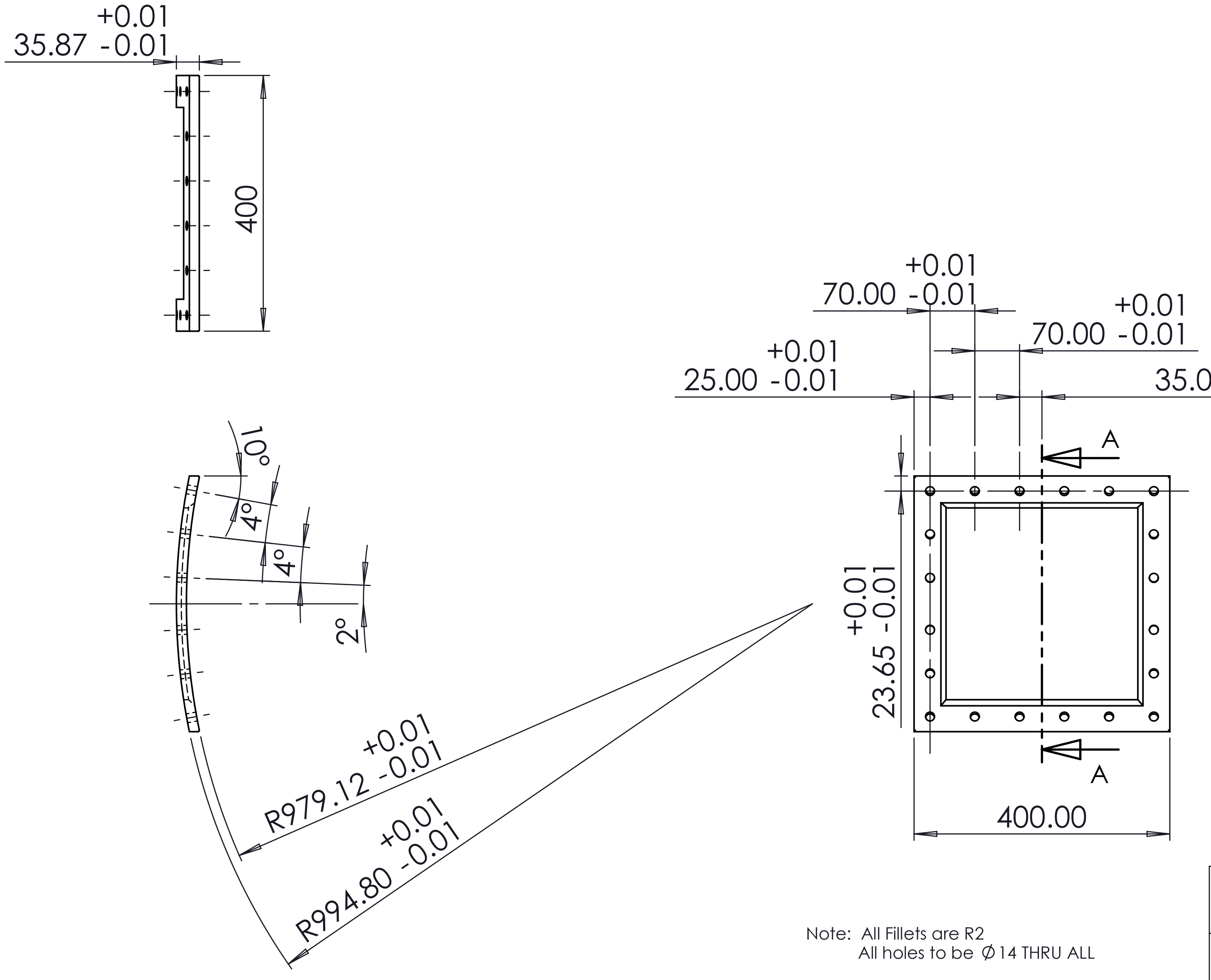

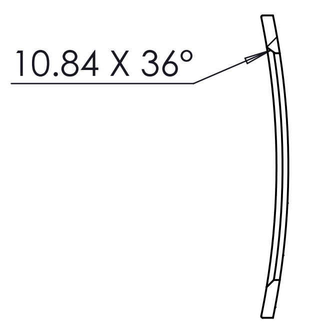

SECTION A-A

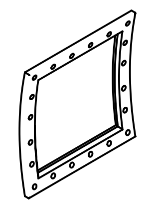

Scale 1:20

Note: All Fillets are R2
All holes to be Ø14 THRU ALL

**SolidWorks Student Edition.
For Academic Use Only.**

A4 Landscape	University of Cape Town Department of Mechanical Engineering				
	Title: Outer_Clamp_R1000_Laminate				
Part Finish	Scale: 1:10		Date: 03/08/2017	Sheet1	of 1
Material: Plain Carbon Steel		Drawn By: Ismail Ghoor GHRISM001 082 258 0609 BISRU Ext: 5339		Drawing Number 04/2015/02/11	

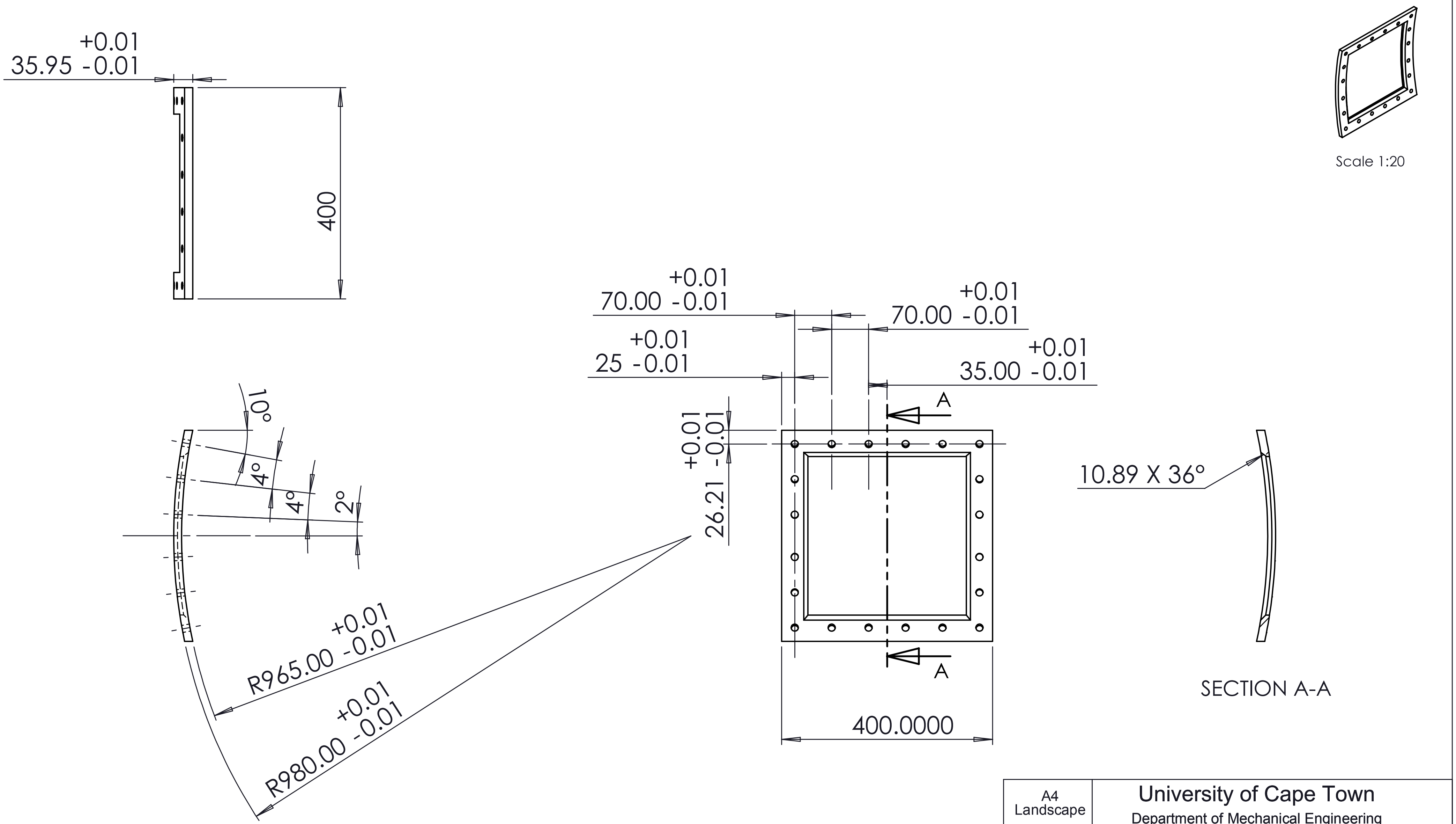

Note: All Fillets are R2
All holes to be ⌀14 THRU ALL

SolidWorks Student Edition.
For Academic Use Only.

A4 Landscape	University of Cape Town Department of Mechanical Engineering			
	Title: Outer_Clamp_R1000_V2			
Part Finish	Scale: 1:10	Date: 29/04/2015	Sheet1	of 1
Material: Plain Carbon Steel	Drawn By:	Ismail Ghoor GHRISM001 082 258 0609 BISRU Ext: 5339	Drawing Number 04/2015/02/10	

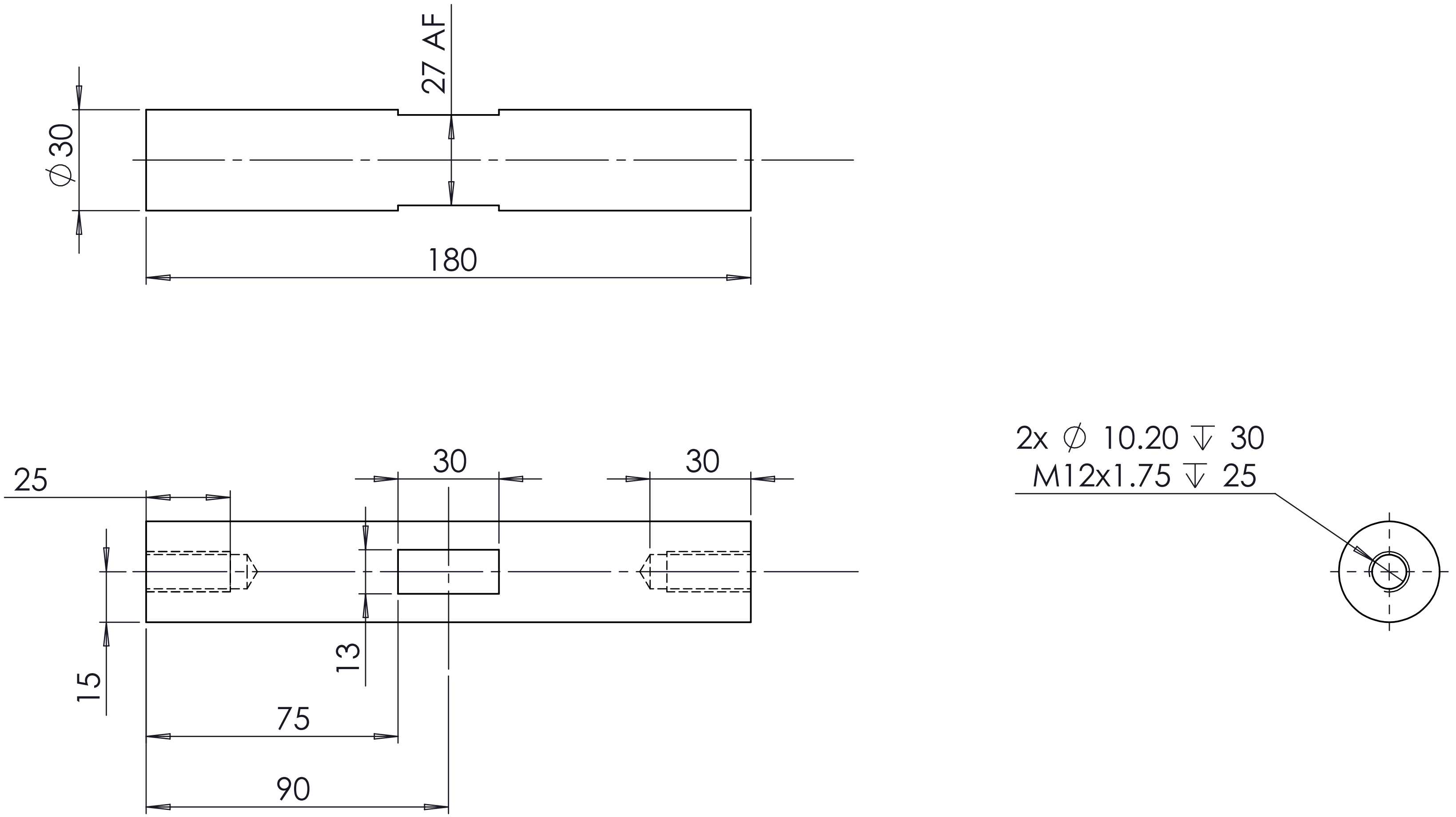

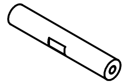
Scale 1:10

Note: Quantity = 8

A4 Landscape	University of Cape Town Department of Mechanical Engineering			
⊕◁	Title: Spacer			
Part Finish	Scale: 1:2	Date: 13/05/2015	Sheet1	of 1
Material: Plain Carbon Steel	Drawn By:	Ismail Ghoor GHRISM001 082 258 0609 BISRU Ext: 5339	Drawing Number 03/2015/01/03	

Appendix C

Image Processing Validation

Method used to analyse

In order to determine the delaminated areas on the panels, the software “Analyzing Digital Images” (ADI) was used. The software incorporates useful digital image processing tools that can mask certain pixels based on their colour code. The method employed was to colour the areas red and use the filter to mask the area of interest. The program calculates the masked area and returns the area in a specified unit that the user has used scale the image. A full process description through is shown in the next section and the validation method is detailed.

Validation

In order to validate the area calculation via the tool, known areas were assessed and analysed as to how much area there was compared to the original. Red blocks of known pixel sizes were drawn in Photoshop CC 2017 and imported into the ADI and scaled according to the plate size. In this case the 400 mm horizontal length of the plate. This process is shown in Figure C.1. Next the image needs to be masked. This is accomplished by moving the Red colour slider to 99%. This masks the red area in the image, as shown in Figure C.2. A block was drawn around the whole image to calculate the masked area, as shown in Figure C.3. Results from this calibration test are show in Table C.1 where the actual known, masked area is compared to what was recognised by ADI masking software. These difference between the actual and the masked area from all calibration tests were under 1%. The screenshots of the spatial analysis are shown in Figures C.4, C.5, C.6 and C.7.

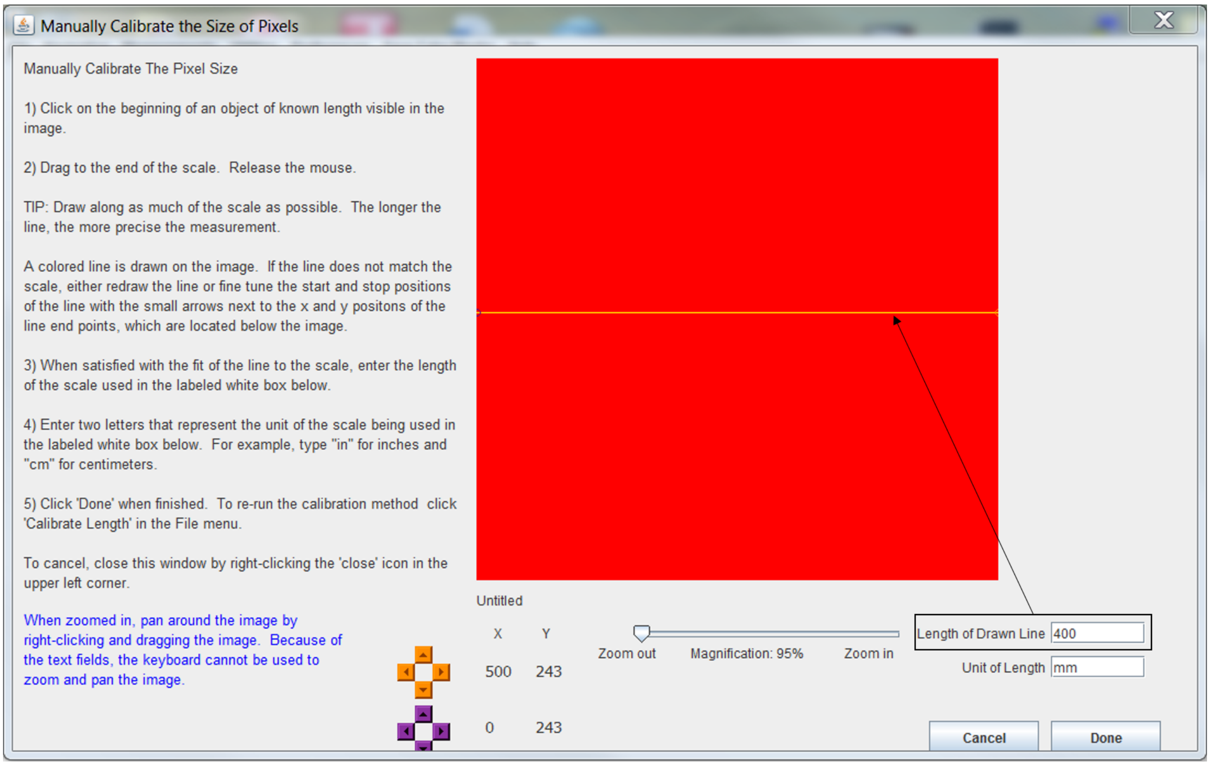

Manually Calibrate The Pixel Size

1) Click on the beginning of an object of known length visible in the image.

2) Drag to the end of the scale. Release the mouse.

TIP: Draw along as much of the scale as possible. The longer the line, the more precise the measurement.

A colored line is drawn on the image. If the line does not match the scale, either redraw the line or fine tune the start and stop positions of the line with the small arrows next to the x and y positons of the line end points, which are located below the image.

3) When satisfied with the fit of the line to the scale, enter the length of the scale used in the labeled white box below.

4) Enter two letters that represent the unit of the scale being used in the labeled white box below. For example, type "in" for inches and "cm" for centimeters.

5) Click 'Done' when finished. To re-run the calibration method click 'Calibrate Length' in the File menu.

To cancel, close this window by right-clicking the 'close' icon in the upper left corner.

When zoomed in, pan around the image by right-clicking and dragging the image. Because of the text fields, the keyboard cannot be used to zoom and pan the image.

X	Y
500	243
0	243

Magnification: 95%

Length of Drawn Line 400

Unit of Length mm

Figure C.1: Screenshot of the ADI scaling step

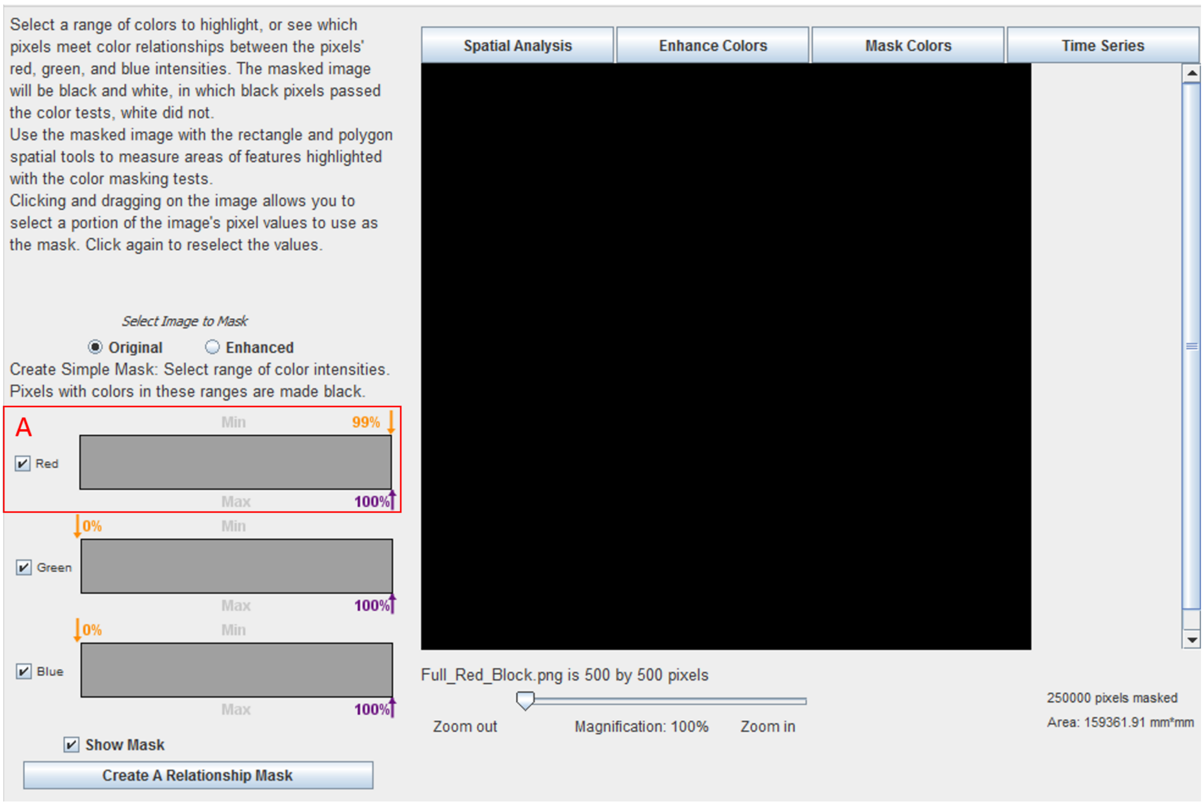

Select a range of colors to highlight, or see which pixels meet color relationships between the pixels' red, green, and blue intensities. The masked image will be black and white, in which black pixels passed the color tests, white did not.
Use the masked image with the rectangle and polygon spatial tools to measure areas of features highlighted with the color masking tests.
Clicking and dragging on the image allows you to select a portion of the image's pixel values to use as the mask. Click again to reselect the values.

Select Image to Mask

● Original ○ Enhanced

Create Simple Mask: Select range of color intensities.
Pixels with colors in these ranges are made black.

☑ Red: Min 99%, Max 100%
☑ Green: Min 0%, Max 100%
☑ Blue: Min 0%, Max 100%

☑ Show Mask

Full_Red_Block.png is 500 by 500 pixels

Magnification: 100%

250000 pixels masked
Area: 159361.91 mm*mm

Figure C.2: Screenshot of the ADI masking step

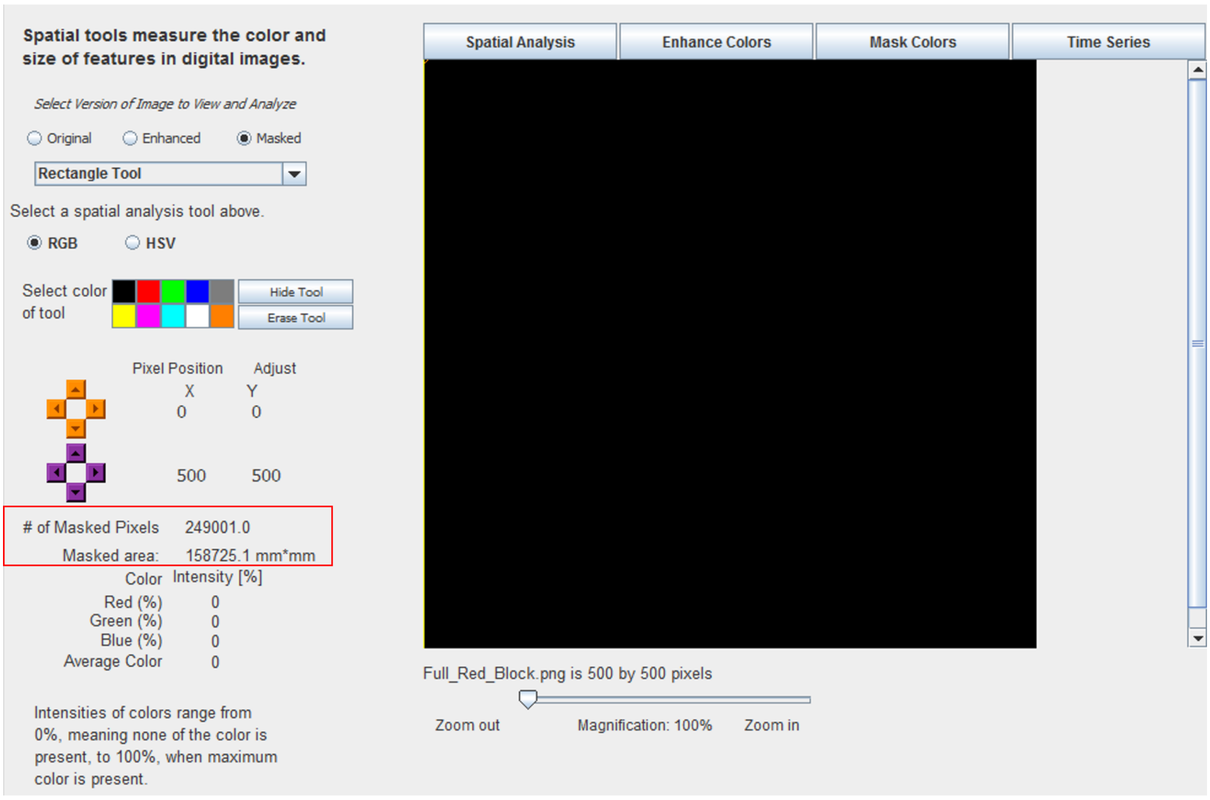

Spatial tools measure the color and size of features in digital images.

Select Version of Image to View and Analyze

○ Original ○ Enhanced ● Masked

Rectangle Tool

Select a spatial analysis tool above.

● RGB ○ HSV

Select color of tool

	Pixel Position X	Adjust Y
	0	0
	500	500

# of Masked Pixels 249001.0

Masked area: 158725.1 mm*mm

Color	Intensity [%]
Red (%)	0
Green (%)	0
Blue (%)	0
Average Color	0

Intensities of colors range from 0%, meaning none of the color is present, to 100%, when maximum color is present.

Full_Red_Block.png is 500 by 500 pixels

Magnification: 100%

Figure C.3: Screenshot of the ADI spatial analysis step

Table C.1: Comparing masked area with ADI analysis of masked area

	Masked Area		
Name of Test Area	Actual	ADI Analysis	Difference
Full Square	100.00%	99.20%	0.80%
Half	50.00%	49.78%	0.22%
Quarter	25.00%	24.98%	0.02%
Eighth	25.00%	24.90%	0.10%
Small ones	5.56%	5.73%	0.17%

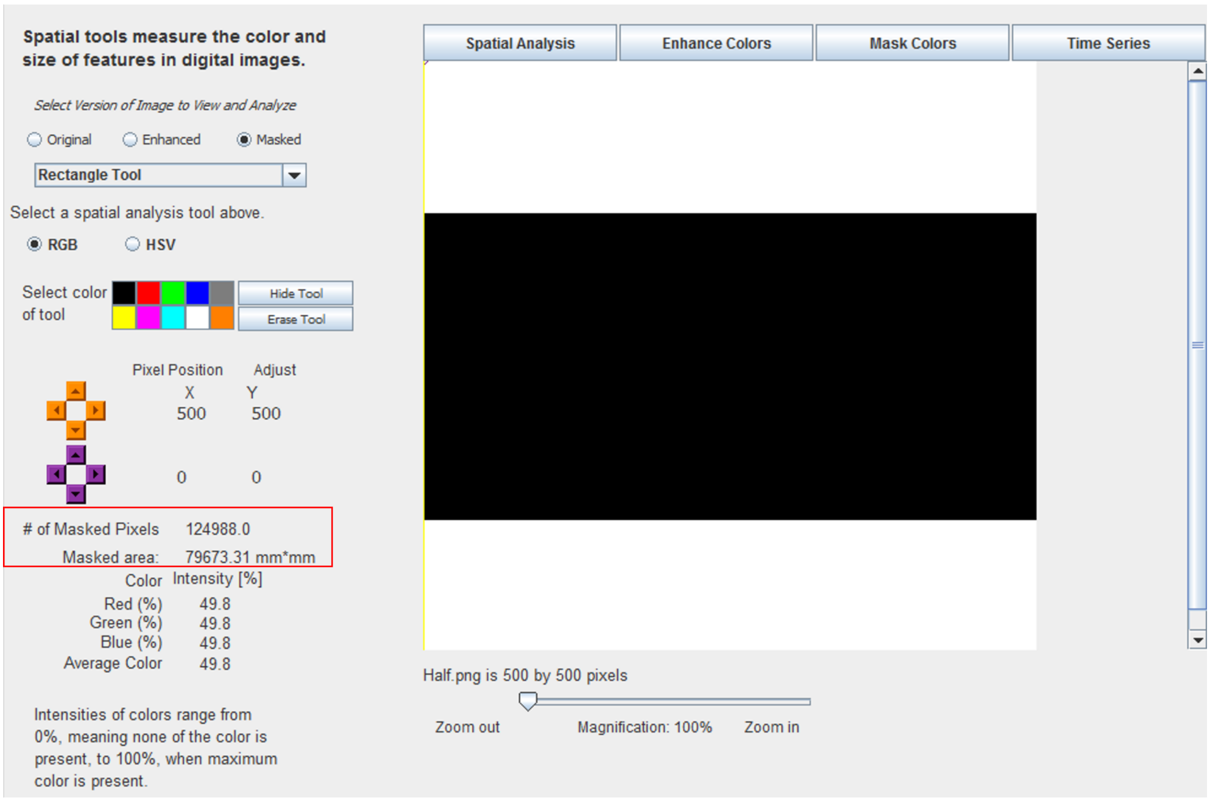

Spatial tools measure the color and size of features in digital images.

Select Version of Image to View and Analyze

○ Original ○ Enhanced ● Masked

Select a spatial analysis tool above.

● RGB ○ HSV

Select color of tool

Pixel Position Adjust
X 500 Y 500
0 0

# of Masked Pixels 124988.0
Masked area: 79673.31 mm*mm

Color	Intensity [%]
Red (%)	49.8
Green (%)	49.8
Blue (%)	49.8
Average Color	49.8

Intensities of colors range from 0%, meaning none of the color is present, to 100%, when maximum color is present.

Half.png is 500 by 500 pixels

Magnification: 100%

Figure C.4: Half block masking test

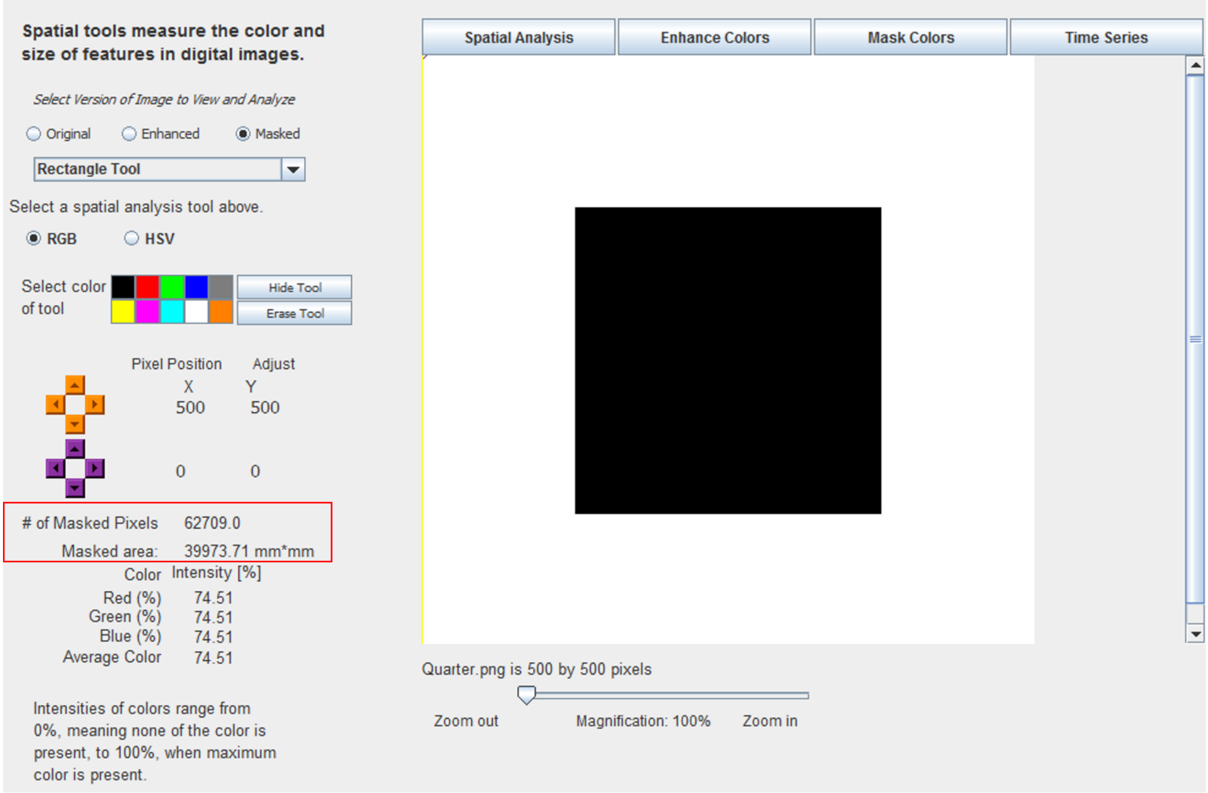

Spatial tools measure the color and size of features in digital images.

Select Version of Image to View and Analyze

○ Original ○ Enhanced ● Masked

Select a spatial analysis tool above.

● RGB ○ HSV

Select color of tool

Pixel Position Adjust
X 500 Y 500
0 0

# of Masked Pixels 62709.0
Masked area: 39973.71 mm*mm

Color	Intensity [%]
Red (%)	74.51
Green (%)	74.51
Blue (%)	74.51
Average Color	74.51

Intensities of colors range from 0%, meaning none of the color is present, to 100%, when maximum color is present.

Quarter.png is 500 by 500 pixels

Magnification: 100%

Figure C.5: Quarter block masking test

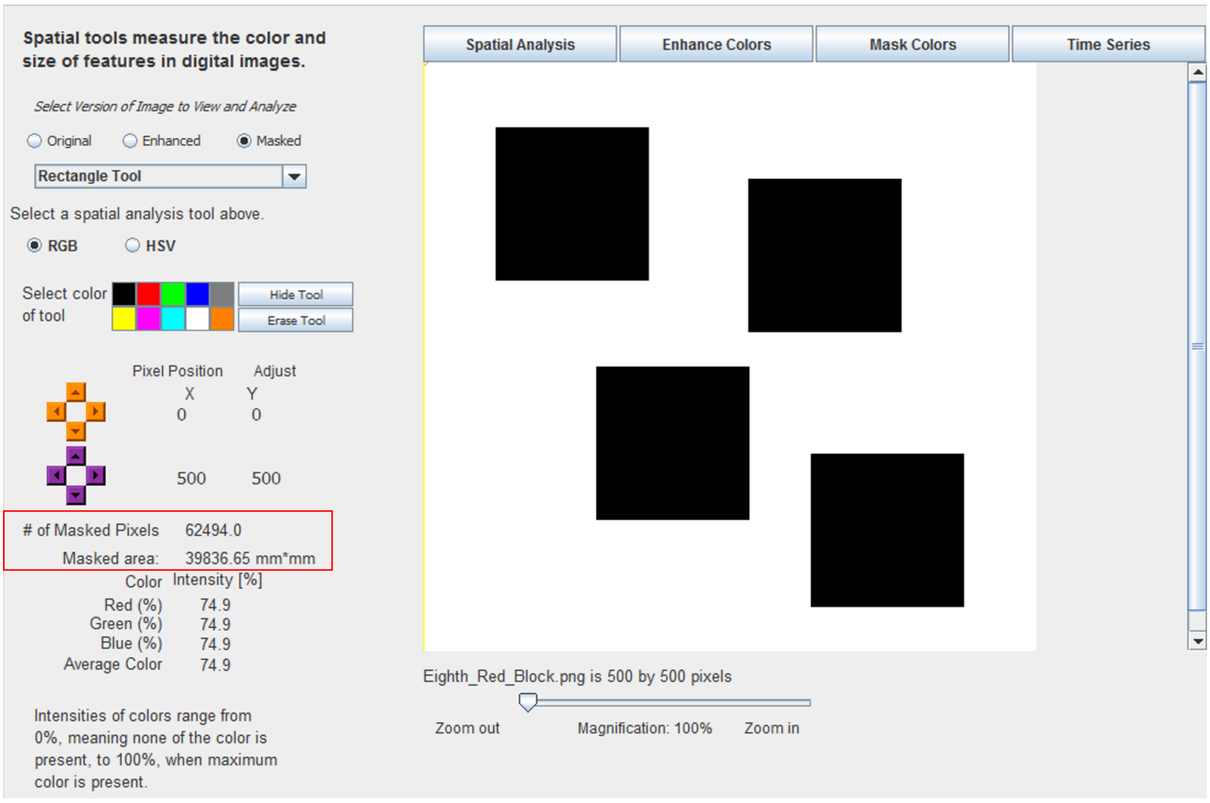

Spatial tools measure the color and size of features in digital images.

Select Version of Image to View and Analyze

○ Original ○ Enhanced ● Masked

Rectangle Tool

Select a spatial analysis tool above.

● RGB ○ HSV

Select color of tool

	Pixel Position	Adjust
	X	Y
	0	0
	500	500

# of Masked Pixels 62494.0
Masked area: 39836.65 mm*mm

Color	Intensity [%]
Red (%)	74.9
Green (%)	74.9
Blue (%)	74.9
Average Color	74.9

Intensities of colors range from 0%, meaning none of the color is present, to 100%, when maximum color is present.

Eighth_Red_Block.png is 500 by 500 pixels

Zoom out Magnification: 100% Zoom in

Figure C.6: Eighth block masking test

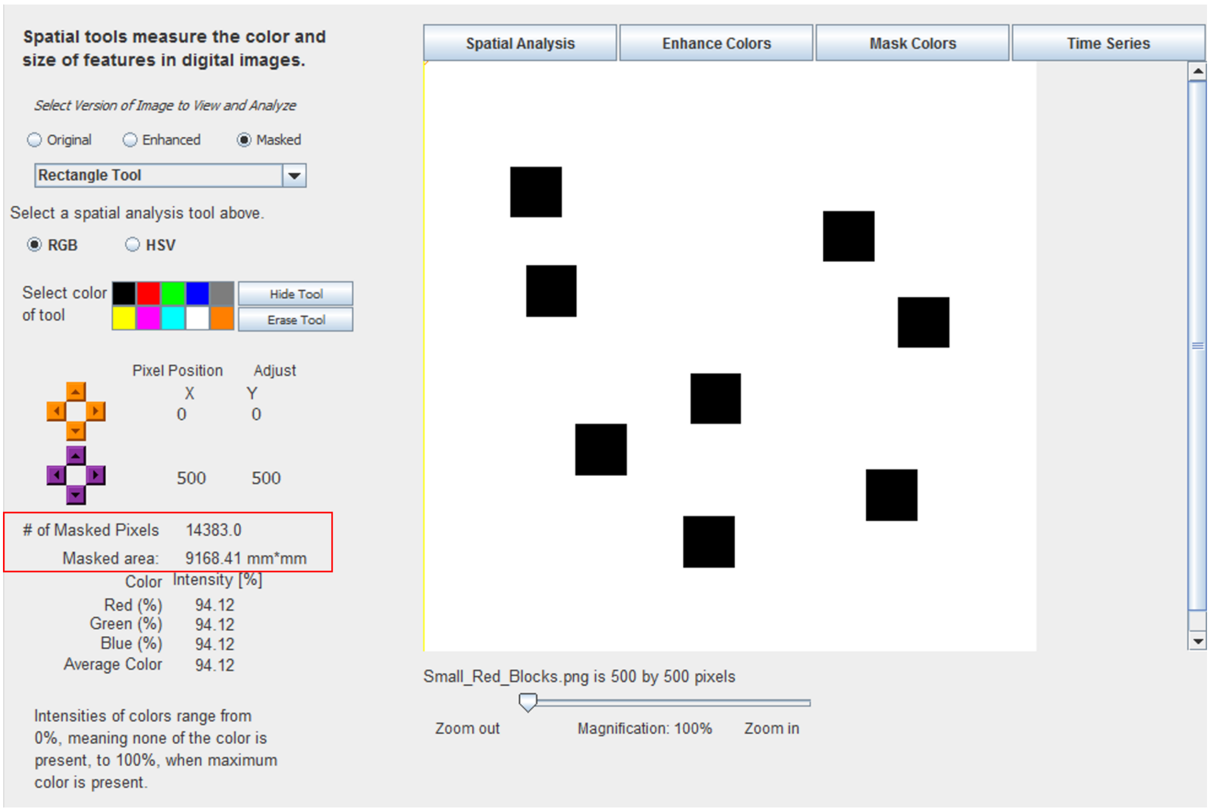

Spatial tools measure the color and size of features in digital images.

Select Version of Image to View and Analyze

○ Original ○ Enhanced ● Masked

Rectangle Tool

Select a spatial analysis tool above.

● RGB ○ HSV

Select color of tool

	Pixel Position	Adjust
	X	Y
	0	0
	500	500

# of Masked Pixels 14383.0
Masked area: 9168.41 mm*mm

Color	Intensity [%]
Red (%)	94.12
Green (%)	94.12
Blue (%)	94.12
Average Color	94.12

Intensities of colors range from 0%, meaning none of the color is present, to 100%, when maximum color is present.

Small_Red_Blocks.png is 500 by 500 pixels

Zoom out Magnification: 100% Zoom in

Figure C.7: Random small block masking test

Appendix D

Thermoforming Procedure and Arrangement

Detailed Procedure

Table D.1: Thermoforming lay up and procedure

Step	Procedure
1	Clean mould with acetone
2	Wax mould with 3 layers of wax
3	Cut the individuals cores for each panel size
4	Chamfer the core edges
5	Cut required material as lay up drawing
6	Mark of area with a marker on the mould
7	Place 2 cores longitudinally
8	Attach thermocouple to top and bottom side of one core
9	Place heating blanket on top of cores
10	Place felt on top of the heating blanket
11	Mark out border with tacky tape
12	Cut pleats and start the vacuum bagging the assembly
13	Once you approach the end front end attached the conical port to vacuum bag
14	Seal bag completely
15	Adjust voltage dial of the heating blanket until the top side temperature reaches 85 °C
16	Maintain the temperature at 85 °C
17	Carefully monitor the through bottom side temperature to 60 degrees
18	The core should start to bend at this point
19	Turn vacuum pump on and maintain top side temperature between 90 °C
20	Continue to maintain temperature for 30 minutes
21	After 30 minutes switch off heating blanket
22	Allow core to cool to ambient temperature
23	Turn vacuum pump off
24	The core will spring back a little

Arrangements For Thermoforming

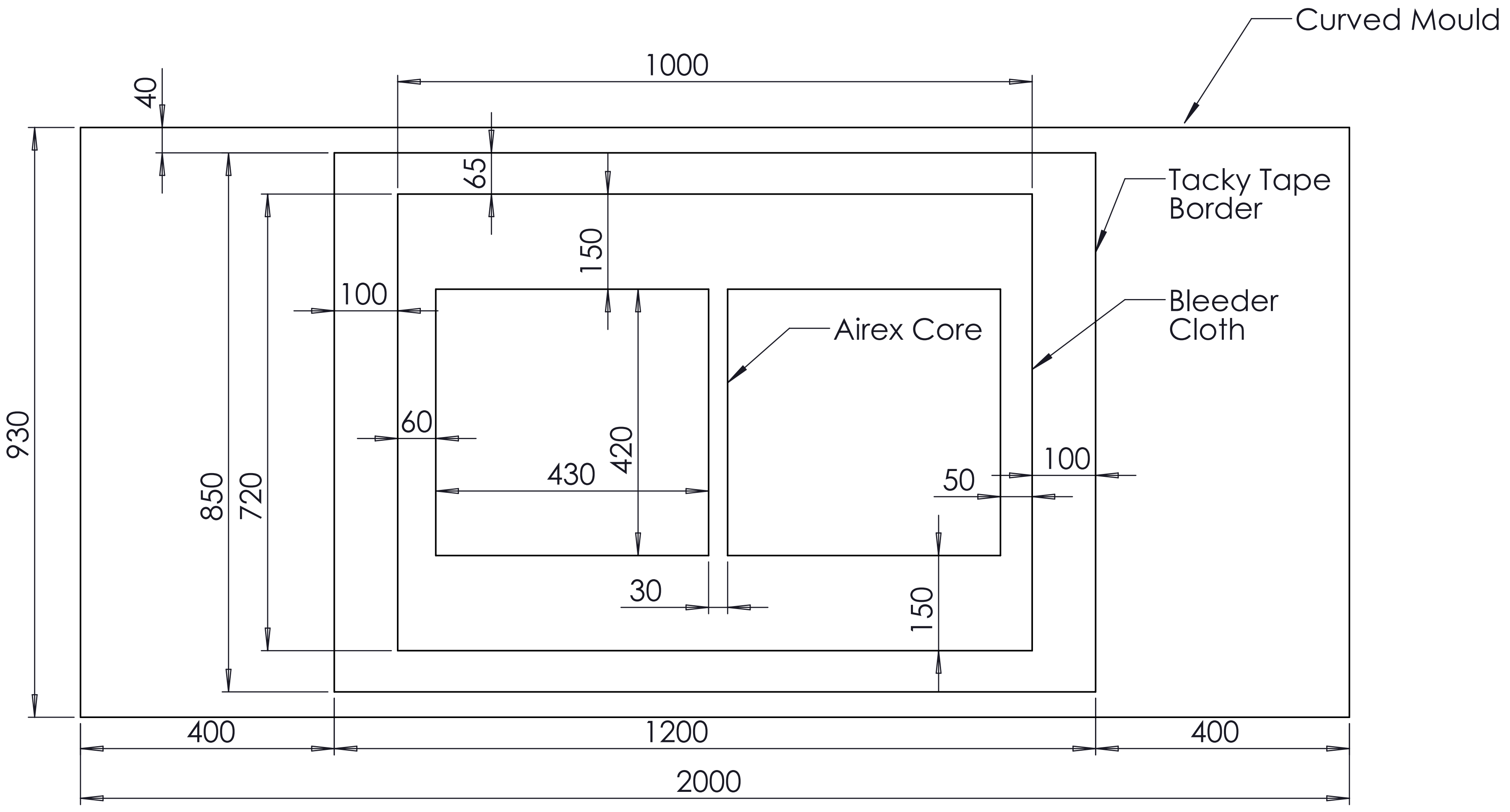

A4 Landscape	University of Cape Town Department of Mechanical Engineering			
	Title: Thermoforming_layup_R500			
Part Finish	Scale: 1:10	Date: 08/09/2017	Sheet1	of 1
Material:	Drawn By: Ismail Ghoor GHRISM001 082 258 0609 BISRU Ext: 5339		Drawing Number TFR500/2015/01	

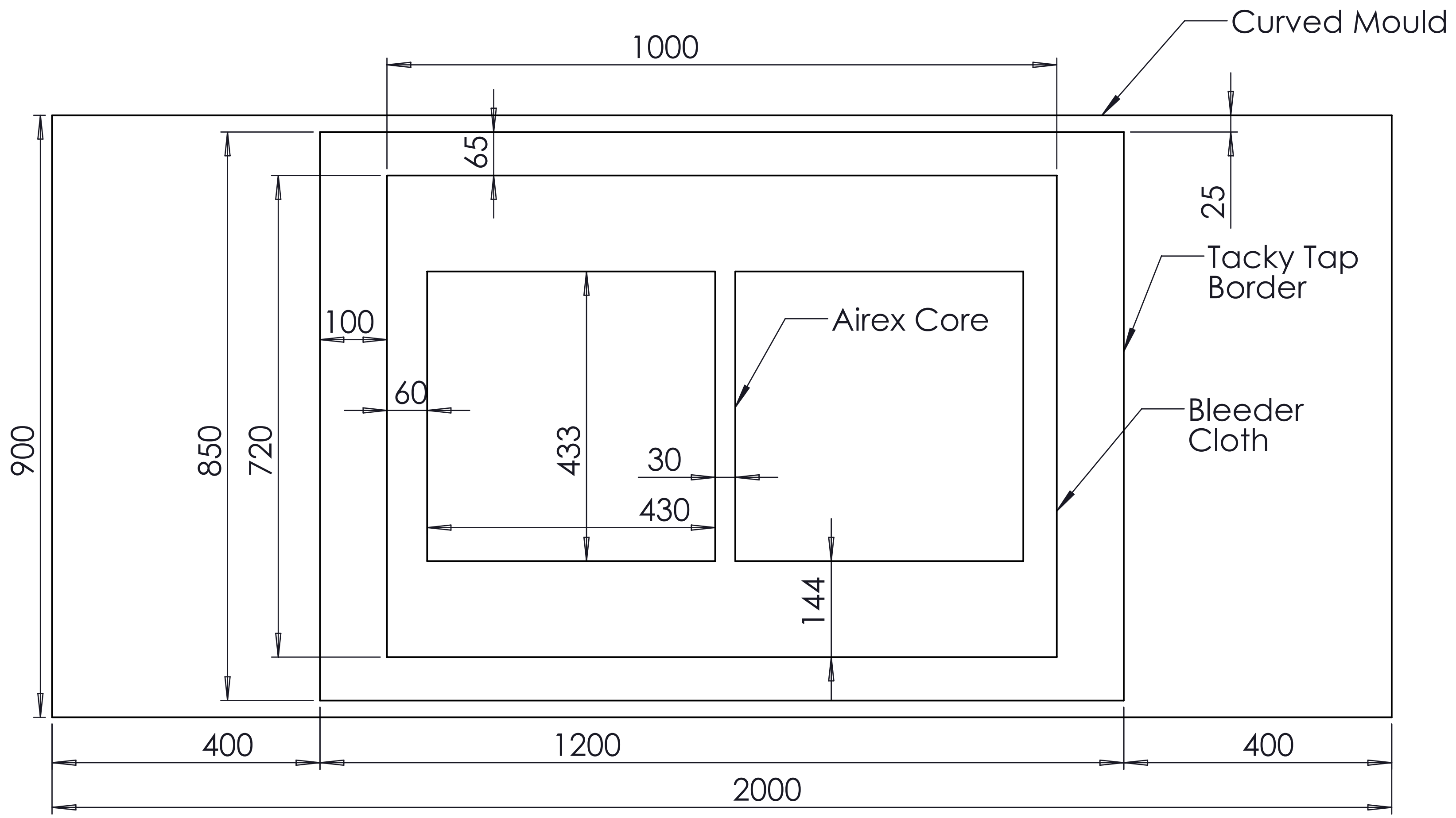

A4 Landscape	University of Cape Town Department of Mechanical Engineering			
	Title: Thermoforming_layup_R1000			
Part Finish	Scale: 1:10	Date: 08/09/2017	Sheet1	of 1
Material:	Drawn By: Ismail Ghoor GHRISM001 082 258 0609 BISRU Ext: 5339		Drawing Number TFR1000/2015/02	

Appendix E

Blast Derivation

E.0.3 Ballistic Pendulum Theory

The blast tests were performed using the blast chamber at the Blast Survivability and Impact Research Unit (BISRU). The ballistic pendulum was used to determine the impulse transferred to a target specimen as a result of a blast load. A schematic of the set up is shown in Figure E.1. It consists of an I-beam suspended in air by four spring steel cables, test rig and counter balancing masses. The impulse witnessed by the target plate was determined from the amplitude of the swing of the ballistic pendulum. The pendulum displacement was recorded by means of a laser displacement sensor (not shown in Figure E.1). The sensor measures the displacement of the laser displacement pad.

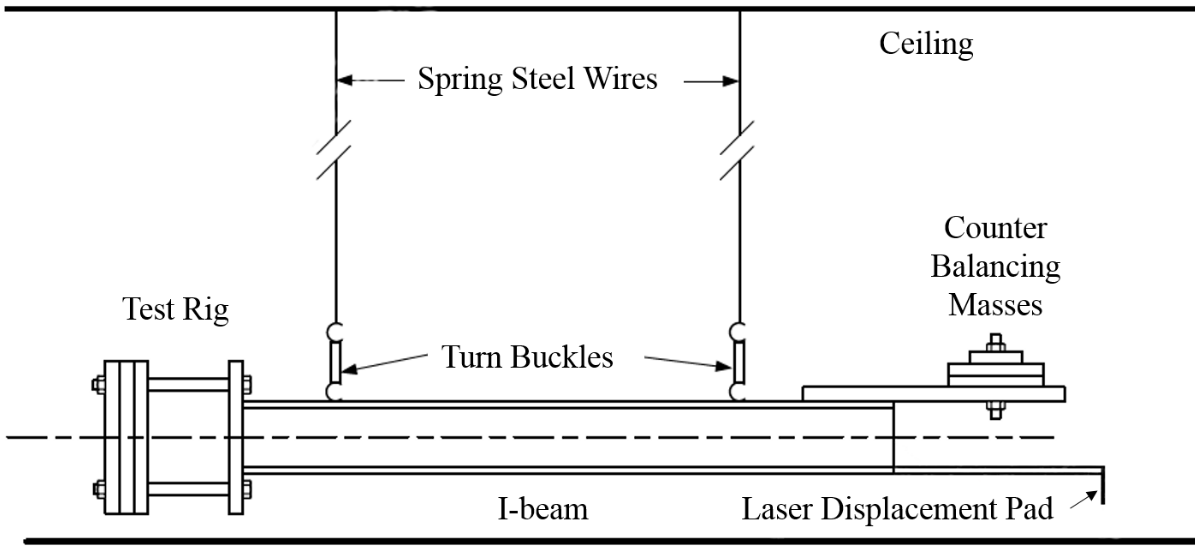

Figure E.1: Schematic of the blast pendulum adapted from [13]

In order to calculate the impulse, the ballistic pendulum was treated as a simple pendulum where the rotational inertia of the pendulum and the mass of the connecting cables were ignored. Figure E.2 illustrates a diagram of a simple pendulum. Simple pendulum theory requires that the swing amplitude, θ, (See Figure E.2) of the pendulum satisfy $sin\theta \approx \theta$ and that the pendulum undergoes only two dimensional motion. The pendulum amplitude was controlled by adjusting the total mass of the pendulum whilst the pendulum was balanced in all directions. This is done in order to maintain its orientation and keep the motion two dimensional.

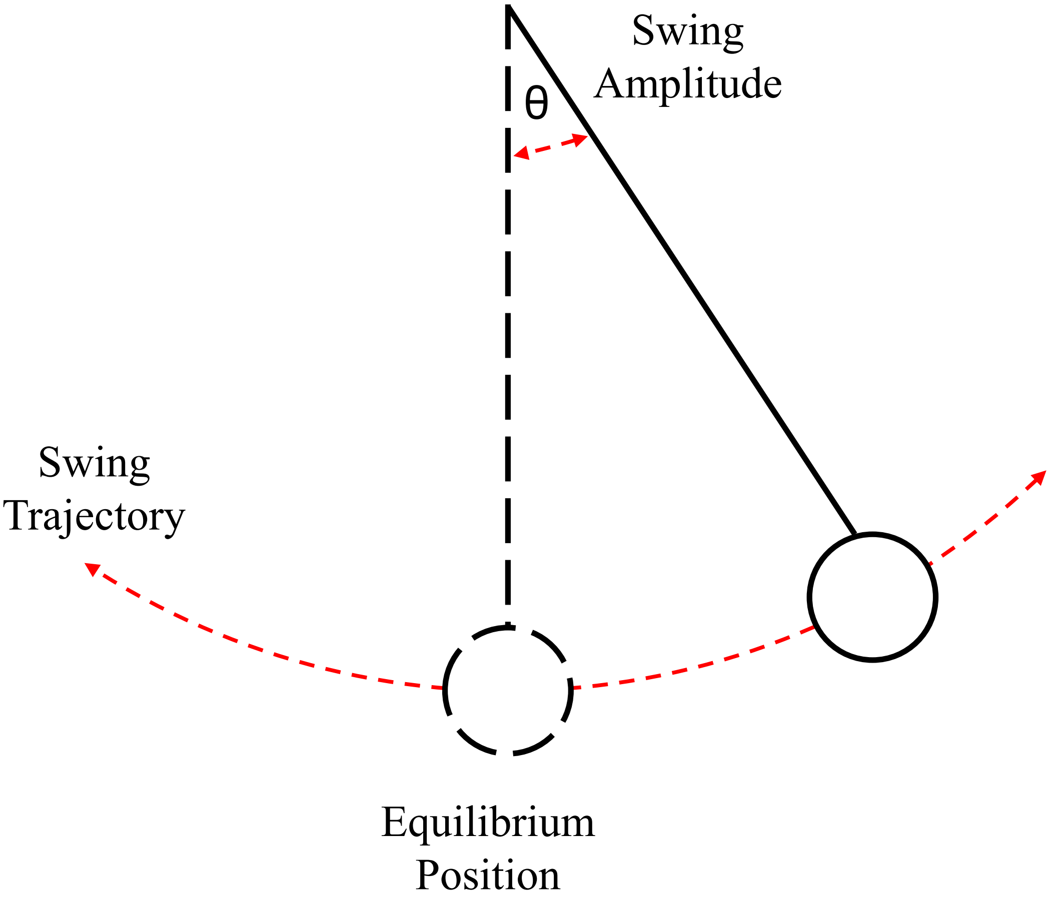

Figure E.2: Illustration of simple pendulum movement adapted from [13]

The linearised equation of motion for a simple pendulum is expressed as,

$$\ddot{x} + 2\beta\dot{x} + \omega_n^2 x = 0 \tag{E.1}$$

where $\beta = \frac{C}{2m_p}$ and $\omega_n = \frac{2\pi}{T}$ where C is the damping coefficient, m_p is the total mass of the pendulum and T is the natural period of the pendulum motion.

The solution to Equation E.1 is given by:

$$x(t) = \frac{(e^{-\beta t})\dot{x}_0 sin(\omega_d t)}{\omega_d} \tag{E.2}$$

where $\dot{x}_0$ is the intial velocity of the pendulum and ω_d is calculated using

$$\omega_d = \sqrt{\omega_n^2 - \beta^2} \tag{E.3}$$

The maximum positive displacement, x_1, of the pendulum occurs at $t = \frac{T}{4}$, and the minimum negative displacement, x_2, occurs at $t = \frac{3T}{4}$, substituting these values into Equation E.2 yields,

$$x_1 = \frac{\dot{x}_0 T}{2\pi} e^{\frac{-\beta T}{4}} \tag{E.4}$$

$$x_2 = \frac{\dot{x}_0 T}{2\pi} e^{\frac{-3\beta T}{4}} \tag{E.5}$$

β is determined by dividing x_1 by x_2 and solving for β.

$$\beta = \frac{2}{T} \ln \frac{x_1}{x_2} \tag{E.6}$$

The initial velocity, $\dot{x}$, of the pendulum is determined by re-arranging Equation E.4 to give:

$$\dot{x}_0 = \frac{2\pi}{T} x_1 e^{\frac{\beta T}{4}} \tag{E.7}$$

Now the impulse transferred can be calculated as

$$I = m_p \dot{x}_0 \tag{E.8}$$

Note that x_1 and x_2 are obtained from the laser displacement sensor.

Appendix F

Spatial Distribution of Failure

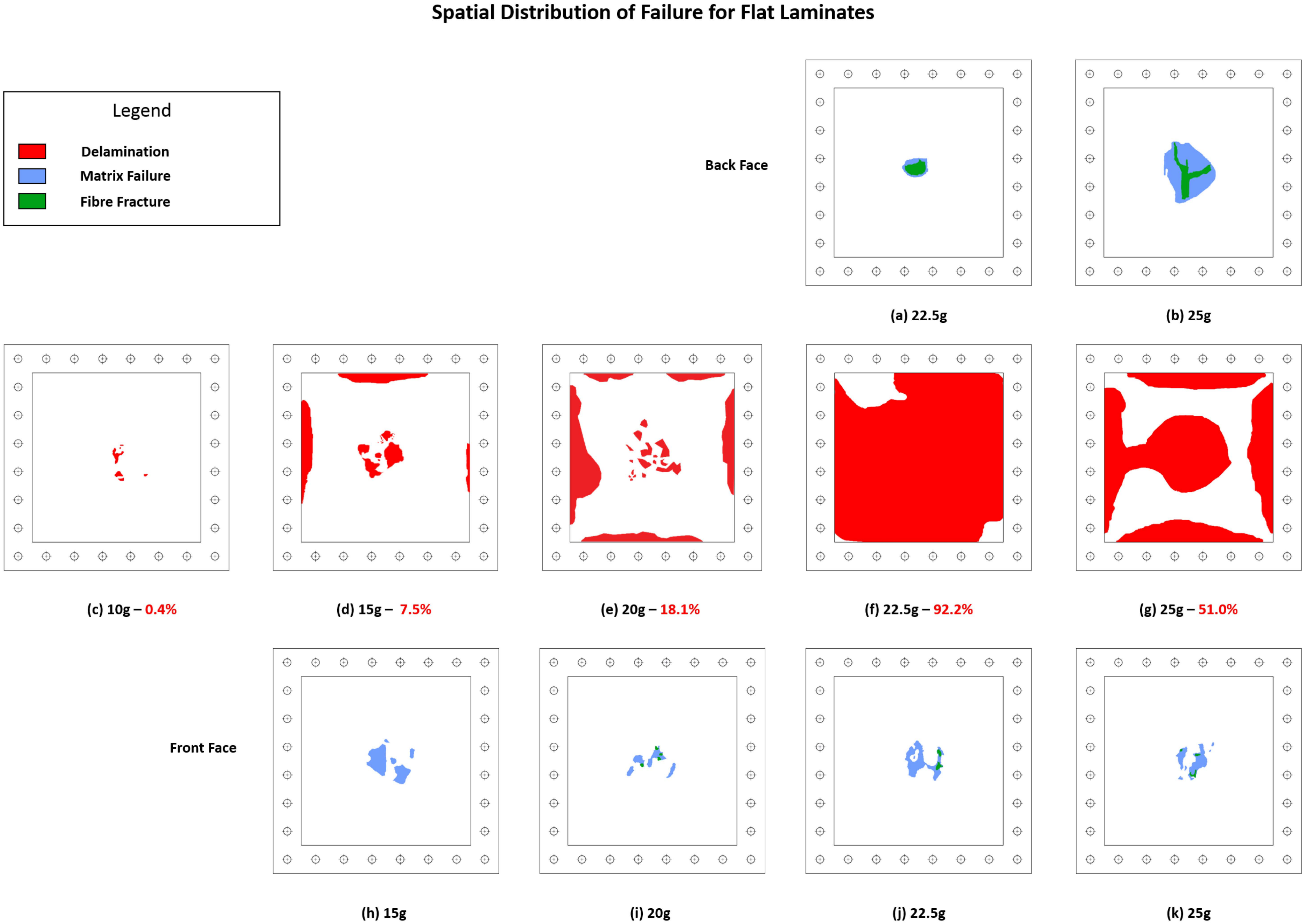

(a) 22.5g

(b) 25g

(c) 10g – 0.4%

(d) 15g – 7.5%

(e) 20g – 18.1%

(f) 22.5g – 92.2%

(g) 25g – 51.0%

(h) 15g

(i) 20g

(j) 22.5g

(k) 25g

Figure F.1: Spatial distribution of delamination(red), matrix failure (blue) and fibre fracture (green) for flat laminate panels

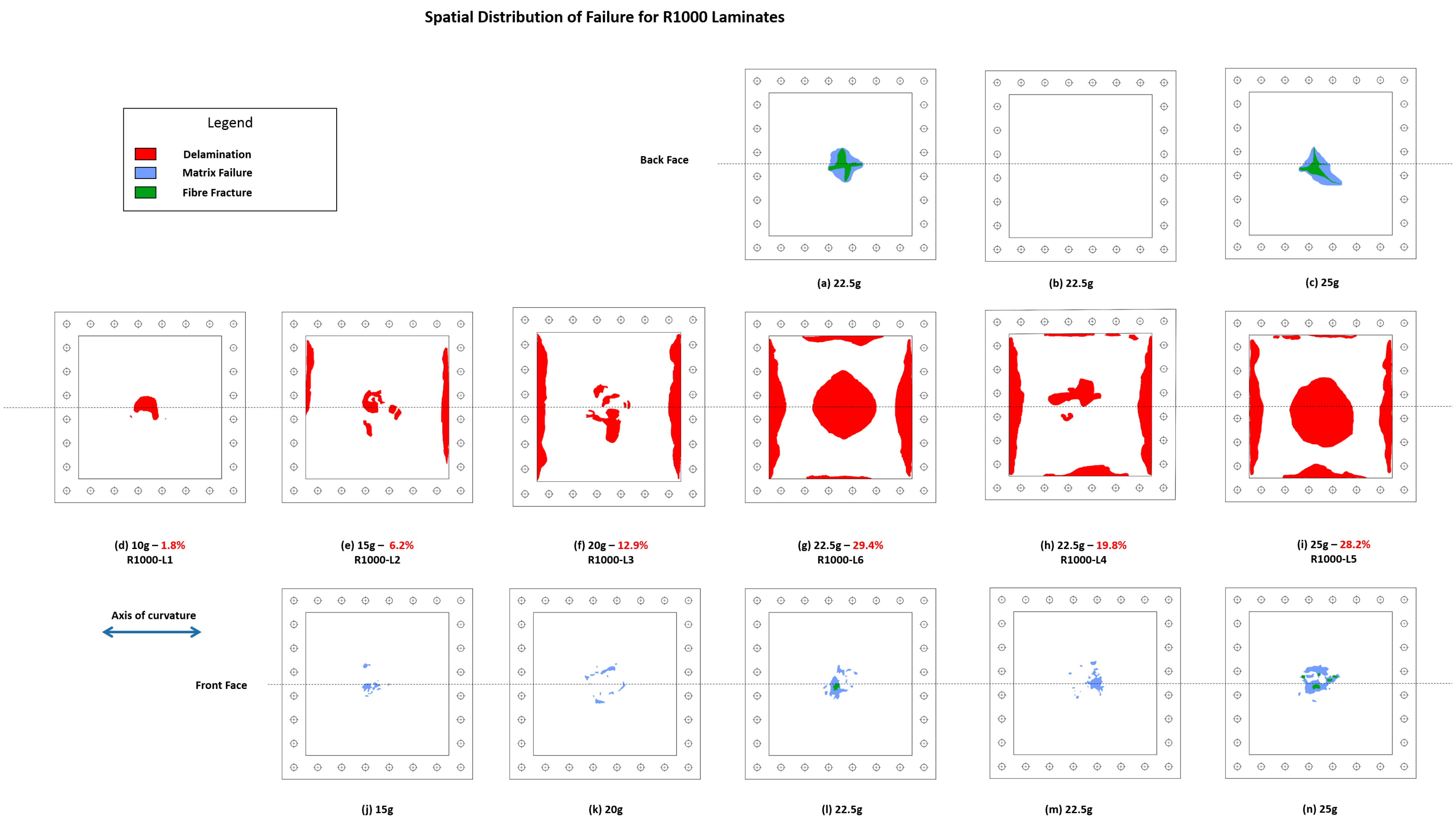

Figure F.2: Spatial distribution of delamination(red), matrix failure (blue) and fibre fracture (green) for R1000 laminate panels

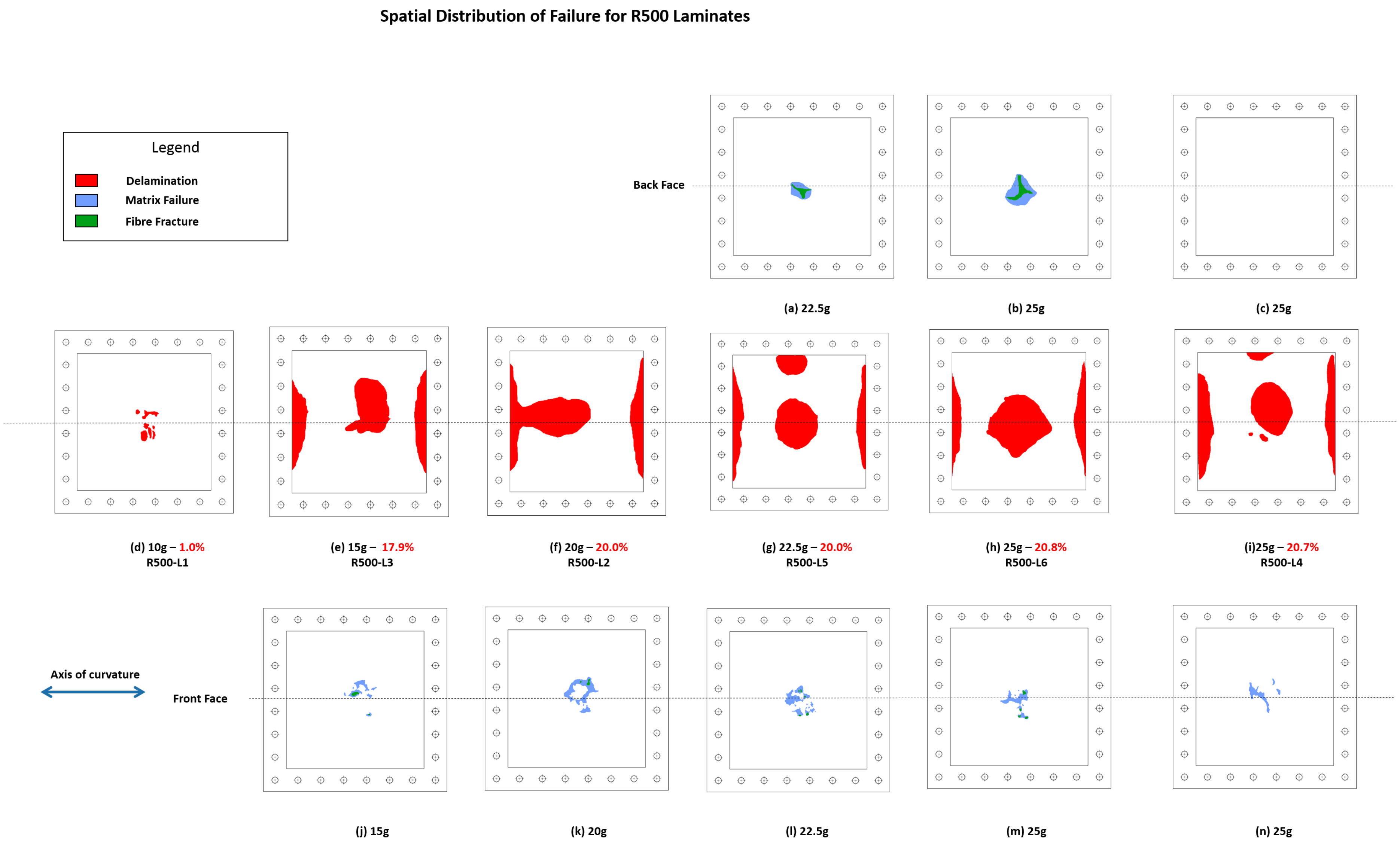

Figure F.3: Spatial distribution of delamination(red), matrix failure (blue) and fibre fracture (green) for R500 laminate panels

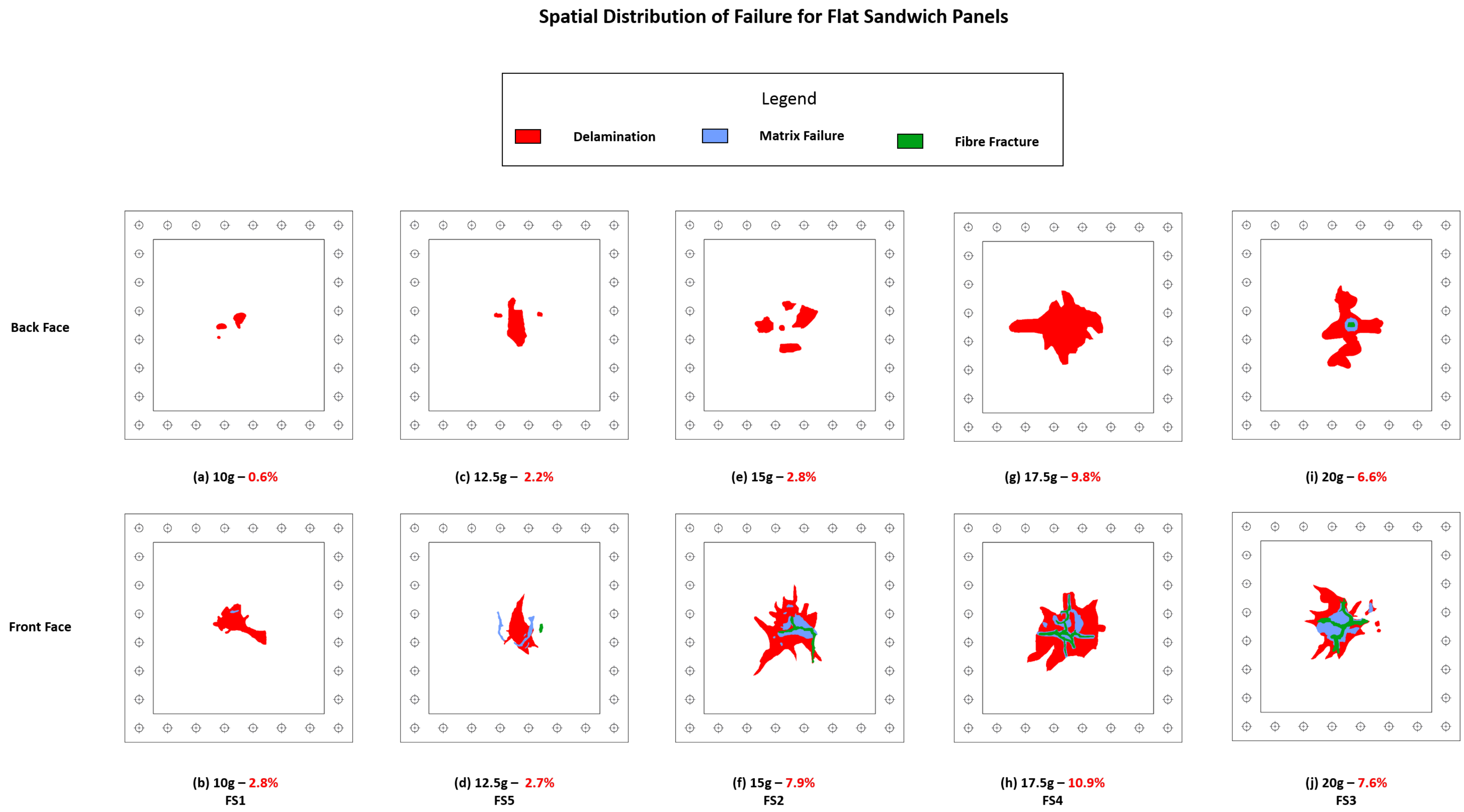

(a) 10g – 0.6%

(c) 12.5g – 2.2%

(e) 15g – 2.8%

(g) 17.5g – 9.8%

(i) 20g – 6.6%

(b) 10g – 2.8%
FS1

(d) 12.5g – 2.7%
FS5

(f) 15g – 7.9%
FS2

(h) 17.5g – 10.9%
FS4

(j) 20g – 7.6%
FS3

Figure F.4: Spatial distribution of delamination(red), matrix failure (blue) and fibre fracture (green) for flat sandwich panels

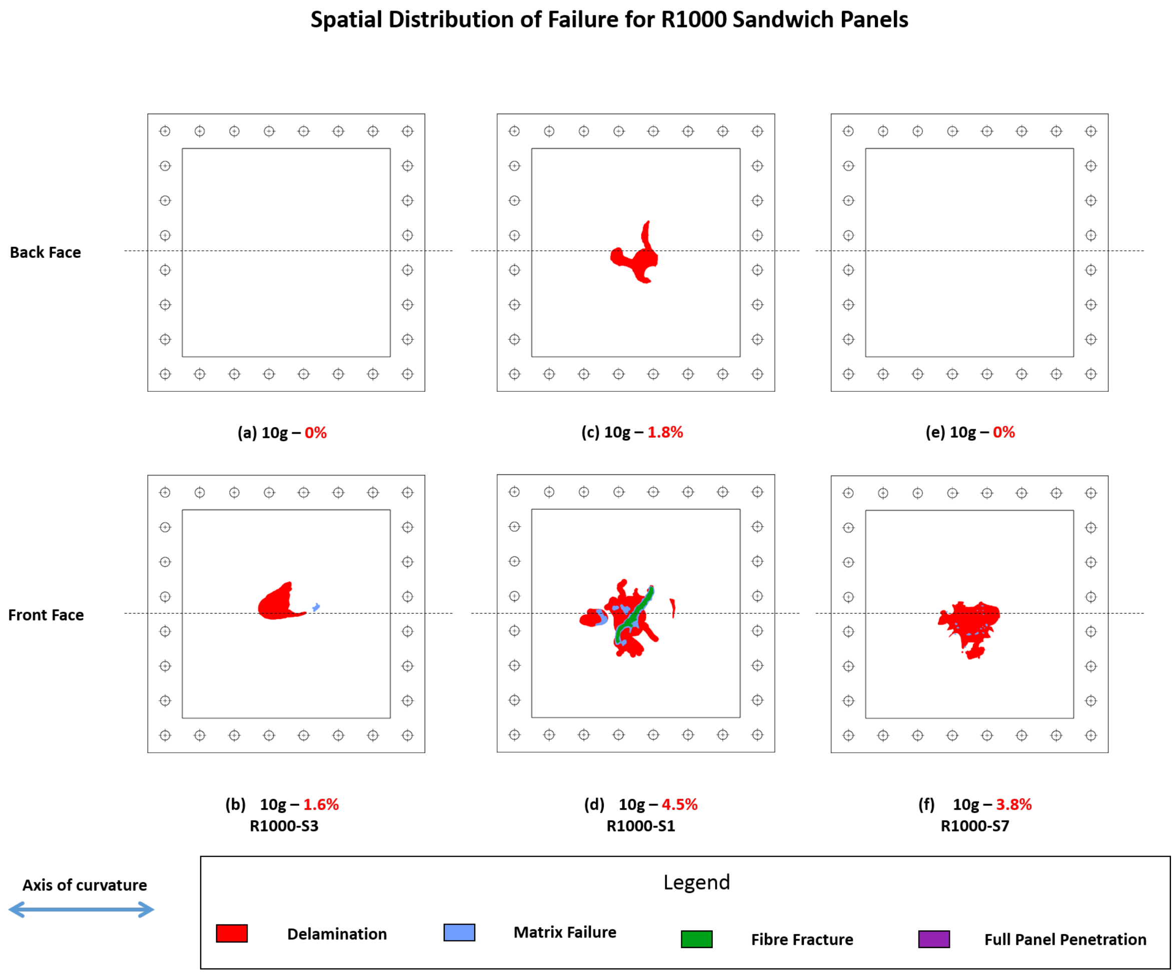

Figure F.5: Spatial distribution of delamination(red), matrix failure (blue) and fibre fracture (green) for selected R1000 sandwich panels

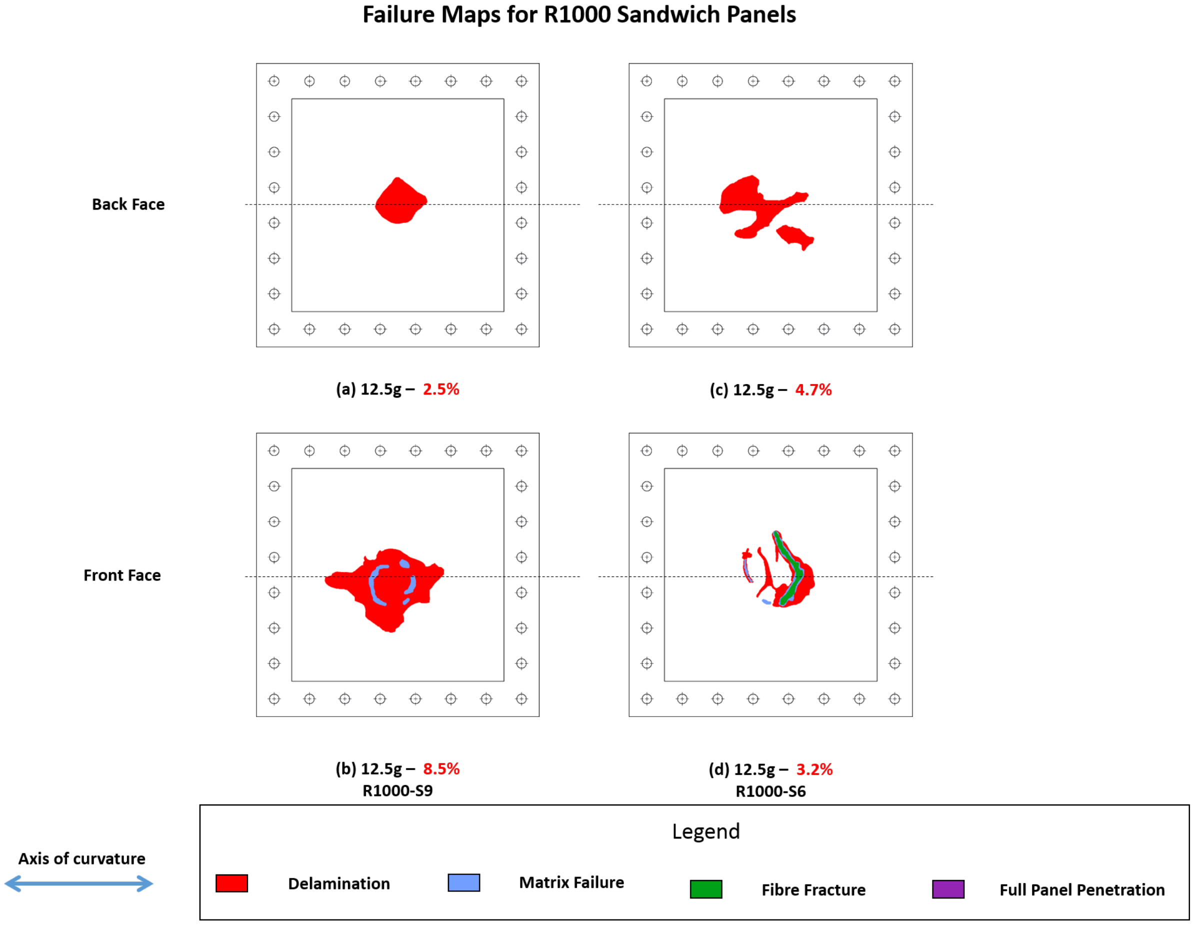

(a) 12.5g – 2.5%

(c) 12.5g – 4.7%

(b) 12.5g – 8.5%
R1000-S9

(d) 12.5g – 3.2%
R1000-S6

Figure F.6: Spatial distribution of delamination(red), matrix failure (blue) and fibre fracture (green) for selected R1000 sandwich panels

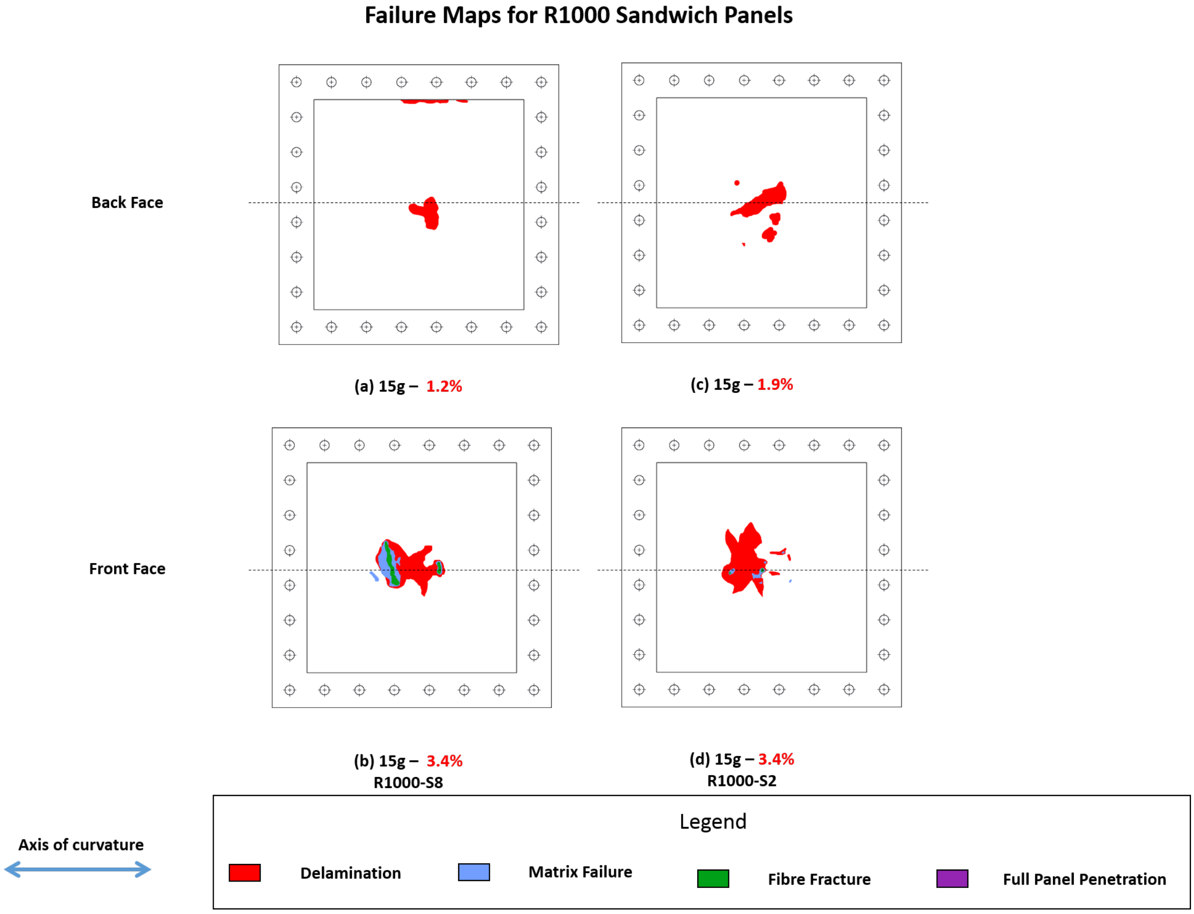

Figure F.7: Spatial distribution of delamination(red), matrix failure (blue) and fibre fracture (green) for selected R1000 sandwich panels

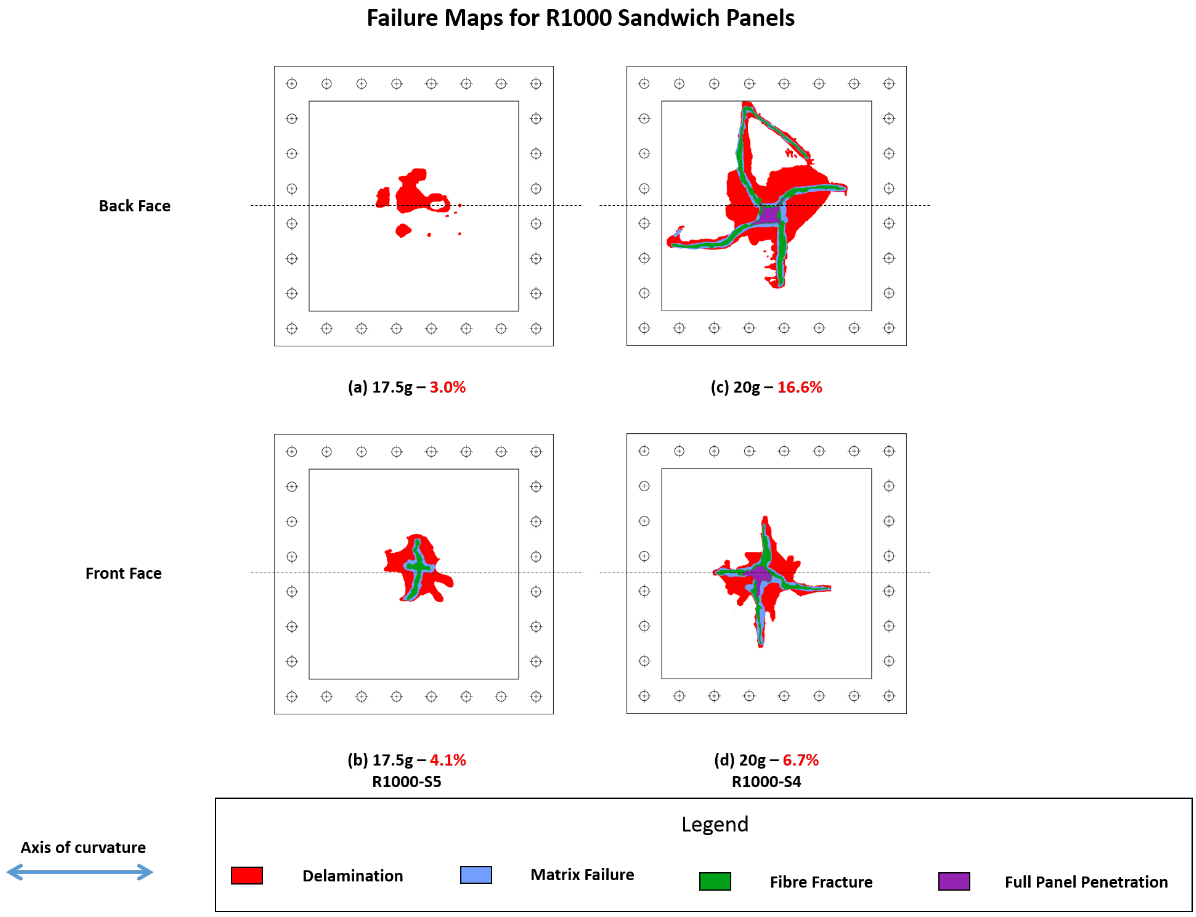

Figure F.8: Spatial distribution of delamination(red), matrix failure (blue), fibre fracture (green) and full panel penetration (purple) for selected R1000 sandwich panels

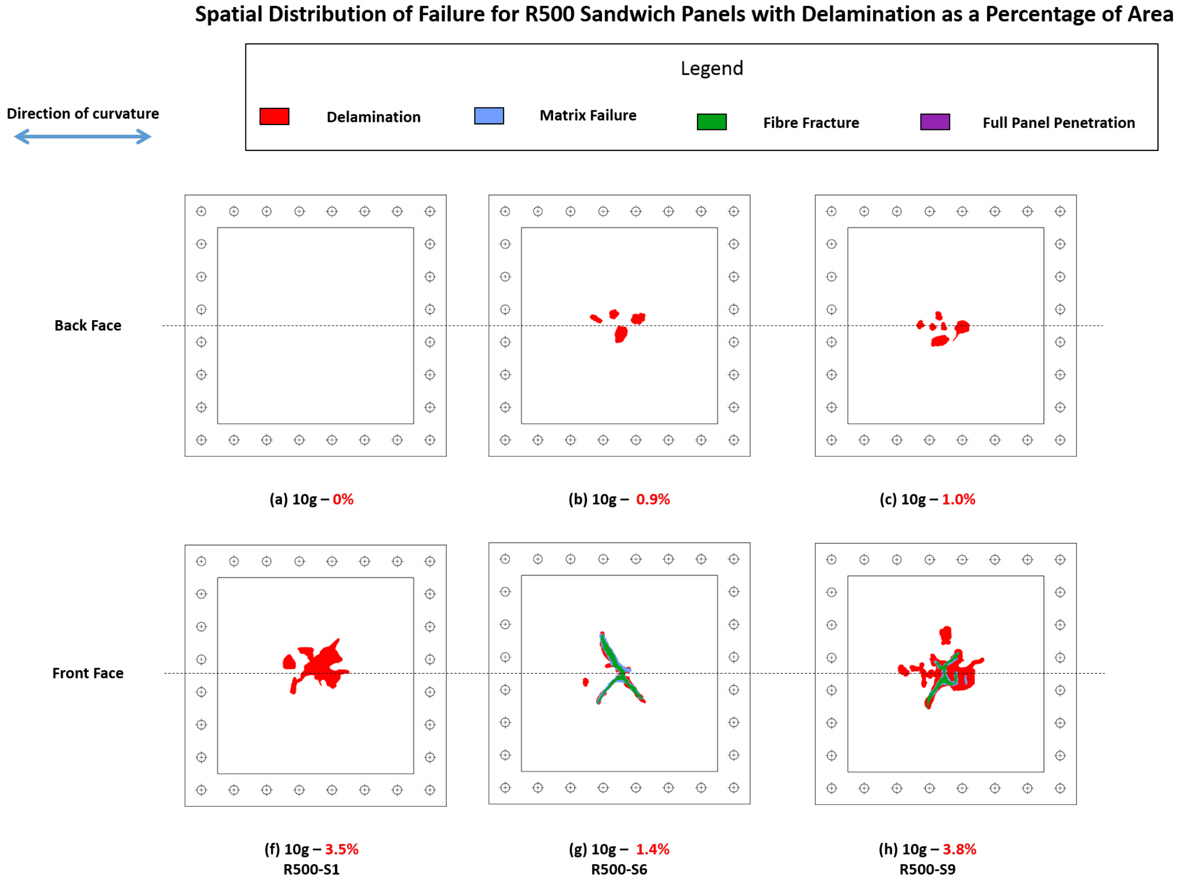

Figure F.9: Spatial distribution of delamination(red), matrix failure (blue) and fibre fracture (green) for selected R500 sandwich panels

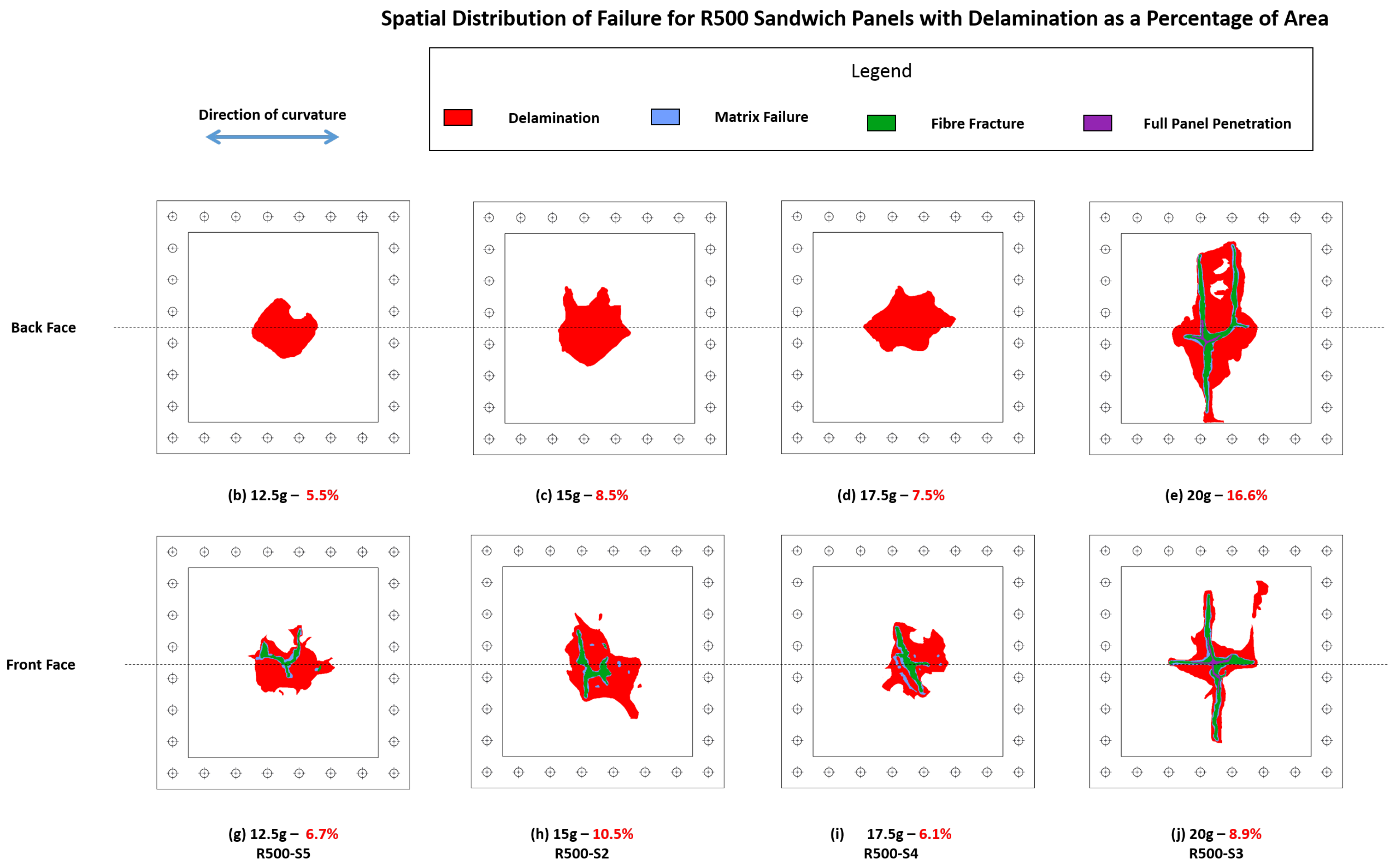

Figure F.10: Spatial distribution of delamination(red), matrix failure (blue), fibre fracture (green) and full panel penetration (purple) for selected R500 sandwich panels

Appendix G

Ethics Form

GHRISM001

EBE Faculty: Assessment of Ethics in Research Projects

Any person planning to undertake research in the Faculty of Engineering and the Built Environment at the University of Cape Town is required to complete this form before collecting or analysing data. When completed it should be submitted to the supervisor (where applicable) and from there to the Head of Department. If any of the questions below have been answered YES, and the applicant is NOT a fourth year student, the Head should forward this form for approval by the Faculty EIR committee: submit to Ms Zulpha Geyer (Zulpha.Geyer@uct.ac.za; Chem Eng Building, Ph 021 650 4791). Students must include a copy of the completed form with the thesis when it is submitted for examination.

Name of Principal Researcher/Student: Ismail Ghoor Department: Mechanical Engineering

If a Student: Degree: Msc (Eng) Supervisor: A/Prof Chris Von Klemperer

If a Research Contract indicate source of funding/sponsorship:

Research Project Title: Blast response of singly curved composite structures

Overview of ethics issues in your research project:

Question 1: Is there a possibility that your research could cause harm to a third party (i.e. a person not involved in your project)?	YES	[✓ NO]
Question 2: Is your research making use of human subjects as sources of data? If your answer is YES, please complete Addendum 2.	YES	[✓ NO]
Question 3: Does your research involve the participation of or provision of services to communities? If your answer is YES, please complete Addendum 3.	YES	[✓ NO]
Question 4: If your research is sponsored, is there any potential for conflicts of interest? If your answer is YES, please complete Addendum 4.	YES	[✓ NO]

If you have answered YES to any of the above questions, please append a copy of your research proposal, as well as any interview schedules or questionnaires (Addendum 1) and please complete further addenda as appropriate.

I hereby undertake to carry out my research in such a way that

- there is no apparent legal objection to the nature or the method of research; and
- the research will not compromise staff or students or the other responsibilities of the University;
- the stated objective will be achieved, and the findings will have a high degree of validity;
- limitations and alternative interpretations will be considered;
- the findings could be subject to peer review and publicly available; and
- I will comply with the conventions of copyright and avoid any practice that would constitute plagiarism.

Signed by:

	Full name and signature	Date
Principal Researcher/Student: Ismail B. Ghoor	Signed by candidate	22/01/2015

This application is approved by:

Supervisor (if applicable):		22-01-2015
HOD (or delegated nominee): Final authority for all assessments with NO to all questions and for all undergraduate research.		22/1/15
Chair : Faculty EIR Committee For applicants other than undergraduate students who have answered YES to any of the above questions.		

ADDENDUM 1:
Please append a copy of the research proposal here, as well as any interview schedules or questionnaires:

ADDENDUM 2: To be completed if you answered YES to Question 2:

It is assumed that you have read the UCT Code for Research involving Human Subjects (available at http://web.uct.ac.za/depts/educate/download/uctcodeforresearchinvolvinghumansubjects.pdf) in order to be able to answer the questions in this addendum.

2.1 Does the research discriminate against participation by individuals, or differentiate between participants, on the grounds of gender, race or ethnic group, age range, religion, income, handicap, illness or any similar classification?	YES	NO
2.2 Does the research require the participation of socially or physically vulnerable people (children, aged, disabled, etc) or legally restricted groups?	YES	NO
2.3 Will you not be able to secure the informed consent of all participants in the research? (In the case of children, will you not be able to obtain the consent of their guardians or parents?)	YES	NO
2.4 Will any confidential data be collected or will identifiable records of individuals be kept?	YES	NO
2.5 In reporting on this research is there any possibility that you will not be able to keep the identities of the individuals involved anonymous?	YES	NO
2.6 Are there any foreseeable risks of physical, psychological or social harm to participants that might occur in the course of the research?	YES	NO
2.7 Does the research include making payments or giving gifts to any participants?	YES	NO

If you have answered YES to any of these questions, please describe how you plan to address these issues (append to form):

ADDENDUM 3: To be completed if you answered YES to Question 3:

3.1 Is the community expected to make decisions for, during or based on the research?	YES	NO
3.2 At the end of the research will any economic or social process be terminated or left unsupported, or equipment or facilities used in the research be recovered from the participants or community?	YES	NO
3.3 Will any service be provided at a level below the generally accepted standards?	YES	NO

If you have answered YES to any of these questions, please describe how you plan to address these issues (append to form)

ADDENDUM 4: To be completed if you answered YES to Question 4

4.1 Is there any existing or potential conflict of interest between a research sponsor, academic supervisor, other researchers or participants?	YES	NO
4.2 Will information that reveals the identity of participants be supplied to a research sponsor, other than with the permission of the individuals?	YES	NO
4.3 Does the proposed research potentially conflict with the research of any other individual or group within the University?	YES	NO

If you have answered YES to any of these questions, please describe how you plan to address these issues(append to form)